



The University of
Nottingham

UNITED KINGDOM · CHINA · MALAYSIA

School of Mathematical Sciences

**Vibroacoustics of complex structures - a wave chaos
approach**

Neekar Majeed Mohammed

Thesis submitted to The University of Nottingham for the

degree of

Doctor of Philosophy

May 2021

Contents

Abstract	v
Acknowledgements	viii
1 Introduction	1
1.1 Motivation	1
1.2 Research scope	3
1.3 Objectives and Description of the work	10
1.4 Outline of the thesis	13
2 Background and literature review	16
2.1 Structural vibration	17
2.1.1 Thin plates	17
2.1.2 Thin shell theory	22
2.2 Acoustic	28
2.3 Wave dynamics—a ray perspective	32
2.3.1 Tunnelling	35

2.3.1.1	Resonant tunnelling	36
2.4	Numerical methods	37
2.5	Conclusion	39
3	Wave transition on shell structures	41
3.1	Introduction	41
3.2	Thin shell theory, short wavelength asymptotics and ray dynamics	44
3.2.1	Wave model for thin shells	45
3.2.2	Eikonal approximation for thin shells	47
3.2.3	Scaled variables	50
3.2.4	Models of shell geometry and dispersion curves	52
3.2.5	Phase portrait for bending rays	60
3.2.6	Transmission and reflection of bending waves: wave ap- proach	64
3.2.7	Wave scattering finite difference solution	66
3.3	Transmission and reflection of bending waves: resonant tunnelling	71
3.3.1	Overview	72
3.3.2	A graph model using complex rays	73
3.3.3	Local scattering matrices	79
3.4	Results	84
3.5	Conclusion	89
4	Sound Radiation	91

4.1	Theory of radiation from surfaces based on phase space densities	94
4.1.1	Correlation function	94
4.1.2	The random wave model (RWM): Diffuse-field	96
4.1.3	Sound Pressure distribution	101
4.1.4	Propagation of Sound radiation field	104
4.2	The Fast Fourier Transform (FFT) method	106
4.2.1	Steps of the calculation	106
4.3	Radiation pattern	109
4.4	Results	111
4.5	Conclusions	124
5	Radiation efficiency of a baffled plate	131
5.1	Radiation efficiency of finite plate with boundary supports	132
5.2	Sound radiation from plate-type structures	137
5.3	Problem setting	141
5.3.1	Sound radiation power in the spatial domain	143
5.3.2	Sound radiation power in the momentum domain	144
5.3.3	Radiation efficiency	147
5.4	Radiation efficiency of finite plate: Diffuse-field	149
5.4.1	Correlation function in momentum space with finite-size effects	150
5.4.2	Rectangular plates	155

5.5	Radiation efficiency of finite plate: mode shape approach	158
5.6	Comparison of the methods	166
5.7	Boundary correction to radiated power: a local approximation . . .	173
5.7.1	Local approximation of boundary contribution: momen- tum space approach	181
5.7.2	Asymptotic Approximation: the large α asymptotics	185
5.8	Conclusion	187
6	Summary	190
A	Preliminary and special functions	199
B	Fourier transformation of mode shapes	203
B.1	Infinite structures	203
B.2	Finite structures	204
C	WKB-approximation	205
C.1	The method of comparison equations	207
D	Corner correction in rectangular case	211
D.1	Infinite corner approximation	213
	Bibliography	215

Abstract

Modelling vibro-acoustics is of crucial importance in many areas of mechanical engineering and industry. In this PhD thesis we develop theoretical and computational methods for modeling vibro-acoustics of mechanical structures. We focus on simple structures such as flat plates and thin shells to investigate the vibro-acoustic response of structures using a phase-space method. These simple structures will provide quantitative guidance to the analysis of the vibro-acoustics response of complex structures.

In this thesis, an analytical model that captures wave effects using ray tracing treatment on thin shells is used. A ray dynamics describing wave transport on curved and smooth thin shells can be obtained from the underlying equations of motion via the Eikonal approximation. We first analyse mid-frequency effects near the ring frequency for thin shells consisting of a curved region smoothly connected to two flat plates. Using classical shell theory, we treat a corresponding ray-tracing limit derived in the short wavelength regime for bending, shear and pressure incident waves. We show that a smooth transition from total reflection to total transmission, along with the occurrence of resonant states, can be described in a ray tracing approximation by extending the treatment to complex rays. We are thus able to approximate the scattering matrix for waves incident on the bend accounting for tunnelling mediated by resonant states and uniformly treating the transition between the limits of totally reflected and totally transmitted waves.

A second contribution of this thesis is to propose a new method to model sound radiation using the vibrational response obtained from a phase space method such as the Dynamical Energy Analysis (DEA) method. The link between the structural response and the acoustic field can be achieved using so-called Wigner transform (WF) techniques. The energy density from a DEA structure-borne sound calculation can be related to field-field correlations of the vibrational displacement and then used to propagate the acoustic field using Rayleigh integral methods. In this way we compute the intensity of the sound pressure radiated from a flat plate. In addition to deriving an acoustic phase-space representation in the classical ray tracing limit, the impact of boundary conditions on acoustic radiation from vibrating flat plates, where the plate vibrations are assumed to be diffusive, has been studied. This technique has the potential to be used for generic complex mechanical structures.

Publications

- [1] N. M. Mohammed, S. C. Creagh, G. Tanner, and D. J. Chappell, “Tunnelling corrections to wave transmissions on shell structures,” in *28th Proc. Int. Conf. on Noise and Vibration Engineering ISMA*, pp. 2349–2362, 2018.
- [2] N. M. Mohammed, S. C. Creagh, and G. Tanner, “Sound radiation from complex vibrating mechanical structures using wigner transformation techniques,” in *14th Proc. Int. Conf. on Mathematical and Numerical Aspects of Wave Propagation WAVES*, p. 530, 2019.
- [3] N. M. Mohammed, S. C. Creagh, and G. Tanner, “Tunnelling around bends—wave scattering in curved shell structures,” *Wave Motion*, vol. 101, p. 102697, 2021.
- [4] N. M. Mohammed, S. C. Creagh, and G. Tanner, “Sound radiation from complex vibrating mechanical structures: phase space method,” *The first draught has been completed*, 2021.

Acknowledgements

I would like to start with the words of the U.S. President John F. Kennedy, used on September 12, 1962, in his historical speech “Address at Rice University in Houston on the Nation’s Space Effort” [1].

“We choose to go to the moon. We choose to go to the moon in this decade and do the other things, not because they are easy, but because they are hard, because that goal will serve to organize and measure the best of our energies and skills, because that challenge is one that we are willing to accept, one we are unwilling to postpone, and one we intend to win, and the others, too”.

First of all, I would like to express my heartfelt gratitude to both my supervisors Dr. Stephen Creagh and Prof. Gregor Tanner for giving me the opportunity to realise this important goal of my life. This work cannot be completed without their supervision and support. The amount of time and energy they have given to support throughout my time at the University of Nottingham cannot be expressed by words, and their patients seem to be unlimited. I am short of words to express my appreciation and sincere gratitude to them. They are great supervisors not only from the academic point of view but also from the perspective of life. The strong work ethic and doing research with the love and passion I learned from them will benefit me for life. It has been (is) a pleasure working with both of them and I am looking forward for our near and far future collaborations.

I am also deeply indebted to thank Dr Sharad Jain, he is from Romax Tech-

nology, for his supportive discussion and supporting my Ph.D. degree. I would also like to express my special thanks to Romax Technology and The University of Nottingham for funding my Ph.D. and giving me the chance to do one of the most important journeys of my life with these two fantastic supervisors.

Next to that, the working environment is a fundamental aspect to be mentioned. I am very thankful to the entire School of Mathematics department, especially the group research: wave chaos group, which provided me with great technical support and a friendly environment.

I have to express my deep gratitude to every member of my family here and for the rest of my life for enduring all the highs and lows with me, but not only throughout this journey, throughout my whole life. I am short of words to convey my absolute love and gratitude to my parents, Majeed and Ruqia, for their unconditional love and continuous encouragement. My heartfelt thanks to them for believing in me and in my abilities. Their love for science and higher education, particularly seeing my father's love and passion for mathematics as a mathematician, made me fall in love with mathematics and do research with all my heart. I would also like to thank them for their prayers for me to be safe, even though they have not been here with me, their prayers have been and are always with me wherever I am. I would therefore like to devote this thesis work to every member of my family, especially my parents and my loving sister, Sakar, because I would not have been able to complete my work without their love and affection.

Finally, this thesis is not the end of my academic research journey, it is just a

starting point. This journey has taught me to be a better researcher. I am passionately looking forward to the academic research journey after my Ph.D. experience. I hope, a few years from now, to look back on this path and see that I have accomplished at least some of the research goals I have, and hope this sentence is not just a hope. Last but not least, I would like to end this part with a quote that reflects my academic and life-long approach to problem solving, hoping to inspire anyone of you.

“Nothing in life is to be feared, it is only to be understood. Now is the time to understand more, so that we may fear less”. - Marie Curie

Chapter 1

Introduction

In this chapter, we introduce and motivate the problem that we are interested in and provide a review of the background and existing literature. Finally, we outline the structure of the thesis by summarising key results and ideas from each chapter.

1.1 Motivation

This work is a joint project of the University of Nottingham and Romax Technology, motivated by the aim of vibration and noise radiated from the gearbox casings. The casing is an essential element of a gear transmission since it covers the mechanical components and maintains the bearings and protects both the inner components against the working atmosphere and the environment from lubricant emissions. It is often the cause of noise among peripheral components. In many

instances, vibration from a gear transmits to a casing, making it vibrate considerably, resulting in acoustic-structure interaction which leads to subsequent external sound radiation and generation of noise [2, 3]. Compared to the noise from the friction of teeth, the frequency of sound is likely to be high. Furthermore, from a commercial point of view, reducing noise pollution results in greater comfort to passengers and drivers. Therefore, in the fight against environmental pollution, any dynamical study of the casing that provides insight into optimizing and reducing the noise generated by gear transmissions is important. Usually, the casings used around gearboxes are complex curved shell-structures see Fig. 1.1. In the design process, the reduction of gearbox noise radiation will take place by studying the wave dynamics of the entire casing structure. Alternatively, one can break the entire structure into simpler substructures and study their dynamics and the acoustic responses.



Figure 1.1: A model of a gearbox [4].

1.2 Research scope

Structural acoustics and vibrations, also termed vibro-acoustics, can be principally defined as a multidisciplinary field of engineering and physics, usually referring to the characterization of either the vibrational response of structures excited by incident sound fields or other fluid excitation or sound power produced by a vibrating structure subjected to external or internal dynamic excitation.

Over the past few years, much research has been conducted in the context of vibrations and noise control of structure-borne sound. Sound propagation in and radiation from complex vibrating mechanical built-up structures is a widely existing acoustic problem in engineering. It is important to understand the mechanisms of sound radiation from realistic structures, particularly structures that display complex boundary conditions, before decisive action can be accomplished at the design stage.

One of the main principles of studying structural vibrations and acoustic radiation is to determine the sound radiation of the medium according to the vibrational response of the structure-borne sound. Modelling the vibro-acoustic response of mechanical systems is a challenging task, especially for large complex mechanical built-up structures in the mid-to-high frequency regime. Usually, deterministic or statistical numerical methods are adopted to analyze the vibration of the complex structure to accomplish surface normal velocities and then perform numerical computation such as the finite element method (FEM) or

boundary element method (BEM) [5, 6, 7, 8, 9] to attain the radiated sound field.

At present, the numerical modelling of vibrations is usually carried out by FEM, which is most significantly established in this application area, and by BEM [7, 10, 11, 12, 13]. FEM is used to find solutions to differential equations that explain a broad range of physical and non-physical problems [14, 15], or to describe them roughly. The BEM is fundamentally derived through discretising an integral equation equivalent to the original partial differential equation [16]. These deterministic techniques can describe geometric details with sufficient accuracy for low-frequency applications. However, high-frequency modelling requires extremely fine meshes to capture the shorter wavelengths. For this purpose, these methods are practically restricted to low-frequency applications. Therefore, more efficient algorithms become desirable, and in particular, high frequency approximation methods become an attractive alternative.

In order to cope with this limitation and leading to relatively small and simple models in comparison with FEM/BEM, for high-frequency modelling, some alternative, statistical techniques such as the Statistical Energy Analysis (SEA) [17] have been developed. In this probabilistic technique, the complex structure is divided into simply connected subsystems and assuming diffuse wave fields and quasi-equilibrium conditions in each of the resulting subsystems. A SEA has found widespread applications in the aviation industry and automotive, as well as in architectural acoustics and has been described in detail in textbooks by Lyon and De Jong [17], Keane and Price [18] and Craik [19]. However, there are short-

comings in SEA that have been addressed by Langley [20] and more recently by Le Bot [21, 22]. One limitation of SEA is that the underlying assumptions are often hard to verify a priori, for example determining the coupling loss factors. It was shown in [23] that significant differences in the coupling parameters can be caused by small variation of material properties. SEA treatment often has problems in capturing the non-trivial way in which the curved shell geometry influences the wave propagation [24] (Langley discovered that the directions of wave propagation and energy propagation can differ substantially, and he suggested that this result should be included in the SEA loss factor calculation).

A high-frequency method such as ray-tracing may be employed as an alternative to SEA, leading to a relaxation of SEA assumptions and works in frequency ranges where FEM or BEM models are becoming too large. Ray-tracing can be used in a wide range of applications such as in acoustics, electromagnetism and optics [25, 26]. A detailed review discussing the transition from waves to rays has been given by Tanner and Søndergaard [27]. Only recently, attempts to implement ray-tracing ideas for structure-borne sound have been considered. In particular, ray-tracing on complex built-up structures has been implemented using the so-called Dynamical Energy Analysis (DEA) [28] describing wave transport in the high-frequency limit.

The DEA method has been formulated on meshes and is based on local ray-tracing approximations in which ray trajectories move along straight lines in each mesh segment. DEA can thus estimate the flow of vibrational energy in shell

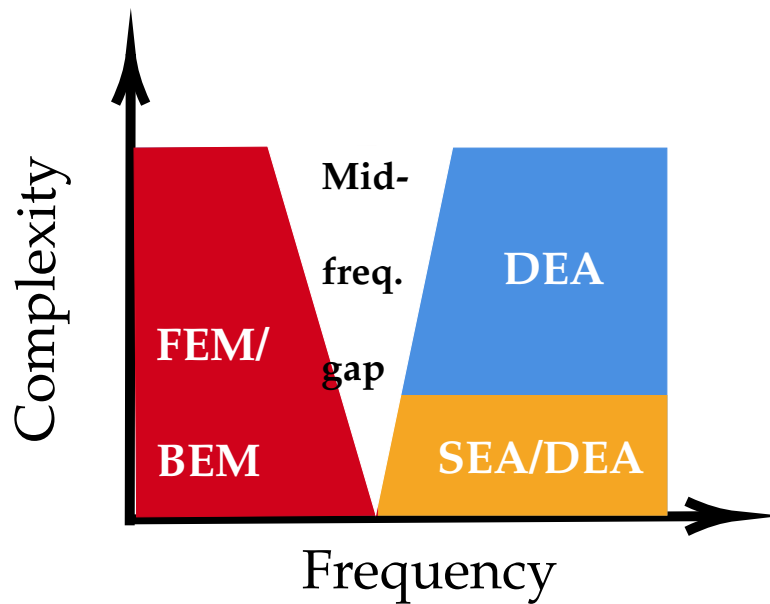


Figure 1.2: Systematic representation of some existing methods in modelling vibrational response.

structures of arbitrary complexity, such as full body-in-blue vehicles [29]. Thus, this phase-space method based on a linear operator approach for propagating ray densities systematically interpolates between SEA and full ray tracing with much more freedom in sub-structuring the total system to be modelled. Figure 1.2 provides an overview of the various methods that have been used in modelling vibrational response of a mechanical structure. DEA describes the ray dynamics well in homogeneous, isotropic, flat plates or on curved shells at high frequencies in the geodesic ray limit. In the case where the curvature of the shell is of the same size as the wavelength, the situation will change as the underlying equations of motion for the curved rays depend on the local radii of curvature. The implementation of curvature corrections in a DEA treatment based on meshed shell

structures has been discussed in [30]. Here, the local ray dynamics is approximated using piecewise straight line segments, including back reflections, which can lead to distortions for moderately curved shells (with radius of curvature comparable to the wavelength). Improvements on this rather ad-hoc approach have been reported in [31, 32]. We will revisit and extend these results in this thesis.

The most straightforward description of an acoustic field is that of a sound pressure field, with the sound pressure varying over the domain and over time. The FEM [33, 34] and the BEM [35, 36, 37, 38] can model the transient acoustic field computationally, allowing arbitrary geometry to be considered but not providing the same physical insight as analytical methods. The most likely fluid domains for acoustic problems are air or water and, in many cases, the linear wave equation is an appropriate model for these fluids.

In order to estimate the sound pressure and the radiated sound power from vibrating a complex structure, computer software must be used. However, in order to make sure that the right models are used, the results have to be compared with the theory. Theory exists for simple structures like flat plates; particularly common calculation are for a rectangular or a circular shapes. Therefore, the sound radiated from plate structures, as well as the influence of boundary conditions on the sound radiated, is studied in this thesis. Besides the fact that studying sound radiation from vibrating plate-like structures serves as a first step to understand and manipulate the dynamics and behaviour of sound radiated from more com-

plex structures, plates with different sizes and aspect ratios are excessively used as important structural components in different forms of transportation vehicles, airplanes, industrial machinery, and as well as buildings and bridges. In many cases, the geometry of structures such as machinery casings, car body shells, hulls of ships, or other structural systems comprised of panels can be divided into sub-structures which have geometries approximately described by flat plates [39], for example see Fig. 1.3 (in this thesis, we examine sound radiation from a simple structure in order to validate our phase space method. The whole boundary integral equation will be used to estimate sound flowing off arbitrary surfaces in the next step). After reducing the complexity of such structures, the dynamics of sound radiation can then be modelled more easily, using either analytical or numerical approaches. Therefore, from studying an isolated plate, for many complex structures, the determination of sound radiation can then be estimated reasonably accurately [40].

Traditionally, acoustic radiation efficiency is evaluated for structure-borne sound. Since the 1960s, acoustic radiation efficiency has been studied extensively, in particular for thin plates. The efficiency of acoustic radiation is typically determined using modal summation, such that the radiation efficiency of a single-mode is often called modal radiation efficiency. Note that both the terms "radiation resistance" and "radiation efficiency" are used in the literature. Radiation efficiency is essentially a normalized radiation resistance with respect to medium properties and surface geometry. Oideon Maidanik in 1962 [41] suggested a statistical ap-

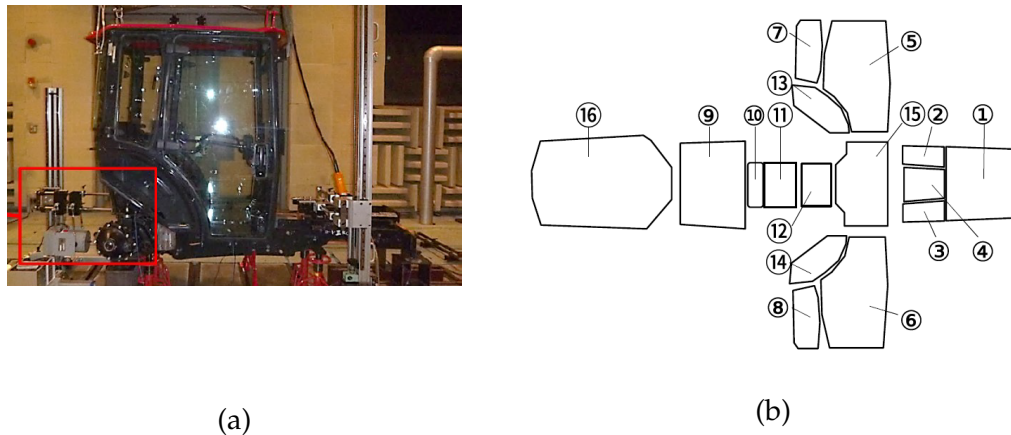


Figure 1.3: (a) Tractor model from Yanmar Co., Ltd. (b) Subsystems of the tractor cabin [39].

proach estimating the structural vibration of ribbed panels in response to acoustic excitation. In the entire frequency spectrum under various wavenumber regions, the radiation resistance of the ribbed panel is studied. Even the effects of different boundary conditions are theoretically and experimentally studied.

Wallace subsequently proposed numerical integrations in 1972 [42, 43] finding approximate solutions for the single-model radiation efficiency of the baffled beam and rectangular plate. In terms of the acoustic power radiated into the far-field, the radiation resistance corresponding to individual modes is computed. Approximations are specifically calculated for various modes shapes over the whole frequency range.

Subsequently, a number of other studies focused on different aspects have been published. Under general boundary conditions, Gomperts tested the acoustic radiation efficiency of a baffled rectangular plate [44]. Results show that imple-

mentation of restrictions in edge areas may not always increase radiated acoustic waves into the far-field. He additionally found that the radiation efficiencies of two-dimensional vibrating structures vary rather impressively from those for one-dimensional vibrating structures. By using a Fourier Transform method in wavenumber space, Heckl studied the radiation patterns of planar sources [45]. A series of asymptotic formulas were published by Leppington *et al.* [46] to estimate the radiation efficiency of different plate wavenumbers, in particular for large structural wavenumbers and near-critical frequencies. In order to analyze the sound power originating from planar sources, Williams [47] suggested expansion in the powers of the structural wavenumber. The Fourier transformation of surface velocities along with its corresponding derivatives is used to derive the mathematical model for estimating acoustic power radiating of a rectangular baffled thin plate under different boundary conditions at low frequencies.

1.3 Objectives and Description of the work

The main objective of this thesis is to establish models for the coupling of structural vibrations calculations with the estimation of acoustic radiation using a phase space method such as DEA.

We had two main focuses to develop: the first one, was to implement curvature effects in the DEA method. The emphasis is therefore placed on a vibrating, curved shell structures. We began by providing insight into the propagation of

waves in curved shells. An analytical model that captures wave effects in a ray-tracing treatment on curved plates has been proposed in Chapter 3. In addition, a case-study for a cylindrical region smoothly connecting to two flat plates has been proposed for three different curvature profiles of the structure. Furthermore, we visit the one-dimensional tunnelling problem in mechanical built-up structures. The model treats wave effects which account for resonant tunnelling using an approximation extending rays to complex rays. We allocate locations of resonance states in the system by a driven resonant condition formula.

To validate the model, the shell's equations of motion for the problem setting has been solved numerically using finite difference methods for all curvature profiles, and the results have been compared to the model results for all of the curvature profiles. The result of the model for smooth curvature profile agrees with the numerical solution. For more sharp and flat top curvature profiles the model formally breaks down, especially close to the transition region between reflection and transmission ranges, although it still gives reasonable qualitative agreement with the numerical solution.

This study provides an important opportunity to advance the understanding of: curvature effects on wave transport and dispersion relations in the mid frequency range, curved ray-tracing, resonant tunnelling in solid structure, complex ray-tracing, resonance state condition, and best choice of curvature distribution along the curved structure.

The second focus in this thesis has been to model sound radiation using the in-

formation from the vibration response obtained using DEA method. DEA gives implicit information about the phase function. To explicitly recover the phase function, we use an inverse Wigner transform approach, which is a quasi-probability distribution that helps analyse radiation from complex sources statistically in free space. Using this method, the field-field correlation function in phase space can be extracted from the energy flow density from DEA.

Plates of various dimensions and aspect ratios are commonly used in automobiles, aircraft, industrial equipment, buildings, and bridges as important structural components. It is helpful to understand the sound radiation from vibrating plates for the purpose of predicting and mitigating noise from complex structures. The spatially averaged vibration velocity and radiation efficiency of the plate are two important factors that affect the radiated sound power of a vibrating plate. Furthermore, the sound directivity and pattern also play a significant role in evaluating sound pressure distributions for external radiation problems. For that we use the Rayleigh integral method [48], which is a method that relates the sound pressure (or velocity potential) at a point in a half-space to the vibration of a plate, as an operator on the field-field correlation function to compute the intensity of sound pressure that has been radiated from the structures. Therefore, based on this method, we extend DEA towards coupling structural vibration calculations with estimating acoustic radiation in the surrounding fluid.

The boundary conditions of a vibrating plate, for frequencies below the critical frequency, are known to have an important effect on its sound radiation. Then,

having the field-field correlation function in phase space, we study the impact of boundary conditions. To investigate this influence systematically, the average radiated power and radiation efficiency are calculated for plate-like structures.

The objectives of this thesis are therefore summarised below:

- Implementing curvature effects in DEA method;
- Extending DEA towards coupling structural vibration calculations with estimating acoustic radiation;
- Recovering phase information from the phase space density of the vibrating structure using the DEA calculation (linking phase space density to the normal surface velocity correlation function);
- Coupling between the structural wave correlation function propagating in a vibrating element with acoustic sound radiation;
- Calculating radiation pattern;
- Capturing the effects of finite size structure along with boundary conditions on the sound radiation field.

1.4 Outline of the thesis

A brief summary of the basic principles of vibration and acoustics that form the basis for much of the work described in the followed chapter will be the material provided in Chapter 2.

In Chapter 3, an analytical model that captures wave effects in a ray-tracing treatment on curved plates has been revisited. Furthermore, a case-study for a cylindrical region smoothly connected to two flat plates, has been proposed for three different curvature profiles of the structure. In addition, we visit the one-dimensional tunnelling problem in mechanical built-up structures. We proposed a graph model which treats the wave effects that account for resonant tunnelling by extending classical rays to complex rays. The model has been validated with a numerical solution of the shell's equations of motion for all curvature profiles.

In Chapter 4, we treat the simplest case of homogeneously diffuse fields on the vibrating structure corresponding to uniform ray densities in phase space. We model the diffuse field explicitly as a random superposition of plane waves using Berry's conjecture [49], modified near edges to account for boundary conditions. In this study, we will utilize the inverse Wigner transform approach within finite domains, which may be regularly or irregularly shaped. The effect of boundary conditions on sound radiation below and above the critical frequency is studied as they form a basis for later chapter. We extend DEA towards coupling structural vibration calculations with estimating acoustic radiation in the surrounding fluid; the method is based on the inverse Wigner transform technique.

The effect of plate boundary conditions in the case of baffled plates is considered in Chapter 5, using the simplest case of homogeneously diffuse fields corresponding to uniform ray densities in phase space. Due to the boundary conditions, this model has been modified to provide corrections near boundaries.

Here, we consider Dirichlet or Neumann boundary conditions. We also present numerous approximations to calculate the radiation efficiency of finite plates assuming diffusive field excitation.

Chapter 2

Background and literature review

This chapter covers some foundational material for this thesis. In order to constructively study the theoretical results presented later, it is only necessary to understand the fundamental equations governing the vibration of the mechanical structure, here of two types, thin plate and thin shells.

The analysis of the governing equations of the vibration of a plate highlights the natural frequency and mode shapes. The evaluation of plate vibrations is essential because the sound waves radiated are straightforwardly associated with the geometrical and dynamical properties of the plate. The structural response, particularly at high frequencies, is sensitive to variations within the material and physical properties [50]. As a consequence, modelling and analysing such situations become critical in numerous acoustic and sound applications related to larger, complicated and irregular structures.

2.1 Structural vibration

The motion of the vibration varies depending on the structure's geometry, properties, and boundary conditions. Different methods are sufficient for different types of structures. Here, we revisit the governing equations for the propagation of elastic waves for two of the structural types, thin plates and thin shells. The thin plate and thin shell can be classified as objects with one of their dimensions, thickness, being smaller than the other two (length, width). The phrase "small" suggests that some approximations to general elasticity equations are sufficient to adequately describe strains and stresses ; consequently, different equations are utilised depending on the level of accuracy required to predict the physical phenomena. There are numerous theories of thin plates and shells that are based on various assumptions and hypotheses (e.g. [51, 52, 53, 54, 55, 56, 57, 58, 59, 60]).

2.1.1 Thin plates

The plate model is a common approximate model used extensively in acoustic studies, particularly with regards to radiation and dispersion. A number of vibro-acoustics models have been constructed with varying complexity to predict the sound insulation characteristics of plate structures. Although thin and thick plates are distinguished based on the ratio of thickness to lateral dimensions [61, 62] in structural mechanics and dynamics, such rules may not be sufficient for vibro-acoustics calculations because they also depend on the material proper-

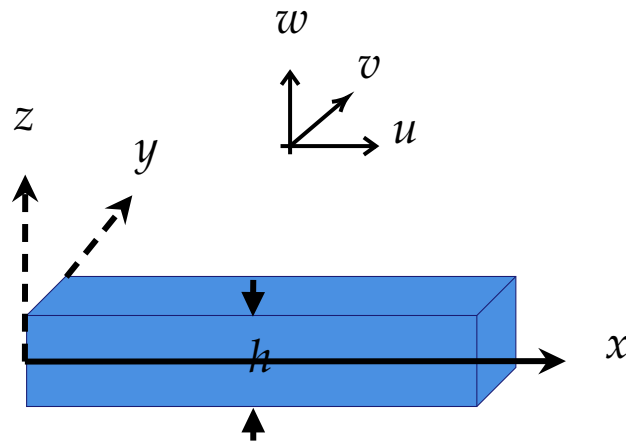


Figure 2.1: A nomenclature scheme for discussing the dynamics of a nominally flat plate. In its undistorted position, the middle surface lies in the $x - y$ plane and particles have displacement components u , v , and w on the middle surface, each of which varies with x and y [63].

ties of the plate. A plate would be considered "thin" in an acoustic context if its thickness is much smaller than the wavelength of an incident or acoustic wave in the adjacent fluid.

Vibrational motion can be described as a wave propagation. In theory, waves can propagate in four main modes, longitudinal (pressure) waves, shear waves, bending (flexural) waves and evanescent bending waves depending on how the particles oscillate. The vibration of a thin plate is governed by a differential equation of the fourth-order.

There is a tremendous amount of study regarding the free vibrations of various geometries of plates. This has emerged from the significance of the plate structure in engineering applications. Just the briefest inclusion can be given to

the subject here. Consider free vibrations of a thin flat plate where the plate is oriented so that the ambient position of its middle surface aligns with the $x - y$ plane, see Fig. 2.1. Thus, the normal component of the displacement w is given by [63]

$$\begin{aligned} \rho_s h \frac{\partial^2 w}{\partial t^2} + \frac{\partial^2}{\partial y^2} \left(B \left(\frac{\partial^2 w}{\partial y^2} + \nu \frac{\partial^2 w}{\partial x^2} \right) \right) + \frac{\partial^2}{\partial x^2} \left(B \left(\frac{\partial^2 w}{\partial x^2} + \nu \frac{\partial^2 w}{\partial y^2} \right) \right) \\ + 2 \frac{\partial^2}{\partial x \partial y} \left(B(1 - \nu) \frac{\partial^2 w}{\partial x \partial y} \right) = 0, \end{aligned} \quad (2.1)$$

where B is the bending stiffness of the plate given by

$$B = \frac{Eh^3}{12(1 - \nu^2)}, \quad (2.2)$$

and ρ_s is the mass density per unit area of the plate, ν is Poisson's ratio, and E is Young's modulus. For plates surrounded by a fluid, an additional term p_{diff} will couple to the Eq. (2.1) to express the pressure difference on either side of the plate [63].

This reduces to the simpler form if the plate is homogeneous, so that ν and D are constants.

$$B \nabla^4 w + \rho_s h \frac{\partial^2 w}{\partial t^2} = 0,$$

where $\nabla^4 = \left(\frac{\partial^2}{\partial x^2} + \frac{\partial^2}{\partial y^2} \right)^2 = \frac{\partial^4}{\partial x^4} + 2 \frac{\partial^4}{\partial x^2 \partial y^2} + \frac{\partial^4}{\partial y^4}$. For a harmonic excitation $w(x, y, t) = \hat{w}(x, y) e^{-i\omega t}$ where $\omega = 2\pi f$ is the angular frequency and f is the natural fre-

quency, this equation is often written in the frequency domain, as

$$\nabla^4 \hat{w} - k_B^4 \hat{w} = 0,$$

where $k_B = (\rho_s h \omega^2 / B)^{1/4}$ is the bending wavenumber, and $k_B^2 = k_x^2 + k_y^2$, where k_x and k_y are the two components of the structural wavevector \mathbf{k}_B in the x and y directions.

The study of finite-plate vibrations is more practical than the infinite case; in low to mid-frequencies, finite-size effects are known to be critical to sound transmission problems. The literature on finite plates is comprehensive and is widely discussed [51, 52, 53, 54, 55, 57, 50, 58, 59, 64]. Among these mechanical properties, in the low-mid frequency range, the vibroacoustic response is known to be influenced by support conditions along the boundaries and these are of importance for noise control. Vibrational studies of structures with different boundary conditions has been given considerable attention [50]. It is generally agreed that there is no exact solution for classical boundary conditions, even for simple plate structures, such as rectangular ones, except in some cases, which require specific supports to be applied to at least one pair of opposite edges [65]. The support of the plate along its boundaries is essential for its vibration and its radiation. Having simple solutions that could illuminate essential concepts and validate methods to be discussed at a later stage, we focus here in particular on two types of boundary supports called simply supported boundary conditions (what we call pseudo Dirichlet boundary conditions in the later chapter) and guided boundary

conditions [66] (what we call pseudo Neumann boundary conditions in the later chapter). For example, boundary conditions for a simply supported rectangular plate of length L_x and width L_y and height h (with $h \ll L_x$ and L_y) are:

$$\begin{aligned}\hat{w} = 0, \frac{\partial^2 \hat{w}}{\partial x^2} + \nu \frac{\partial^2 \hat{w}}{\partial y^2} &= 0 \text{ at } x = 0 \text{ and } x = L_x, \\ \hat{w} = 0, \frac{\partial^2 \hat{w}}{\partial y^2} + \nu \frac{\partial^2 \hat{w}}{\partial x^2} &= 0 \text{ at } y = 0 \text{ and } y = L_y.\end{aligned}$$

Then the normal displacement for the vibrating rectangular plates is a product of sine functions

$$\hat{w}(x, y) = \sin(k_x x) \sin(k_y y), \quad (2.3)$$

where $k_x = \frac{n\pi}{L_x}$ and $k_y = \frac{m\pi}{L_y}$ for $n, m = 1, 2, 3, \dots$, and with $k_{n,m}^2 = k_x^2 + k_y^2$.

On the other hand, boundary conditions for a guided plate [66] are:

$$\begin{aligned}\frac{\partial \hat{w}}{\partial x} = 0, \frac{\partial \hat{w}}{\partial x} \left(\frac{\partial^2 \hat{w}}{\partial x^2} + \nu \frac{\partial^2 \hat{w}}{\partial y^2} \right) &= 0 \text{ at } x = 0 \text{ and } x = L_x, \\ \frac{\partial \hat{w}}{\partial y} = 0, \frac{\partial \hat{w}}{\partial y} \left(\frac{\partial^2 \hat{w}}{\partial y^2} + \nu \frac{\partial^2 \hat{w}}{\partial x^2} \right) &= 0 \text{ at } y = 0 \text{ and } y = L_y.\end{aligned}$$

Then the normal displacement for the vibrating plate is a product of cosine functions

$$\hat{w}(x, y) = \cos(k_x x) \cos(k_y y), \quad (2.4)$$

where $k_x = \frac{n\pi}{L_x}$ and $k_y = \frac{m\pi}{L_y}$ for $n, m = 0, 1, 2, \dots$, with $k_{n,m}^2 = k_x^2 + k_y^2$.

In the next section we present the theory of shells, which is a natural extension of the discussion of plates

2.1.2 Thin shell theory

In acoustics, many modern topics include shells, since man-made objects, such as vehicles, ships, aircraft, spacecraft, and vessels containing fluid, have exterior skins that often adhere to shell-related idealizations. In addition, practical subjects in underwater radiation and dispersion usually have structures that can be idealized as shells in the majority of cases. A shell's fundamental conceptualization is simply that of a curved plate, although the presence of non-zero curvature brings to the mathematical description considerable added complexity. The theory of shells goes all the way back to papers published in the 1880s by Rayleigh [67, 68, 69], Lamb [70], and Love [71]. The focus was primarily on bell vibrations and sound radiation at that time. Of course, over the years, the theory has evolved considerably and has been the topic of hundreds of publications and many books. In the current literature, many different shell models of different levels of complexity are presented in [51, 52, 53, 54, 55, 56, 57, 58, 59, 60, 72], but all more or less agree in their predictions for shells that are sufficiently thin.

Numerous thin-shell theories have been derived to determine the dynamic and vibro-acoustic behaviour of structures. These include Donnell's theory [73, 74, 75], Love-Timoshenko theory [76], and the work of Sanders and Flügge [77]. The acoustically thick and thin shells are distinguished in terms of shell curvature effects on acoustic radiation behaviour. For cylindrical shells, the ring frequency is an important parameter used to indicate the range in which curvature effects

are important. The ring frequency is defined for the condition when the wavelength of extensional waves in the shells is equal to the shell circumference

$$f_{\text{ring}} = \frac{1}{2a\pi} \sqrt{\frac{E}{\rho_s (1 - \nu^2)}}.$$

where a is the radius of cylindrical shell, ρ_s is the density of the material, E is the Young's Modulus and ν is the Poisson ratio. Far above the ring frequency, the structural wavelength is so short that the structural wave propagation is very much controlled by local stiffness. The curvature effects of the shell extremely small, and the structure will behave like a plate. The sound radiation will as a result be governed by the compliances between the total structural wavenumber and the acoustic wavenumber. In this frequency range, the critical frequency defined for the plate is of physical significance because of no dispersion effects for the structural wavenumbers. Below the ring frequency, the curvature changes the stiffness in the axial direction, making the structural wave speed in this direction faster than that in circumferential direction. Then the sound radiation is primarily determined by the behaviour of each individual mode in the total repose. In this case, the physical significant of the critical frequency defined for the plate becomes questionable [78].

In many ways, wave propagation on thin shells is similar to thin plates for which uncoupled in-plane (pressure and shear) and out-plane (flexural or bending) motions are predicted by the leading order or classical approximations. Shell curvature embodies these such that the displacement of concern is a three vector,

and the wave mode is identical to those on thin flat plates: longitudinal, shear, flexural and flexural evanescent. The goal here is to present as simple a model as possible for the thin-shell limit. The model in this thesis are founded on Donnell's shell theory, which is discussed in more detail by Pierce [79], and Norris and Rebinsky [80]. It is possible, of course, to establish governing equations for shells with an arbitrary curvature, and afterward to adapt the outcomes to a specific geometry, for example, a cylindrical-shaped shell. Therefore, the discussion here is for shells of arbitrary form, we reduce the model to a specific geometry of cylindrical-shaped shell jointed to a flat plate in either side later. This topic is a key component of the overall future potential discussion of radiation and underwater sound dispersion using DEA.

An arbitrary thinly walled shell is considered (Fig. 2.2) with density ρ_s , Poisson ratio ν and Young's modulus E . Its wall thickness h is much less than either of its two main curvature radii. $\mathbf{X} = (X, Y)$ is the coordinate system representing the position on the shell with respect to the tangential and perpendicular direction to the middle surface shown in Fig. 2.2 . The corresponding curvilinear coordinates on the shell are $\mathbf{x} = (x, y)$, where $\mathbf{X} = \mathbf{X}(x, y)$, with corresponding direction vectors $\mathbf{a}_\alpha = \mathbf{X}_{,\alpha}$, $\alpha = 1, 2$, and surface normal $\mathbf{a}_3 = \mathbf{a}_1 \wedge \mathbf{a}_2 / |\mathbf{a}_1 \wedge \mathbf{a}_2|$. Greek sub or superscripts assume the values 1 or 2, and the suffix $_{,\alpha}$ denotes differentiation with respect to x^α . The covariant surface metric tensor and the covariant surface curvature tensor, both symmetric, are given by $g_{\alpha\beta} = \mathbf{a}_\alpha \cdot \mathbf{a}_\beta$ and $d_{\alpha\beta} = \mathbf{a}_\alpha \cdot \mathbf{a}_{3,\beta}$ respectively. The contravariant form of the surface metric tensor and the mixed

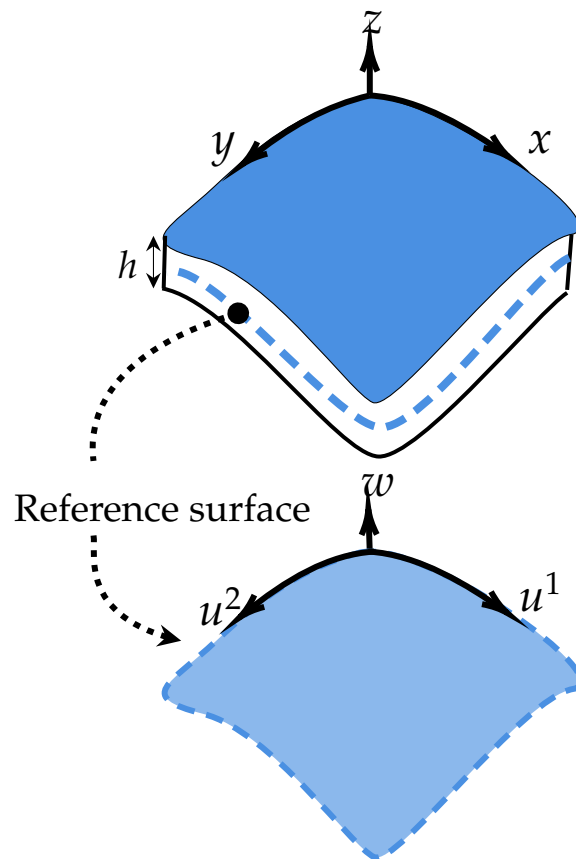


Figure 2.2: Sketch of an arbitrary shell with a curvilinear coordinate scheme for representing surface positions.

form of the curvature tensor are $g^{\alpha\beta}g_{\alpha\beta} = \delta^{\alpha\beta}$, $d_{\alpha}^{\beta} = g^{\alpha\gamma}d_{\gamma\beta}$. The displacement vector of a point originally on the mid-surface of the shell is decomposed into tangential and normal components thus $\mathbf{u} = [u^1 u^2 w]$. The covariant differentiation with respect to x^{α} is denoted by D_{α} and the contravariant differentiation is denoted by $D^{\alpha} = g^{\alpha\gamma}D_{\gamma}$. The equations of motion for a shell in *vacuo* composed of an isotropic material are

$$\rho_s h \frac{\partial^2 u^{\alpha}}{\partial t^2} = D_{\beta} \left(C \left((1 - \nu) \varepsilon^{\alpha\beta} + \nu \varepsilon_{\gamma}^{\gamma} g^{\alpha\beta} \right) \right), \quad (2.5)$$

$$\begin{aligned} \rho_s h \frac{\partial^2 w}{\partial t^2} = & -D_{\alpha} D_{\beta} \left(B(1 - \nu) D^{\alpha} D^{\beta} w \right) - D_{\alpha} D^{\alpha} \left(B \nu D_{\beta} D^{\beta} w \right) - \\ & C \left((1 - \nu) d_{\beta}^{\alpha} \varepsilon_{\beta}^{\alpha} + \nu d_{\alpha}^{\alpha} \varepsilon_{\alpha}^{\alpha} \right), \end{aligned} \quad (2.6)$$

where B and C are the bending stiffness and extensional stiffness given by

$$B = \frac{Eh^3}{12(1 - \nu^2)}, \quad C = \frac{Eh}{1 - \nu^2}. \quad (2.7)$$

The in-surface strains are

$$\varepsilon_{\alpha\beta} = \frac{1}{2} (D_{\alpha} u_{\beta} + D_{\beta} u_{\alpha}) + d_{\alpha\beta} w. \quad (2.8)$$

Later, a simplified version of this shell equation is given for a special case of a shell being bent only along one of the axes and jointed to a flat plate in either side, see also S ndergaard *et al.* [32, 31]. Vibrations that occur on the interface between two linked bodies with varying elastic properties are known as interfacial vibrations. This phenomena for thin-walled structures was apparently discovered for the first time in studies [81, 82] that investigated the analogues of Stoneley's

waves [83] in connected plates and half-strips. Interfacial vibrations of coupled shells of revolution were explored using an asymptotic method in [84]. Some of recent publications within [85] investigated the free interfacial vibrations of infinite closed and open cylindrical shells made of two semi-infinite orthotropic elastic cylindrical shells with differing elastic characteristics. The authors of these works used an asymptotic technique to obtain the dispersion equations as well as formulae for eigenfrequencies, and they discovered asymptotic links between the dispersion equations of the problems under investigation and related problems for joined half-strips and rectangular plates. There is a similarity between edge and interfacial vibrations of thin plates and shells in that the modes are observed in the form of functions exponentially decaying away from an edge or interfacial surface for both forms of localised vibrations. The study by Lawrie and Kaplunov [86] is recommended for a detailed history and overview of edge and interfacial vibrations in plates and shells.

For shell surrounded by a fluid or subjected to any external dynamic loads, additional terms corresponding to the external loadings on the shell surface per unit area, $\mathbf{q} = [q^1, q^2, q^3]$, will be coupled to the shell's equations of motion [87]

$$\begin{aligned} \rho_s h \frac{\partial^2 u^\alpha}{\partial t^2} &= D_\beta \left(C \left((1 - \nu) \varepsilon^{\alpha\beta} + \nu \varepsilon_\gamma^\gamma \delta^{\alpha\beta} \right) \right) + q^\alpha, \\ \rho_s h \frac{\partial^2 w}{\partial t^2} &= -D_\alpha D_\beta \left(B(1 - \nu) D^\alpha D^\beta w \right) - D_\alpha D^\alpha \left(B\nu D_\beta D^\beta w \right) - \\ &C \left((1 - \nu) d_\beta^\alpha \varepsilon_\beta^\alpha + \nu d_\alpha^\alpha \varepsilon_\alpha^\alpha \right) + q^3. \end{aligned} \quad (2.9)$$

These loadings are the acoustic pressure, which is a function of shell displacement

in the acoustic-structure coupling problem. In the paper by Belove *et al.* [87] on fluid-structure interaction, for example, an explicit form of \mathbf{q} can be found. If air is the fluid medium, as it is in most mechanical noise control applications, the acoustic load is normally fairly small and can be ignored. However, if the fluid medium is a liquid, the acoustic radiation load can be extremely crucial and must be considered.

Studying the interactions between structures and sound is important for assessing the structure-borne sound in complex geometries, and therefore, in the next section, we provide insight into the mechanism of interactions.

2.2 Acoustic

Sound waves are not strictly limited to the sense of hearing in the acoustic field but are commonly characterized as small variations in the pressure, temperature, medium density and velocity of the wave-carrying medium such as air, which is induced by disturbances such as a solid vibrating surface or jet flows, etc. These variations in the medium, spatially, are a sound field.

To gain an understanding of the fundamental characteristics of mechanical vibrations as they contribute to sound radiation and sound propagation, the simple wave method is used. Such interactions between sound waves and solid structures' mechanical vibrations form a very important component of engineering vibration and noise control. All kinds of waves can be retained in structures, i.e.

compressive (longitudinal) waves, flexural (transverse or bending) waves, shear waves, and torsional waves, since solids can store energy in shearing and compression. As fluids can store only energy in compression, only compressive (longitudinal) waves can be sustained. Flexural (bending) waves are the only form of structural wave that plays a direct role in sound radiation and transmission, for reasons that will become evident later in Chapter 4. At this point the main explanation is that the bending velocity of the wave particles is perpendicular to the direction of the wave propagation, leading to efficient energy exchange between the fluid and the structure. Besides any mechanical excitation in the solid, which in the first instance could be the primary source of vibration, fluctuating pressures can produce an acoustic radiation load on any arbitrary surface in close proximity to that surface. If air is the fluid medium, as is typically the case in engineering noise control, this acoustic load is usually extremely small and, from the bending wave particle velocity of the structure surface, the sound pressure field can be calculated in regions away from the source. If the fluid medium, however, is a liquid, the acoustic radiation load may be extremely critical and must be taken into account - the forces acting on the structure are modified by the radiation load, there will be a feedback coupling between the structure and the fluid and then the structure will be "fluid loaded". However, this study is primarily concerned with structure-borne sound with air as the fluid medium. Sometimes, these conditions reflect traditional noise control problems of the engineering industry, such as plate, shell and cylinder sound radiation in industrial

environments. As such, in this thesis, fluid-loading impacts can be neglected.

The sound pressure p at any point $\mathbf{r} = (x, y, z)$ in the medium radiated by a vibrating structure satisfies the classical Helmholtz equation expressed as

$$\nabla^2 p(\mathbf{r}) + k_A^2 p(\mathbf{r}) = 0, \quad (2.10)$$

where k_A denotes the acoustic wave number and c is the velocity of sound.

The magnitude of the sound pressure in practice is evaluated as the sound pressure level and measured on the decibel scale defined by

$$SPL = 10 \log_{10} \frac{p^2(\mathbf{r})}{p_{ref}^2} = 20 \log_{10} \left| \frac{p(\mathbf{r})}{p_{ref}} \right|, \quad (2.11)$$

where p_{ref} is the reference pressure of $20 \mu\text{Pa}$.

From an arbitrary vibrating body the radiation of sound can be formulated at its most fundamental level in an integral equation containing Green's function, which has an imposed radiation condition – that means that the radiated sound pressure integral equation is outward travelling sound waves. In Eq. (2.12), Green's function is introduced and describes solutions to the wave equation. The integral equation is attributable to Kirchhoff in its most general form, though Helmholtz amended it for single frequency (harmonic) applications. In the advanced literature, the derivation of the integral and a discussion about the condition of radiation are given [88, 89]. The integral is often referred to as the Kirchhoff-Helmholtz integral equation, and along with some examples, Fahy [40] gives a useful discussion on its physical significance. For any arbitrary body

in the surrounding fluid, the Kirchhoff–Helmholtz integral equation relates harmonic surface vibrational motion to the radiated sound pressure field; that is

$$c(\mathbf{r}) p(\mathbf{r}) = \int_{\Omega} \left\{ p(\mathbf{r}') \frac{\partial G}{\partial \mathbf{n}_{\mu}}(\mathbf{r}', \mathbf{r}) - i\omega \rho_0 w(\mathbf{r}') G(\mathbf{r}', \mathbf{r}) \right\} d\mathbf{r}', \quad (2.12)$$

where \mathbf{r} is a position vector at some receiver position in the sound field, \mathbf{r}' is a position vector on the vibrating body, $c(\mathbf{r})$ is the sound pressure coefficient. When \mathbf{r} is located outside the structure, $c(\mathbf{r})$ is taken to be 1, when \mathbf{r} is located on the smooth structure, $c(\mathbf{r})$ is taken to be 1/2. It should be noted that the fluctuations of acoustic pressure are a function of both space and time, so $\tilde{p}(\mathbf{r}, t) = p(\mathbf{r})e^{-i\omega t}$. The first and second terms on the right side of the equation are called single-layer potential and double-layer potential respectively. \mathbf{n}_{μ} denotes the outer normal direction of the structural surface, and the Green function $G(\mathbf{r}', \mathbf{r})$ in free space satisfies the following equation:

$$\nabla^2 G(\mathbf{r}', \mathbf{r}) + k_A^2 G(\mathbf{r}', \mathbf{r}) = \delta(x - x_0) \delta(y - y_0) \delta(z - z_0),$$

where δ is Delta function, the Green function in free space is

$$G(\mathbf{r}', \mathbf{r}) = \frac{e^{-ik_A R}}{4\pi R},$$

where $R = \sqrt{(x' - x)^2 + (y' - y)^2 + z^2}$ denotes the distance between (x', y') on the plate and (x, y, z) in space.

It is important to note that the normal vibrational velocity of the surface and the pressure of the surface are interconnected and not independent. In fact, the

Green analytical functions can only be constructed for geometries such as plates, cylinders etc, other than those reasonably represented by combinations of point sources. In the advanced literature [88, 40], examples concerning source configurations of practical interest are found. The normal derivative of the Green function can be chosen to be zero by an appropriate selection of co-ordinates (for example, for planer structures the normal derivative of the Green function is zero), i.e. eliminating the requirement for knowledge of surface pressure distributions, thereby only knowledge of the surface vibrational velocity is needed. Analytical solutions are usually not possible on arbitrary, complex, three-dimensional bodies, such as large industrial machinery etc., and the standard procedure is either to use experimental techniques to determine the Green function or to use numerical techniques to solve the integral equation [40].

Sound radiation for a particular case of a planar source located in the infinite baffle will be addressed in Chapters 4 and 5.

In the next section, we will concentrate on the interaction between wave and ray dynamics. We begin by briefly giving insight to the short-wavelength approximations.

2.3 Wave dynamics—a ray perspective

Ray tracing in physics is a method for the estimation of the path of waves or particles through a system with reflecting surfaces (such as a curved surface),

absorbing properties, and areas of varying propagation velocity. Wave fronts may change direction, reflect off surfaces, or bend, complicating analysis under these circumstances. By repeatedly moving idealistic narrow beams called rays through the medium by discrete quantities, ray-tracing solves the problem.

A useful guiding idea in wave propagation problems in elastodynamics and acoustics is the concept of wave energy travelling along rays, particularly in areas such as acoustic microscopy, underwater acoustics, or seismology [90]. In room acoustics, the link between wave problems and the descriptions of an underlying long-term ray dynamics was considered very early [91], but more systematic studies began only in the late 1980s.

In quantum mechanics, the relationship between wave and ray dynamics became a focused subject in the 1970's. A new way forward to examine the imprint of regular or chaotic ray dynamics on the related wave problem was introduced by Gutzwiller using small wavelength approximations of the Green function in the time and frequency domains [92] and the discovery in the asymptotic regime of the duality between eigenfrequencies and periodic rays. This way of thinking was picked up in the acoustic community in the early to mid 1990s [93, 94, 95, 96, 97, 98] and is gaining growing attention in the context of engineering.

In this study, we analyse some aspects of the correspondence between rays and waves with a motivation to establish techniques to find or approximate solutions to wave problems by studying the properties of the associated system. The

ordinary, conventional approach to this exercise is based on the wave equation's eikonal approximation [99, 100, 101]. The golden age of the eikonal approximation in quantum mechanics and quantum field theory dates back to the 1950s and 1960s. The eikonal approximation emerged way back in optics before it was born in the study of quantum mechanics [102]. The key benefit offered by the eikonal approximation is that in the language of differential equations the equations are reduced to differential equations in a single variable.

The eikonal approximation is also known as the Wentzel, Kramers, and Brillouin approach (WKB), or the semiclassical or quasiclassical approximation depending on the field of application. Where the wave equation under consideration describes waves propagating in a medium that slowly varies in space and time relative to the wavelength and frequency of the wave solutions of interest, this formalism is assumed.

A WKB approach often studies processes which involve only few scattering events such as the reflection off a multi-layered surface area [103], or the scattering from obstacles such as cracks [104]. By considering ray dynamics in the complex plane, it is possible to treat effects associated with boundaries like surface waves or diffraction [105, 106, 107].

The ray solutions are in general not straight lines and may encounter turning points or caustics: that is, the curvature profile of the shell may act as a barrier. In a process that is analogous to tunnelling of a quantum particle through a potential energy barrier [108], partial reflection from or transmission through such curva-

ture barriers may arise and is similarly treated here using complex solutions of the ray equations: calculation of such curvature tunnelling is the focus of Chapter 3. The following sections therefore concentrate on the context of tunnelling.

2.3.1 Tunnelling

Tunnelling is exemplified by a quantum phenomenon where a particle enters and crosses a region where its potential energy exceeds its total energy. Energy conservation would not allow this to occur, according to classical physics, and the particle is fully reflected by the barrier. In fact, as an important phenomenon in the fields of physics, chemistry and biology, quantum mechanical tunnelling is a rather interdisciplinary concept [109, 110, 111]. Along with interference, quantization, resonance and non-adiabatic transformation, this represents one of the most important quantum mechanical effects [112, 113].

There is a certain peculiarity in the calculation of probability for a classically forbidden region from the point of view of mathematics: the idea of motion inevitably occurs here in imaginary time or along a complex trajectory [114, 115]. In terms of classical trajectories the semiclassical method WKB for the probability of tunnelling (in a static potential) can be reformulated in complex times as a simple change of variables. In this thesis, the WKB method is used to study the effect of curvature on curved surface scattering.

2.3.1.1 Resonant tunnelling

A fascinating quantum phenomenon is resonant tunnelling. It demonstrates that quantum particles are capable of moving through an opaque barrier in a semi-bound state with high probability [116, 117]. Resonant tunnelling is commonly defined as a one-dimensional (1D) phenomenon, but resonant tunnelling has also been investigated in higher dimensions (see, for example, [118, 119]). However since the key characteristics of resonant tunnelling occur in 1D, much of the study focused on the simplest 1D systems. Thermal noise influences tunnelling and resonant tunnelling, and the accumulation of particles in the bound state clearly changes the potential since they are rarely stationary processes. It is well understood that tunnelling can cause activation (higher energy) in the presence of an oscillating barrier and can therefore significantly increase tunnelling potentials.

The foundations of quantum mechanics [120, 121], nanotechnology [122, 123, 124], electronics [125], and also biology and biochemistry [126, 127] have studied this phenomenon. As energy in the incoming particle coincides with the energy of the quasi-bound state, the resonant tunnelling effect occurs. The particle stays within the well for an exponentially long time in the quasi-bound state if the barrier is very opaque. Whenever the particle is trapped within the well, it does not have time to escape from the well, thus, its state has to vary with the changes in the well, and its energy varies with the eigenenergy of the quasi-bound state. The delicate mechanism of these effects in a complex mechanical structure will

be explored in the next chapter.

Since the groundbreaking work of Esaki et al. [128, 129], several authors have theoretically and experimentally investigated the resonant tunnelling phenomenon through a one-dimensional double-barrier system [130, 131, 132, 117, 133, 134]. In this thesis the resonant tunnelling condition, the reflection and the transmission coefficients for a symmetrical mechanical structure are derived analytically.

The work in [32, 31] has used thin-shell models to incorporate curvature effects in ray-tracing models, which we extend in Chapter 3 to include wave features such as evanescent corrections and resonant tunnelling.

More often the structures to be studied have complex shapes, leading to the fact that analytical functions can not be used to describe the primary spatial variables distribution of the vibrated system, so it is appropriate to employ numerical methods.

2.4 Numerical methods

In this study, for a number of reasons for which main points are described below, we are interested in a phase space method such as DEA [135] for numerically modeling structure-borne sound and vibration in complex structures:

- DEA is applicable in the mid-to-high frequency range and is effective in computing than conventional deterministic methods (such as FEM and BEM).

- DEA offers more structural information compared to the traditional SEA [2] and is less problematic with regard to subsystem division.
- In terms of (linear) transport equations, the DEA method predicts the flux of vibrational wave energy through complex structures. Then these equations are discretized on meshes and solved.
- In DEA, the energy flow is tracked through a mesh that can be interpreted as ray tracing using ray densities rather than individual rays.
- DEA can use existing FEM meshes where there is no need for remodelling. Computing time in DEA is independent of frequency.
- The mesh resolution needed does not depend on frequency and can be selected to be coarser than in FEM. Only the geometry need to be resolved.

The DEA implementation on meshes is referred to as Discrete Flow Mapping. The concept behind DFM is described briefly here, see references [135, 136, 137, 30] for more information. With DFM vibroacoustic energy densities, including multi modal propagation and curved surfaces, can be computed in complex structures at high frequencies. A transfer operator is used in DFM to describe the flow of energy through the boundaries of the structure's subsystems. The flow of energy is expressed by a ray density ρ , i.e., the flow of energy over a given surface is given by the surface ray density at \mathbf{s} with direction \mathbf{p} . The density $\rho(\mathbf{s}, \mathbf{p})$, is transported via the boundary integral operator from one boundary to the adjacent boundary

intersection, then the transfer operator is discretised using a set of basis functions of the phase space. This will be explored in more detail in Chapter 4.

The study of interactions between simple structures, such as plate-type and shell structures, and sound is important in order to gain an understanding of the fundamental characteristics of mechanical vibrations as they contribute to sound radiation and sound propagation using the DEA phase-space method and also to assess structure-borne sound in more complex geometries. The following chapters therefore concentrate on the context of vibro-acoustic modeling for simple structures.

2.5 Conclusion

This chapter provided some foundational information for preparing the principal thesis material. The basic equations governing the structural vibration of the mechanical system here, two of the structural types: thin plate and thin shell, are revised and better understood in order to study the theoretical results discussed in the later chapters. The evaluation of plate vibrations is essential because the sound waves radiated are associated with the geometrical and dynamical properties of the plate. The structural response is sensitive to variations within the material and physical properties, particularly at high frequencies. As a result, in various acoustic and sound applications related to larger, complex and irregular structures, modeling and analysis of such situations is important.

In the next chapter, the resonant tunnelling condition and transmission coefficient along with reflection coefficient are derived theoretically for a symmetrical two-dimensional complex mechanical structure.

Chapter 3

Wave transition on shell structures

3.1 Introduction

Starting from the general equations for thin shells of arbitrary curvature, a well-known approach to describe ray dynamics for bending and in-plane waves is due to Pierce [79], obtained by deriving a local dispersion relation for different wave modes in the short-wavelength regime. In the special case of shells being homogeneous and thin, somewhat simpler dispersion relations have been derived by Norris and Rebinsky [80] which will form the basis of our work. Asymptotic techniques describing the wave dynamics in thin-walled shells have also been discussed in a book by Mikhasev and Tovstik [85] with particular attention given to the modified Wentzel-Kramers-Brillouin (WKB) method. Different asymptotic regimes for the dynamics of curved shells have been considered by Kaplunov *et al.* [138] as well as Babich and Kiselev [139].

Following [80], we deduce a ray dynamics by interpreting the dispersion curves as the contour lines of a Hamilton function from which Hamilton's equations of motion for the rays are obtained. These equations depend – along with material parameters and the thickness – on the local radii of curvature. The ray solutions are in general not straight lines and may encounter turning points or caustics: that is, the curvature profile of the shell may act as a barrier. In a process that is analogous to tunnelling of a quantum particle through a potential energy barrier [108], partial reflection from or transmission through such curvature barriers may arise and is similarly treated here using complex solutions of the ray equations: calculation of such curvature tunnelling is the focus of the chapter.

For the sake of simplicity and following [31, 32], we will study the ray and wave dynamics for a particular example – two plates joined by curved section with a specified curvature profile along the circumferential direction as shown in Fig. 3.1. This assumed geometry simplifies the analysis by making the problem have one effective degree of freedom. We also concentrate on incident waves that are of bending type: in the parameter regimes we consider, these do not couple significantly to in-plane modes and, having the shorter wavelength, are more appropriately treated by ray techniques. In a pure ray-tracing picture, incident rays approaching the curved region of the plate are either totally reflected or totally transmitted, depending on the angle of incidence. However, the solutions of the shell's equations of motion show a smooth, wavelength-dependent transition between total reflection or transmission, interspersed with resonance states. This

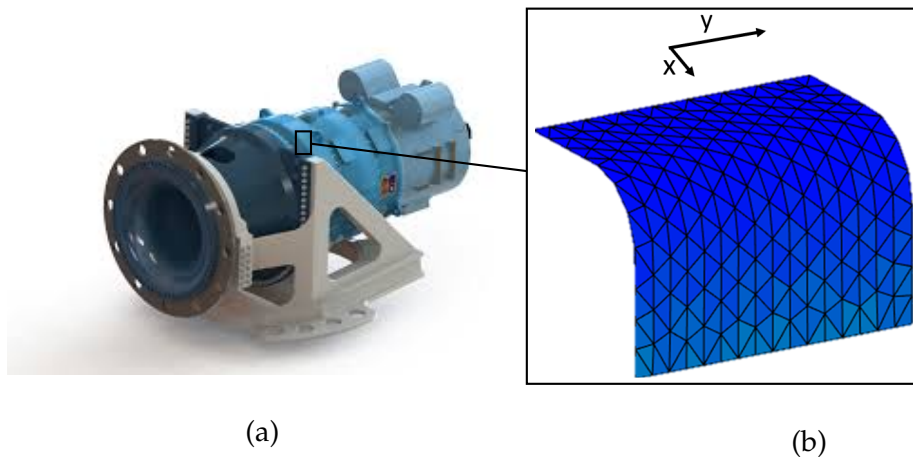


Figure 3.1: (a) A model of a wind turbine gearbox from Romax Technology; (b) a quarter cylindrical ridge connected to flat plates on either side equivalent to the structure considered in [32].

was also observed in [32], but not treated ray-dynamically.

In the context of quantum mechanics, such tunnelling effects are well established [108] and can be understood using a range of approximation techniques, based on extending ray dynamics to complex coordinates. The aim of this chapter is to extend such complex ray theory to the scattering of bending waves in a curved shell. For problems with several degrees of freedom, the use of complex solutions of ray dynamics to treat tunnelling phenomena remains a challenging problem that may require extension of chaotic dynamics to the complex domain (see [140, 141], for example) or show behaviour associated with coupling between complex orbits and chaotic [142] or resonant structures [143] typical of nonintegrable Hamiltonian systems (see [144, 145] for other aspects of multidimensional tunnelling). In this chapter we treat problems that are globally integrable and

therefore the topology of complex solutions can be explicitly described, allowing simpler analytical approximation [146] of the tunnelling features observed. However it should be noted that for more general shell geometries all the complexity of generic multidimensional tunnelling problems [144, 145] can arise.

The chapter is structured as follows. In Sec. 3.2 we briefly introduce the dispersion curves used to characterise ray dynamics on a cylindrical shell, describe the curvature profiles to be used in numerical illustrations and describe the basic assumptions of the WKB approximation, along with defining scaled, dimensional variables which make small and large parameters evident. In Sec. 3.3, we devise a model for resonant tunnelling based on a graph approach, and the theory for incorporating the relevant complex orbits into approximation of reflection and transmission amplitudes is discussed. Explicit numerical illustrations of the theory are offered in Sec. 3.4, comparing the WKB approach with full wave calculations, while conclusions are given in Sec. 3.5.

3.2 Thin shell theory, short wavelength asymptotics and ray dynamics

Numerous thin-shell theories have been derived to determine the dynamic and vibro-acoustic behaviour of thin-shell structures. These include Donnell's theory [147] and generalisations thereof [79, 63]; for more details also about other approaches, see the book by Leissa [72] and a review article by Qatu [148]. The

calculations in this chapter are based on Donnell's shell theory, which is discussed in more detail by Pierce [79], and Norris and Rebinsky [80]. In particular, we follow Søndergaard *et al.* [31, 32], who have applied this approach to the case of an isotropic, cylindrical shell. The work of [31, 32] has used thin-shell models to incorporate curvature effects in ray-tracing models, which we extend in this chapter to include wave features such as evanescent corrections and resonant tunnelling.

3.2.1 Wave model for thin shells

We consider the case of a cylindrical shell extending to $\pm\infty$ in the y direction and a varying radius of curvature $R(x)$ in the circumferential x direction such as, for example, shown in Fig. 3.1. The thickness of the shell is h , its (volume-) density ρ_s with Poisson ratio ν and Young's modulus E . It is assumed that the shell is thin, so that in particular $h \ll R$ (see Sec. 3.2.3 for more detail about assumed small and large parameters). We let $\mathbf{x} = (x, y)$ denote curvilinear coordinates on the shell, where y is a coordinate along the cylindrical axis of the structure and x is an arc length perpendicular to it. The displacement of a point originally on the reference surface within the shell is denoted by $\mathbf{u}(x, y, t) = [u(x, y, t) \ v(x, y, t) \ w(x, y, t)]$. The simplified shell theory presented in [32] reduces the elastic equations to the

following set of partial differential equations,

$$\begin{aligned}\frac{1}{c_p^2} \frac{\partial^2 u}{\partial t^2} &= \frac{\partial^2 u}{\partial x^2} + \frac{(1+\nu)}{2} \frac{\partial^2 v}{\partial x \partial y} + \frac{(1-\nu)}{2} \frac{\partial^2 u}{\partial y^2} + \frac{\partial}{\partial x} (\kappa(x)w) \\ \frac{1}{c_p^2} \frac{\partial^2 v}{\partial t^2} &= \frac{\partial^2 v}{\partial y^2} + \frac{(1+\nu)}{2} \frac{\partial^2 u}{\partial x \partial y} + \frac{(1-\nu)}{2} \frac{\partial^2 v}{\partial x^2} + \nu \kappa(x) \frac{\partial w}{\partial y} \\ \frac{1}{c_p^2} \frac{\partial^2 w}{\partial t^2} &= -\frac{B}{C} \Delta^2 w - \kappa(x) \left(\frac{\partial u}{\partial x} + \nu \frac{\partial v}{\partial y} + \kappa(x)w \right),\end{aligned}\quad (3.1)$$

where B and C are the bending and extensional stiffnesses given by Eq. (2.7), and

$$c_p^2 = \frac{C}{\rho_s h} = \frac{E}{\rho_s (1-\nu^2)}$$

is the pressure wave velocity, while $\kappa(x)$ denotes the local curvature in the x direction.

We take advantage of the translational symmetry in the y direction to seek wave solutions in the form

$$\mathbf{u}(x, y, t) = \hat{\mathbf{u}}(x) e^{ik_y y - i\omega t}, \quad (3.2)$$

where the wavenumber component k_y and the frequency ω are constants and $\hat{\mathbf{u}} = (\hat{u}, \hat{v}, \hat{w})^T$. Substituting the ansatz (3.2) into the PDE system (3.1) and denoting $k_p = \omega/c_p$ leads to the following system of ODE's in the variable x :

$$\frac{d^2 \hat{u}}{dx^2} + \left(k_p^2 - \frac{(1-\nu)}{2} k_y^2 \right) \hat{u} + ik_y \frac{(1+\nu)}{2} \frac{d\hat{v}}{dx} + \frac{d}{dx} (\kappa(x)\hat{w}) = 0 \quad (3.3a)$$

$$\frac{(1-\nu)}{2} \frac{d^2 \hat{v}}{dx^2} + \left(k_p^2 - k_y^2 \right) \hat{v} + ik_y \left(\frac{(1+\nu)}{2} \frac{d\hat{u}}{dx} + \nu \kappa(x)\hat{w} \right) = 0 \quad (3.3b)$$

$$\frac{B}{C} \left(\frac{d^4 \hat{w}}{dx^4} - 2k_y^2 \frac{d^2 \hat{w}}{dx^2} + k_y^4 \hat{w} \right) + \left(\kappa^2(x) - k_p^2 \right) \hat{w} + \kappa(x) \left(\frac{d\hat{u}}{dx} + i\nu k_y \hat{v} \right) = 0 \quad (3.3c)$$

3.2.2 Eikonal approximation for thin shells

Next, we look for approximate solutions to these ODE's in WKB form,

$$\hat{\mathbf{u}}(x) = \mathbf{a}(x)e^{iS(x)}, \quad (3.4)$$

where the components of $\mathbf{a} = [a_u, a_v, a_w]^T$ are the amplitudes in the in-plane directions x and y and in the direction normal to the shell, respectively. The gradient of the phase function $S(x)$ defines a local wavenumber in the x direction

$$k_x(x) = \frac{dS}{dx}. \quad (3.5)$$

All of these amplitude and phase functions depend parametrically on k_y and ω , although these dependencies have been suppressed in our notation. Note that in order to treat evanescence effects in the wave transport problem, we must allow the phase function $S(x)$ to be complex-valued as discussed in following sections.

For simplicity of notation, we have not explicitly identified a large parameter in our notation so far, but the Eikonal expansion to follow assumes that the length scale over which the curvature changes is much greater than the typical local wavelength. We correspondingly impose that $\mathbf{a}(x)$ varies over these longer length scales. Note that for simple smooth curvature profiles over which the bending angle is $O(1)$, this longer length scale can be effectively identified with the minimum radius of curvature, but the Eikonal expansion fails when the curvature changes rapidly, even if the radius of curvature itself remains large (for example, if the shell's curvature profile has sharp transitions from flat limit to curved region).

Substituting the ansatz (3.4) into the equations of motion (3.3) and neglecting terms containing derivatives in \mathbf{a} , (thus assuming that the amplitudes \mathbf{a} vary slowly along x compared to $S(x)$), we deduce that k_x must satisfy an Eikonal equation of the form

$$D(x, k_x; k_y, \omega) = 0,$$

where the function $D(x, k_x; k_y, \omega)$ is defined by

$$\begin{aligned} D(x, k_x; k_y, \omega) &= \begin{vmatrix} k_x^2 + \frac{1-\nu}{2}k_y^2 - k_p^2 & \frac{1+\nu}{2}k_xk_y & -i\kappa(x)k_x \\ \frac{1+\nu}{2}k_xk_y & k_y^2 + \frac{1-\nu}{2}k_x^2 - k_p^2 & -i\nu\kappa(x)k_y \\ -i\kappa(x)k_x & -i\nu\kappa(x)k_y & k_p^2 - \kappa^2(x) - \frac{B}{C}k^4 \end{vmatrix} \\ &= \left(k_p^2 - \frac{1}{2}k^2(1-\nu)\right) \left((k_p^2 - k^2) \left(k_p^2 - \frac{Bk^4}{C}\right) - k_p^2\kappa^2(x) \right) \\ &\quad + (1-\nu^2)\kappa^2(x)k_y^2 \left(k_p^2 - \frac{1}{2}(1-\nu)k_y^2\right), \end{aligned} \tag{3.6}$$

and $k^2 = k_x^2 + k_y^2$. It should be emphasized that the asymptotic treatment here is a short wavelength approximation, that is, the local wavenumber is substantially larger than the reciprocal of the length scales over which the curvature radii change. For a treatment of the low-frequency, long wavelength asymptotics, see [138].

The secular equation (3.6) provides a dispersion relation for modes propagating in curved plates and can be interpreted as a Hamilton function for an underlying ray dynamics. The method of characteristics leads to equations of motion

of the form

$$\dot{x} = \frac{\partial D}{\partial k_x}, \quad (3.7a)$$

$$\dot{k}_x = -\frac{\partial D}{\partial x}, \quad (3.7b)$$

describing a ray dynamics for energy transport on curved and homogeneous smooth thin shells.

The Hamiltonian (3.6) provided the basis for the work in [31, 32] and accounts for ray dynamics of both bending and in-plane waves at sufficiently high frequencies. For moderate curvature, each of these modes locally defines a separate level set of $D(x, k_x; k_y, \omega) = 0$ (see Fig. 3.3, discussed in Sec. 3.2.4). The ratio of radius of curvature to plate thickness provides a second large parameter, independent of frequency. This second large parameter can be exploited to use ray equations for bending modes even for moderate frequencies for which the wavelength of in-plane modes is not particularly small in comparison with the length scales of the curved region. In this second regime we find nontrivial deflection of rays associated with the bending mode, which is the focus of the rest of this chapter. In order to describe the regime we need a more systematic treatment of the large and small parameters in the problem, which we provide in the next subsection by defining scaled variables.

3.2.3 Scaled variables

In order to more formally identify small and large parameters behind the Eikonal expansion, we define scaled variables. We start by choosing a length scale L characteristic of the problem: a convenient choice would be the minimum radius of curvature achieved over the curved section of the shell. Then the scaled plate thickness

$$H = \frac{h}{L} \quad (3.8)$$

is a natural small parameter for the problem. Note that since $h \ll R$ is a necessary condition for the thin shell equations (3.1) to hold in the first place, we implicitly assume that $H \ll 1$ throughout this work. We define corresponding scaled coordinates and curvature profile

$$X = \frac{x}{L}, \quad Y = \frac{y}{L} \quad \text{and} \quad \mathcal{K}(X) = L\kappa(x)$$

along with the scaled wavenumber variables

$$K_x = Lk_x, \quad K_y = Lk_y \quad \text{and} \quad K = Lk.$$

We also define a scaled frequency

$$\Omega = \frac{L\omega}{c},$$

where $c = \sqrt{E/\rho_s}$, and the following scaled wavenumbers

$$K_P = Lk_P = \sqrt{1 - \nu^2}\Omega, \quad K_S = \sqrt{2(1 + \nu)}\Omega, \quad K_B = (12(1 - \nu^2))^{1/4} \sqrt{\frac{\Omega}{H}},$$

respectively, characterising pressure, shear and bending modes in the flat limit.

Then the Hamiltonian (3.6) can, after scaling by a constant factor, be written in terms of these scaled parameters and variables in the following form

$$D'(X, K_x; K_y, \Omega) = (K^2 - K_S^2)(K^2 - K_P^2)(K_B^4 - K^4) + \frac{12}{H^2} \mathcal{K}^2(X) \left[K_P^2(K^2 - K_S^2) - (1 - \nu^2)K_y^2(K_y^2 - K_S^2) \right]. \quad (3.9)$$

Having identified $H = h/L$ as a natural small parameter, in terms of which $\mathcal{K} = O(1)$, we concentrate in the rest of this chapter on a frequency regime such that

$$\Omega = O(1).$$

Then the in-plane, scaled wavenumbers are similarly such that

$$K_P = O(1) \quad \text{and} \quad K_S = O(1),$$

while the scaled bending wavenumber

$$K_B = O\left(\frac{1}{\sqrt{H}}\right)$$

is a large parameter.

We also focus in the following on bending waves whose angle of incidence is such that $K_y \sim K \sim K_B = O(1/\sqrt{H})$: then there is no significant coupling to in-plane modes through the curved section of the plate. In this case the scaled Hamiltonian can be approximated at leading order by

$$D'(X, K_x; K_y, \Omega) = D''(X, K_x; K_y, \Omega) \left(1 + O\left(\frac{1}{H}\right) \right),$$

where

$$D''(X, K_x; K_y, \Omega) = K^4(K_B^4 - K^4) - \frac{\mathcal{K}^2(X)}{\Omega^2} K_B^4 K_y^4 \quad (3.10)$$

and assuming that the scaled curvature is $\mathcal{K}(X) = O(1)$ in the region of maximum curvature of the plate. Then the terms remaining in $D''(X, K_x; K_y, \Omega)$ are both of $O(K_B^8) = O(1/H^4)$ for bending waves in the curved region, so there is significant deflection of rays there.

3.2.4 Models of shell geometry and dispersion curves

We now set out explicit examples of dispersion relations obtained from (3.9). For illustrations of the ray picture we consider a family of curvature functions previously used in [32], albeit with different parameter values, chosen here so that the problem behaves generically around the critical case between total transmission and total reflection of rays. By choosing as the length scale L the minimum radius of curvature over the curved region, these are in scaled coordinates of the form

$$\mathcal{K}(X) = \frac{f(X)}{f(0)}, \quad (3.11)$$

where

$$f(X) = \frac{1}{2} \left(\operatorname{erf} \left(\frac{X + X^*}{\delta X} \right) - \operatorname{erf} \left(\frac{X - X^*}{\delta X} \right) \right), \quad (3.12)$$

with the parameters X^* and δX respectively controlling the location at which the shell transitions from flat to curved, and the sharpness of that transition.

Fig. 3.2 shows three different curvature profiles used in this chapter, as a function of real X in part (a) and as X moves along the imaginary axis in part (b): this latter aspect is relevant to the discussion of complex rays in later sections.

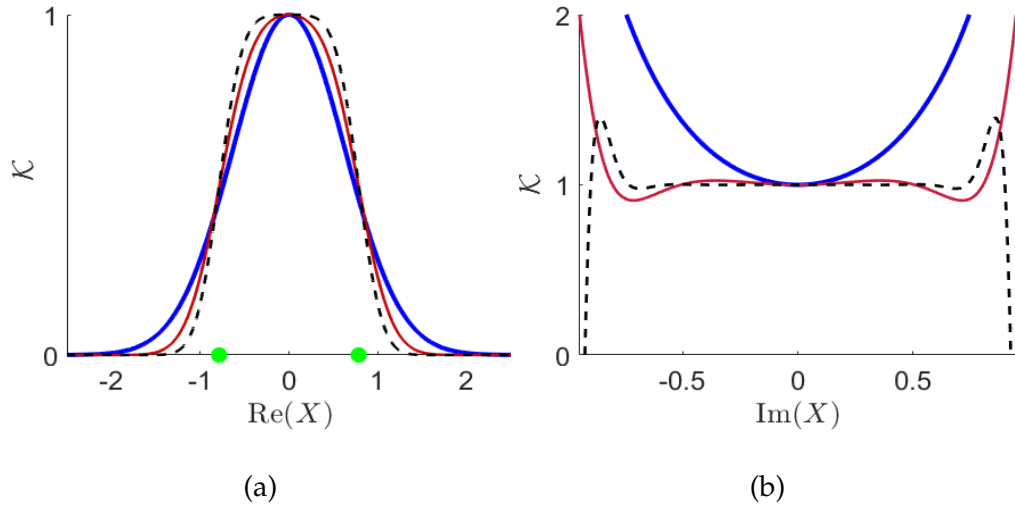


Figure 3.2: Curvature profiles for three different sets of parameter values used in examples later. (a) curvature $\mathcal{K}(X)$ as a function of real X ; in each case the profile is scaled to have a maximum value $\mathcal{K}_{\max} = \mathcal{K}(0) = 1$ here. Part (b) shows a section of the curvature profiles along the imaginary X -axis: this will be useful to understand the dynamics of complex orbits in later sections. (Blue thick solid curves correspond to $X^* = 0.42$ and $\delta X = 0.8136$, red thin solid curves to $X^* = 0.7776$ and $\delta X = 0.42$ and black dashed curves to $X^* = 0.7853$ and $\delta X = 0.2928$).

Going from the blue to the red to the black curve, the profile (as a function of real X) transitions from a generic quadratic maximum, Gaussian-like in shape, to one with sharper transition and a rather flat maximum. In all cases, we have $\mathcal{K}(X) \rightarrow 0$ in the asymptotic flat regions $X \rightarrow \pm\infty$ and the maximum curvature $\mathcal{K}_{\max} = 1$ is achieved at $X = 0$. The area under each of the curves in Fig. 3.2 is the total angle over which the plate bends through the curved region. In all the examples, the two flat regions of the plate are perpendicular to each other: that is, all curvature profiles in Fig. 3.2 have been fixed to have an area under the curve equal to $\pi/2$.

The curvature along the imaginary X axis, plotted in part (b) of Fig. 3.2, will play a significant role in understanding the dynamics of complex orbits controlling reflection and transmission by tunnelling. For each of the three profiles shown, there is a local minimum in the imaginary direction. In the case of the flatter profiles shown in red and especially black, however, this local minimum is rather shallow and the profile is seen to oscillate, with growing amplitude, within the window plotted. (In fact even for the profile shown in blue the profile oscillates further along the imaginary axis, outside of the window plotted.) This feature becomes important in the treatment of complex rays in later sections.

We next describe explicit dispersion relations obtained in scaled variables, using the same material properties as in [32], that is, $\nu = 0.28$, $E = 195$ GPa and $\rho_s = 7700$ kg/m³, for which $c = \sqrt{E/\rho_s} = 5032$ ms⁻¹. Then, for example, $\mathcal{K}_{\max} = 1$ and $H = 6 \times 10^{-4}$ is achieved for a shell with thickness 0.5mm and maximum

radius of curvature 0.833m, while a frequency of $f = \omega/(2\pi) = 1009\text{Hz}$ results in a scaled frequency $\Omega = 1.05$.

Figure 3.3 shows corresponding level sets $D' = 0$ defined in the (K_x, K_y) plane for two fixed values of scaled curvature \mathcal{K} and for two values of Ω : an example with $\Omega > 1$ is shown in (a) and an example with $\Omega < 1$ is shown in (b). In each case the dashed lines are for the flat limit $\mathcal{K} = 0$, for which the level set consists of three concentric circles. The outermost level curve corresponds to the bending mode, the middle level curve corresponds to shear waves and the innermost to pressure waves. In this limit, the wave velocity of each mode is independent of the direction of propagation and we note that, for the parameter values chosen here, the bending wavenumber is significantly greater than the two in-plane wavenumbers (see inset). As curvature increases, the circular symmetry of the flat limit is increasingly broken and, if the curvature is large enough, the bending component of the level set becomes non-convex. This transition corresponds to the green curve in Fig. 3.4. The case illustrated in Fig. 3.3a, for which $\Omega = 1.05$ and $\mathcal{K}_{\max} = 1$, shown by solid curves, is beyond this transition. If $\mathcal{K}_{\max}/\Omega > 1$ then the dispersion curves undergo a second transition (blue curve in Fig. 3.4) as the maximum of $\mathcal{K}(x)$ is approached. Here the bending curves collide with those for the in-plane modes and the level set develops a more complex structure for (K_x, K_y) near $(0, 0)$, as seen in Fig. 3.3(b), for example.

In the following we restrict our attention to rays approaching the curved region in the bending mode, corresponding to the outermost level curves in Fig. 3.3.

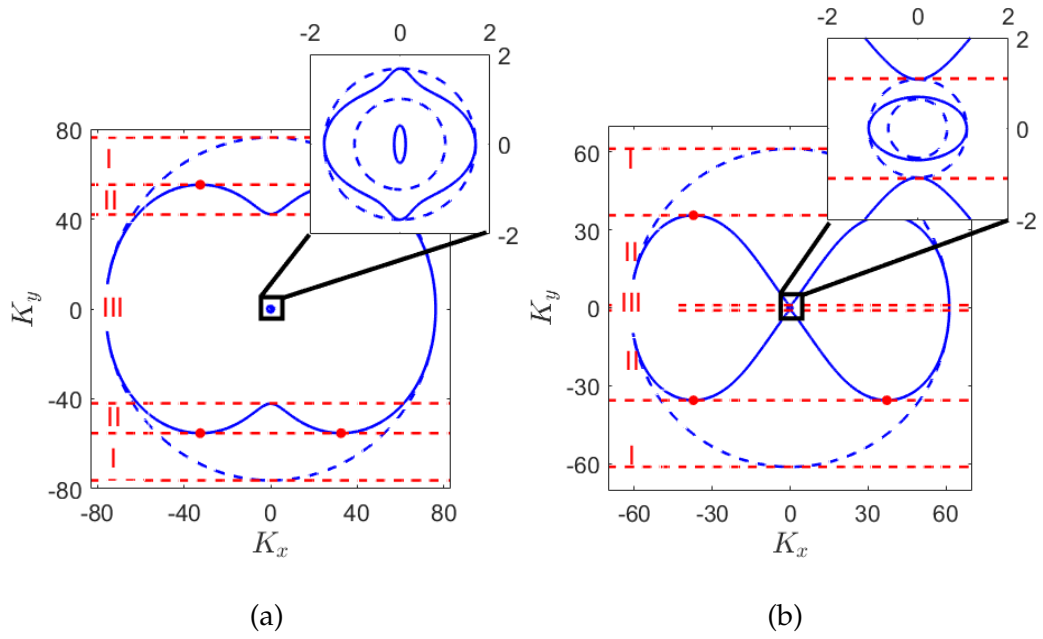


Figure 3.3: Dispersion curves, represented by level curves $D' = 0$ in the (K_x, K_y) -plane and for fixed X are illustrated: an example with $\Omega > 1$ is shown in (a) and an example with $\Omega < 1$ is shown in (b). In each case, the blue dashed curves represent isotropic dispersion relations for the limit of a flat plate; the outer circle corresponds to bending modes, the middle circle (see inset) to shear modes and the smallest circle (see inset) represents pressure modes. The solid blue lines represent dispersion relations achieved for the maximum value $\mathcal{K}_{\max} = 1$ of the curvature profiles in Sec. 3.2.4. In (a), we identify three regions according to how incoming rays are reflected or transmitted by the curved region: rays with $K_y \in \text{I}$ are reflected and with those with $K_y \in \text{II}$ and III are transmitted. Incident waves in region II may experience resonant tunnelling, whereas those in region III do not. We also identify by red dots the values of K_y connecting to fixed points of the system as explained in more detail in Sec. 3.2.5.

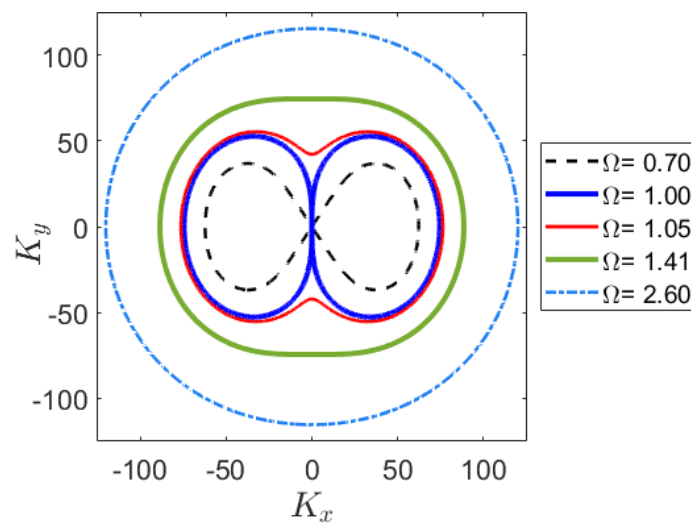


Figure 3.4: Level curves of the simplified Hamiltonian in (3.10) are plotted in scaled coordinates for a range of values of scaled frequency Ω . These simplified dispersion curves do not capture the more complicated structure around $(0, 0)$, as expanded in insets of Fig. 3.3, but provide a good description of them everywhere else in the (K_x, K_y) -plane.

As such rays approach the curved region, the wave vector (K_x, K_y) must stay on the deforming level set $D' = 0$, while K_y remains fixed. To understand the possible outcomes, we identify three regions for the case $\mathcal{K}_{\max}/\Omega < 1$, labelled I, II and III, in Fig. 3.3a. A ray starting in region I does not have a compatible wave vector at the point of maximum curvature, which is an analogue of a "forbidden region" in quantum-mechanical scattering. Here the value of K_y is large enough that the corresponding ray is deflected by the curved region and reflected back to the flat plate section from which it came. Rays starting in regions II and III do have compatible wave vectors at the point of maximum curvature: for these rays the value of K_y is small enough that they can reach the region of maximum curvature and are transmitted to the other side. The difference between regions II and III is that in region II new compatible solutions (K_x, K_y) appear as the level set is deformed: these new solutions are not directly accessible to rays arriving from the flat region but instead define trapped modes localised in the region of maximal curvature. Such trapped or localized modes have been shown to exist in elastic waveguides that have either axial width [149, 150] or axial curvature variations [151], and they appear to exist in a wide range of elastic geometries [85, 152]. Gridin *et al.* [151] showed that trapped modes exist in elastic plates with bends, and that these modes localise their energy in the regions of maximal curvature and decrease exponentially towards infinity. Based on simple existence criteria dependent on Poisson's ratio, they have provided guidance as to when trapping occurs. This work is analogous to the asymptotic method developed by

Kaplunov *et al.* [149] on localized vibrations in straight plates of varying width with mixed stress-clamped/free boundary conditions, where trapped modes can also exist around the places where the thickness is either a minimum or a maximum. The physical explanation of the existence of localised or trapped modes in the literature, particularly the work of Gridin *et al.* [151], is similar to the physical interpretation of the trapped modes occurrence in our study. The primary mathematical difference is that in our model, we employ a thin shell approximation, and resonances appear as K_y increases, whereas in their model, they employ a relatively thick bent plate and assume $K_y = 0$, so trapped modes exist around the cut-off frequency. There is another distinction, which we will demonstrate in the following section, in that in our method, the trapped modes decay exponentially for a while before starting to oscillate again, allowing scattering and resonant tunnelling, whereas in Gridin's work, the trapped modes exponentially decay all the way to infinity, preventing tunnelling out the trapped modes.

In region III there are no such trapped modes. In the case $\mathcal{K}_{\max}/\Omega > 1$, illustrated in Fig. 3.3(b), region III has shrunk to a small gap in which all components of the dispersion curve interact for (K_x, K_y) near $(0, 0)$.

Our focus here is on the transition between regions I and II, where corresponding incident plane waves transition from being completely reflected to being completely transmitted. Although there is near complete transmission in region II, for some incident angles the trapped modes may locally mediate peaks in transmission in analogy to resonant tunnelling in quantum mechanics [116]. There are

no such trapped modes in region III and therefore no resonant tunnelling. Although here there is still some small fraction of incident energy reflected for rays with $|K_y| \ll K_B$, this is typically so small that it is in practical terms unimportant. Therefore, although the simplified Hamiltonian (3.10) does not capture the structure of the dispersion curves near the origin of the (K_x, K_y) plane, as shown in the insets of Fig. 3.3, it does give a good description of the dispersion curves around the transition between regions I and II and can be used as a basis to understand the resonant tunnelling calculations to follow. Contours of this simplified Hamiltonian are illustrated using scaled coordinates in Fig. 3.4. Note that the ring frequency provides a typical scale for the frequency range in which curvature effects are important: it is $O(1)$ in the scaled variables used here. For example, for the material parameters chosen in the illustration above, the general expression for it, [153]

$$\Omega_{\text{ring}} = \frac{1}{\sqrt{1 - \nu^2}},$$

takes the value $\Omega_{\text{ring}} = 1.042$.

3.2.5 Phase portrait for bending rays

In this subsection we present the phase portrait obtained in the (X, K_x) plane from the scaled Hamiltonian in (3.9).

Figure 3.5 shows topologically distinct trajectories for the same parameter values as used in Fig 3.3. Each of these trajectories in the phase plane is a level curve

defined by $D'(X, K_x; K_y, \Omega) = 0$. We fix Ω throughout and vary K_y as an initial condition to obtain different contours. Depending on K_y , rays approaching the curved part of the plate are reflected, transmitted or approach a fixed point along a separatrix. These correspond respectively to rays arriving from the flat limit in regions I, II \cup III or the boundary between regions I and II in Fig. 3.3.

Rays approaching the curved region with sufficiently small values of K_y , in regions II or III in Fig. 3.3, are transmitted to the flat asymptotic region on the other side of the bend: rays of this type are labelled A in Figure 3.5. As the magnitude of K_y approaches a threshold value K_y^\sharp , corresponding to the boundary between I and II in Fig. 3.3, the incident ray approaches a separatrix orbit labelled B in the phase plane of Figure 3.5. The corresponding ray paths form the stable and unstable manifolds of a fixed point in the phase plane. These form analogues of dividing surfaces used in chemical reaction theory to divide reactants from products [154]. The fixed point represents a trajectory moving along the line $X = 0$, see Fig. 3.5b. When $|K_y| > K_y^\sharp$, rays are deflected by the curved part of the plate: these are labelled C in Fig. 3.5. When $K_y^* < |K_y| < K_y^\sharp$, where K_y^* corresponds to the boundary between regions II and III in Fig. 3.3, there are also topologically distinct orbits labelled D in Fig. 3.5; these orbits are closed in the (X, K_x) phase plane. The corresponding ray paths are trapped in the region of the bend and oscillate along it as shown in Fig. 3.5(c). They are related to trapped bending modes to be discussed in Section 3.3, see also [151]. These trapped rays cannot be reached from initial conditions in the flat regions of the plate. Incoming bending

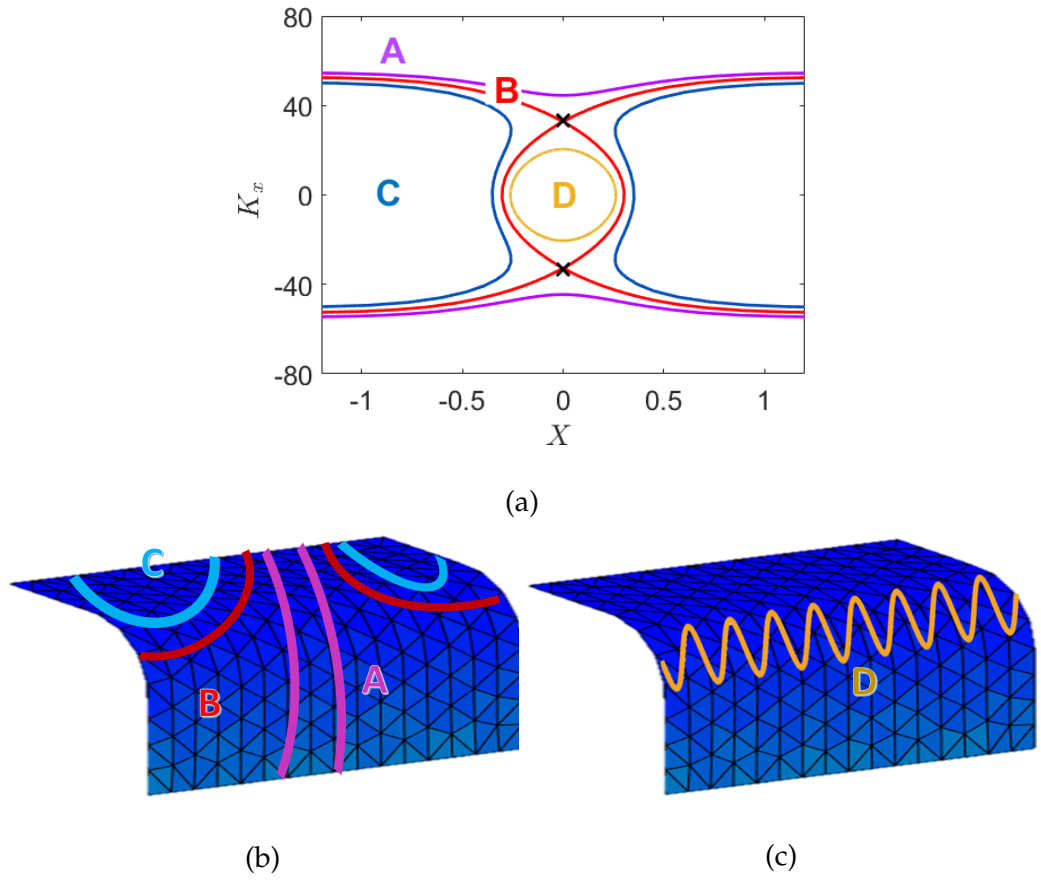


Figure 3.5: (a) Ray dynamics in a phase plane corresponding to a bending mode moving across a curved plate with the curvature profile shown in Fig. 3.2 (blue line); the magenta curve (A) is an example of a transmitted ray crossing the curved region; the red curve (B) corresponds to the ray approaching the fixed point thus forming a separatrix in the phase plane; the blue curve (C) represents a reflected ray; the closed yellow curve (D) shows a trapped ray oscillating along the curved part of the plate. The black crosses signify the fixed points at coordinates $(X, K_x; K_y) = (X, K_x^\sharp; K_y^\sharp)$. (b), (c) Typical ray paths are shown (schematically) on the curved plate using the same colour codes as in (a).

waves can couple into these trapped modes evanescently and these orbits play an important role in the “resonant tunnelling” mechanisms as set out in Section 3.3.

The key dividing structures in Fig. 3.5 are thus the hyperbolic fixed points (denoted by black crosses in Fig. 3.5a) at the threshold values $K_y = \pm K_y^\sharp$ and their corresponding stable and unstable manifolds shown as red curves. The coordinates of the fixed points ($X = 0, K_x = \pm K_x^\sharp$) can be determined by imposing the conditions

$$D'(X = 0, K_x^\sharp; K_y^\sharp, \Omega) = 0 \quad \text{and} \quad \left. \frac{\partial D'}{\partial K_x}(X = 0, K_x; K_y^\sharp, \Omega) \right|_{K_x = K_x^\sharp} = 0 \quad (3.13)$$

on the scaled Hamiltonian in (3.9). Although the exact solutions of the fixed point condition (3.13) can not be given in closed form in general, we can find approximate solutions using the Hamiltonian (3.10). Noting that $\partial D''/\partial K_x = 0 \Leftrightarrow \partial D''/\partial K = 0$ (at fixed K_y), the second of these conditions then implies

$$(K_x^\sharp)^2 + (K_y^\sharp)^2 = \frac{1}{\sqrt{2}} K_B^2 \left(1 + O\left(\frac{1}{H}\right) \right)$$

while the first yields

$$(K_y^\sharp)^2 = \frac{\Omega}{2\mathcal{K}_{\max}} K_B^2 \left(1 + O\left(\frac{1}{H}\right) \right).$$

Note, however, that the phase portrait in Fig. 3.5 has been constructed using the full Hamiltonian $D'(X, K_x; K_y, \Omega)$ in (3.9) and not the approximate Hamiltonian $D''(X, K_x; K_y, \Omega)$ in (3.10).

It is geometrically simpler to characterise incoming rays by an asymptotic angle of arrival

$$\theta_0 = \arcsin \frac{K_y}{K_B}$$

rather than wavenumber component K_y . We denote in particular by θ_0^\sharp the asymptotic angle of arrival of the separatrix orbit approaching the hyperbolic fixed point. From the preceding discussion this can be approximated by

$$\theta_0^\sharp = \arcsin \sqrt{\frac{\Omega}{2\mathcal{K}_{\max}}} \left(1 + O\left(\frac{1}{H}\right) \right).$$

An analysis based solely on the presented phase portrait, the summarised steps of the calculation are shown in Fig. 3.6, would thus suggest that waves are predominantly reflected when $\theta_0 > \theta_0^\sharp$ and transmitted when $\theta_0 < \theta_0^\sharp$. Modification of this simple ray picture based on tunnelling effects are presented in section 3.3.

3.2.6 Transmission and reflection of bending waves: wave approach

Wave-based methods mean methods that solve the whole equations of motion for a given geometry with given boundary conditions and thus are in principle capable of modelling all the wave's properties, interference, dispersion, and diffraction. Their effects are most important in practice for low frequencies, where finite difference methods (FD), FEM, and BEM are most commonly used. In this work, we apply FD scheme as described in [32] to solve the shell's equations of motion (3.3) numerically.

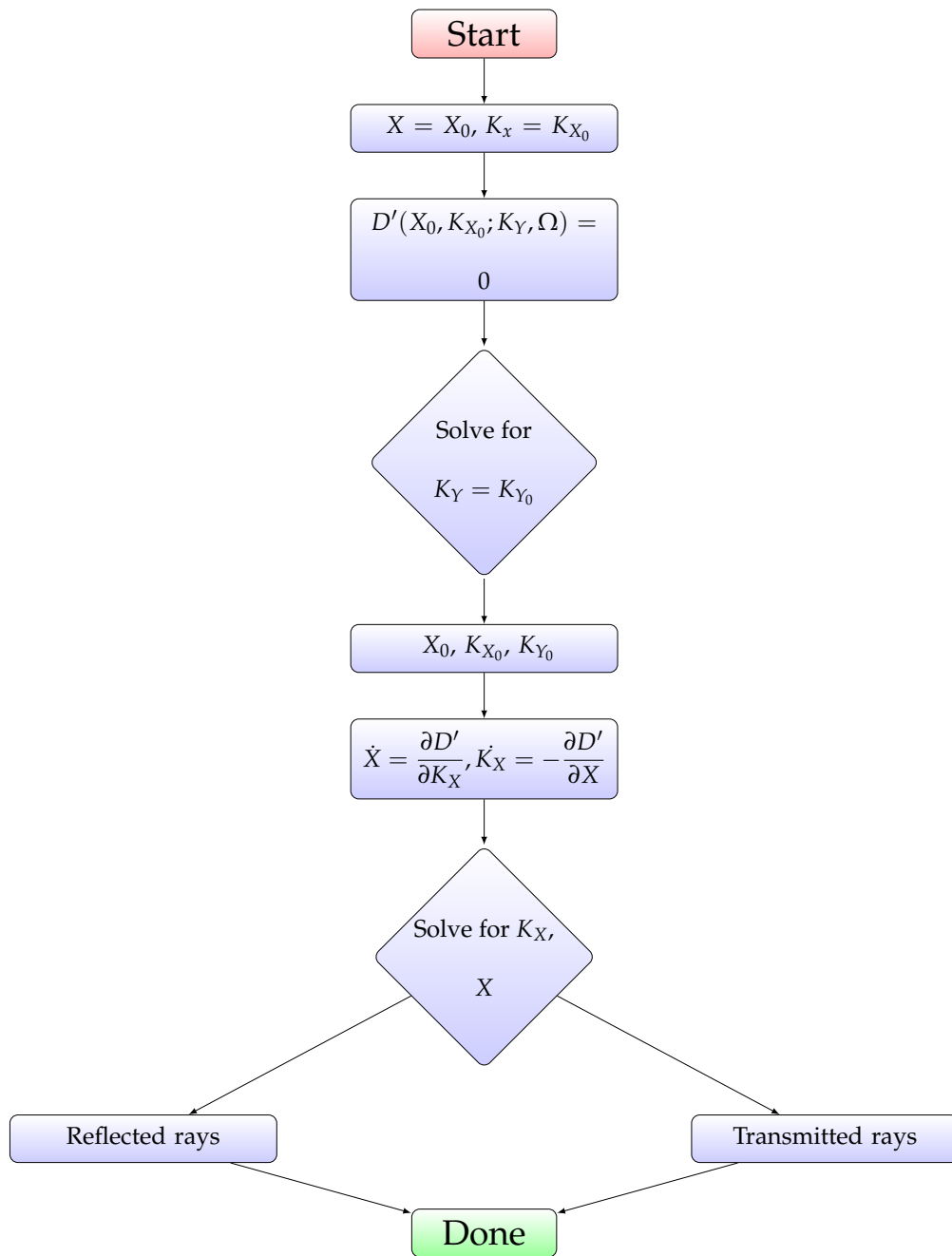


Figure 3.6: Steps of calculating phase portrait.

3.2.7 Wave scattering finite difference solution

The formulation of the scattering problem has been discussed in [32]. The curved region is connected by means of interfaces with flat plates on each side. One can formulate a scattering problem, first by imposing a set of conditions on these interfaces to allow to formulate the set of ODEs 3.3 as a boundary value problem, and afterwards, by considering the flow of incoming and outgoing wave fields on these interfaces. Presuming that the interfaces sit in asymptotically flat regions and, as such, the interfaces themselves do not give rise to phenomena of reflection and transmission; only the interior area between the interfaces regulates the dispersing properties.

First, for shortness of exposure, the above ODE framework for the scaled displacement vector can be composed in shorthand form

$$\mathcal{D}\hat{\mathbf{U}} = \mathbf{0},$$

where

$$\hat{\mathbf{U}} = \frac{\hat{\mathbf{u}}}{L}.$$

It is assumed that each interface follows the conditions of continuity set out in Ref. [155], i.e. continuity of displacement, rotation, friction, bending moment and (Kirchhoff) shear force

$$\mathbf{U}^+ = \mathbf{U}^-, \quad (3.14)$$

$$\frac{d\mathbf{U}^+}{dX} = \frac{d\mathbf{U}^-}{dX}, \quad (3.15)$$

$$\frac{\partial^2 W^+}{\partial X^2} + \nu \frac{\partial^2 W^+}{\partial Y^2} = \frac{\partial^2 W^-}{\partial X^2} + \nu \frac{\partial^2 W^-}{\partial Y^2}, \quad (3.16)$$

$$\frac{\partial^3 W^+}{\partial X^3} + (2 - \nu) \frac{\partial^3 W^+}{\partial X \partial Y^2} = \frac{\partial^3 W^-}{\partial X^3} + (2 - \nu) \frac{\partial^3 W^-}{\partial X \partial Y^2}. \quad (3.17)$$

Because \mathbf{U} is just a function of X and the material properties of the entire geometry are constant, the interface conditions may be simplified to the following.

$$\mathbf{U}^+ = \mathbf{U}^-, \quad (3.18)$$

$$\frac{d\mathbf{U}^+}{dX} = \frac{d\mathbf{U}^-}{dX}, \quad (3.19)$$

$$\frac{d^2 W^+}{dX^2} = \frac{d^2 W^-}{dX^2}, \quad (3.20)$$

$$\frac{d^3 W^+}{dX^3} = \frac{d^3 W^-}{dX^3}. \quad (3.21)$$

The superscripts define each quantity as we reach the interface from either the inner area " - " containing the ridge, or the outer regions " + " within flat limits outside the interfaces on either side of the bend. In the following, we will refer to the internal region as D^- , and to the association of the external regions as D^+ , see Figure 3.7. The waves (i.e. the wave modes) in D^+ that are scattered by D^- , which are essentially those of classical plate theory, will be one (or more) of bending (b), evanescent bending (e), shear (s) or pressure (p) type. In the vector $\hat{\mathbf{U}}$, \hat{W} defines the sum of the bending wave contributions and a linear combination of \hat{U} and \hat{V} will each give an in-plane wave type. Only bending incident modes \hat{W}^{inc} have been considered in this work, coming from the exterior flat limit D^+

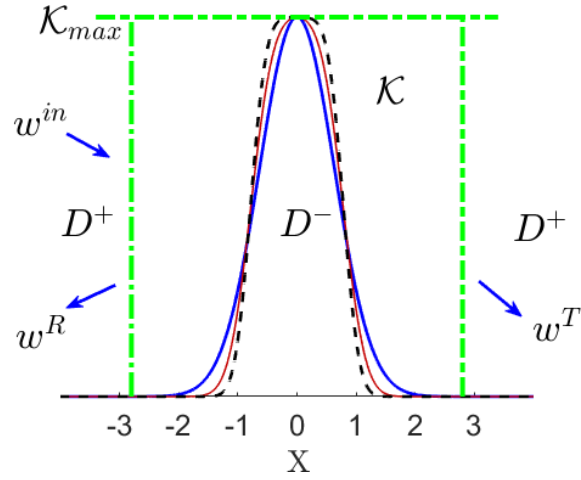


Figure 3.7: The curvature distributions with subdivision for the numerical calculation into interior D^- region, a cylindrical ridge with the maximum curvature \mathcal{K}_{\max} , connected to exterior D^+ regions, flat plates on either side, where $\mathcal{K}(X) = 0$. The D^+ and D^- interfaces are located within the flat regions $\mathcal{K}(X) = 0$ (which are represented by the green dashed vertical lines). The curvature increases smoothly from the interfaces to $\mathcal{K}(0) = \mathcal{K}_{\max}$ for $X \in D^-$.

and being scattered by the bend in D^- , but it is straightforward to extend to other incident wave types. Plane wave scattering was considered to investigate directional properties. In addition, the notation of the location of the interface to the right of D^- is denoted by $X = X^r$ and the interface to the left is correspondingly denoted by $X = X^l$. An incident unit amplitude bending wave with associated wavenumber K_x^b in the X -direction coming in from the left side of D^- can then be written as

$$\hat{W}^{\text{inc}}(X) = e^{iK_x^b(X-X^l)}.$$

Also, to write the resulting scattered waves in a descriptive form, $X_T = X - X^r$ and $X_R = X - X^l$ have been introduced. Denote the scattered wave type by the symbols $\alpha \in \{b, e, s, p\}$ and indicate whether the scattered wave is reflected (R ; arising in the same side of the bend as incident wave sent in) or transmitted (T ; arising in the other side of the bend as incident wave sent in) by the symbol $\beta \in \{R, T\}$, then the scattered wave can be written as

$$\phi_\beta^\alpha(X) = A_\beta^\alpha(X) e^{\pm i K_x^b X_\beta},$$

where the sign \pm prescribes by the value of β , positive for $\beta = T$ and negative for $\beta = R$, and A_β^α demonstrates wave amplitude. The relationship between \mathbf{u} and A_β^α with $\theta \in (-\pi/2, \pi/2)$, representing the angle between X -axis and the scattered wave directions, can be described as follows

$$\hat{U}^\beta(X) = \pm A_\beta^p \exp(\pm i K_x^p X_\beta) \cos \theta - A_\beta^s \exp(\pm i K_x^s X_\beta) \sin \theta \quad (3.22)$$

$$\hat{V}^\beta(X) = A_\beta^p \exp(\pm i K_x^p X_\beta) \sin \theta \pm A_\beta^s \exp(\pm i K_x^s X_\beta) \cos \theta \quad (3.23)$$

$$\hat{W}^\beta(X) = A_\beta^b \exp(\pm i K_x^b X_\beta) + A_\beta^e \exp(-K_x^b |X_\beta|). \quad (3.24)$$

Therefore, the total wave field in D^+ to the left and right of D^- are given respectively by

$$\hat{\mathbf{U}}^l = \left[\hat{U}^R \quad \hat{V}^R \quad \hat{W}^R + \hat{W}^{\text{inc}} \right]',$$

$$\hat{\mathbf{U}}^r = \left[\hat{U}^T \quad \hat{V}^T \quad \hat{W}^T \right]',$$

where $\hat{\mathbf{U}}^r$ and $\hat{\mathbf{U}}^l$ play the role of $\hat{\mathbf{U}}^+$ on the right and left interfaces, respectively.

By connecting the plane wave ansatz in D^+ for $\hat{\mathbf{U}}^l$ and $\hat{\mathbf{U}}^r$ described above with

the interior problem for $\hat{\mathbf{U}} = \hat{\mathbf{U}}^-$ in D^- through the interface conditions (3.18) to (3.21), the scattering problem can then be generated. The scattering solutions $\hat{\mathbf{U}}^l$ and $\hat{\mathbf{U}}^r$ and the scattering coefficients A_{β}^{α} , can be extracted once this scattering problem is solved.

In the ODE system (3.3), the differential operator D involves both bending and in-plane waves, along with the coupling between them. Using second order accurate centered finite difference formulas on a set of equi-spaced grid points, each of the equations in the system is discretized.

According to the conditions (3.18) to (3.21), the FD solution in D^- is matched to the scattering solution and its derivatives in D^+ at the interfaces between D^- and D^+ . In the FD-solution in D^- , derivatives that appear in the coupling conditions are implemented using one-sided finite difference operators with second-order accuracy. The incident wave in D^+ produces a forcing term which drives the finite difference model in D^- . At the left interface, forward difference formulae are used and backward difference formulae at the right interface are used. Combining the interior finite difference equations with the discretized interface coupling conditions leads to a matrix problem often form

$$\begin{bmatrix} * & * & 0 \\ * & \mathbf{D} & * \\ \mathbf{0} & * & * \end{bmatrix} \begin{bmatrix} \mathbf{R} \\ \hat{\mathbf{U}}_{\Delta} \\ \mathbf{T} \end{bmatrix} = \begin{bmatrix} * \\ \mathbf{0} \\ \mathbf{0} \end{bmatrix}$$

with scattering coefficients

$$\mathbf{R} = \left[A_R^b \quad A_R^e \quad A_R^p \quad A_R^s \right]^T$$

and

$$\mathbf{T} = \left[A_\tau^b \quad A_\tau^e \quad A_\tau^p \quad A_\tau^s \right]^T.$$

Here, the finite difference solution in the interior of Ω_- is represented by

$$\hat{\mathbf{U}}_\Delta = \left[\hat{U}_i \quad \hat{V}_i \quad \hat{W}_i \right]^T, \quad i = 1, \dots, N-1$$

As in the previous section, we restrict the analysis to bending excitations. This implies that only the bending mode is active for smooth joints, with negligible conversion to in-plane modes. Therefore, the reflection and transmission probabilities become

$$P(\text{Transmit}) = |A_\tau^b|^2 \quad \text{and} \quad P(\text{Reflect}) = |A_R^b|^2.$$

In the next section, we compare the results of the numerical solution of the full wave scattering problem derived and discussed here with the approximations to be established in the following sections.

3.3 Transmission and reflection of bending waves: resonant tunnelling

We describe next how complex ray solutions can be used to describe transmission and reflection near the critical angle θ_0^\sharp .

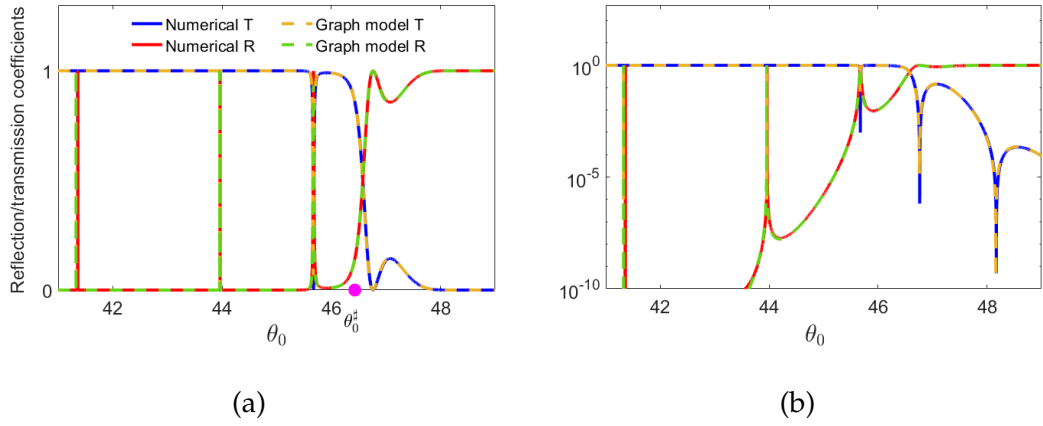


Figure 3.8: The fractions of transmitted (blue and yellow) and reflected (red and green) wave intensities are shown as a function of incident angle for a plane wave approaching the curved region from the flat limit using (a) a linear scale and (b) a log scale. Solid lines represent a full wave calculation as described in Sec. 3.2.6 using Eq. (3.3); dashed lines represent the approximations described in the text. The critical angle here is $\theta_0^\# = 46.4^\circ$ and the calculations have been done for the parameter values given in Sec. 3.2.4 and for the curvature profile shown in blue in Fig. 3.2.

3.3.1 Overview

To give an overview over the features to be described in detail later, we show the reflection and transmission coefficients, that is, the reflected and transmitted power as a fraction of the incident power of a plane wave arriving at the bend, as a function of the incident angle θ_0 in Fig. 3.8. The calculations are done for the curvature profile shown as blue curves in Fig. 3.2. We compare numerical solutions of the full wave problem (3.3) (blue and red curves) with approxima-

tions that are to be developed in the remainder of this chapter (green and yellow dashed curves). For the full-wave solution, we apply a finite difference scheme as described in the previous section.

The main features are consistent with the ray-dynamical picture outlined in the previous section. For incoming angles $\theta_0 < \theta_0^\sharp$ (with $\theta_0^\sharp = 46.4^\circ$ here), the transmission coefficient is close to unity and the reflection coefficient is small. In line with Fig. 3.5, the corresponding rays (of type A) all pass over the curved region of the shell. Above this threshold, when $\theta_0 > \theta_0^\sharp$, the transmitted wave amplitude falls to zero: this is again consistent with Fig. 3.5, where the corresponding rays (of type C) are all deflected by the curved region.

The results in Fig. 3.8 deviate in two important ways from the simple ray picture sketched in the previous section (the phase space based solution), however. First, there is a transition region near the critical angle θ_0^\sharp in which the transmission and reflection coefficients change smoothly rather than discontinuously as a function of θ_0 . Second, at angles below this transition region, there are sharp resonances which are related to resonant tunnelling facilitated by the trapped orbits of type D in Fig. 3.5. Both of these features are explained quantitatively in the next sections by extending the ray analysis to use *complex rays*.

3.3.2 A graph model using complex rays

In the following, we provide a complex-ray analysis of the transmission and reflection coefficients such as plotted in Fig. 3.8. In the quasi one-dimensional case

here, this can be done most efficiently in a graph model based on the main features of the phase-space shown in Fig. 3.5 and, including transitions due to complex orbits leading to tunnelling corrections, in Fig. 3.9. The orbits shown in Fig. 3.9a are the dominant dynamical features describing the behaviour below the critical point, for which $\theta_0 < \theta_0^\sharp$. Fig. 3.9b describes the behaviour for $\theta_0 > \theta_0^\sharp$.

The calculations in this section borrow from two approaches in the areas of wave chaos and semiclassical approximation of quantum mechanics. The first is the use of graph models (or "quantum graphs"), in which wave solutions transported along networks of bonds are connected at vertices by local scattering matrices. Imposing global consistency of such locally connected solutions leads to explicit solutions for important features of the system as a whole, such as scattering matrices and resonance conditions. Reference [156] provides a good overview of the most important results and concepts in this context. Second is the use of uniform asymptotic approximation to characterise the connection of local WKB solutions across hyperbolic fixed points, where primitive WKB approximation breaks down. A detailed exposition of these so-called connection formulae that is valid for the effectively one-dimensional context needed here can be found in the classic review article [157] (also see Appendix C for the key principles). We also note that this topic has had renewed attention in recent years in the context of chemical reaction rates [154], where transport across phase space bottlenecks is treated by similar methods, extended to more general Hamiltonians and higher dimensions: although these reaction-rate problems are physically very distinct,

their phase-space geometry and WKB approximation are very similar to the problem at hand [158]. We will not give a detailed re-derivation of the required results in this chapter but simply quote the most important equations from these references.

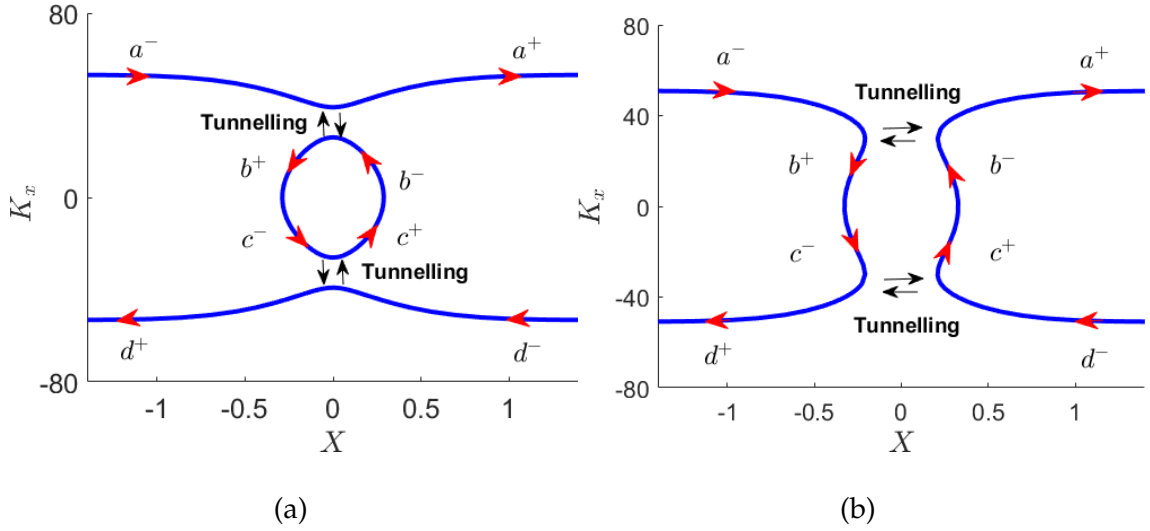


Figure 3.9: Phase space dynamics relevant for resonant tunnelling.

Each orbit in phase space can be used to define an approximate solution of WKB type matching plane waves as $x \rightarrow \pm\infty$ with corrections due to the curved region near $x = 0$. We write the full wave solution as linear combinations of these WKB solutions in each region with corresponding amplitudes $(a^\pm, b^\pm, c^\pm, d^\pm)$ as denoted in Fig. 3.9. For example, a^- denotes the amplitude of a wave incoming from the left and a^+ the amplitude of a corresponding outgoing wave to the right following transmission, whereas d^+ denotes a corresponding reflection amplitude.

Our aim is to calculate a scattering matrix connecting these amplitudes, de-

fined so that

$$\begin{bmatrix} a^+ \\ d^+ \end{bmatrix} = \begin{bmatrix} t_{\text{tot}} & r_{\text{tot}} \\ r_{\text{tot}} & t_{\text{tot}} \end{bmatrix} \begin{bmatrix} a^- \\ d^- \end{bmatrix} \equiv \sigma_{\text{tot}} \begin{bmatrix} a^- \\ d^- \end{bmatrix}. \quad (3.25)$$

The transmission and reflection coefficients such as those shown in Fig. 3.8 are then obtained using

$$T = |t_{\text{tot}}|^2 \quad \text{and} \quad R = |r_{\text{tot}}|^2.$$

The scattering process can be schematically displayed in a graph model as shown in Fig. 3.10. We find the total scattering matrix σ_{tot} by subdividing the problem into local scattering problems and associated node scattering matrices σ_{node} .

We first treat scattering at the nodes of the graph in Fig. 3.10 corresponding to the region in phase space surrounding either of the two hyperbolic fixed points. Wave amplitudes connecting local WKB solutions approaching and leaving the upper fixed point in Fig. 3.9 can be related in the form

$$\begin{bmatrix} a^+ \\ b^+ \end{bmatrix} = \begin{bmatrix} t_{\text{node}} & r_{\text{node}} \\ r_{\text{node}} & t_{\text{node}} \end{bmatrix} \begin{bmatrix} a^- \\ b^- \end{bmatrix} \equiv \sigma_{\text{node}} \begin{bmatrix} a^- \\ b^- \end{bmatrix}. \quad (3.26)$$

We obtain by symmetry for the lower fixed point

$$\begin{bmatrix} c^+ \\ d^+ \end{bmatrix} = \sigma_{\text{node}} \begin{bmatrix} c^- \\ d^- \end{bmatrix}. \quad (3.27)$$

Explicit formulas can be given for the matrix elements of the node scattering matrix σ_{node} based on a uniform WKB treatment of wave propagation near a hyperbolic fixed point, as discussed below.

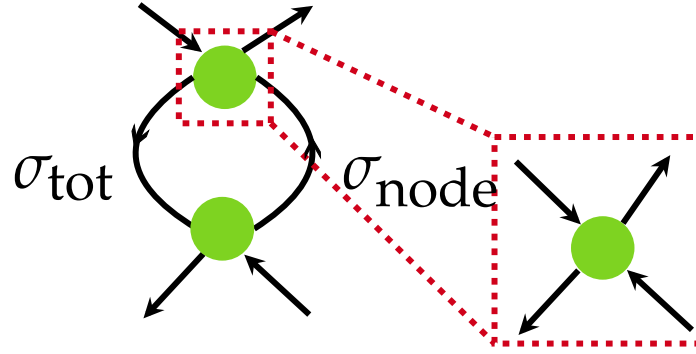


Figure 3.10: Schematic representation of the graph model.

Wave transport along the bonds between nodes in the graph is achieved by applying a simple phase shift determined by the optical phase length of the corresponding ray segment. By matching the local WKB solutions between the upper and lower nodes we may write

$$\begin{bmatrix} b^- \\ c^- \end{bmatrix} = \begin{bmatrix} 0 & -ie^{iS} \\ -ie^{iS} & 0 \end{bmatrix} \begin{bmatrix} b^+ \\ c^+ \end{bmatrix} \equiv \sigma_X \begin{bmatrix} b^+ \\ c^+ \end{bmatrix}, \quad (3.28)$$

where S denotes a phase integral (or action) of an orbit passing from the upper to the lower node or vice versa. The details of the transformation σ_X depends on the phase conventions used to write each of the local WKB solutions. The factor $(-i)$ is due to connecting WKB solutions across turning points between nodes [157].

We can use (3.28) to eliminate the amplitudes (b^\pm, c^\pm) from the total scattering problem and write (3.25) in the form

$$\sigma_{\text{tot}} = t_{\text{node}} I + r_{\text{node}} \sigma_X \frac{1}{1 - t_{\text{node}} \sigma_X} r_{\text{node}},$$

where I denotes the identity matrix. The treatment suggested here is in fact a special case of constructing a scattering matrix for a wave dynamics on general

graphs [156]. The total scattering matrix can also be expressed as a sum over all possible paths between branches approaching and leaving the nodes. Written explicitly in terms of matrix elements, this matrix equation leads to the following relations,

$$r_{\text{tot}} = \frac{-i r_{\text{node}}^2 e^{iS}}{1 + t_{\text{node}}^2 e^{2iS}} \quad (3.29a)$$

and

$$t_{\text{tot}} = t_{\text{node}} \left[1 - \frac{r_{\text{node}}^2 e^{2iS}}{1 + t_{\text{node}}^2 e^{2iS}} \right] = t_{\text{node}} \left[\frac{1 + (t_{\text{node}}^2 - r_{\text{node}}^2) e^{2iS}}{1 + t_{\text{node}}^2 e^{2iS}} \right] \quad (3.29b)$$

for total reflection and transmission, respectively.

Resonant tunnelling occurs when the denominator becomes small, that is,

$$1 + t_{\text{node}}^2 e^{2iS} \approx 0.$$

Below the critical angle θ_0^\sharp , we find that transmission across a node is almost total, so that $t_{\text{node}} \approx 1$ and such resonances arise near parameters for which

$$S = \left(n + \frac{1}{2} \right) \pi,$$

where n is integer. This Bohr-Sommerfeld type quantisation condition is satisfied by parameter values near those supporting a trapped, resonant mode confined to the region of maximum curvature and associated with orbits of type D in Fig. 3.5. Incoming waves couple into such trapped modes at resonance and show enhanced reflection (and correspondingly depressed transmission), as seen

in the numerical calculation of Fig. 3.8. We show in the next section that the results described here allow a detailed quantitative comparison of such resonant tunnelling effects.

3.3.3 Local scattering matrices

In the following, we will derive the local scattering matrices σ_{node} and σ_X , starting with σ_{node} . The problem of transmission and reflection of local WKB solutions around a hyperbolic fixed point has been extensively studied in the context of quantum mechanics. In its simplest form, it is understood by solving the problem of transmission across a quadratic potential barrier [157], (Appendix C reiterates a few fundamental aspects while emphasising the necessity of WKB approximation), but can also be treated by using more general transformations of phase-space coordinates around generic hyperbolic fixed points as we encountered here: see [154] for a discussion of phase space geometry and [158] for a corresponding discussion from the point of view of WKB approximation, for example.

The main ingredient is to find a complex periodic orbit γ_i connecting disconnected branches of the level curves illustrated in Fig. 3.9. This is obtained by solving Hamilton's equations (3.7) while letting the "time" variable run along a contour in the complex plane. One can show that there are periodic solutions connecting each pair of branches near a hyperbolic fixed point [158]. These are illustrated in Figs. 3.11a-3.11b for $K_y < K_y^\sharp$ and in Figs. 3.12a-3.12b for $K_y > K_y^\sharp$.

One finds in this case that the period in complex time is in fact imaginary, and so is the corresponding orbit action, which we denote

$$\oint_{\gamma_i} K_x dX = 2i\Theta, \quad (3.30)$$

(where Θ is in fact a function of the parameters K_y and Ω). By choosing the imaginary-time contour to move *downwards* in the complex plane, the imaginary action Θ is negative when $K_y > K_y^\sharp$ and positive when $K_y < K_y^\sharp$ [158]. This leads to near complete transmission for $K_y < K_y^\sharp$ and near complete reflection for $K_y > K_y^\sharp$ as discussed in more detail below.

Note that any such complex periodic orbit is one of a continuous family of equivalent orbits, so that collectively they define a two-dimensional manifold. A real starting point can be displaced continuously along the (real) level curve of the Hamiltonian function, corresponding to the blue curves in Fig. 3.9. Subsequent evolution in imaginary time will generate different periodic curves on a complexified level set $D'(X, K_x; K_y, \Omega) = 0$ (which defines a manifold of two real dimensions in complexified phase space), but each of these periodic curves will have the same period and imaginary action Θ as a consequence of Cauchy's theorem.

With an appropriate choice of phase convention for local WKB solutions, the local reflection and transmission coefficients can then be expressed in the forms [157, 158]

$$r_{\text{node}} = \frac{-ie^{-i\delta}}{\sqrt{1 + e^{-2\Theta}}}, \quad (3.31a)$$

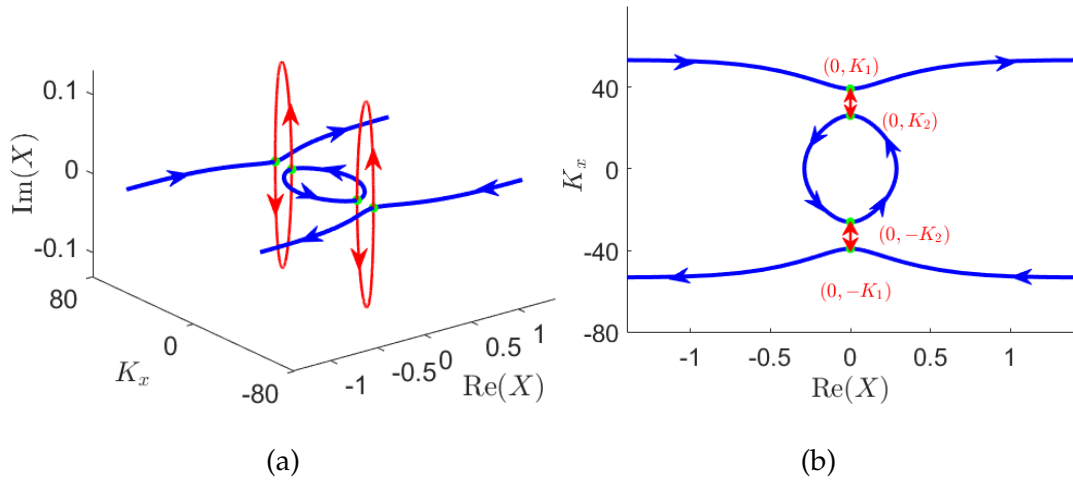


Figure 3.11: Real and complex (tunnelling) orbits are shown for the case $K_y < K_y^\sharp$. In (a) we provide a 3D representation in which a degree of freedom corresponding to the imaginary part of X is included; in (b) the corresponding projection onto the real phase plane is shown. Red curves show examples of tunnelling orbits of imaginary period: for these orbits, real initial conditions can be found, indicated by green dots, from which integration in imaginary time leads to periodic evolution largely confined to $\text{Re}(K_x)$ and $\text{Im}(X)$. There is also a separate real periodic orbit corresponding to the closed blue curve.

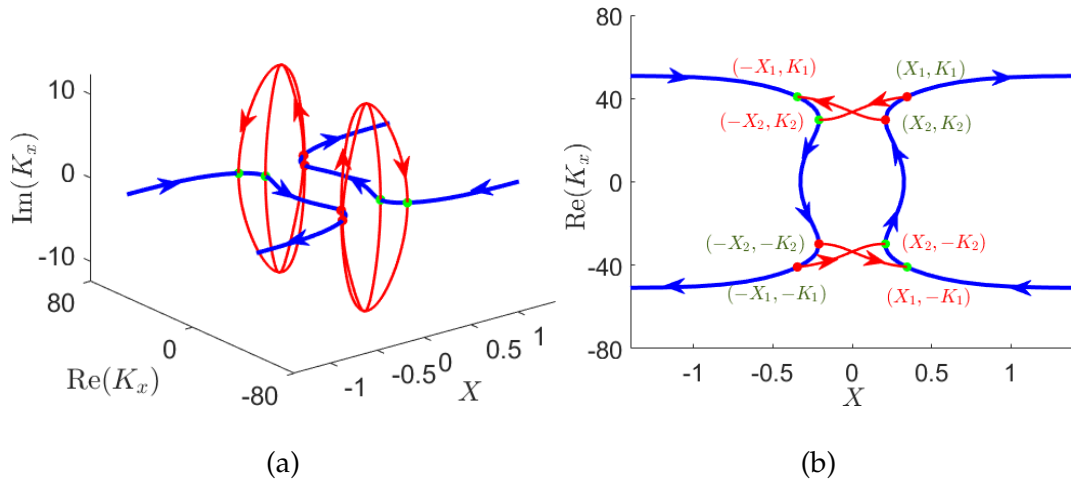


Figure 3.12: Real and complex (tunnelling) orbits for the case $K_y > K_y^\sharp$. The format is similar to Fig. 3.11a-3.11b except that the 3D plot is obtained by including the imaginary part of K_x rather than of X . As with Fig. 3.11a-3.11b, the red curves show examples of tunnelling orbits of imaginary period, but note that here dynamics is predominantly in components $\text{Re}(X)$ and $\text{Im}(K_x)$ rather than $\text{Re}(K_x)$ and $\text{Im}(X)$. In contrast to Fig. 3.11a-3.11b, where symmetry of reflection in X suggests a particular real initial condition for each tunnelling orbit, here there are many, equally plausible real initial conditions. For example, imaginary-time evolution from the turning point (X_2, K_2) on the right first returns to the real phase plane at coordinates $(-X_1, K_1)$, which is not a turning point. Conversely evolution from (X_1, K_1) , which is not a turning point, first returns to the real phase plane at turning point $(-X_2, K_2)$.

and

$$t_{\text{node}} = \frac{e^{-\Theta - i\delta}}{\sqrt{1 + e^{-2\Theta}}}, \quad (3.31b)$$

where

$$\delta(\Theta) = \frac{\Theta}{\pi} \log \left| \frac{\Theta}{\pi e} \right| + \arg \Gamma \left(\frac{1}{2} - \frac{i\Theta}{\pi} \right). \quad (3.32)$$

Note that σ_{node} is unitary and that, in particular,

$$|r_{\text{node}}|^2 + |t_{\text{node}}|^2 = 1.$$

Note also that the derivation of this result assumes that the fixed point in question is of generic hyperbolic type [154, 158] which necessitates that the maxima of the curvature profiles in Fig. 3.2 are quadratic. This is unambiguously true for the curvature profile represented by blue curves in Fig. 3.2. The maxima for the other profiles in Fig. 3.2, while being also strictly quadratic, are very shallow, so that effectively higher-order terms in a normal form representation [154] are in practice not negligible. The problem is therefore expected to be well described by these generic results only for extremely small values of the small parameter H defined in (3.8). The approximations used here are therefore challenged by these examples but we will find nevertheless that there is qualitative consistency with the full-wave results, as described in the next section.

There is also a real periodic orbit γ_r , which defines a real action by

$$\oint_{\gamma_r} K_x dX = 2S. \quad (3.33)$$

Below the threshold ($|K_y| < K_y^\sharp$), the closed orbit corresponds to the blue curves in Fig. 3.11a-3.11b. The action S is then simply the area enclosed by the closed orbit in the real phase plane. It is this action S that is used to define the matrix σ_X in (3.28). A corresponding action can be obtained for $|K_y| > K_y^\sharp$ by a somewhat more complicated integration path involving segments of complex evolution but having overall a net real displacement in the complex time plane. For example, starting at the top right turning point (X_2, K_2) in Fig. 3.12b and evolving in negative imaginary time first returns the trajectory to the real phase plane at $(-X_1, K_1)$. From there, evolution in real time brings the orbit to the bottom left turning point at $(-X_2, -K_2)$. From here, evolution in positive imaginary time returns the trajectory to the real phase plane at $(X_1, -K_2)$ and subsequent evolution in real time brings the orbit back to its starting position at (X_2, K_2) . If the segments of the imaginary-time evolution are in opposite directions in the complex plane, the net action for this orbit is real, and defines S through (3.33). Again as a result of Cauchy's theorem, this real action does not change if the integration path in the complex time plane is deformed, or alternative initial conditions are chosen.

3.4 Results

We first test the results of the the graph model described in the previous section for the curvature profile with a generic quadratic maximum represented by blue

curves in Fig. 3.2a. A comparison of numerically calculated transmission and reflection fractions against the predictions of the graph model has already been shown in Fig. 3.8. We find in this case that there is detailed, qualitative and quantitative agreement between the graph models and full-wave numerical results. This agreement includes both the smooth transition across $\theta_0 = \theta_0^\sharp$ and the positions and shape of resonant scattering peaks for $\theta_0 < \theta_0^\sharp$. Above the transition, there is accurate reproduction of the zeros of the transmitted fraction, evident in the log plot of part (b).

We have also compared the results of the graph model to the flatter curvature profiles represented by red and black curves in Fig. 3.2, which have been designed to challenge the assumptions of the model and to test how it might fail. First, although these profiles have strictly-speaking quadratic maxima, these are in practice very shallow so that approximations (3.31a-3.31b) would require extremely small values of the thickness parameter H in order to be valid. Second, the X coordinate of the tunnelling orbit shown in Fig. 3.11, which is for incidence below the transition angle, evolves along the imaginary axis. Therefore its dynamics uses the profiles shown in Fig. 3.2b. For the flatter profiles these show a shallow local minimum and then begin to oscillate as a function of $\text{Im}(X)$ (the generic profile in blue also oscillates for large enough $\text{Im}(X)$ but at scales that do not have impact on the calculations here). We will observe that this leads to bifurcations in the tunnelling orbit that qualitatively affect the reflection and transmission coefficients.

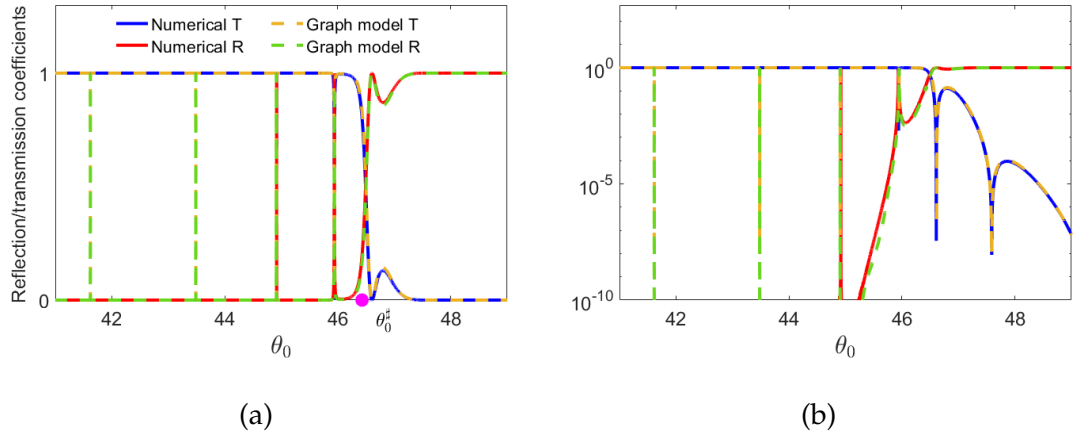


Figure 3.13: Transmission and reflection coefficients shown here using the same conventions as in Fig. 3.8 but for the intermediate curvature profile represented by the red curve in Fig. 3.2. The agreement here is still very good, but compared to Fig. 3.8 small deviations are noticeable especially near $\theta_0 = \theta_0^{\ddagger}$ due to the behaviour of the curvature profile around $X = 0$.

For the middle curvature profile (red curve), there is reasonable agreement across the transition region, as shown in Fig. 3.13, although this agreement is not as close as in Fig. 3.8. For the flattest profile (black curve in Fig. 3.2), the reflection and transmission coefficients show reasonable agreement above the transition (see Fig. 3.14b), but there are significant quantitative differences across the transition region. Here the second derivative of the curvature profile is so small at its peak that (3.31a-3.31b) do not adequately describe the behaviour of σ_{node} near the transition. Far enough above the transition, however, where $\Theta \gg 1$ and $\delta \approx 0$, the primitive approximations $r_{\text{node}} \approx -i$ and $t_{\text{node}} \approx e^{-\Theta}$ are valid and agreement is better.

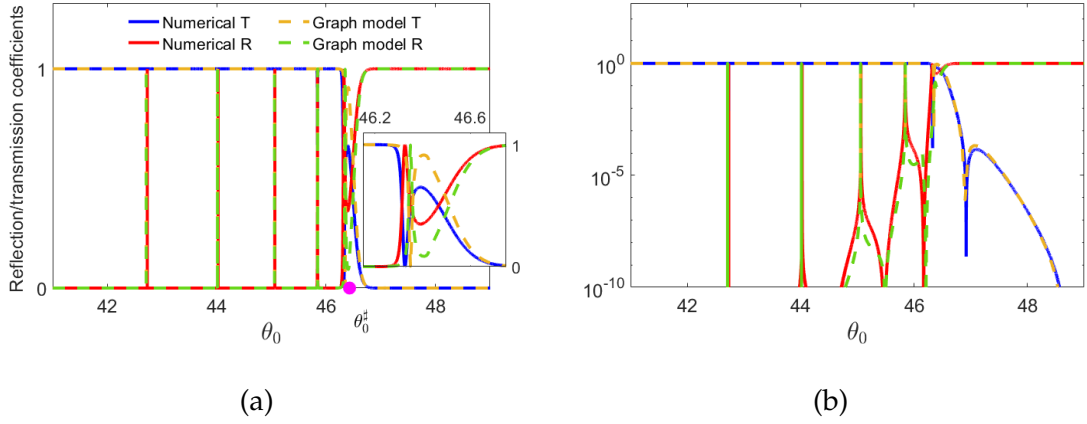


Figure 3.14: Transmission and reflection coefficients shown here use the same conventions as in Fig. 3.8 but for the flattest curvature profile represented by a black curve in Fig. 3.2. Although quantitative agreement is poor across the transition region, there is qualitative similarity and features away from the transition are well reproduced.

Below the transition (where $\theta_0 < \theta_0^\sharp$), there are even starker deviations, which arise due to the oscillation of $\mathcal{K}(X)$ along the imaginary axis (see Fig. 3.2b). The tunnelling orbit undergoes a bifurcation at an incident angle θ_0^b below θ_0^\sharp (and in fact θ_0^b is quite near θ_0^\sharp for the flattest curvature profile). This bifurcation is illustrated in Fig. 3.15 for the intermediate curvature profile. In Fig. 3.15b we show a phase portrait obtained by plotting level curves $D' = 0$ of the Hamiltonian (as θ_0 or K_y are varied) in a plane with axes $(K_x, \text{Im}(X))$ (where symmetries mean that D' remains real): when $\theta_0 = \theta_0^b$ the corresponding level curves form a separatrix dividing a short tunnelling orbit of the form seen in Fig. 3.11 from a more complicated orbit with an extra lobe shown by the red curves in In Fig. 3.15a. Here the

complex orbit with the smallest imaginary action is obtained by taking a shortcut across the real orbit shown in green in Fig. 3.15a. It is the action of this truncated complex orbit that dominates tunnelling rates when $\theta_0 < \theta_0^b$.

The detailed behaviour of such complex phase portraits depends critically on the behaviour of the curvature profile along the imaginary X axis. This behaviour can be significantly different even for profiles that look quite similar along the real axis. We therefore do not propose to give a systematic accounting of such additional structure in this chapter: treatment of conversion rates around the angle θ_0^b at which the shortcut appears would require an analysis at least as complicated as that behind (3.31a-3.31b) and might then need to be revisited for each new family of curvature profiles treated, if their behaviour along the imaginary X axis is different. Instead we simply provide a simplified calculation to demonstrate in broad terms that such bifurcations are able to explain what is observed for the curvature profiles in Fig. 3.2.

Far enough below the transition, where Θ is negative and large in magnitude and $\delta \approx 0$, the primitive approximations $r_{\text{node}} \approx -ie^\Theta$ and $t_{\text{node}} \approx 1$ are valid. In plotting the results of the graph model in Figs. 3.13 and 3.14, we have replaced e^Θ by $\text{Re}(e^\Theta)$ for $\theta_0 < \theta_0^b$. Because $\text{Re}(\Theta) \neq 0$ here, this is an oscillatory function of θ_0 and has zeroes, for example. These oscillations and zeroes agree well with those observed in calculations from the full wave model, seen in Figs. 3.13b and 3.14b. Such bifurcations of the complex tunnelling orbit therefore provide an means of understanding more complex behaviour in scattering from plate bends.

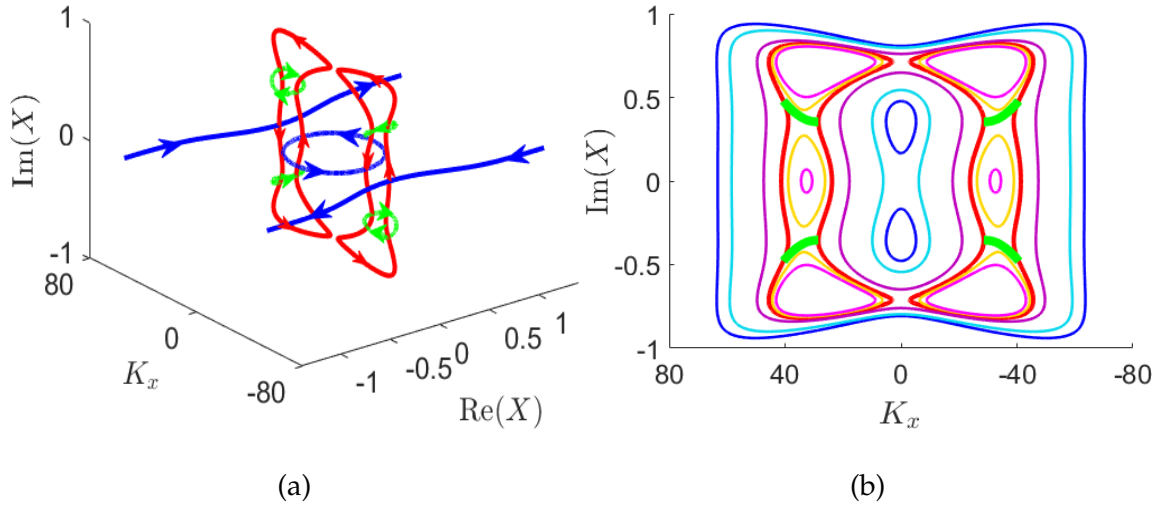


Figure 3.15: Real and complex orbits for the second curvature profile (red line in Fig. 3.2) are shown for the case $K_y < K_y^\sharp$. Some of the complex orbits with real initial conditions ($X = 0$) change geometry due to bifurcations. In (a) the bifurcation occurs close to $(\text{Re}(X), \text{Im}(X), K_x) = (0, \pm 0.36, 38)$; here, the red curves show examples of tunnelling orbits with imaginary action (long orbits) and the green curves show examples of tunnelling orbits with real action. In (b), the phase-space $(K_x, \text{Im}(X))$ of complex orbits with imaginary action for the second curvature profile are shown.

3.5 Conclusion

We have provided an analysis of the transition between complete reflection and complete transmission of bending waves incident on a curved section of a thin shell. The analysis is based on complex ray theory and extends the treatment based on real ray dynamics provided in [31, 32]. These results allow us to model a smooth transition where complete transmission turns to complete reflection as

an incidence angle increases, and also to model resonance effects where reflection is enhanced by coupling to local modes trapped in the curved region of the plate.

For a generic curvature profile with a simple quadratic maximum, the analysis works extremely well not only in explaining the smooth transition between complete reflection and complete transmission, but also reproduces in detail phenomena such as reflection mediated by trapped resonances (resonant tunnelling).

We have also compared the predictions of the model to scattering properties of curvature profiles with flat maxima. Here the assumptions made to derive the model begin to fail and we observe quantitative deviations from its predictions. Nevertheless the model succeeds in describing qualitatively the reflection and transmission rates calculated numerically from a full wave treatment, including resonance positions and fluctuations in reflection and transmission rates arising due to bifurcations of the underlying complex orbit to more complicated forms.

In large build-up systems, determining the distribution of vibrational energy also reveals apparently random fluctuations. Statistical approaches are preferred here, which suggest certain assumptions about the underlying ray dynamics, such as diffusive behaviour. This approach completely avoids the actual ray dynamics and can explain the generic, universal features of wave systems; the techniques will be addressed in more detail in the next chapter.

Chapter 4

Sound Radiation

In nature, sound radiation from irregular geometries and complex structures is stochastic and may approach unpredictable ranges which are difficult to estimate using conventional deterministic approaches. It is important to model these radiations both in open space and in enclosures in the context of vibro-acoustics [159]. In this context, a two-point correlation function provides the natural solution of the structural vibration problem [160]. In addition, by presenting the correlation function as a Wigner function, an explicit quantitative link can be made between the normal surface velocity correlation function and phase space densities [160]. The Wigner Distribution Function (WDF) method has been created with regard to quantum mechanics [161], and yet has provided far-reaching applications also for microwaves [162] and in optics [163, 164]. The method implemented below uses a connection between the field-field correlation function (CF) and the WDF [165, 166, 167]. Both quantities have been intensively studied in the

physics and optics literatures, as well as in the context of electromagnetic waves for a planar source [168, 169, 170, 171]. Berry's conjecture assumes a universal CF in the presence of ray chaos, which is similar to Gaussian random field correlations [172, 49, 173]. After sufficient averaging, non-universal corrections can be obtained by making a connection between the Green function of the system and the CF. This conjecture establishes a connection between the underlying ray dynamics and random wave fields [27].

In general, prior studies of sound radiation have dealt with simple rectangular plates or strips [43]. Below a critical frequency (the frequency at which a structural wavenumber matches the acoustic wavenumber) and when the modal density is low, Berry *et al.* [174] studied the influence of boundary conditions on sound radiation. It is well established that the radiation of sound through a given mode, excited below its modal critical frequency, is due to the edges and corners of the plate for a finite, simply supported, baffled plate [43]. While for free and guided boundary conditions the radiation efficiency is almost the same in low order modes, in higher modes the radiation efficiency is considerably larger than in the guided boundary condition [175].

In this chapter, we treat the simplest case of homogeneously diffuse fields on the vibrating structure, corresponding to uniform ray densities in phase space. We model the diffuse field explicitly as a random superposition of plane waves using Berry's conjecture [49], modified near edges to account for boundary conditions. Such diffuse fields are naturally characterised by a two-point correlation

function, set out in more detail in this chapter. The WDF provides the connection between DEA and CFs [160] which allows us to account for local variations of this model. In this study, we will utilize the WDF approach within finite domains, which may be regularly or irregularly shaped. Furthermore, in this chapter, we extend DEA towards coupling structural vibration calculations with estimating acoustic radiation in the surrounding fluid; the method is based on the WDF technique. In addition, the effect of boundary conditions on sound radiation below and above the critical frequency is studied as they form a basis for the following chapter. To highlight the calculation using phase-space methods, we take as an example the simply supported and guided rectangular plate. A guided boundary is introduced [66] instead of considering a clamped (or free) edge for which the plate modes are more complicated [44]. The guided boundary has unconstrained displacement and zero rotation while the simply supported boundary has unconstrained rotation but zero displacement. The effect of guided boundary conditions was also explored by Yoo [175].

The objectives of this chapter using the DEA phase-space methods are summarized as follows:

- recovering phase information from the phase space density of the vibrating structure using the DEA calculation (linking phase space density to the normal surface velocity CF);
- coupling between the structural waves CF propagating in a vibrating ele-

ment with acoustic sound radiation;

- calculating the radiation pattern;
- capturing the effects of finite size along with boundary conditions on the sound radiation field.

A wider goal is later to modify this work to account for variations of the ray densities described by phase space simulations obtained for example from DEA calculations.

4.1 Theory of radiation from surfaces based on phase space densities

4.1.1 Correlation function

Consider a flat plate occupying an area $\Omega \subset \mathbb{R}^2$ as illustrated in Fig 4.2a. Denote by w the normal surface velocity field of the plate and let k_B and k_A be the bending and acoustic wavenumbers respectively. Consider a source normal surface velocity CF

$$\Gamma_{\Omega}(\mathbf{x}, \mathbf{x}') = \langle w(\mathbf{x})w^*(\mathbf{x}') \rangle, \quad (4.1)$$

where $\langle \cdot \rangle$ denotes time intervals, frequency or local spatial averaging and $\mathbf{x}, \mathbf{x}' \in \Omega$. After sufficient averaging, the quantity Γ_{Ω} can be linked to phase space densities using Wigner transformation [160] as shown below. The WDF of an operator

is defined as

$$W_{\Gamma}(\bar{\mathbf{x}}, \mathbf{p}) = \int e^{-ik_A \mathbf{p} \cdot \mathbf{s}} \Gamma\left(\bar{\mathbf{x}} + \frac{\mathbf{s}}{2}, \bar{\mathbf{x}} - \frac{\mathbf{s}}{2}\right) d\mathbf{s}, \quad (4.2)$$

where $\mathbf{s} = \mathbf{x} - \mathbf{x}'$ and $\bar{\mathbf{x}} = (\mathbf{x} + \mathbf{x}')/2$ with inverse Wigner transformation given by

$$\Gamma(\mathbf{x}, \mathbf{x}') = \left(\frac{k_A}{2\pi}\right)^d \int e^{ik_A(\mathbf{x}-\mathbf{x}') \cdot \mathbf{p}} W_{\Gamma}\left(\frac{\mathbf{x} + \mathbf{x}'}{2}, \mathbf{p}\right) d\mathbf{p}, \quad (4.3)$$

d is the dimension of the structure. In physical shells, $d = 2$.

From the phase-space dynamics, in our case corresponding to a boundary map or more generally the Poincaré map on a surface of section, one can derive classical phase space densities ρ_{Ω} . The initial density ρ_{Ω}^0 can then be related to a boundary ray density that arrives directly from an internal source distribution. Mapping the subsequent reflections of the source ray density leads to the iterated densities $\rho_{\Omega}^0 \rightarrow \rho_{\Omega}^1 \rightarrow \cdots \rho_{\Omega}^n \rightarrow \cdots$ that can be represented in the lossless limit [176] in terms of the (linear) integral operator \mathcal{B} defined as,

$$\mathcal{B}[\rho_{\Omega}^n](X) = \rho_{\Omega}^{n-1}(\varphi^{-1}(X)) = \int dX' \delta(X - \varphi(X')) \rho_{\Omega}^{n-1}(X'), \quad (4.4)$$

where $X = (\bar{\mathbf{x}}, \mathbf{p})$ denotes the phase space coordinates on the boundary of the surface of section $\partial\Omega$ (where $\bar{\mathbf{x}} \in \Omega$ and $\mathbf{p} \in \mathbb{R}^2$ denotes momentum space), and $\varphi : X' \rightarrow X$ is a classical map that defines the flow of trajectories after a single reflection from the surface of the segment back to itself. The operator \mathcal{B} is also known as Frobenius-Perron (FP) operator [176]. For considering effects such as absorption and mode conversion, as well as uncertainty, the integral representation in (4.4) is useful, see [137]. The stationary phase space density $\rho_{\Omega}(\bar{\mathbf{x}}, \mathbf{p})$ on

the boundary of the plate at a given frequency ω induced by an initial boundary distribution is then obtained using

$$\rho_\Omega = \mathcal{B}\rho_\Omega + \rho_\Omega^0 \Rightarrow \rho_\Omega = \frac{1}{1 - \mathcal{B}}\rho_\Omega^0 = \sum_{n=0}^{\infty} \mathcal{B}^n \rho_\Omega^0 = \sum_{n=0}^{\infty} \rho_\Omega^n. \quad (4.5)$$

Effective computational tools have been developed for the calculation of ρ_Ω , and thus indirectly for the mean of Γ_Ω . Among these, the fast phase-space propagation method, DEA, is especially applicable for complex structures, which have been used in a variety of engineering applications, along with the DFM mesh implementation [135, 136, 30, 39].

Although phase information has been neglected in the DEA method, phase and interference information can be recovered by linking the phase space density ρ_Ω to the normal surface velocity CF, Γ_Ω , using the WDF. The classical stationary density can then be approximated by

$$\rho_\Omega \approx \langle W_\Gamma \rangle, \quad (4.6)$$

by choosing appropriate frequency averaging, local (spatial) averaging or both [160]. Thus, using Eq. (4.6) and Eq. (4.3), the full correlation function Γ_Ω can be written as

$$\langle \Gamma_\Omega(\mathbf{x}, \mathbf{x}') \rangle = \frac{k_A^2}{(2\pi)^2} \int_{\mathbb{R}^2} e^{ik_A \mathbf{p} \cdot (\mathbf{x} - \mathbf{x}')} \rho_\Omega \left(\frac{1}{2}(\mathbf{x} + \mathbf{x}'), \mathbf{p} \right) d\mathbf{p}. \quad (4.7)$$

4.1.2 The random wave model (RWM): Diffuse-field

In both acoustics and elastodynamics, the concept of random or diffusive wave fields in irregularly formed reverberant bodies has played an important role [177,

178, 179, 180]. For the sake of simplicity and to better understand the problem, the simplest case of uniform ray densities in phase space corresponding to homogeneously diffuse fields is considered, here

$$\rho_{\Omega}(\bar{\mathbf{x}}, \mathbf{p}) = \frac{4\pi}{k_A^2} \delta\left(\mathbf{p}^2 - \frac{k_B^2}{k_A^2}\right). \quad (4.8)$$

The prefactor in Eq. (4.8) selected to give normalisation in Eq. (4.9). The inverse Wigner transform of the phase space density in Eq. (4.8), as defined in Eq. (4.7), gives the bulk properties of the corresponding diffuse field, which is characterised by a two-point correlation function, which takes the form

$$\Gamma_0(\mathbf{x}, \mathbf{x}') = J_0(k_B |\mathbf{x} - \mathbf{x}'|), \quad (4.9)$$

where J_0 denotes the zero order Bessel function of the first kind. We assume a planar plate occupying a region Ω , with $\mathbf{x} = (x, y)$ and $\mathbf{x}' = (x', y')$ denoting pairs of points in Ω . The correlation function Γ_0 represents the bulk model whenever \mathbf{x}, \mathbf{x}' are far from the boundary $\partial\Omega$. This corresponds to Berry's conjecture that the individual eigenfunctions associated with classically chaotic trajectories for confined quantum waves can be modelled statistically by a plane wave superposition with fixed wave number k which have been sampled randomly over wave directions and phases, with average spatial correlation

$$\Gamma_0(\mathbf{x}, \mathbf{x}') = \langle w(\mathbf{x})w^*(\mathbf{x}') \rangle,$$

where, in a random phase space model

$$w(\mathbf{x}) = \sqrt{\frac{2}{N}} \sum_{n=1}^N \cos(k_B x \cos \theta_n + k_B y \sin \theta_n + \phi_n).$$

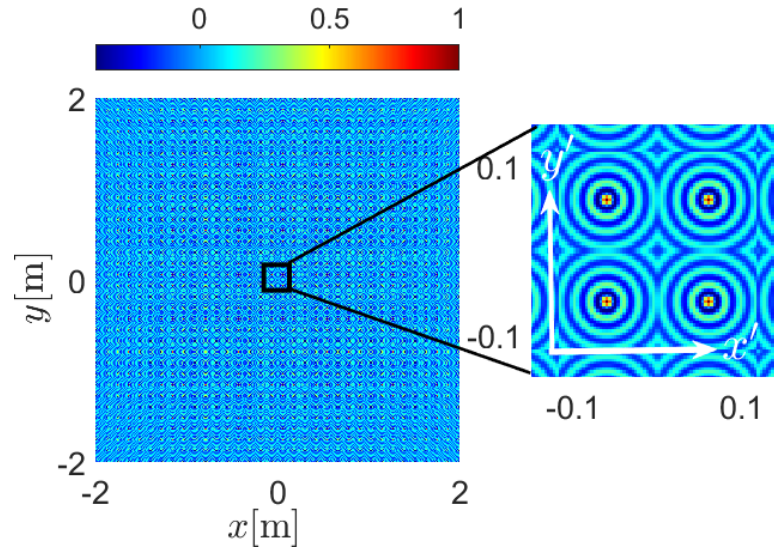


Figure 4.1: A mosaic representation of the 4-D correlation function $\Gamma_0(\mathbf{x}, \mathbf{x}')$.

The CF for a two-dimensional calculation is a four-dimensional matrix with coordinates (x, y, x', y') . It is difficult to visualize a four-dimensional matrix, and we therefore view the CF as a mosaic representation. A mosaic plot is a graphical technique used to display data from two or more qualitative variables [181], which shows the same information graphically in either one variable [182] or two variables [183, 184]. It provides a summary of the data and allows the relationship between different variables to be established. Here, the mosaic representation contains both (x, y) and (x', y') coordinates. Figure 4.1 shows a mosaic representation of the bulk model of the CF, which is a 2D visualization.

Near boundaries, the model described in (4.9) needs to be modified to include corrections due to the boundary conditions. In these notes, we consider *pseudo Dirichlet* (Dbc) or *pseudo Neumann* (Nbc) boundary conditions; obviously, such boundary conditions only apply to second order equations such as the Helmholtz

equation and may in general serve only as simplified models representing *simply supported* or *guided* boundary conditions for bending modes in plates. Using the simplified Dirichlet or Neumann boundary conditions serves as a proof-of-principle demonstration that such boundary corrections dominate acoustic radiation below the critical frequency.

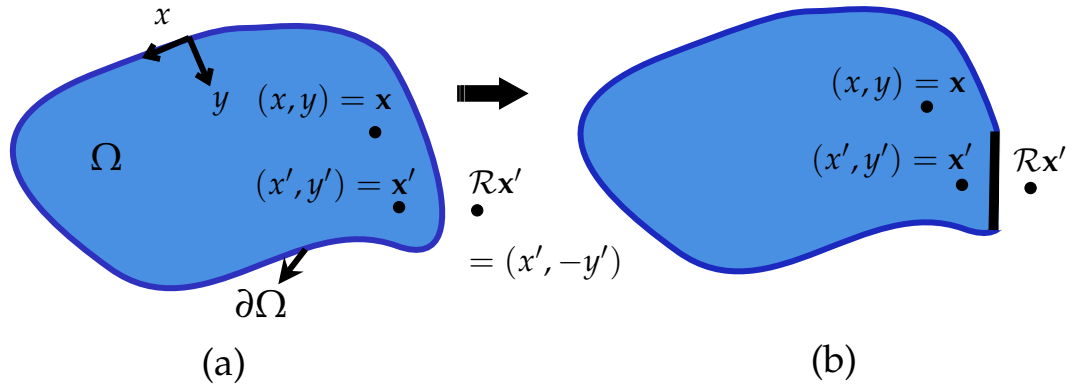


Figure 4.2: (a) Local coordinates and method of images for an arbitrary domain Ω . (b) Approximation of boundaries in terms of straight edges.

Correlation functions near a boundary, taking into account boundary conditions, have been described by Berry [185] in a boundary-modified random plane-wave model to satisfy Dbc or Nbc along a straight line. We use these results for the case of a straight edge, which can be presented as a method-of-images addition to the bulk correlation function; that is,

$$\Gamma_{\Omega}(\mathbf{x}, \mathbf{x}') = J_0(k_B |\mathbf{x} - \mathbf{x}'|) \pm J_0(k_B |\mathbf{x} - \mathcal{R}\mathbf{x}'|). \quad (4.10)$$

Here, $\mathcal{R}\mathbf{x}'$ denotes a reflection of \mathbf{x}' through the edge and the \pm signs apply to Nbc and Dbc, respectively. For other boundary conditions, the corrections are

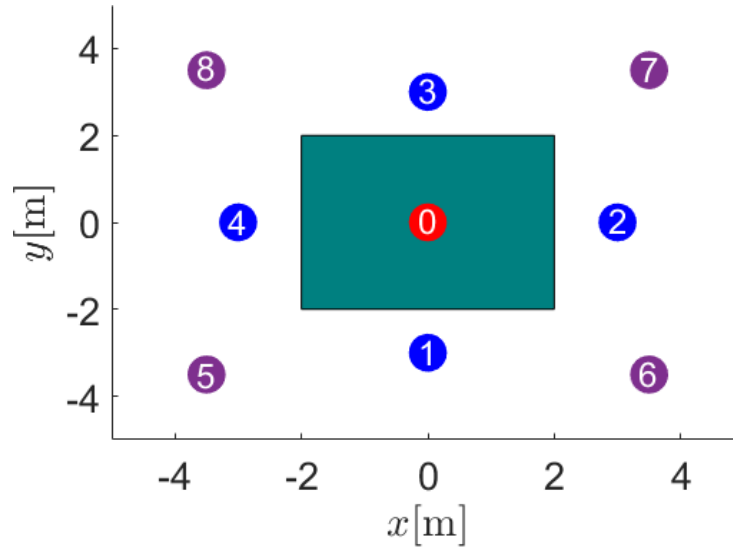


Figure 4.3: Method of images for a $(4\text{m}) \times (4\text{m})$ rectangular plate. (0) the bulk model of the CF is $\Gamma_0(\mathbf{x}, \mathbf{x}') = J_0(k_B |(x - x', y - y')|)$; (1)-(4) corresponds to the "image" of the CF at nearest edge, e.g. (1) is the "image" of the CF at $y_0 = -2$, and is $\Gamma_1(\mathbf{x}, \mathbf{x}') = J_0(k_B |(x - x', y + y' + 4)|)$; (5-8) corresponds to the "image of image" of the CF at nearest corner, e.g. (5) is the "image of image" of the CF at $(x_0, y_0) = (-2, -2)$, and is $\Gamma_5(\mathbf{x}, \mathbf{x}') = J_0(k_B |(x + x' + 4, y + y' + 4)|)$.

more complicated but can be obtained using a similar approach. The result above is valid only for a straight edge but we adapt this to apply approximately near general boundaries as illustrated in Fig. 4.2.

In the case of a rectangular plate, four "image" corrections correspond to each edge and four "image of image" corrections correspond to each corner should be applied to the bulk model, e.g. for the configuration in Fig. 4.3, the spatial representation of the full correlation function, as shown in Fig. 4.3, in Eq. (4.10)

can be written as

$$\Gamma_{\Omega}(\mathbf{x}, \mathbf{x}') = \Gamma_0(\mathbf{x}, \mathbf{x}') \pm \sum_{l=1}^4 \Gamma_l(\mathbf{x}, \mathbf{x}') + \sum_{ll=5}^8 \Gamma_{ll}(\mathbf{x}, \mathbf{x}'), \quad (4.11)$$

where $\Gamma_l(\mathbf{x}, \mathbf{x}')$ is a single image correction based on the distance from the nearest straight edge and $\Gamma_{ll}(\mathbf{x}, \mathbf{x}')$ provides higher-order corrections in the form of “images of images” based on the distance from the nearest corner.

In the next section we give the theory of calculating acoustic pressure $p(\mathbf{x}, z)$ at a point $(\mathbf{x}, z) = (x, y, z) \in \mathbb{R}^3$ from a flat vibrating surface.

4.1.3 Sound Pressure distribution

We use as a basis for our calculation the Kirchoff-Helmholtz equation for irregularly shaped vibrating bodies, which can be further simplified, for planar structures, to the well-known Rayleigh integral [48]. Using Figure 4.4 for the plate coordinates, the pressure p at any point $(\mathbf{x}, z) = (x, y, z)$, radiated by a vibrating plate set in an infinite rigid baffle, is then determined by

$$p(\mathbf{x}, z) = -\frac{i\rho_0\omega}{2\pi} \int_{\Omega} w(\mathbf{x}') \frac{e^{ik_A R}}{R} d\mathbf{x}', \quad (4.12)$$

where $R = \sqrt{(x - x')^2 + (y - y')^2 + z^2}$, c_0 is the speed of sound in the surrounding medium and ρ_0 is the fluid density. This can be written in the form of a convolution [186]

$$p(\mathbf{x}, z) = w(\mathbf{x}) * h_g(\mathbf{x}, z), \quad (4.13)$$

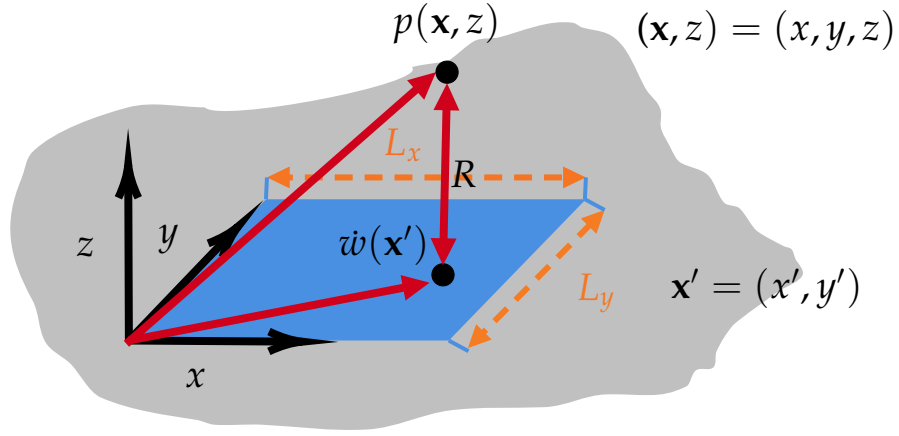


Figure 4.4: Schematic view of a rectangular plate with a length of L_x and width of L_y ; relation between surface vibration and sound pressure.

where the surface normal velocity $w(\mathbf{x})$ is assumed to be zero beyond the plate boundary, $*$ denotes a two-dimensional convolution in \mathbf{x} (see Appendix A), and

$$h_g(\mathbf{x}, z) = -2i\rho_0\omega g(\mathbf{x}, z) = -i\rho_0\omega \frac{e^{ik_A\sqrt{x^2+y^2+z^2}}}{2\pi\sqrt{x^2+y^2+z^2}}, \quad (4.14)$$

where $g(\mathbf{x}, z)$ is Green's function for the 3D Helmholtz equation.

Taking the Fourier transforms with respect to x and y on both sides of Eq. (4.13) with the use of Figure 4.5 for the plate coordinates in the momentum domain, and then applying the convolution theorem (see Appendix A) we get [186]

$$P(\mathbf{p}, z) = W(\mathbf{p})H_g(\mathbf{p}, z), \quad (4.15)$$

where

$$H_g(\mathbf{p}, z) = \mathcal{F}\{h_g(\mathbf{x})\} = \rho_0c_0 \frac{e^{ik_A T(\mathbf{p})z}}{T(\mathbf{p})}, \quad (4.16)$$

where $P(\mathbf{p}, z)$, $W(\mathbf{p})$ denote the momentum representation of the sound pressure and the normal surface velocity respectively, z denotes the distance above the

plate and $k_A \mathbf{p}$ is the wave-vector component in the (x, y) -plane; $H_g(\mathbf{p}, z)$ is the propagator.

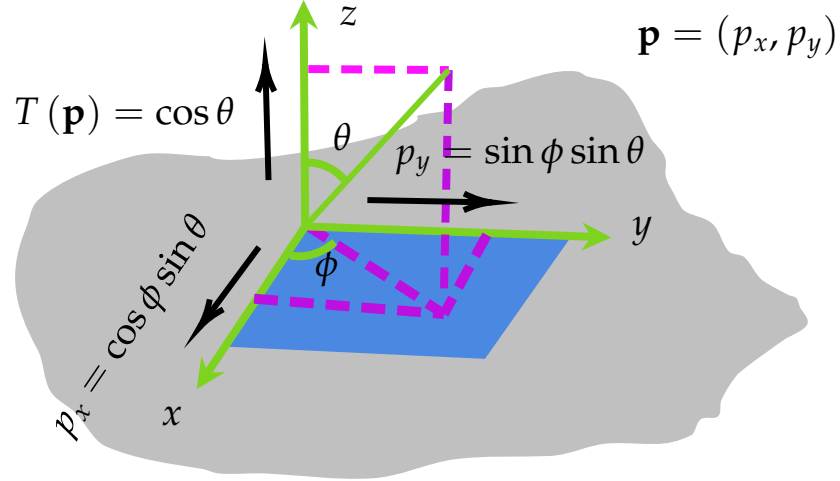


Figure 4.5: Schematic representation of the coordinates of the plates in momentum space.

In this work, the normal component of the unit wave vector is defined as [187, 169]

$$T(\mathbf{p}) = \begin{cases} \sqrt{1 - |\mathbf{p}|^2} & \text{for } |\mathbf{p}|^2 \leq 1, \\ i\sqrt{|\mathbf{p}|^2 - 1} & \text{for } |\mathbf{p}|^2 > 1. \end{cases} \quad (4.17)$$

The case $|\mathbf{p}|^2 \leq 1$ corresponds to propagation of acoustic waves, which contribute to the far-field sound radiation, while $|\mathbf{p}|^2 > 1$ corresponds to evanescent propagation, which does not contribute to the far-field sound radiation but maybe detectable in the near-field. In the next section we connect the structural response from DEA to the sound pressure and for that we need the acoustic correlation function.

4.1.4 Propagation of Sound radiation field

The goal of this work is to predict acoustic emissions from complex, noisily driven vibrating structures using methods that combine well with DEA phase-space simulation methods. In this setting, we have seen that the vibration and subsequent radiated acoustic fields are naturally described statistically in the form of field-field correlation functions. In addition, vibrations and the associated radiation can also be represented in momentum space due to wave phenomena. This presentation is often also extremely effective when it comes to explaining the physics that underlies the phenomenon. Here we work with a correlation function in momentum representation, defined by

$$\Gamma_p(\mathbf{p}, \mathbf{p}'; z) = \langle P(\mathbf{p}, z) P^*(\mathbf{p}', z) \rangle, \quad (4.18)$$

$$= G_H(\mathbf{p}, \mathbf{p}'; z) \Gamma_\Omega(\mathbf{p}, \mathbf{p}'). \quad (4.19)$$

where

$$G_H(\mathbf{p}, \mathbf{p}'; z) = \frac{\rho_0^2 c_0^2}{T(\mathbf{p}) T^*(\mathbf{p}')} e^{ik_A z [T(\mathbf{p}) - T^*(\mathbf{p}')]} \quad (4.20)$$

and

$$\Gamma_\Omega(\mathbf{p}, \mathbf{p}') = \mathcal{F} \{ \Gamma_\Omega(\mathbf{x}, \mathbf{x}') \} = \int_\Omega \int_\Omega e^{-ik_A \mathbf{p} \cdot \mathbf{x}} \Gamma_\Omega(\mathbf{x}, \mathbf{x}') e^{ik_A \mathbf{p}' \cdot \mathbf{x}'} \, d\mathbf{x} \, d\mathbf{x}', \quad (4.21)$$

$P(\mathbf{p}, z)$ is given in Eq. (4.15) and $\Gamma_\Omega(\mathbf{x}, \mathbf{x}')$ is given in Eq. (4.7). After propagating the sound pressure field from the surface of the structure to the distance of interest, denoted z , the inverse Fourier transformation is applied.

$$\Gamma_p(\mathbf{x}, \mathbf{x}'; z) = \mathcal{F}^{-1} \{ \Gamma_p(\mathbf{p}, \mathbf{p}'; z) \}. \quad (4.22)$$

Therefore, the amplitude of the sound pressure field at distance z far from the planar radiator is then given by

$$\langle |p(\mathbf{x}, z)|^2 \rangle = \Gamma_p(\mathbf{x}, \mathbf{x}; z). \quad (4.23)$$

This approach allows us to quantify acoustic radiation from vibrating structures being approximated by phase-space simulation methods such as DEA. It applies to arbitrary planar shapes, but in the following we focus on rectangular plates.

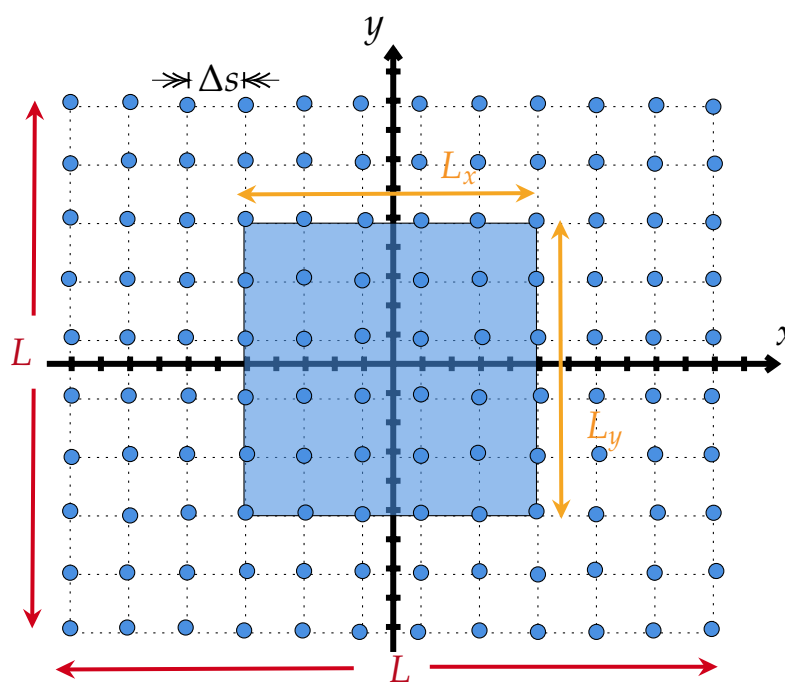


Figure 4.6: Schematic representation of a sampled rectangular plate set in a baffle for the calculation of sound radiation using the FFT.

4.2 The Fast Fourier Transform (FFT) method

By using the Fast Fourier Transform (FFT), the velocity transformation described in Eq. (4.21) can be solved much faster. The FFT is a technique that calculates the discrete Fourier Transform (DFT) and reduces the number of computations needed for a data set of size N from $\mathcal{O}(N^2)$, which arises if one use the traditional way of computing the numerical integration in the Fourier transform, to $\mathcal{O}(N \log N)$ [188]. Furthermore, as a built-in FFT feature is given by many programming languages, such as MATLAB, the role of programming it is much minimized.

4.2.1 Steps of the calculation

The numerical evaluation of Rayleigh's integral formula was carried out by Williams [186] using the FFT algorithm for any shape of planar radiators with any given velocity in the source plane. The main advantage of this approach is its computing speed, which is much faster than simple two-dimensional numerical integration. The method is intended to calculate the radiated pressure in the near-field of the source. Here this method is expanded to provide the intensity of the sound pressure field (matrix) in the near-field as well as in the far-field in order to provide insight into the radiated sound direction.

The application of this method to compute $p(\mathbf{x}, z)$ with FFT can be summarized in the following on the basis of the information of $\rho_{\Omega}(\mathbf{x}', \mathbf{p})$:

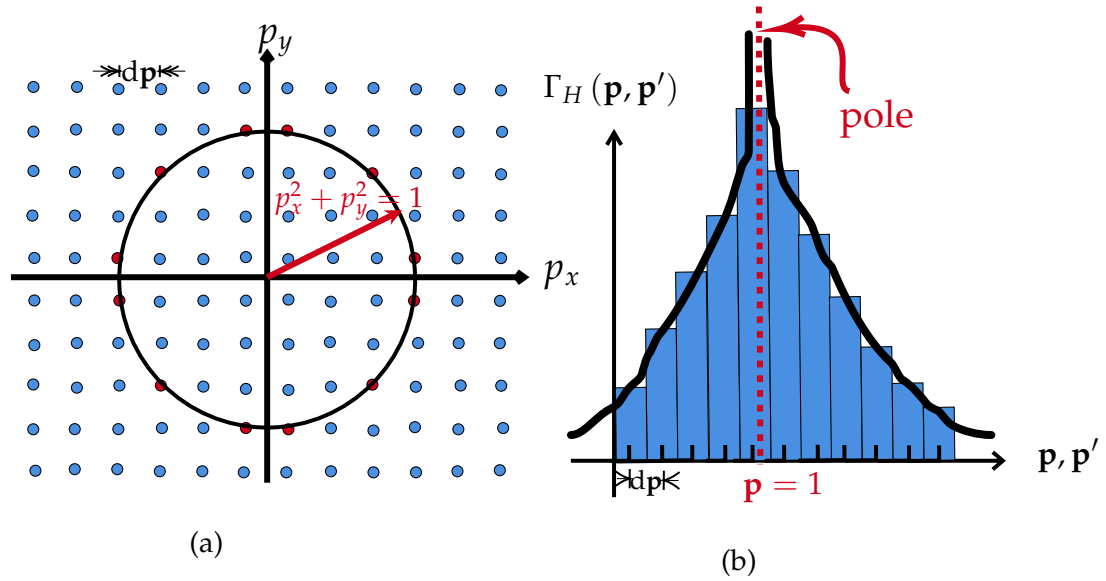


Figure 4.7: (a) Radiation circle with sample points in \mathbf{p} space. (b) Poles arise when a sample point coincides with the radiation circle.

- Calculate the inverse Wigner transform of the phase space density $\rho_\Omega(\mathbf{x}', \mathbf{p})$ to obtain the normal surface velocity correlation function $\Gamma_\Omega(\mathbf{x}, \mathbf{x}')$;
- Calculate the discrete Fourier transform of $\Gamma_\Omega(\mathbf{x}, \mathbf{x}')$ using the four-dimensional FFT algorithm to obtain $\Gamma_\Omega(\mathbf{p}, \mathbf{p}')$;
- Transform $\Gamma_\Omega(\mathbf{p}, \mathbf{p}')$ into the acoustic correlation distribution $\Gamma_p(\mathbf{p}, \mathbf{p}'; z)$ using Eq. (4.19);
- Calculate the inverse discrete Fourier transform (IDFT) using IFFT to get the acoustic propagated correlation function $\Gamma_p(\mathbf{x}, \mathbf{x}'; z)$.

On each point of a baffled plate with dimensions $L \times L$, the normal surface velocity correlation function is defined. With the sample spacing of Δs , the points are

sampled. As can be seen in Figure 4.6, the plate itself takes up a region at the centre of this baffled plate. The normal surface velocity correlation function is equal to $\Gamma_{\Omega}(\mathbf{x}, \mathbf{x}')$ on the surface of the plate and is equal to zero on the rest of the baffle. Truncation of the FFT leads to so-called replicated sources because the region beyond the truncated area (for example, the area beyond that shown in Figure 4.6) is effectively periodic. L must therefore be chosen to be sufficiently large to avoid producing a bias error in the analysis due to the pressure field $p(\mathbf{x}, z)$ overlapping with that of the repeated sources.

As can be seen from Eq. (4.20), the propagator Γ_H contains singularities at $T(\mathbf{p}) = 0$ or at $T^*(\mathbf{p}') = 0$. Therefore, in the evaluation of the integral in Eq. (4.22) even though the integral value is finite, there is slow convergence when the values of sample points of the coordinates coincide with the radiation circle i.e. $|\mathbf{p}| = 1$ or $|\mathbf{p}'| = 1$. Figure 4.7 shows when this occurs and a radiation circle given by the equation $|\mathbf{p}|^2 = p_x^2 + p_y^2 = 1$ is described in it. The sample points are shown in the momentum space. For the sampling points inside the radiation circle, $k_z = kT(\mathbf{p})$ is real, and the dots represent the propagation of plane waves with wave numbers $k_x = kp_x, k_y = kp_y$. On the other hand, k_z is imaginary for points which fall beyond the radiation circle and which represent evanescent waves. The same is valid for the complex conjugation of k_z , i.e. $k_z^* = kT^*(\mathbf{p})$. If the radiation circle crosses a lattice point, our FFT results will fail. The following strategy, while not systematic, is found to provide sufficiently accurate results. For example, by selecting the sample points in the middle of rectangular inte-

gration sections of length $d\mathbf{p}$, the singularity can be avoided (see Fig. 4.6b). The sample spacing $d\mathbf{p}$ must, of course, be selected to be small enough to achieve a smooth outcome.

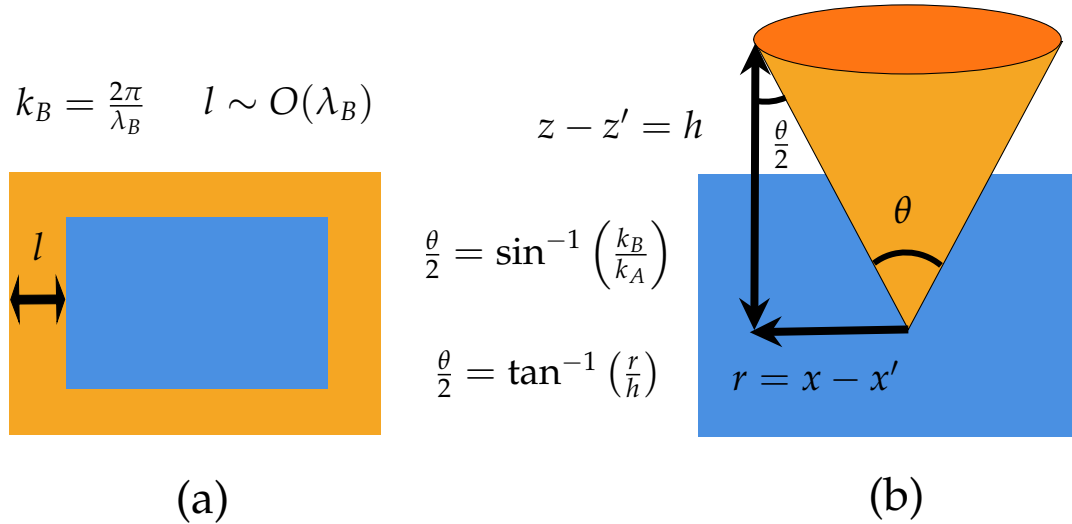


Figure 4.8: Schematic representation of radiation (a) below and (b) above the critical frequency.

4.3 Radiation pattern

The distinction between sound radiation from finite structures in the case $k_B < k_A$ and in the case $k_B > k_A$, for the CF defined in Eq. (4.10), is demonstrated in figure 4.8. The radiated sound pressure level, based on theoretical suggestions, goes to infinity when $k_B = k_A$. In fact, of course, this is not true in reality, because every real surface is finite in extent. In practice, it should be noted that the sound radiation from finite structures at $k_B = k_A$ is very large [189]. In addition, the radiated

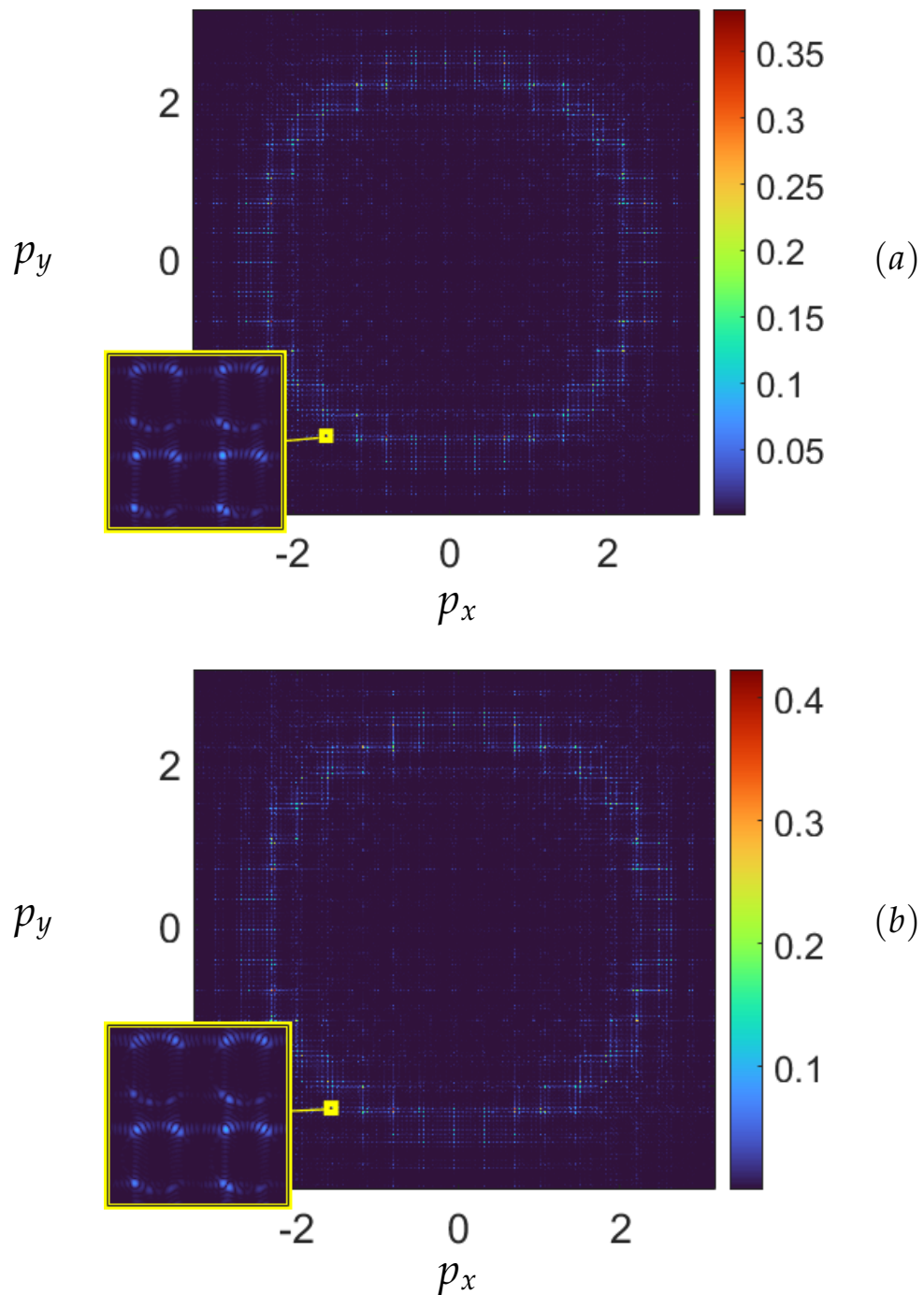


Figure 4.9: Mosaic representation of the 4-D surface normal velocity CF $\Gamma_{\Omega}(\mathbf{p}, \mathbf{p}')$ below the critical frequency $k_B/k_A = 2.5$ (i.e. $k_B > k_A$) in the momentum space for (a) plate with Dbcs (b) plate with Nbcs.

sound decays with distance from the source for finite structures. The frequency for which $k_A = k_B$ is called the critical frequency and the principle of a critical frequency is very important for finite structure sound radiation. The study in this chapter, while being limited to finite plates, shows that if $k_B < k_A$ there is very efficient sound radiation to the surrounding medium at some angle θ , which is determined by the respective wave vectors of the finite structure. However, unlike infinite plates, sound radiation may also occur below the critical frequency. This is mostly due to the presence of end or boundary conditions for mechanical excitation of the structure; for acoustic excitation, it is due to both the forced response of the structure at the frequency of excitation and the boundary conditions. In the following chapter, these processes of sound radiation from finite structures at frequencies below the critical frequency will be addressed.

4.4 Results

The results achieved using the mathematical model in the previous sections are presented in this section. As stated earlier, it is difficult to visualize as a four-dimensional CF matrix with (x, y, x', y') coordinates, and we view it as a mosaic representation, as the mosaic representation includes both the coordinates (x, y) and (x', y') . Figure 4.9 shows mosaic representations of the normal surface velocity CF in momentum space obtained from Eq. (4.21) with the excitation bending wavenumber $k_B = 10 \text{ m}^{-1}$ and corresponding acoustic wavenumber $k_A = 4 \text{ m}^{-1}$

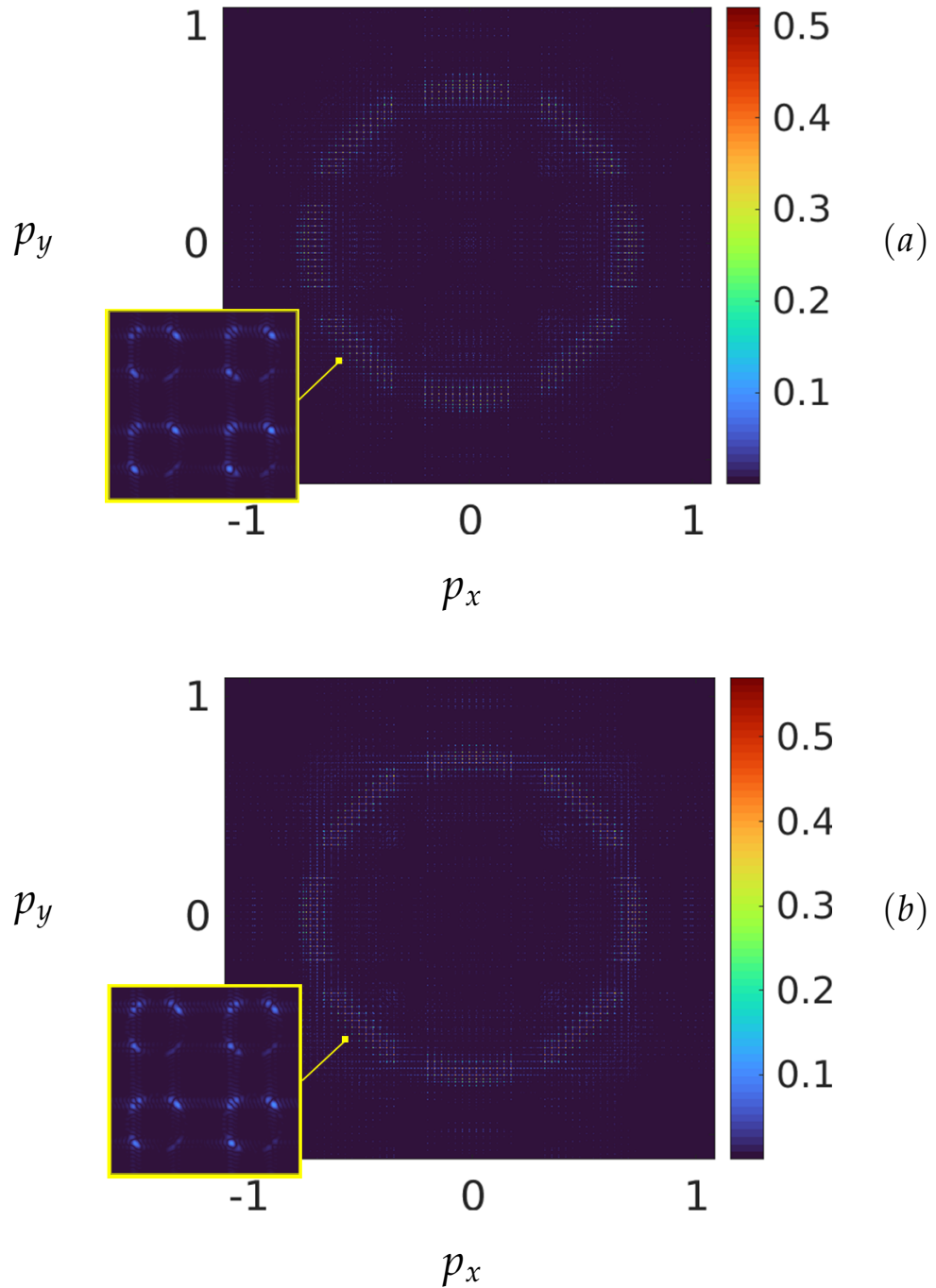


Figure 4.10: Mosaic representation of the 4-D surface normal velocity CF $\Gamma_{\Omega}(\mathbf{p}, \mathbf{p}')$ above the critical frequency $k_B/k_A = 0.7$ (i.e. $k_B < k_A$) in the momentum space for (a) plate with DBCs (simply supported plate) (b) plate with NBCs (guided boundary conditions).

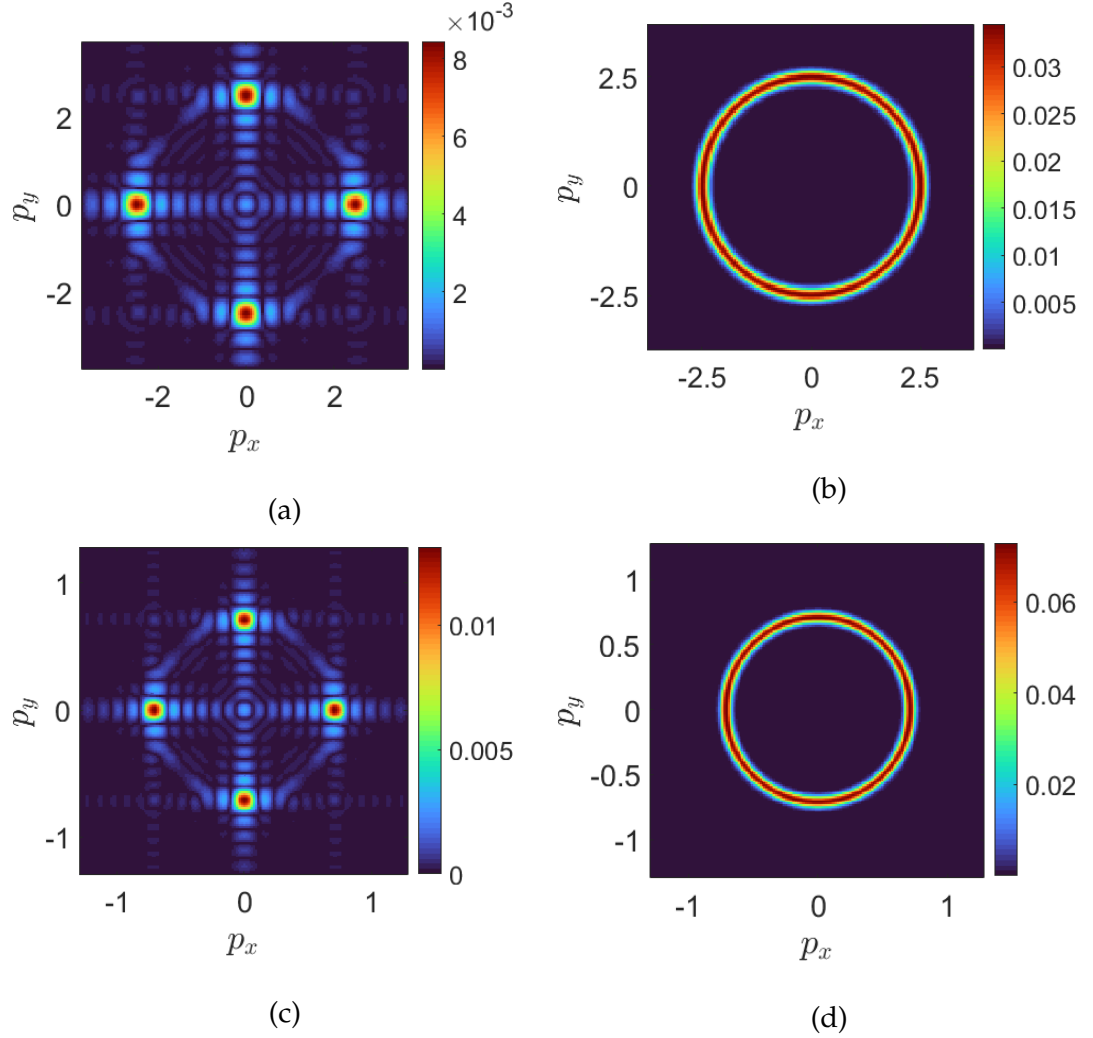


Figure 4.11: (a) The CF, $\tilde{\Gamma}_\Omega(p_x, p_y, 0, 0)$, in momentum space for the case $k_B/k_A = 2.5 > 1$ setting (p'_x, p'_y) at $(0, 0)$; (b) diagonal of CF matrix $\tilde{\Gamma}_p(\mathbf{p}, \mathbf{p})$ in momentum space in the case $k_B/k_A = 2.5 > 1$; (c) The CF, $\tilde{\Gamma}_\Omega(p_x, p_y, 0, 0)$, in momentum space for the case $k_B/k_A = 0.7 < 1$ setting (p'_x, p'_y) at $(0, 0)$; (d) diagonal of CF matrix $\tilde{\Gamma}_p(\mathbf{p}, \mathbf{p})$ in momentum space for the case $k_B/k_A = 0.7 < 1$.

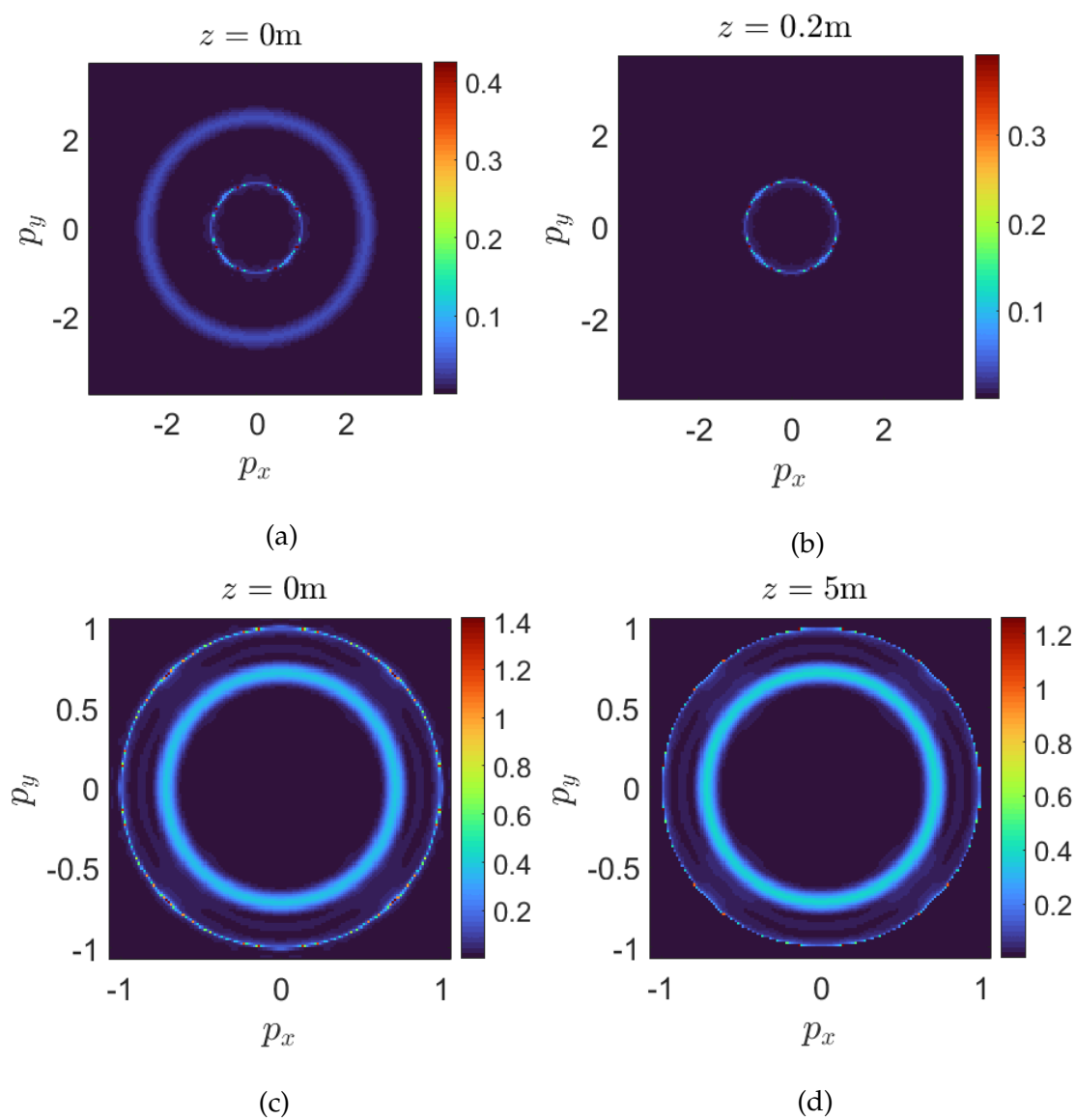


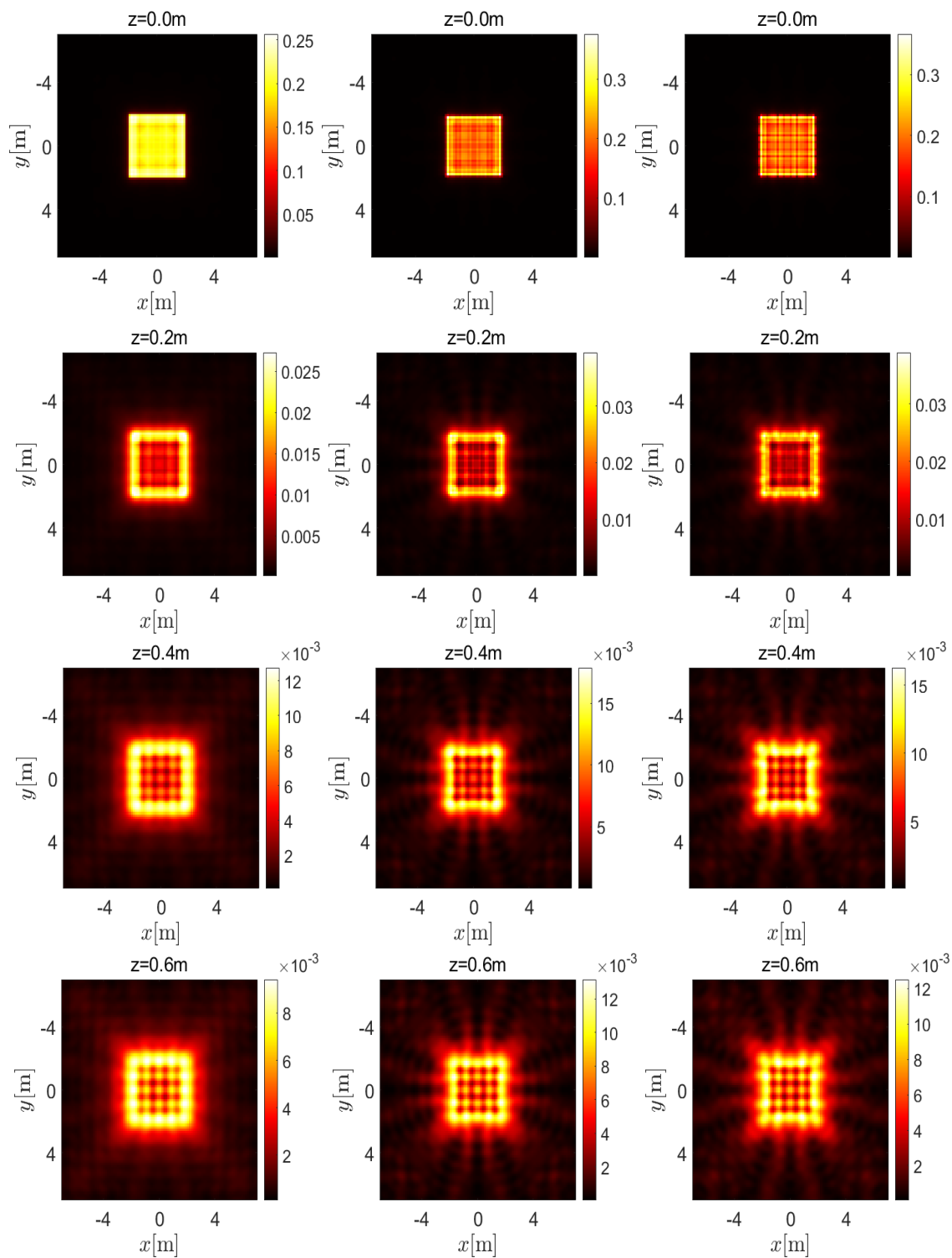
Figure 4.12: The scaled acoustic intensity $\Gamma_p(\mathbf{p}, \mathbf{p}; z) / (\rho_0 c_0)^2$ in the momentum space below the critical frequency propagated from (a) $z = 0$ (b) to $z = 0.2\text{m}$; above the critical frequency propagated from (c) $z = 0$ (d) to $z = 5\text{m}$.

for a plate with dimensions given in Fig. 4.1 and having either Dbc's shown in Fig. 4.9a or Nbc's shown in Fig. 4.9b.

In the case of $k_B < k_A$ ($k_B/k_A = 0.7$), mosaic representations of the results of the normal surface velocity CF in momentum space are also shown for both bcs in Fig. 4.10a and Fig. 4.10b. For both boundary conditions, that is Dbc's and Nbc's, and for both cases $k_B/k_A < 1$ and $k_B/k_A > 1$, a similar pattern can be seen for the normal surface velocity CF in the momentum domain which is an impulse ring at a radius of k_B/k_A with slightly different amplitude. These results agree with the phase space density in Eq. (4.8).

We notice that the mosaic representation of CF is unclear, and therefore present 2D CF plots to facilitate better visualization and analysis from here onward. There are two different ways of presenting the following CF results, even in a two-dimensional representation. The first way to show CF is to fix (p'_x, p'_y) coordinates and plot the CF as a function of (p_x, p_y) or vice versa. The coordinate points of (p'_x, p'_y) are set to $(0, 0)$ here, as shown in Fig. 4.11a and Fig. 4.11c.

The second way for a four-dimensional CF to be represented in a two-dimensional plot is to plot the corresponding intensity obtained by setting $\mathbf{p} = \mathbf{p}'$ as shown in Fig. 4.11b and Fig. 4.11d. Basically, this corresponds to the elements along the diagonal of the CF matrix. The intensity graph allows us to capture the actual power of the radiated sound pressure field. The maximum amplitude of the measured signal is provided by the radiation pattern along the CF matrix diagonal. The plots of the acoustic intensity in the momentum space shown in Fig. 4.12 are



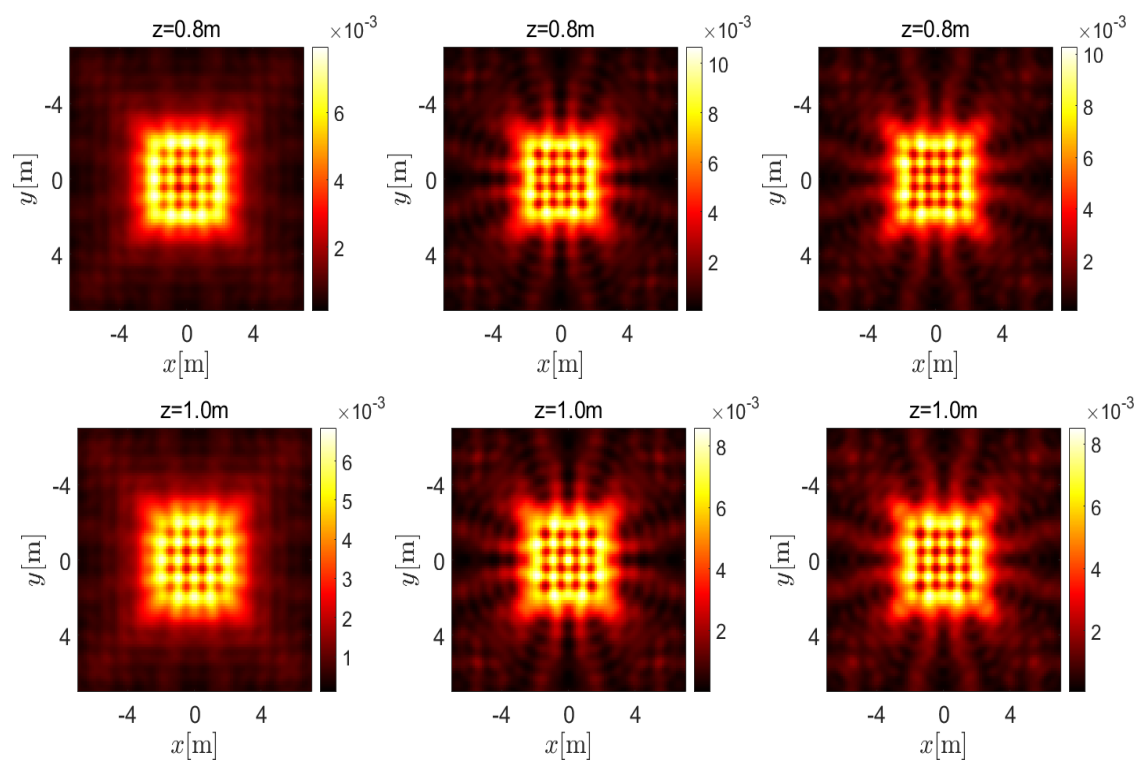
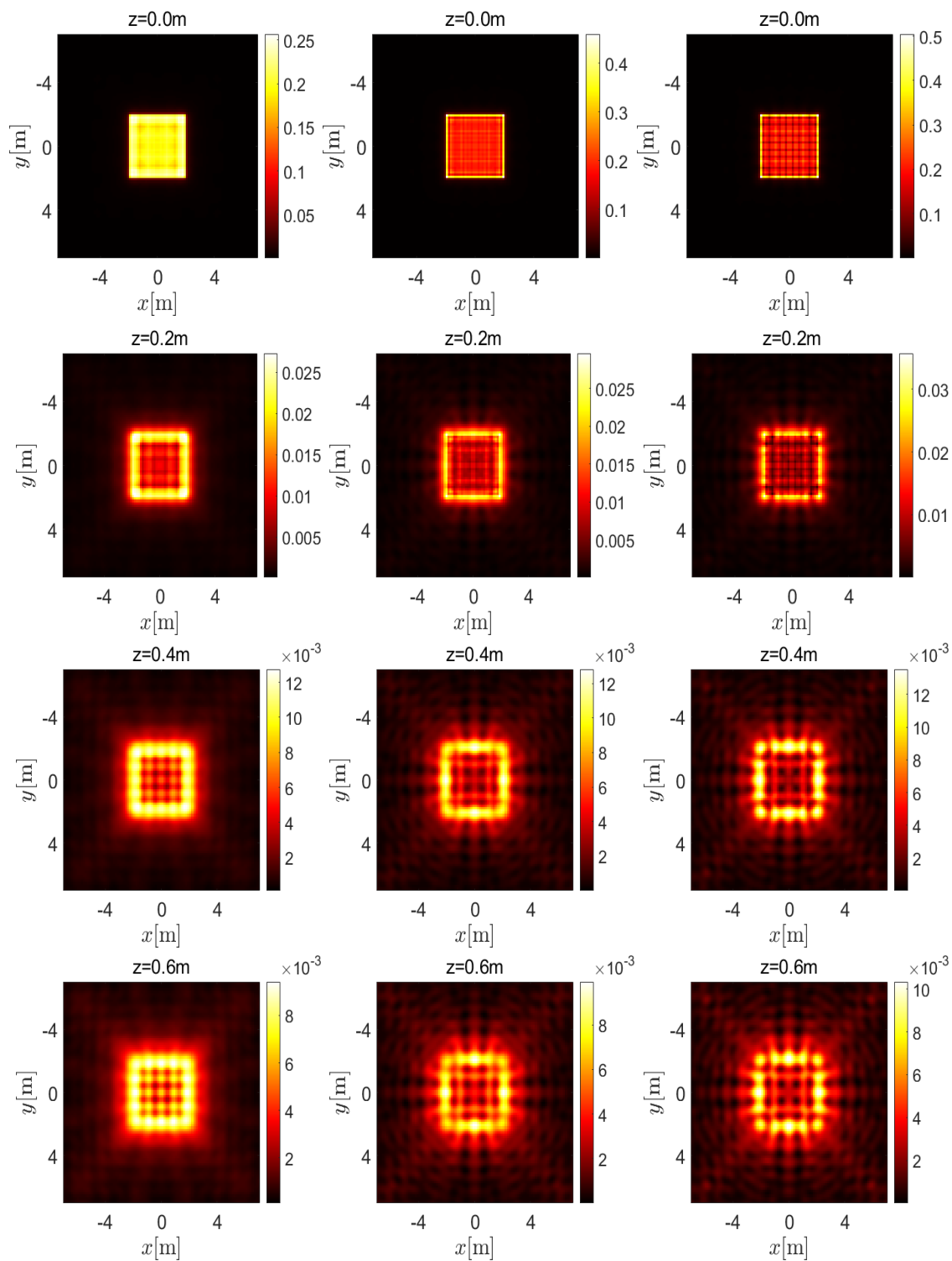


Figure 4.13: The scaled acoustic intensity $|p(\mathbf{x}, z)|^2 / (\rho_0 c_0)^2$ below the critical frequency $k_B/k_A = 2.5$: first column corresponds to sound radiation from the diffuse field propagation measured at different distances; second column corresponds to adding Dbs to the diffuse field (effect of one image); third column corresponds to the effect of image of image.



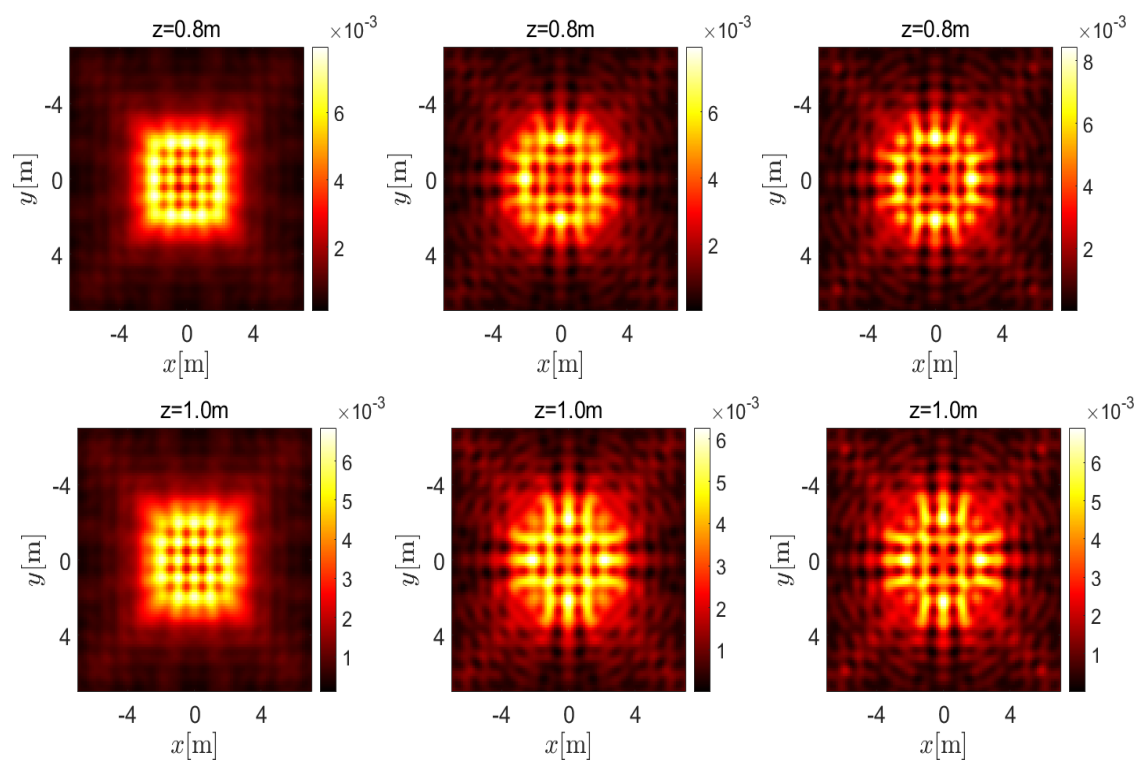


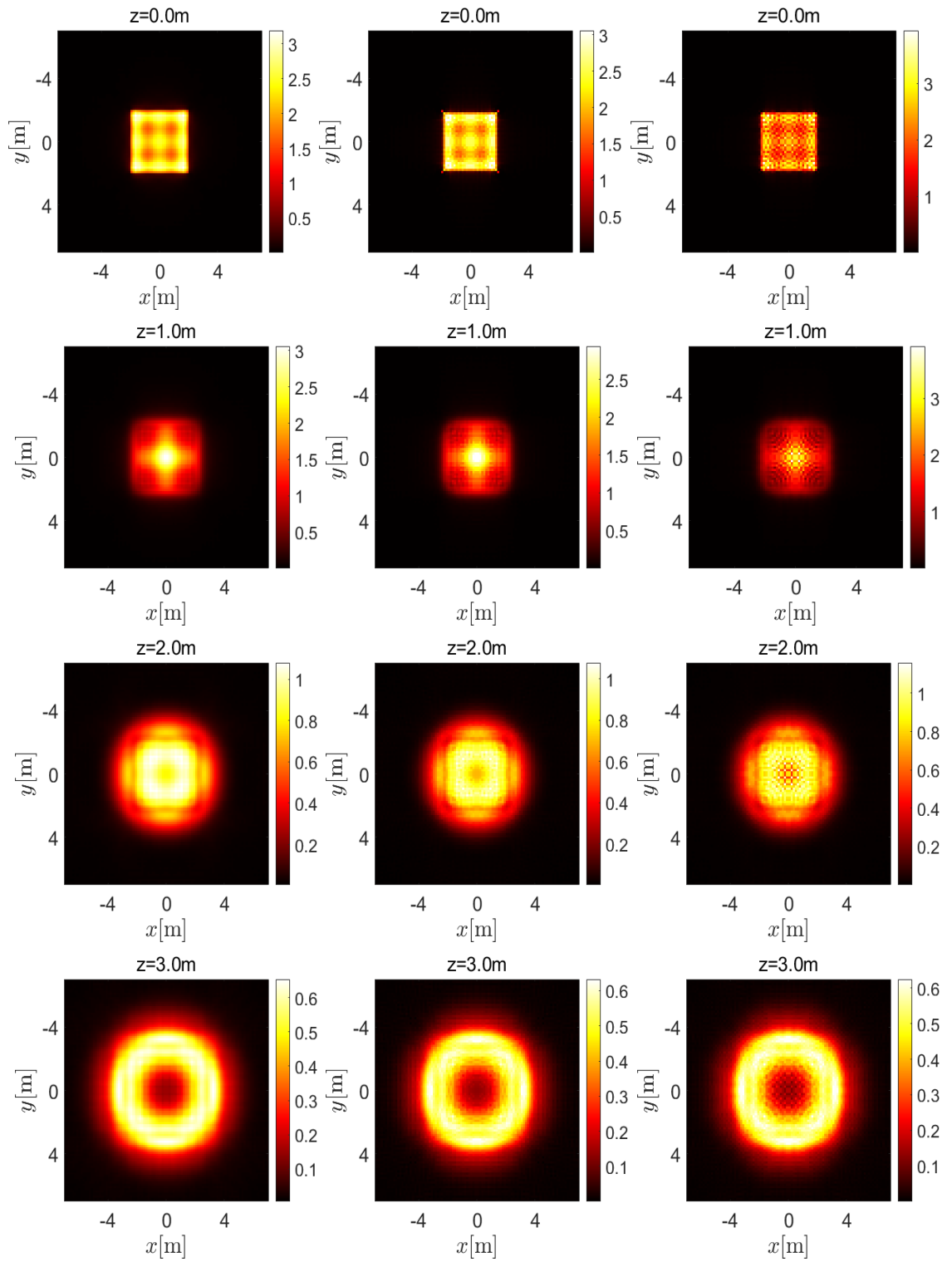
Figure 4.14: The scaled acoustic intensity $|p(\mathbf{x}, z)|^2 / (\rho_0 c_0)^2$ below the critical frequency $k_B/k_A = 2.5$: first column corresponds to sound radiation from the diffuse field propagation measured at different distances; second column corresponds to adding N_{bc} s to the diffuse field (effect of one image); third column corresponds to the effect of image of image.

obtained from Eq. (4.19) by setting $\mathbf{p} = \mathbf{p}'$.

From Fig. 4.12 we observe that in the case $k_B/k_A > 1$ the ring with radius k_B/k_A corresponding to the structure vibration falls outside the radiation circle $|\mathbf{p}| = 1$. This observation means that the sound radiation of the excited plate with a wavenumber below the modal critical wavenumber is dominated by the evanescent components in the near field. This leads to substantial decrease in the maximum value of sound radiation intensity as we move away from the plate, as the maximum value of the color bar in Fig. 4.12a, Fig. 4.12b, Fig. 4.13 as well Fig. 4.14 can be seen to decrease significantly as we step away from the source, which corresponds to the essential contribution of the evanescent components. Conversely the ring with the radius k_B/k_A corresponding to the structure vibration falls inside the radiation circle $|\mathbf{p}| = 1$ for the case $k_B/k_A < 1$. This observation implies that the sound radiation of the excited plate with a wavenumber above the critical wavenumber is dominated by the components of the propagated waves and the plate effectively radiates to the far-field in a cone at some angle θ which is defined in Fig. 4.8 and given by,

$$\frac{\theta}{2} = \sin^{-1} \left(\frac{k_B}{k_A} \right). \quad (4.24)$$

Using the steps of the calculation of sound intensity in the spatial space as defined in the previous section, the effect of boundary conditions in both cases, that is below and above the critical frequency, was studied and presented in Fig. 4.13, Fig. 4.14, Fig. 4.15 and Fig. 4.16. The sound intensity CF calculated in the spatial



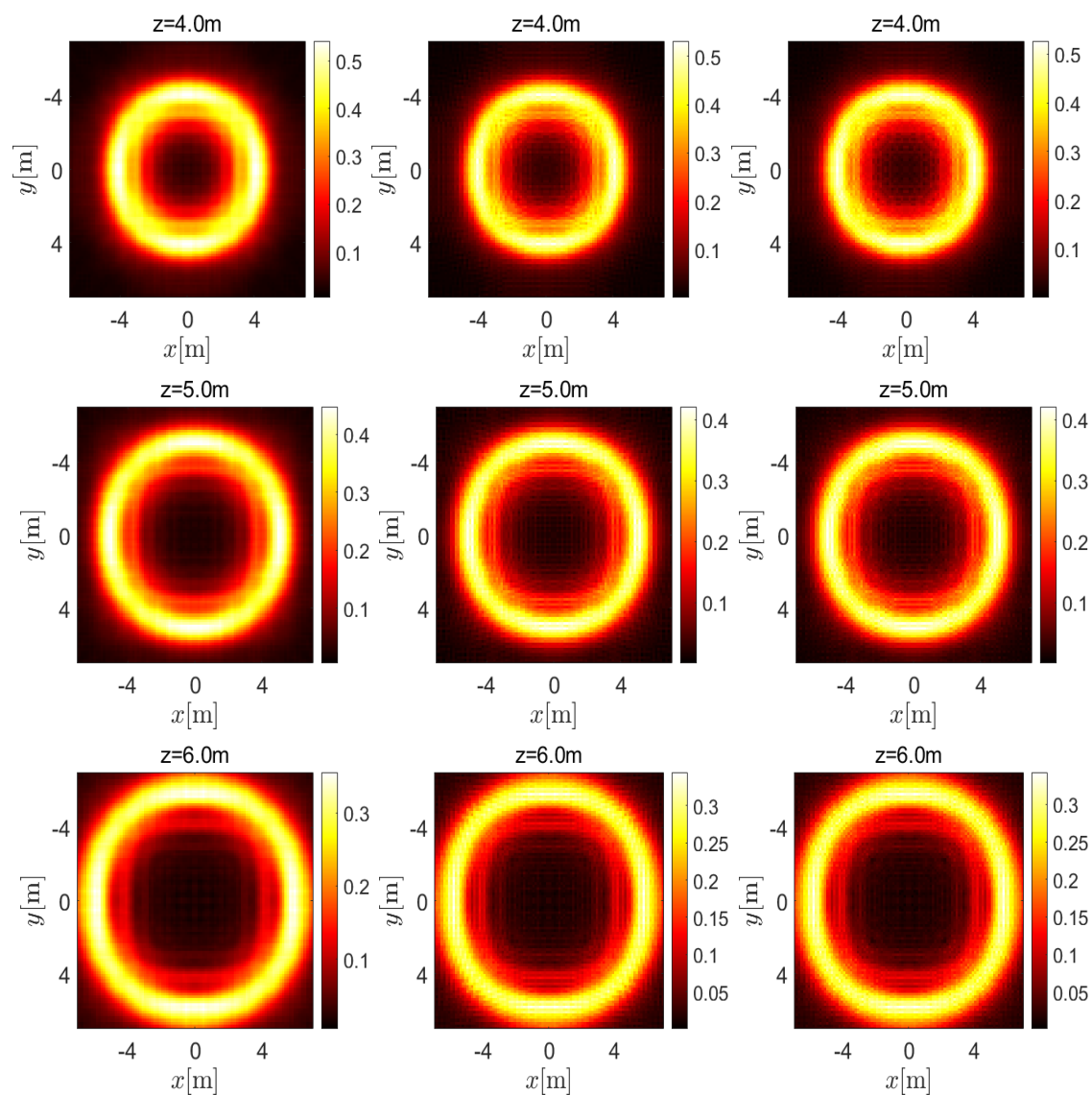


Figure 4.15: The scaled acoustic intensity $|p(\mathbf{x}, z)|^2 / (\rho_0 c_0)^2$ above the critical frequency $k_B/k_A = 0.7$: first column corresponds to sound radiation from the diffuse field propagation measured at different distances; second column corresponds to adding DBCs to the diffuse field (effect of one image); third column corresponds to the effect of image of image.

domain $\Gamma_p(\mathbf{x}, \mathbf{x}; z) = |p(\mathbf{x}, z)|^2$ is obtained from Eq. (4.22). Below the critical frequency, sound essentially radiates from the edges and corners of the plate, while above the critical frequency, the entire surface of the plate radiates sound into the air (see also Fig. 4.17). Figure 4.13 and Figure 4.14 also show that below the critical frequency $k_B/k_A > 1$, the acoustic disturbances for a finite plate with either Dbc (Fig. 4.13) or Nbc (Fig. 4.14), are confined to a layer near its boundary (on the scale of the wavelengths $l \simeq \lambda_B$ as described in Fig. 4.8) and decrease rapidly with distance away from the plate. We account for boundary conditions using a single image correction as given in Eq. (4.10) based on the distance from the nearest straight edge. Here, using a single image correction per edge, the normal velocity CF for the rectangular plate can be written as

$$\Gamma_{\Omega}(\mathbf{x}, \mathbf{x}') = \Gamma_0(\mathbf{x}, \mathbf{x}') \pm \sum_{l=1}^4 \Gamma_l(\mathbf{x}, \mathbf{x}'). \quad (4.25)$$

Higher-order corrections should be included in the exact treatment of boundary conditions as given in Eq. (4.11). But these are found not to substantially affect the outcome in the treated wavelength range in the form of "images of images" as can be seen in Fig. 4.13, Fig. 4.14, Fig. 4.15 and Fig. 4.16.

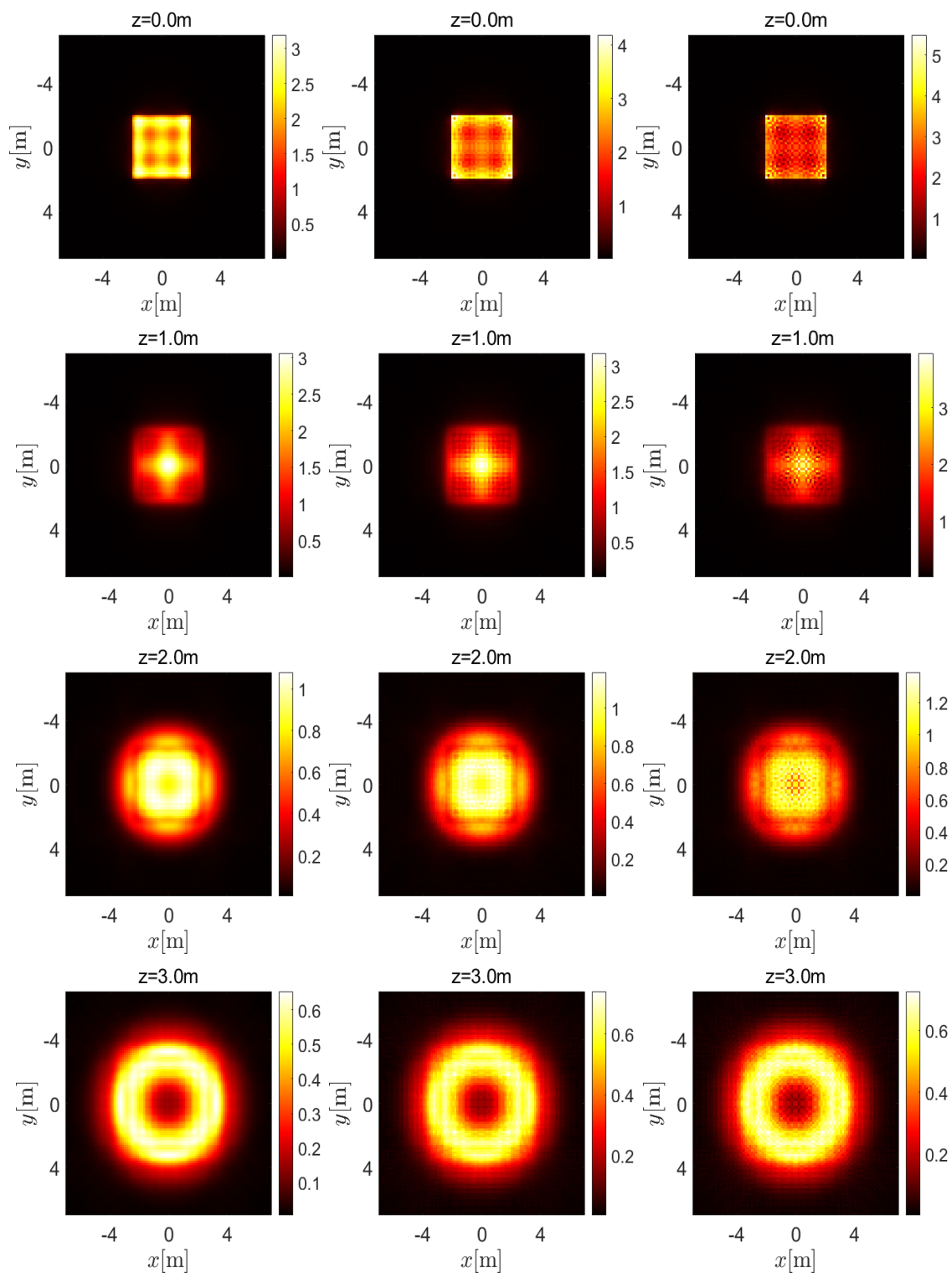
Figure 4.17b shows that in the case of $k_B/k_A < 1$, the sound radiation intensity has a cone pattern with an angle given by Eq. (4.24), as we stated earlier. We have also plotted the sound radiation intensity along the line $y = 0$ in the case $k_B/k_A > 1$ in Fig4.17a, as can be seen most of the contribution comes from the edge of plate.

The effects of both boundary conditions, i.e. Dbc and Nbc, on the sound radiation below and above the critical frequency are compared in Fig. 4.19. This results shows that the sound radiation intensity is relatively small and increases as the frequency increases. Although Fig. 4.19a shows that for $k_B/k_A > 1$ the maximum value of the color bar for the Nbc case is greater than the Dbc case on the surface of the plate (i.e. $z = 0$) (this could be due to the presence of the evanescent components in the near field.), the total radiated power for the Dbc case is greater than the Nbc case, which is shown in the next chapter. We have also investigated the impact of boundary conditions in the case of $k_B/k_A > 1$ in Fig. 4.18 near one of the edge of the plate $y = 2$. These results indicate that the sound radiation from plates with Nbc gives a greater contribution at $z = 0$, but when we step away from the edge, plates with Dbc gives greater contribution and the average is given by the bulk contribution.

4.5 Conclusions

The statistical properties of wavefunctions in complex or chaotic geometries are modelled by a random superpositions of plane waves.

The propagation scheme for predicting the sound pressure from complex structure in both the near-and far-field has been developed by using DEA approximation. DEA is a phase-space approximation of the wave dynamics, which allows us to detect the “kinetic” motion of the wave propagation and it can be used to make



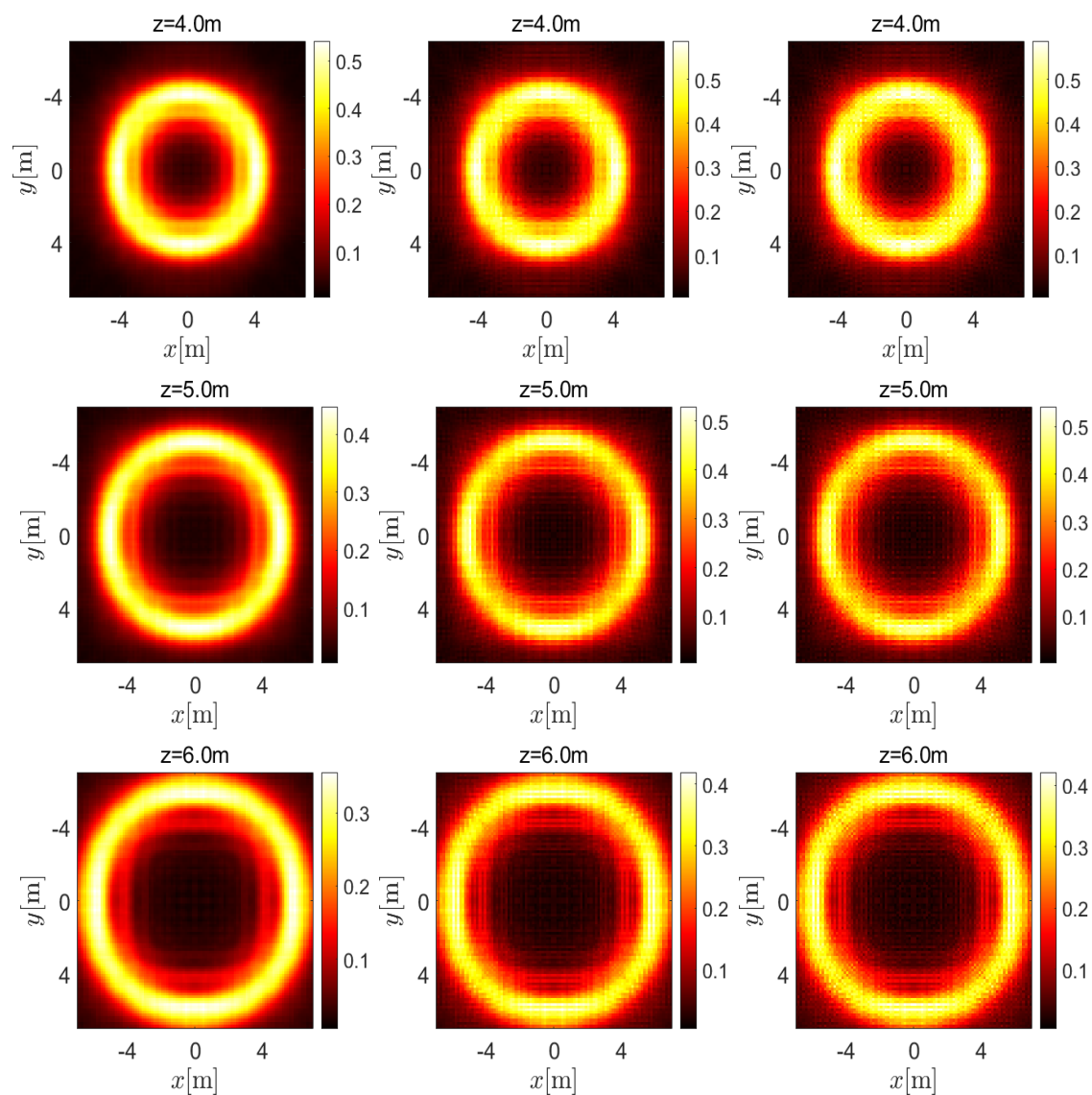


Figure 4.16: The scaled acoustic intensity $|p(\mathbf{x}, z)|^2 / (\rho_0 c_0)^2$ above the critical frequency $k_B/k_A = 0.7$: first column corresponds to sound radiation from the diffuse field propagation measured at different distances; second column corresponds to adding Nbc to the diffuse field (effect of one image); third column corresponds to the effect of image of image.

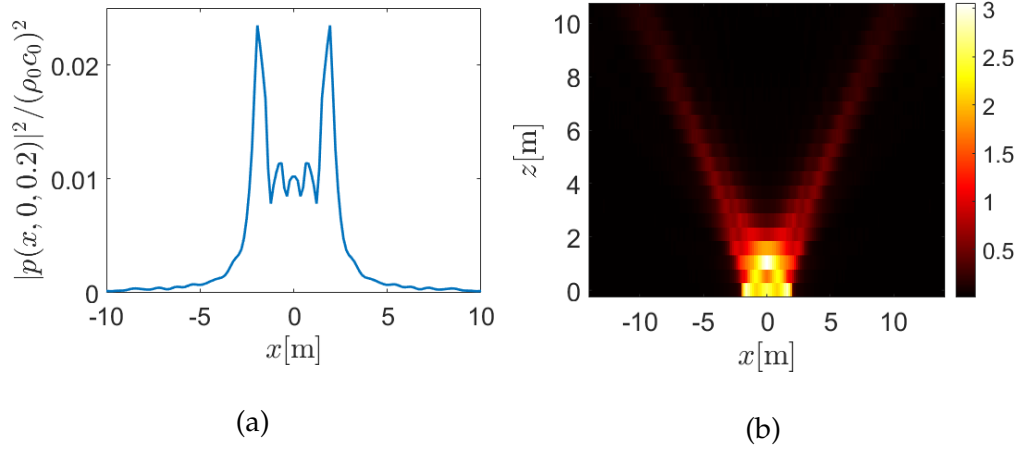


Figure 4.17: (a) Plot of $|p(x, y = 0, z = 0.2)|^2 / (\rho_0 c_0)^2$ with $k_B/k_A = 2.5$. (b) Plot of $|p(x, y = 0, z)|^2 / (\rho_0 c_0)^2$ with $k_B/k_A = 0.7$.

an analogy between the evolution of underlying ray trajectories in phase-space and the evolution of waves in configuration space. A method based on the FFT is proposed for the propagated sound from a baffled flat plate, the physical understanding of which is simple and computationally efficient. In addition, finite size effects and boundary effects on the sound pressure field have been evaluated and observed in the calculations.

The FFT technique is not efficient where more integration segments are required to define the baffled area. At low frequency, due to the overlapping pressure, this requires a larger baffle and thus more sample points to overcome the bias error. In addition, a finer resolution is required to provide good precision for higher modes that are important at high frequencies. In the next chapter, we present different ways of calculating the radiation efficiency of finite plates for diffuse fields. An approximation is proposed for the radiation efficiency of plates

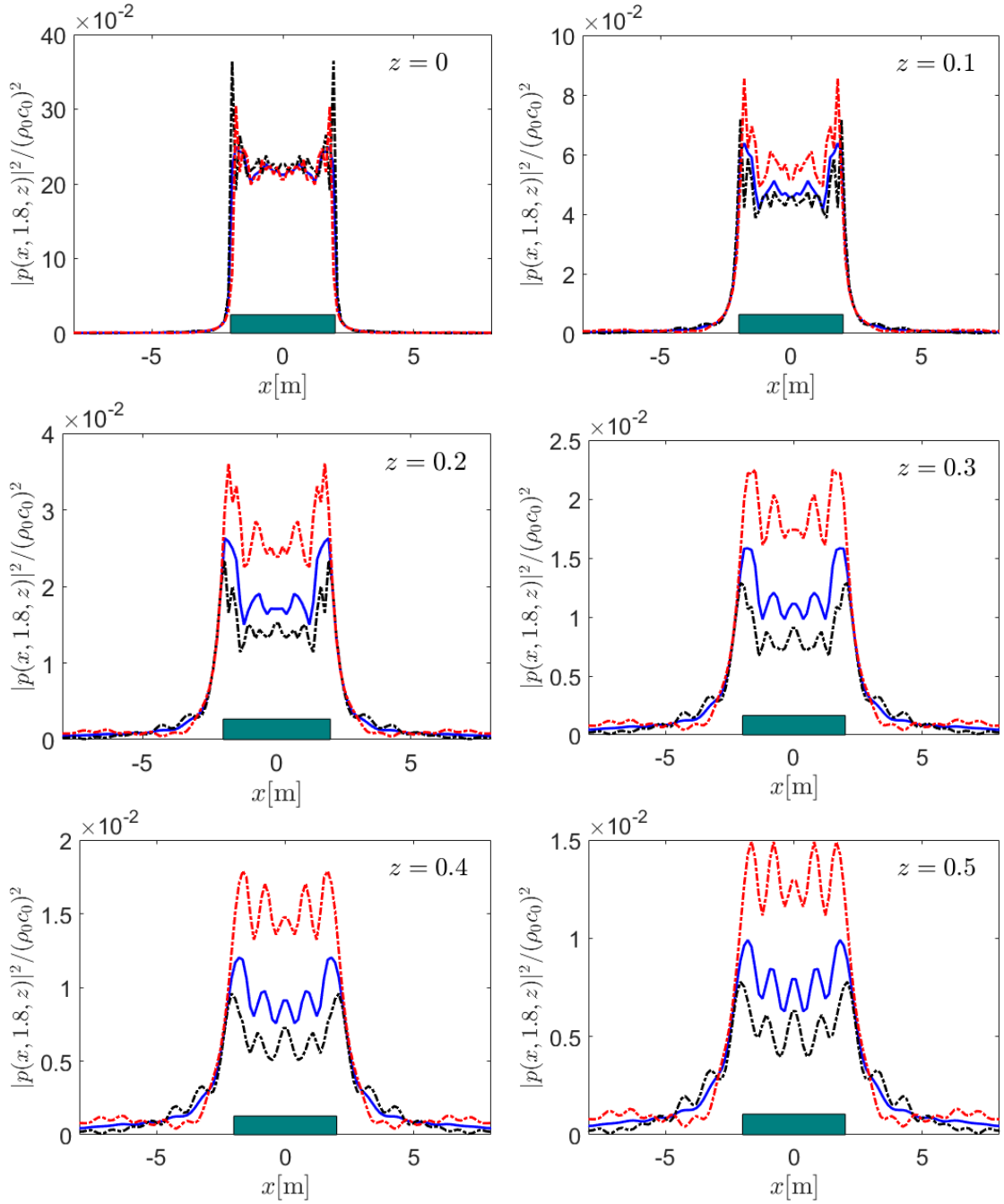
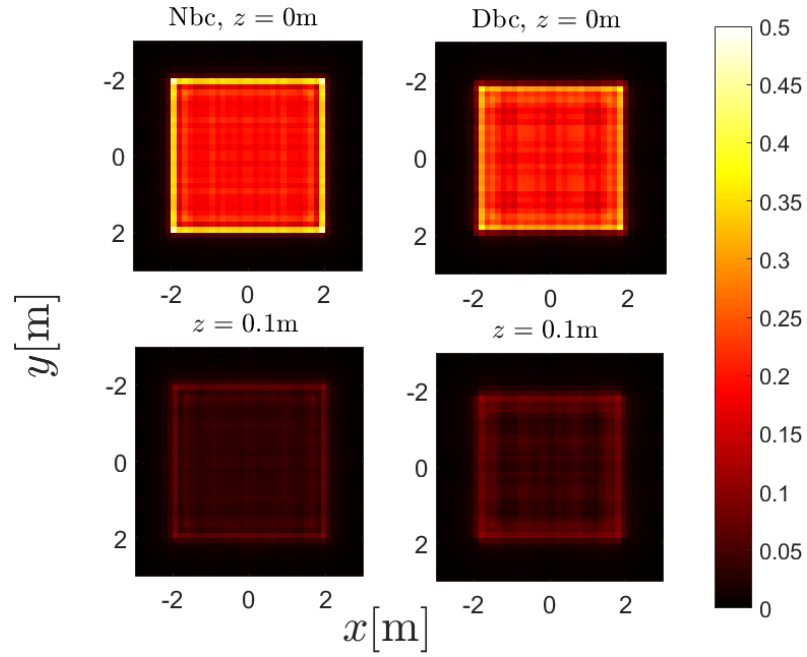
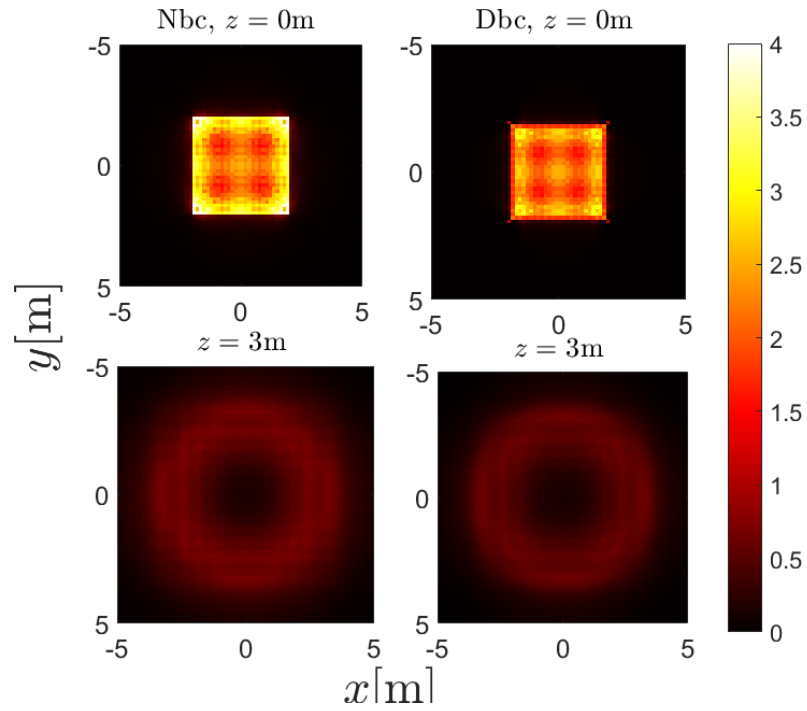


Figure 4.18: A comparison of acoustic disturbances $|p(x, y = 1.8, z = a)|^2 / (\rho_0 c_0)^2$ with $k_B/k_A = 2.5$ near the boundary of plates with diffuse field excitation without boundary conditions (—), with Dbc (---) and Nbc (-.-).



(a)



(b)

Figure 4.19: A comparison of acoustic disturbances $|p(x, y, z = a)|^2 / (\rho_0 c_0)^2$ near the boundary of plates with diffuse field excitation with Dbc and Nbc (a) with $k_B/k_A = 2.5$; (b) with $k_B/k_A = 0.7$.

with different boundary conditions, the physical understanding of which is simple and computationally accurate. Future research will focus on the performance of this method against the existing approaches for calculating sound radiation and modifying the approximation for more complex structure.

Chapter 5

Radiation efficiency of a baffled plate

The purpose of this chapter is to extend the existing methods for calculating the radiation efficiency of plate-like structures to take into account the distribution of vibration velocities from phase-space methods such as DEA. In principle, the radiation efficiency of a plate in the frequency range under consideration can be obtained as a sum over eigenmodes of plate vibration [190]. The boundary conditions of a vibrating plate, for frequencies below the critical frequency, are known to affect its sound radiation. To study this effect systematically, a random wave model (diffuse field) is used to calculate the average radiation efficiency and radiated power for a planar structure set into an infinite baffle. Whereas in the literature there are analytical expressions for simple structures such as rectangular plates with simply supported boundary conditions [43] or for edges in guided conditions [44, 191] (these studies are based on mode shape, but our work, to our knowledge, is the first to use random plane wave models to explore the effect of

boundary conditions on the sound radiation of the structure), for other cases a numerical approach is required. Therefore, in order to verify our findings in this chapter, these two boundary conditions have been considered. Various methods and approximations have also been used in this chapter to describe the effects of boundary conditions on acoustic radiation for vibrating, flat plates, where the plate vibrations are assumed to be diffuse. These methods are then used to obtain the average radiation efficiency of a rectangular plate set in an infinite baffle. The results were tested against analytical expressions for the approximation of structural vibrations using basic approximate formulas for mode shapes and natural frequencies. Although these methods tested for rectangular plates, the underlying calculation in this chapter extends to plates of arbitrary shape.

5.1 Radiation efficiency of finite plate with boundary supports

It is essential to be able to calculate the noise radiated by a vibrating structure during its design stage in many engineering applications. In most cases, the structures under consideration, whether industrial equipment, vehicles or civil structures, such as bridges, can be subdivided into smaller parts; thin vibrating panels are also critical components responsible for the radiation of noise. A typical technique to evaluate the noise produced is to calculate the vibrational velocities of each part and estimate their acoustic power levels and radiation efficiency. Study-

ing the radiation efficiency of the elementary components is particularly useful in order to be able to characterize the acoustic performance of the structure they form.

For an arbitrary structure, the radiation efficiency, denoted σ , is a dimensionless quantity. It is defined to be the sound power Π radiated from one side of a vibrating surface, normalised by the sound power Π_0 radiated by a large piston with the same surface area (in the next section, quantitative definitions of Π and Π_0 will be given). It thus describes the efficiency with which the sound is radiated by the structure compared to a piston with the same surface area [40, 41, 64, 192, 43] and can be written

$$\sigma = \frac{\Pi}{\Pi_0}. \quad (5.1)$$

The radiation efficiency Eq. (5.1) for free waves on an infinite flat plate [189] is

$$\sigma = \begin{cases} 0 & \text{for } k_B > k_A, \\ \frac{1}{\sqrt{1-(k_B/k_A)^2}} & \text{for } k_B < k_A, \end{cases} \quad (5.2)$$

where k_B denotes structure wavenumber and k_A denotes acoustic wavenumber. Equation (5.2) shows that for a given frequency, if the wavelength of a wave on an infinite plate is smaller than the acoustic wavelength (i.e. $k_B > k_A$) no net sound is radiated from the plate. On the other hand, if its wavelength is larger than the acoustic wavelength (i.e. $k_B \leq k_A$) then the plate radiates a sound wave into the surrounding fluid. Thus this result implies that sound radiation is only

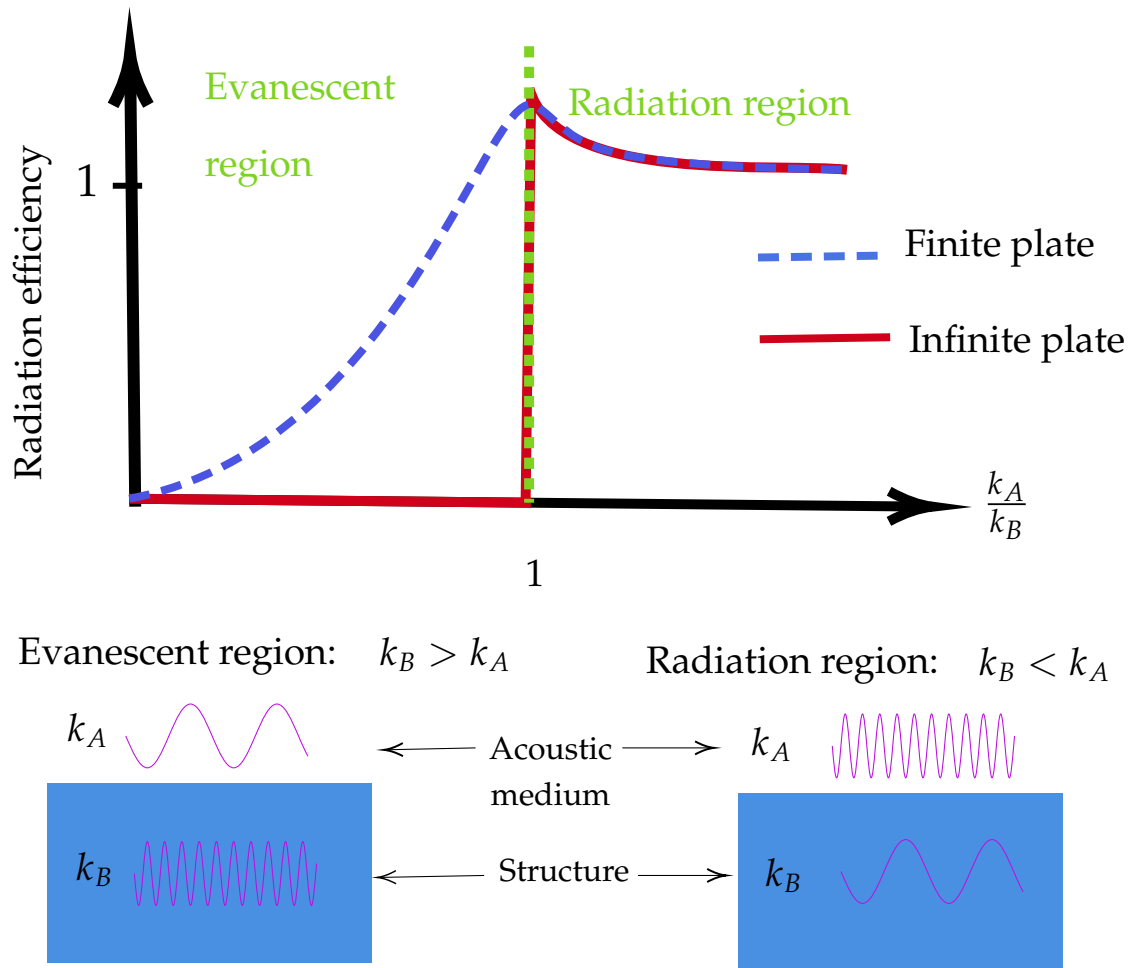


Figure 5.1: Schematic representation of radiation efficiency for structural vibration. For $k_B/k_A > 1$ acoustic wavelength is longer than vibrational wavelength, so radiation is suppressed, whereas for $k_B/k_A < 1$ acoustic wavelength is shorter than vibrational wavelength so the plate radiates a sound wave into the surrounding fluid.

nonzero for waves where its vibrational wavelength is longer than the acoustic wavelength. If the plate structure is finite, in other words if there are discontinuities, such as boundaries, change of thickness, ribs etc. then at these locations scattering of waves will result. The Fourier transform of the scattered vibrational field will generally contain wave components whose wavelength is longer than the acoustic wavelength ($k_B < k_A$) even if the incident waves are such that their wavelength are smaller than acoustic wavelength ($k_B > k_A$). These components will contribute to the acoustic power and radiate acoustic energy. This concludes that, unlike the infinite plate, the radiation efficiency of the finite plate smoothly interpolates between $k_B > k_A$ (evanescent region) and $k_B \leq k_A$ (radiation region) as a function of frequency. The difference between the radiation efficiency of finite and infinite structures is shown in the schematic representation in Figure 5.1.

In calculations of plate radiation, simply supported boundaries are often used because this assumption simplifies the calculations. Several authors have reviewed other boundary conditions for the baffled case [193, 194, 191, 174]. For frequencies up to half the critical frequency, Maidanik [193] observed that the radiation efficiency of a clamped plate is 3 dB higher than that of a plate which is simply supported. Leppington et al. [194] have also proposed that below the critical frequency the calculation of a simply supported plate should be adjusted to approximately 3 dB for a clamped plate. An extended model for five different kinds of edge condition, ranging from free to restrained edges has been sug-

gested by Gomperts [191]. Simple approximations were given in this paper for the low-frequency range. More edge-constrained plates are shown to often not have greater radiation efficiencies than those that are less edge-constrained. It was found that a guided plate has a lower radiation efficiency than that of a simply supported plate below the first resonance frequency [191]. A plate with a mixture of simply supported and clamped edges was also found to have about the same radiation efficiency (difference < 1 dB) as a plate that is simply supported. Berry et al. [174] have also suggested a formulation for general boundary conditions. By choosing a family of trial functions matching the geometry of the boundary conditions, a Rayleigh-Ritz technique was used. For a single forcing location, the radiation efficiency of multi-modal responses was measured. In the average sense, apart from the antisymmetric resonances occurring for particular cases, the radiation efficiency for clamped and simply supported plates was found to be almost equal. In the cases of guided-guided and free-free edges, the same phenomenon was also noticed.

As mentioned earlier, the boundary conditions of the vibrating plate are known to influence its sound radiation for frequencies below the critical frequency. In order to systematically investigate this effect, the simplest case of homogeneously diffuse field corresponding to uniform ray densities in phase space, including boundary conditions corrections, which have been already studied in the previous chapter, is used to calculate the average radiation efficiency and radiated power of the planar structure set in an infinite baffle in this chapter. We also

consider pseudo Dirichlet (Dbc) or pseudo Neumann (Nbc) boundary conditions here, as in the previous chapter, which usually only serve as simplified models representing simply supported or guided boundary conditions for bending modes in plates. For the purpose of simplicity, we will refer to pseudo Dirichlet and pseudo Neumann boundary conditions as Dirichlet and Neumann boundary conditions from now on.

We present numerous ways to calculate the radiation efficiency of finite plates assuming diffusive field excitation in the following sections.

5.2 Sound radiation from plate-type structures

In this section, we give an overview of the main features of the derived models and approximations to be described in detail later for the clarification of the reader.

As stated in Chapter 4, the common model of wave propagation in complex or chaotic geometries is the Random Wave Model, in which the statistical properties of wave functions are modeled and characterised by a two-point correlation function (diffuse field). Here we recapitulate the most important features.

Denote by w the normal displacement field of the plate. The bulk properties of the corresponding diffuse field for a simple random superposition of plane waves is characterised by a two-point correlation function given by

$$\Gamma_0(\mathbf{x}, \mathbf{x}') = J_0(k_B |\mathbf{x} - \mathbf{x}'|),$$

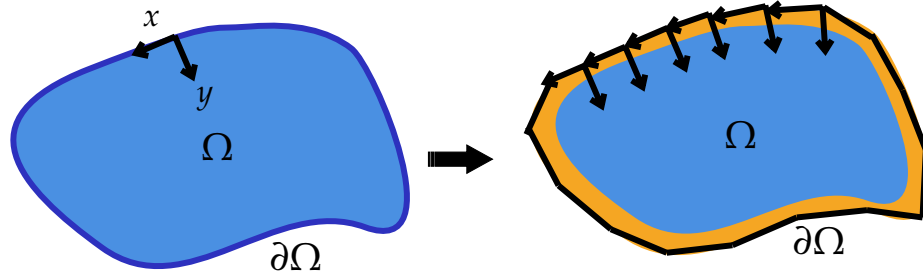


Figure 5.2: For the case $\alpha > 1$ radiation efficiency σ dominated by contributions near boundary. In this case, general boundary shape of plates $\partial\Omega$ can locally approximated by straight edge and curvature effects are neglected at leading order.

where J_0 denotes zero order Bessel function of the first kind and $\langle \cdot \rangle$ denotes frequency or spatial averaging. We assume a planar plate occupying a region Ω , with $\mathbf{x} = (x, y)$ and $\mathbf{x}' = (x', y')$ denoting pairs of points in Ω . The correlation function Γ_0 represents the bulk model whenever \mathbf{x}, \mathbf{x}' are far from the boundary $\partial\Omega$. Near boundaries, this model needs to be modified to include corrections due to the boundary conditions.

Recall Eq. (4.10) for the normal surface velocity correlation function $\Gamma_\Omega(\mathbf{x}, \mathbf{x}')$ including the bulk contributions with a fixed k_B and edge boundary corrections at $y = 0$

$$\Gamma_\Omega(\mathbf{x}, \mathbf{x}') = J_0(k_B |\mathbf{x} - \mathbf{x}'|) \pm J_0(k_B |\mathbf{x} - \mathcal{R}\mathbf{x}'|), \quad (5.3)$$

where $\mathcal{R}\mathbf{x}'$ denotes a reflection of \mathbf{x}' through the edge and the \pm signs apply to Nbc and Dbc, respectively.

Radiation efficiency Eq. (5.1) can be extended to take into account the two-

point correlation function with a more detailed derivation to be followed in Sec. 5.3.1 and Sec. 5.3.3. For a diffuse field, Eq. (5.1) can be used to find the radiation efficiency σ based on the two-point correlation function Γ_Ω inside the domain according to

$$\sigma = \frac{2k_A \int_\Omega \int_\Omega g(\mathbf{x}, \mathbf{x}') \Gamma_\Omega(\mathbf{x}, \mathbf{x}') \, d\mathbf{x} \, d\mathbf{x}'}{\int_\Omega \Gamma_\Omega(\mathbf{x}, \mathbf{x}) \, d\mathbf{x}}, \quad (5.4)$$

where g is the imaginary part of free space Green function in 3D; that is,

$$g(|\mathbf{x} - \mathbf{x}'|) = \frac{\sin(k_A |\mathbf{x} - \mathbf{x}'|)}{4\pi |\mathbf{x} - \mathbf{x}'|} = \text{Im } G(\mathbf{x}, \mathbf{x}').$$

Denoting the ratio between k_B and acoustic wave number k_A by α , i.e.

$$\alpha = \frac{k_B}{k_A},$$

we find for $\alpha < 1$, that is, above the critical frequency, that the bulk contribution dominates and the plate is a good radiator. For $\alpha > 1$, the bulk contribution to the integral in the numerator of Eq. (5.4) vanishes in the limit of large plates ($\Omega \rightarrow \mathbb{R}^2$). The integral is then dominated by contributions near the boundary, see Fig. 5.2, which arise from two mechanisms: (i) as the integral of the bulk contribution to Γ_Ω is truncated (the integration domain is finite), phase cancellations are incomplete near the boundary; (ii) boundary corrections due to modifications of the bulk correlation function as discussed in Eq. (5.3) – and depending on the boundary conditions – give significant contributions. Both of these effects are of the same order.

Interestingly — and somewhat unexpectedly — we also find that the radiation efficiency for the Dirichlet case is larger than for the Neumann case below

the critical frequency ($\alpha > 1$). Given that acoustic radiation below $\alpha = 1$ comes mainly from the boundaries of a plate, one might have expected intuitively that the Neumann case with non-zero amplitude on the boundary to be the more efficient radiator in comparison to Dirichlet. Why this is not the case is not immediately clear from the integral in (5.4); the boundary corrections are oscillatory and the sign of their net contribution is not obvious in the form given. Therefore, we give some insight into where the different contributions come from by looking at various approximations including a large α asymptotics of the expression (5.4).

We further approximate (5.4) in the following manner to better understand the relative strengths of radiation from Dirichlet and Neumann boundary conditions. For $\alpha > 1$, we have stated earlier that the radiated power self-cancels in the integral in the numerator of Eq. (5.4) unless \mathbf{x} and \mathbf{x}' are both close to the boundary (on the scale of the wavelength). For a general boundary shape $\partial\Omega$, the curvature effects are neglected in the leading order within this layer, see Fig. 5.2, and the integral in Eq. 5.4 is locally approximated by an integration over an infinite half plane.

We now summarise the main results obtained from the calculation with a more detailed derivation to follow in Sec. 5.4 and Sec. 5.7. The local calculation leads us to an approximation of radiation efficiency of the form

$$\begin{aligned}\sigma &\simeq \frac{\int_{\partial\Omega} d\mathbf{x}}{\mathcal{A}} \times \text{integrals independent of geometry} \\ &= \frac{\ell}{k_A \pi^2 \mathcal{A}} f(\alpha),\end{aligned}\tag{5.5}$$

where

$$f(\alpha) = \int_0^{2\pi} d\phi \int_0^1 dp_r \frac{p_r}{\sqrt{1-p_r^2} \sqrt{\alpha^2 - p_r^2 \cos^2 \phi}} \begin{cases} \frac{\alpha^2 - p_r^2 \cos^2 \phi}{(\alpha^2 - p_r^2)^2} & \text{Dbc,} \\ \frac{p_r^2 \sin^2 \phi}{(\alpha^2 - p_r^2)^2} & \text{Nbc,} \end{cases}$$

ℓ is the perimeter length and \mathcal{A} is the area of Ω . The geometry of the plate enters the expression in Eq. (5.5) via its dependency on \mathcal{A} and ℓ alone, the boundary conditions have an effect on $f(\alpha)$ only.

From this calculation, we find in Sec. 5.7.2 asymptotic results for $f(\alpha)$ in the limit $\alpha \rightarrow \infty$ of the form

$$\sigma \simeq \frac{2\ell}{\mathcal{A}\pi k} \begin{cases} \frac{1}{\alpha^3} & \text{Dbc,} \\ \frac{1}{3\alpha^5} & \text{Nbc.} \end{cases}$$

Surprisingly, the Dirchlet case has not only have a larger radiation efficiency for $\alpha > 1$, but its asymptotics differ fundamentally from the Neumann case by scaling with a different power for large α .

5.3 Problem setting

Consider a plate set in an infinite baffle subject to harmonic excitation of the form $e^{-i\omega t}$ (which is implied throughout the chapter) radiating into an air-filled half-space, illustrated in Fig. 5.3. We aim to compute the structure's sound-radiated power output in terms of the correlation function of the surface velocities; doing this instead of the more usual calculation in terms of the surface velocities itself

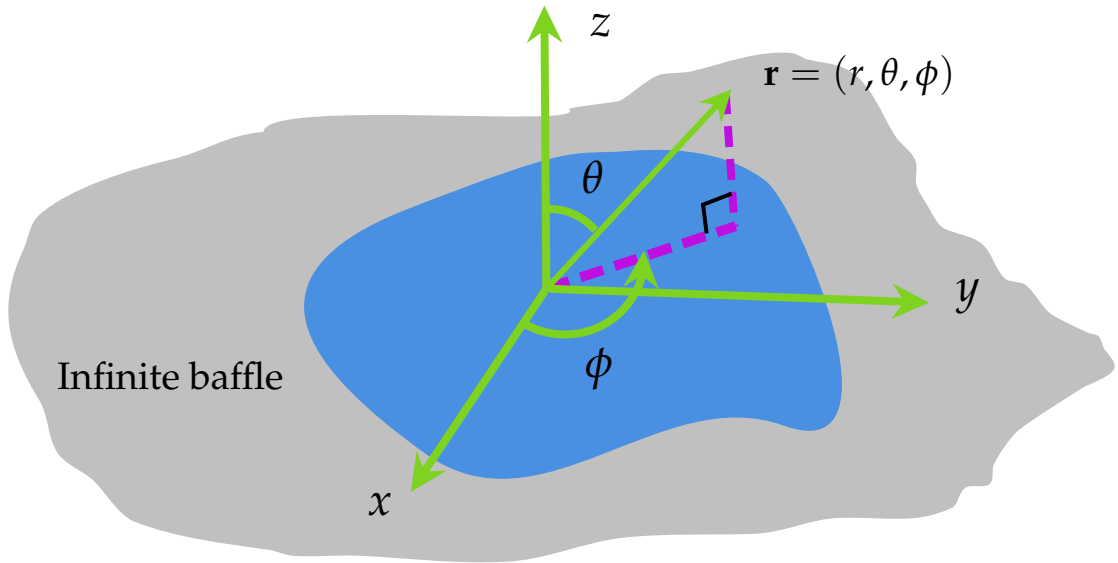


Figure 5.3: Geometry of vibrating structure.

allows us to treat the more general case of disordered plate excitation. Analytical expressions, for arbitrary single-frequency excitation, for the sound radiation from finite planar surfaces, have been provided by, for example, Junger and Feit [88], Fahy [40] and Cremer et al [192]. Overall, these solutions are restricted to the far-field. Theoretical expressions for near-field sound power radiated in areas near the point of excitation were also given by Cremer et al [192]. In all of the above studies, Rayleigh's equation (4.12) is the starting point and analytical expressions are derived for modal radiated power and radiation efficiency.

In literature, there are two main ways of calculating sound-radiated power. The first way is to integrate the far-field acoustic intensity over a hemisphere that contains the source of sound

$$\Pi = \int_{\phi=0}^{2\pi} \int_{\theta=0}^{\pi/2} \frac{|p(r, \theta, \phi)|^2}{2\rho_0 c_0} r^2 \sin \theta \, d\theta \, d\phi, \quad (5.6)$$

where c_0 and ρ_0 are the speed of sound in air and the density of air respectively and $p(r, \theta, \phi)$ is the acoustic pressure at some point in the far-field which is obtained using Rayleigh's equation (see Chapter 4). The second route requires the integration of the acoustic intensity over the surface of the vibrating structure. This surface, denoted Ω , is finite for baffled radiators, covering only the non-baffled field. With $d\mathbf{x} = dx dy$, we have

$$\Pi = \frac{1}{2} \text{Re} \left\{ \int_{\Omega} p(\mathbf{x}, 0) w^*(\mathbf{x}) d\mathbf{x} \right\}, \quad (5.7)$$

where $\text{Re}\{\}$ denotes the real part of the expression in brackets and $w^*(\mathbf{x})$ is the surface velocity at $z = 0$ at a location $\mathbf{x} = (x, y)$ on the structure, where $*$ refers to complex conjugation. The second approach will be taken in this work, which will eventually lead to an expression that describes total sound radiated power for a fixed k_B (or for an individual mode) as a function of frequency obtained from the phase space method, as shown in Eq. (5.5).

In particular, we will write Eq. 5.7 in terms of surface velocity correlation function, either in the spatial domain or in the wavenumber domain (or momentum domain), because we are interested in classically chaotic systems or irregular geometry which is best characterized by a two-point correlation function.

5.3.1 Sound radiation power in the spatial domain

For the planar structure under consideration here, the Rayleigh integral (4.12) for the acoustic pressure $p(\mathbf{x}, z)$ in Eq. (5.7) produces the familiar integral for total

sound-radiated power [64, 195],

$$\begin{aligned}
 \Pi &= \frac{1}{2} \operatorname{Re} \left\{ \frac{-i\omega\rho_0}{2\pi} \int_{\Omega} \int_{\Omega} \frac{e^{-ik_A|\mathbf{x}-\mathbf{x}'|}}{|\mathbf{x}-\mathbf{x}'|} w^*(\mathbf{x}') w(\mathbf{x}) \, d\mathbf{x}' \, d\mathbf{x} \right\}, \\
 &= \frac{\omega\rho_0}{4\pi} \int_{\Omega} \int_{\Omega} \frac{\sin(k_A|\mathbf{x}-\mathbf{x}'|)}{|\mathbf{x}-\mathbf{x}'|} w^*(\mathbf{x}') w(\mathbf{x}) \, d\mathbf{x}' \, d\mathbf{x}, \\
 &= \omega\rho_0 \int_{\Omega} \int_{\Omega} g(|\mathbf{x}-\mathbf{x}'|) w^*(\mathbf{x}') w(\mathbf{x}) \, d\mathbf{x}' \, d\mathbf{x}, \tag{5.8}
 \end{aligned}$$

where g is defined by

$$g(|\mathbf{x}-\mathbf{x}'|) = \frac{\sin(k_A|\mathbf{x}-\mathbf{x}'|)}{4\pi|\mathbf{x}-\mathbf{x}'|} = \operatorname{Im} G(\mathbf{x}, \mathbf{x}').$$

Equation (5.8) can be generalised for stationary random fields by taking an ensemble average over time intervals, frequency or local spatial averaging; that is

$$w^*(\mathbf{x}') w(\mathbf{x}) \rightarrow \langle w^*(\mathbf{x}') w(\mathbf{x}) \rangle \equiv \Gamma_{\Omega}(\mathbf{x}, \mathbf{x}'). \tag{5.9}$$

Substituting Eq. (5.9) into Eq. (5.8), the total radiation power can next be written as

$$\Pi = \omega\rho_0 \int_{\Omega} \int_{\Omega} g(|\mathbf{x}-\mathbf{x}'|) \Gamma_{\Omega}(\mathbf{x}, \mathbf{x}') \, d\mathbf{x}' \, d\mathbf{x}. \tag{5.10}$$

5.3.2 Sound radiation power in the momentum domain

An equivalent way of evaluating the total radiated power given in Eq. (5.10) is to transform the surface velocity and the corresponding surface pressure field in Eq. (5.7) from the spatial domain to the momentum domain via Fourier transformation. Since, in the case of a finite plate in a rigid baffle, $w(\mathbf{x})$ represents the surface normal velocity of the plate and is zero on the baffle, the surface normal velocity

$w(\mathbf{x})$ can also be expressed as an integral over the momentum domain. Referring to Appendix A for the two-dimensional inverse Fourier transformation, the surface normal velocity can be written

$$w^*(\mathbf{x}) = \frac{k_A^2}{4\pi^2} \int_{\mathbb{R}^2} W^*(\mathbf{p}) e^{-ik_A \mathbf{p} \cdot \mathbf{x}} d\mathbf{p}, \quad (5.11)$$

and the surface pressure field is

$$p(\mathbf{x}, 0) = \frac{k_A^2}{4\pi^2} \int_{\mathbb{R}^2} P(\mathbf{p}, 0) e^{ik_A \mathbf{p} \cdot \mathbf{x}} d\mathbf{p}, \quad (5.12)$$

where $W(\mathbf{p})$, $P(\mathbf{p}, 0)$ are Fourier transformation of the surface normal velocity and the surface pressure respectively, $\mathbf{p} = (p_x, p_y) = (\sin \theta \cos \phi, \sin \theta \sin \phi)$ and $d\mathbf{p} = dp_x dp_y$. Thus, by substituting Eq. (5.11) and Eq. (5.12) into Eq. (5.7), we find

$$\Pi = \frac{k_A^4}{32\pi^4} \text{Re} \left\{ \int_{\Omega} \int_{\mathbb{R}^2} \int_{\mathbb{R}^2} P(\mathbf{p}, 0) W^*(\mathbf{p}') e^{ik_A \mathbf{p} \cdot \mathbf{x}} e^{-ik_A \mathbf{p}' \cdot \mathbf{x}} d\mathbf{p} d\mathbf{p}' d\mathbf{x} \right\}. \quad (5.13)$$

As the surface normal velocity $w(\mathbf{x})$ is assumed to be zero beyond the plate boundary, the range of the double integration over the surface Ω can be expanded to $-\infty$ to ∞ and using the delta function relation (see Appendix A)

$$\frac{k_A^2}{4\pi^2} \int_{\mathbb{R}^2} e^{ik_A \mathbf{p} \cdot \mathbf{x}} e^{-ik_A \mathbf{p}' \cdot \mathbf{x}} d\mathbf{x} = \delta(\mathbf{p} - \mathbf{p}'), \quad (5.14)$$

where

$$\delta(\mathbf{p} - \mathbf{p}') = \delta(p_x - p'_x) \delta(p_y - p'_y).$$

Substituting Eq. (5.14) into Eq. (5.13) then yields

$$\Pi = \frac{k_A^2}{8\pi^2} \text{Re} \left\{ \int_{\mathbb{R}^2} P(\mathbf{p}, 0) W^*(\mathbf{p}) d\mathbf{p} \right\}. \quad (5.15)$$

At the structure–fluid interface, by using wave and boundary matching the surface pressure in momentum space is related to the momentum representation of the surface normal velocity by using Eq. (4.15) at $z = z' = 0$,

$$P(\mathbf{p}, 0) = \frac{\rho_0 c_0}{T(\mathbf{p})} W(\mathbf{p}), \quad (5.16)$$

where $T(\mathbf{p})$ is given in Eq. (4.17). Substituting Eq. (5.16) into Eq. (5.15) the equation for power becomes,

$$\Pi = \frac{\rho_0 c_0 k_A^2}{8\pi^2} \operatorname{Re} \left\{ \int_{\mathbb{R}^2} \frac{W(\mathbf{p})W^*(\mathbf{p})}{T(\mathbf{p})} d\mathbf{p} \right\} = \frac{\rho_0 c_0 k_A^2}{8\pi^2} \operatorname{Re} \left\{ \int_{\mathbb{R}^2} \frac{W(\mathbf{p})W^*(\mathbf{p})}{\sqrt{1-\mathbf{p}^2}} d\mathbf{p} \right\}. \quad (5.17)$$

The area within the radiation circle $|\mathbf{p}| = 1$ includes the radiation circle itself, defined by Ω_r , identified by

$$\int_{\Omega_r} d\mathbf{p} \equiv \int_{|\mathbf{p}| \leq 1} d\mathbf{p} \equiv \int_{-1}^1 dp_y \int_{-\sqrt{1-p_y^2}}^{\sqrt{1-p_y^2}} dp_x. \quad (5.18)$$

As the integrand is imaginary for $|\mathbf{p}| > 1$, i.e, no radiation outside of Ω_r

$$\operatorname{Re} \left\{ \int_{\mathbb{R}^2} \frac{W(\mathbf{p})W^*(\mathbf{p})}{T(\mathbf{p})} d\mathbf{p} \right\} \rightarrow \int_{\Omega_r} \frac{W(\mathbf{p})W^*(\mathbf{p})}{T(\mathbf{p})} d\mathbf{p},$$

Therefore, the integral (5.17) can be rewritten by restricting the integration limits, to Ω_r , that is,

$$\Pi = \frac{\rho_0 c_0 k_A^2}{8\pi^2} \int_{\Omega_r} \frac{W(\mathbf{p})W^*(\mathbf{p})}{T(\mathbf{p})} d\mathbf{p}. \quad (5.19)$$

Also, Eq. (5.19) can be generalised to stationary random fields by taking an ensemble average over time intervals, frequency or local spatial averaging

$$W(\mathbf{p})W^*(\mathbf{p}) \rightarrow \langle W(\mathbf{p})W^*(\mathbf{p}) \rangle = \langle |W(\mathbf{p})|^2 \rangle = \Gamma_{\Omega}(\mathbf{p}, \mathbf{p}),$$

where $\Gamma_{\Omega}(\mathbf{p}, \mathbf{p})$ is the diagonal of the momentum representation of surface normal velocity $\Gamma_{\Omega}(\mathbf{x}, \mathbf{x}')$ with $\mathbf{x}, \mathbf{x}' \in \Omega$. Thus Eq. (5.19) can be rewritten for random fields as

$$\Pi = \frac{\rho_0 c_0 k_A^2}{8\pi^2} \int_{\Omega_r} \frac{\Gamma_{\Omega}(\mathbf{p}, \mathbf{p})}{T(\mathbf{p})} d\mathbf{p}. \quad (5.20)$$

It is hence shown that Eq. (5.10) and Eq. (5.20) are equivalent when sufficient assumptions are made and both equations lead to comparable outcomes. Whether to use one equation or the other for a given circumstance is then a matter of computational convenience.

5.3.3 Radiation efficiency

By combining the sound power radiated Π with the sound power radiated by a large piston Π_0 with the same surface area the radiation efficiency σ (5.1) can be eventually calculated. If Π is the sound power radiated by the structure with angular frequency ω to a medium with a density ρ_0 , having area Ω and with normal surface velocity $w(\mathbf{x})$, then Π_0 is defined by

$$\Pi_0 = \frac{1}{2} \rho_0 c_0 \langle |w(\mathbf{x})|^2 \rangle = \frac{1}{2} \rho_0 c_0 \int_{\Omega} |w(\mathbf{x})|^2 d\mathbf{x} = \frac{1}{2} \rho_0 c_0 \int_{\Omega} w(\mathbf{x}) w^*(\mathbf{x}) d\mathbf{x}. \quad (5.21)$$

Eq. (5.21) can be rewritten in terms of the surface velocity correlation function, either in the spatial domain,

$$\Pi_0 = \frac{1}{2} \rho_0 c_0 \int_{\Omega} \Gamma_{\Omega}(\mathbf{x}, \mathbf{x}) d\mathbf{x}, \quad (5.22)$$

or in the wavenumber domain (momentum domain),

$$\Pi_0 = \frac{\rho_0 c_0 k_A^2}{8\pi^2} \int_{\mathbb{R}^2} \Gamma_\Omega(\mathbf{p}, \mathbf{p}) \, d\mathbf{p}, \quad (5.23)$$

using the same identity as in Eq. (5.14). For this reason, the radiation efficiency can also be rewritten in two equivalent forms, either using Eq. (5.10) and Eq. (5.22)

$$\sigma = \frac{2k_A \int_\Omega \int_\Omega g(\mathbf{x}, \mathbf{x}') \Gamma_\Omega(\mathbf{x}, \mathbf{x}') \, d\mathbf{x} \, d\mathbf{x}'}{\int_\Omega \Gamma_\Omega(\mathbf{x}, \mathbf{x}) \, d\mathbf{x}}, \quad (5.24)$$

or using Eq. (5.20) and Eq. (5.23),

$$\sigma = \frac{\int_{\Omega_r} \Gamma_\Omega(\mathbf{p}, \mathbf{p}) \frac{1}{T(\mathbf{p})} \, d\mathbf{p}}{\int_{\mathbb{R}^2} \Gamma_\Omega(\mathbf{p}, \mathbf{p}) \, d\mathbf{p}}. \quad (5.25)$$

The denominator Π_0 in Eq. (5.22) for a diffuse field excitation normalised such that $\Gamma_\Omega(\mathbf{x}, \mathbf{x}) = 1$ and is equal to

$$\Pi_0 = \frac{1}{2} \rho_0 c_0 \mathcal{A}. \quad (5.26)$$

Therefore, we can rewrite Eq. (5.25) using Eq. (5.20) and Eq. (5.26) as

$$\sigma = \frac{k_A^2}{4\pi^2 \mathcal{A}} \int_{\Omega_r} \Gamma_\Omega(\mathbf{p}, \mathbf{p}) \frac{1}{T(\mathbf{p})} \, dp. \quad (5.27)$$

Having outlined the general process for the radiation of acoustic power from plate like structures and the radiation efficiency, let us now carry out a more detailed study by analysing some particular cases of practical interest.

5.4 Radiation efficiency of finite plate: Diffuse-field

We now demonstrate how the normal surface velocity CF for a finite plate structure can be written in terms of a normal surface velocity CF for an infinite plane.

Let the confined plate normal surface velocity CF be

$$\Gamma_{\Omega}(\mathbf{x}, \mathbf{x}') = \chi_{\Omega}(\mathbf{x})\Gamma(\mathbf{x}, \mathbf{x}')\chi_{\Omega}(\mathbf{x}'), \quad (5.28)$$

where $\mathbf{x}, \mathbf{x}' \in \mathbb{R}^d$ and Ω is the domain of the plate. χ_{Ω} denotes projection onto functions supported in Ω defined in spatial space by

$$\chi_{\Omega}(\mathbf{x}) = \begin{cases} 1 & \text{if } \mathbf{x} \in \Omega, \\ 0 & \text{otherwise.} \end{cases}$$

Thus

$$\Gamma_{\Omega}(\mathbf{x}, \mathbf{x}') = \begin{cases} \Gamma(\mathbf{x}, \mathbf{x}') & \text{if } \mathbf{x}, \mathbf{x}' \in \Omega, \\ 0 & \text{otherwise} \end{cases}$$

Equation (5.3) can be rewritten as

$$\Gamma(\mathbf{x}, \mathbf{x}') = \Gamma_0(\mathbf{x}, \mathbf{x}') \pm \Gamma_1(\mathbf{x}, \mathbf{x}'), \quad (5.29)$$

where

$$\Gamma_0((\mathbf{x}, \mathbf{x}') = J_0(\alpha k_A |\mathbf{x} - \mathbf{x}'|),$$

and

$$\Gamma_1(\mathbf{x}, \mathbf{x}') = J_0(\alpha k_A |(x - x', y + y')|).$$

5.4.1 Correlation function in momentum space with finite-size effects

Let us denote the Fourier transformation of the terms in Eq. (5.29) as follows.

First

$$H(\mathbf{p}) = \int_{\mathbb{R}^d} \chi_{\Omega}(\mathbf{x}) e^{-ik\mathbf{p}\cdot\mathbf{x}} d\mathbf{x} = \int_{\Omega} e^{-ik\mathbf{p}\cdot\mathbf{x}} d\mathbf{x}, \quad (5.30)$$

defines a characteristic function of the domain Ω . Then define

$$\begin{aligned} \hat{\Gamma}_0(\mathbf{p}, \mathbf{p}') &= \int_{\mathbb{R}^{2d}} \Gamma_0(\mathbf{x}, \mathbf{x}') e^{-ik\mathbf{p}\cdot\mathbf{x} + ik\mathbf{p}'\cdot\mathbf{x}'} d\mathbf{x} d\mathbf{x}', \\ &= \int_{\mathbb{R}^{2d}} J_0(\alpha k |\mathbf{x} - \mathbf{x}'|) e^{-ik\mathbf{p}\cdot\mathbf{x} + ik\mathbf{p}'\cdot\mathbf{x}'} d\mathbf{x} d\mathbf{x}', \end{aligned} \quad (5.31)$$

and

$$\begin{aligned} \hat{\Gamma}_1(\mathbf{p}, \mathbf{p}') &= \int_{\mathbb{R}^{2d}} \Gamma_1(\mathbf{x}, \mathbf{x}') e^{-ik\mathbf{p}\cdot\mathbf{x} + ik\mathbf{p}'\cdot\mathbf{x}'} d\mathbf{x} d\mathbf{x}' \\ &= \int_{\mathbb{R}^{2d}} J_0(\alpha k |(x - x', y + y')|) e^{-ik\mathbf{p}\cdot\mathbf{x} + ik\mathbf{p}'\cdot\mathbf{x}'} d\mathbf{x} d\mathbf{x}', \end{aligned} \quad (5.32)$$

where d denotes the space dimension (here $d = 2$) and k is acoustic wavenumber (after shortening the notation; in the previous sections it is denoted by k_A). We perform a change of variables as follows:

$$\mathbf{s} = \mathbf{x} - \mathbf{x}', \quad (5.33a)$$

$$\bar{\mathbf{x}} = \frac{\mathbf{x} + \mathbf{x}'}{2}, \quad (5.33b)$$

for position variables and

$$\mathbf{q} = \mathbf{p} - \mathbf{p}', \quad (5.33c)$$

$$\bar{\mathbf{p}} = \frac{\mathbf{p} + \mathbf{p}'}{2}, \quad (5.33d)$$

for momentum variables. Then Eq. (5.31) yields

$$\begin{aligned}
\hat{\Gamma}_0(\bar{\mathbf{p}} - \mathbf{q}/2, \bar{\mathbf{p}} + \mathbf{q}/2) &= \int_{\mathbb{R}^4} J_0(\alpha k |\mathbf{s}|) e^{-ik\mathbf{q}\cdot\bar{\mathbf{x}} - ik\bar{\mathbf{p}}\cdot\mathbf{s}} \, d\mathbf{s} \, d\bar{\mathbf{x}} \\
&= \left(\frac{2\pi}{k}\right)^2 \delta(\mathbf{q}) \int_{\mathbb{R}^2} J_0(\alpha k |\mathbf{s}|) e^{-ik\bar{\mathbf{p}}\cdot\mathbf{s}} \, d\mathbf{s} \\
&= \frac{16\pi^3}{k^4} \delta(\mathbf{q}) \delta(\bar{\mathbf{p}}^2 - \alpha^2). \tag{5.34}
\end{aligned}$$

Thus expressing Eq. (5.34) in terms of the original variables \mathbf{p} and \mathbf{p}' we get

$$\hat{\Gamma}_0(\mathbf{p}, \mathbf{p}') = \frac{16\pi^3}{k^4} \delta(\mathbf{p} - \mathbf{p}') \delta\left(\left(\frac{\mathbf{p} + \mathbf{p}'}{2}\right)^2 - \alpha^2\right). \tag{5.35}$$

Similarly, we go through the same steps for $\hat{\Gamma}_1(\mathbf{p}, \mathbf{p}')$. We perform a change of variables in the same way as we do in Eq. (5.33). Substituting Eq. (5.33) into Eq. (5.32) yields

$$\begin{aligned}
\hat{\Gamma}_1(\bar{\mathbf{p}} - \mathbf{q}/2, \bar{\mathbf{p}} + \mathbf{q}/2) &= \int_{\mathbb{R}^4} J_0\left(\alpha k \sqrt{s_x^2 + (2\bar{y})^2}\right) e^{-ik\mathbf{q}\cdot\bar{\mathbf{x}} - ik\bar{\mathbf{p}}\cdot\mathbf{s}} \, d\mathbf{s} \, d\bar{\mathbf{x}}, \\
&= \left(\frac{2\pi}{k}\right)^2 \delta(q_x) \delta(\bar{p}_y) \times \\
&\quad \int_{\mathbb{R}^2} J_0\left(\alpha k \sqrt{s_x^2 + (2\bar{y})^2}\right) e^{-ikq_y\bar{y} - ik\bar{p}_x s_x} \, ds_x \, d\bar{y}.
\end{aligned}$$

Making use of the relation [196]

$$J_0(\alpha \sqrt{x^2 + y^2}) = \frac{1}{2\pi} \int_0^{2\pi} d\theta \cos(\alpha \cos \theta x) \cos(\alpha \sin \theta y),$$

we obtain

$$\begin{aligned}
\hat{\Gamma}_1((\bar{\mathbf{p}} - \mathbf{q}/2, \bar{\mathbf{p}} + \mathbf{q}/2) &= \frac{2\pi}{k^2} \delta(q_x) \delta(\bar{p}_y) \int_0^{2\pi} d\theta \int_{\mathbb{R}^2} ds_x d\bar{y} \\
&\quad \times e^{-ikq_y\bar{y} - ik\bar{p}_x s_x} \cos(\alpha k s_x \cos \theta) \cos(2\alpha k \bar{y} \sin \theta), \\
&= \frac{2\pi}{k^2} \delta(q_x) \delta(\bar{p}_y) \int_0^{2\pi} d\theta \mathcal{F} \{ \cos(\alpha k s_x \cos \theta) \} \mathcal{F} \{ \cos(2\alpha k \bar{y} \sin \theta) \}, \\
&= \frac{16\pi^3}{k^4} \delta(q_x) \delta(\bar{p}_y) \int_0^{2\pi} d\theta \delta(\bar{p}_x^2 - \alpha^2 \cos^2 \theta) \\
&\quad \times \delta\left(\frac{q_y^2}{4} - \alpha^2 \sin^2 \theta\right) |\alpha^2 \sin \theta \cos \theta|, \\
&= \frac{8\pi^3}{k^4} \delta(q_x) \delta(\bar{p}_y) \delta\left(\bar{p}_x^2 + \left(\frac{q_y}{2}\right)^2 - \alpha^2\right). \tag{5.36}
\end{aligned}$$

Expressing Eq. (5.36) in terms of the original variables \mathbf{p} and \mathbf{p}' we get

$$\hat{\Gamma}_1(\mathbf{p}, \mathbf{p}') = \frac{8\pi^3}{k^4} \delta(p_x - p'_x) \delta\left(\frac{p_y + p'_y}{2}\right) \delta\left(\left(\frac{p_x + p'_x}{2}\right)^2 + \left(\frac{p_y - p'_y}{2}\right)^2 - \alpha^2\right). \tag{5.37}$$

Now, the Fourier transformation of Eq. (5.28) results in

$$\begin{aligned}
\hat{\Gamma}_\Omega(\mathbf{p}, \mathbf{p}') &= \mathcal{F} \{ \chi_\Omega(\mathbf{x}) \hat{\Gamma}(\mathbf{x}, \mathbf{x}') \chi_\Omega(\mathbf{x}') \} \\
&= \left(\frac{2\pi}{k}\right)^{-4} H(\mathbf{p}) * \hat{\Gamma}(\mathbf{p}, \mathbf{p}') * \bar{H}(\mathbf{p}') \\
&= A(\mathbf{p}, \mathbf{p}') \pm B(\mathbf{p}, \mathbf{p}'),
\end{aligned}$$

where $*$ denotes convolution, \bar{H} represents conjugate of H , and

$$A(\mathbf{p}, \mathbf{p}') = \left(\frac{2\pi}{k}\right)^{-4} H(\mathbf{p}) * \hat{\Gamma}_0(\mathbf{p}, \mathbf{p}') * \bar{H}(\mathbf{p}'),$$

and

$$B(\mathbf{p}, \mathbf{p}') = \left(\frac{2\pi}{k}\right)^{-4} H(\mathbf{p}) * \hat{\Gamma}_1(\mathbf{p}, \mathbf{p}') * \bar{H}(\mathbf{p}').$$

Using the convolution theorem and Eq. (5.35) we can show that

$$\begin{aligned}
A(\mathbf{p}, \mathbf{p}') &= \left(\frac{2\pi}{k}\right)^{-4} \int_{\mathbb{R}^4} d\mathbf{p}'' d\mathbf{p}''' H(\mathbf{p} - \mathbf{p}'') \hat{\Gamma}_0(\mathbf{p}'', \mathbf{p}''') \bar{H}(\mathbf{p}' - \mathbf{p}''') \\
&= \frac{1}{\pi} \int_{\mathbb{R}^4} d\mathbf{p}'' d\mathbf{p}''' H(\mathbf{p} - \mathbf{p}'') \delta(\mathbf{p}'' - \mathbf{p}''') \\
&\quad \times \delta\left(\left(\frac{\mathbf{p}'' + \mathbf{p}'''}{2}\right)^2 - \alpha^2\right) \bar{H}(\mathbf{p}' - \mathbf{p}''') \\
&= \frac{1}{\pi} \int_{\mathbb{R}^2} d\mathbf{p}'' H(\mathbf{p} - \mathbf{p}'') \delta(\mathbf{p}''^2 - \alpha^2) \bar{H}(\mathbf{p}' - \mathbf{p}'').
\end{aligned}$$

Converting $\mathbf{p}'' = (p_x'', p_y'')$ to polar coordinates $\mathbf{p}_r = (p_r \cos \theta, p_r \sin \theta)$ results in

$$A(\mathbf{p}, \mathbf{p}') = \frac{1}{2\pi} \int_0^{2\pi} d\theta H(\mathbf{p} - \mathbf{p}_\alpha) \bar{H}(\mathbf{p}' - \mathbf{p}_\alpha) = \langle H(\mathbf{p} - \mathbf{p}_\alpha) \bar{H}(\mathbf{p}' - \mathbf{p}_\alpha) \rangle, \quad (5.38)$$

where $\mathbf{p}_\alpha = (\alpha \cos \theta, \alpha \sin \theta)$ and average $\langle \cdot \rangle$ is over direction of \mathbf{p}_α .

Using similar steps to simplify $B(\mathbf{p}, \mathbf{p}')$ yields

$$\begin{aligned}
B(\mathbf{p}, \mathbf{p}') &= \left(\frac{2\pi}{k}\right)^{-4} \int_{\mathbb{R}^4} d\mathbf{p}'' d\mathbf{p}''' H(\mathbf{p} - \mathbf{p}'') \hat{\Gamma}_1(\mathbf{p}'', \mathbf{p}''') \bar{H}(\mathbf{p}' - \mathbf{p}''') \\
&= \frac{1}{2\pi} \int_{\mathbb{R}^4} d\mathbf{p}'' d\mathbf{p}''' H(\mathbf{p} - \mathbf{p}'') \delta(p_x'' - p_x''') \delta\left(\frac{p_y'' + p_y'''}{2}\right) \\
&\quad \times \delta\left(\left(\frac{p_x'' + p_x'''}{2}\right)^2 + \left(\frac{p_y'' - p_y'''}{2}\right)^2 - \alpha^2\right) \bar{H}(\mathbf{p}' - \mathbf{p}''') \\
&= \frac{1}{\pi} \int_{\mathbb{R}^2} d\mathbf{p}'' H(\mathbf{p} - \mathbf{p}'') \delta(p_x''^2 + p_y''^2 - \alpha^2) \bar{H}(p_x' - p_x'', p_y' + p_y'').
\end{aligned}$$

Converting $\mathbf{p}''' = (p_x''', p_y''')$ to polar coordinates $\mathbf{p}_r = (p_r \cos \theta, p_r \sin \theta)$ yields

$$\begin{aligned}
B(\mathbf{p}, \mathbf{p}') &= \frac{1}{2\pi} \int_0^{2\pi} d\theta H(p_x - \alpha \cos \theta, p_y - \alpha \sin \theta) \bar{H}(p_x' - \alpha \cos \theta, p_y' + \alpha \sin \theta), \\
&= \frac{1}{2\pi} \int_0^{2\pi} d\theta H(\mathbf{p} - \mathbf{p}_\alpha) \bar{H}(p_x' - \alpha \cos \theta, p_y' + \alpha \sin \theta), \\
&= \langle H(\mathbf{p} - \mathbf{p}_\alpha) \bar{H}(p_x' - \alpha \cos \theta, p_y' + \alpha \sin \theta) \rangle. \quad (5.39)
\end{aligned}$$

Consequently, $\hat{\Gamma}_\Omega$ can be written as

$$\hat{\Gamma}_\Omega(\mathbf{p}, \mathbf{p}') = A(\mathbf{p}, \mathbf{p}') \mp B'(\mathbf{p}, \mathbf{p}'), \quad (5.40)$$

where

$$B'(\mathbf{p}, \mathbf{p}') = -B(\mathbf{p}, \mathbf{p}'), \quad (5.41)$$

and the \mp signs apply to Nbc and Dbc respectively. We will demonstrate later in the chapter that B' is a positive quantity when structural waves have a wavenumber larger than acoustic wavenumber, i.e. $\alpha > 1$.

We can simplify A and B by replacing H and \bar{H} in Eq. (5.38) and Eq. (5.39) respectively. Recalling Eq. (5.30) for the function H , where \bar{H} is given by complex conjugate of Eq. (5.30), we obtain

$$\begin{aligned} A(\mathbf{p}, \mathbf{p}') &= \langle H(\mathbf{p} - \mathbf{p}_\alpha) \bar{H}(\mathbf{p}' - \mathbf{p}_\alpha) \rangle, \\ &= \frac{1}{2\pi} \int_0^{2\pi} d\theta \int_\Omega \int_\Omega e^{-ik(\mathbf{p} - \mathbf{p}_\alpha) \cdot \mathbf{x}} e^{ik(\mathbf{p}' - \mathbf{p}_\alpha) \cdot \mathbf{x}'} d\mathbf{x} d\mathbf{x}'. \end{aligned}$$

Changing the variables \mathbf{x} and \mathbf{x}' as in Eq. (5.33) gives

$$A(\mathbf{p}, \mathbf{p}') = \frac{1}{2\pi} \int_0^{2\pi} d\theta \int_{\Omega_{\bar{\mathbf{x}}}} \int_{\Omega_{\mathbf{s}}} e^{-ik(\mathbf{p} - \mathbf{p}') \cdot \bar{\mathbf{x}}} e^{-ik(\frac{\mathbf{p} + \mathbf{p}'}{2} - \mathbf{p}_\alpha) \cdot \mathbf{s}} d\mathbf{s} d\bar{\mathbf{x}},$$

where $\Omega_{\bar{\mathbf{x}}} = \{\bar{\mathbf{x}} : \bar{\mathbf{x}} = \frac{\mathbf{x} + \mathbf{x}'}{2} \text{ where } \mathbf{x}, \mathbf{x}' \in \Omega\}$ and $\Omega_{\mathbf{s}} = \{\mathbf{s} : \mathbf{s} = \mathbf{x} - \mathbf{x}' \text{ where } \mathbf{x}, \mathbf{x}' \in \Omega\}$; note that $\Omega_{\bar{\mathbf{x}}}$ is essentially the domain itself Ω , i.e. $\Omega_{\bar{\mathbf{x}}} = \Omega$ and $\Omega_{\mathbf{s}}$ depends on $\bar{\mathbf{x}}$. Thus

$$A(\mathbf{p}, \mathbf{p}') = \frac{1}{2\pi} \int_0^{2\pi} d\theta \int_{\Omega_{\bar{\mathbf{x}}}} e^{-ik(\mathbf{p} - \mathbf{p}') \cdot \bar{\mathbf{x}}} d\bar{\mathbf{x}} \int_{\Omega_{\mathbf{s}}} e^{-ik(\frac{\mathbf{p} + \mathbf{p}'}{2} - \mathbf{p}_\alpha) \cdot \mathbf{s}} d\mathbf{s}. \quad (5.42)$$

Similarly, $B'(\mathbf{p}, \mathbf{p}')$ can be expressed as

$$\begin{aligned} B'(\mathbf{p}, \mathbf{p}') &= - \left\langle H(\mathbf{p} - \mathbf{p}_\alpha) \bar{H}(p'_x - \alpha \cos \theta, p'_y + \alpha \sin \theta) \right\rangle, \\ &= \frac{-1}{2\pi} \int_0^{2\pi} d\theta \int_{\Omega} \int_{\Omega} e^{-ik(\mathbf{p} - \mathbf{p}_\alpha) \cdot \mathbf{x}} e^{ik[(p'_x - \alpha \cos \theta)x' + (p'_y + \alpha \sin \theta)y']} d\mathbf{x} d\mathbf{x}'. \end{aligned}$$

Changing the variables \mathbf{x} and \mathbf{x}' as in Eq. (5.33), we get

$$\begin{aligned} B'(\mathbf{p}, \mathbf{p}') &= \frac{-1}{2\pi} \int_0^{2\pi} d\theta \int_{\Omega_{\bar{\mathbf{x}}}} \int_{\Omega_s} e^{-ik[(p_x - p'_x)\bar{x} + (p_y - p'_y - 2\alpha \sin \theta)\bar{y}]} \\ &\quad \times e^{-ik[(\frac{p_x + p'_x}{2} - \alpha \cos \theta)s_x + (\frac{p_y + p'_y}{2})s_y]} d\mathbf{s} d\bar{\mathbf{x}}, \end{aligned}$$

Thus

$$\begin{aligned} B'(\mathbf{p}, \mathbf{p}') &= \frac{-1}{2\pi} \int_0^{2\pi} d\theta \int_{\Omega_{\bar{\mathbf{x}}}} e^{-ik[(p_x - p'_x)\bar{x} + (p_y - p'_y - 2\alpha \sin \theta)\bar{y}]} d\bar{\mathbf{x}} \\ &\quad \int_{\Omega_s} e^{-ik[(\frac{p_x + p'_x}{2} - \alpha \cos \theta)s_x + (\frac{p_y + p'_y}{2})s_y]} d\mathbf{s}. \end{aligned} \quad (5.43)$$

Now one can obtain $\Gamma_{\Omega}(\mathbf{p}, \mathbf{p})$ from Eq. (5.40),

$$\Gamma_{\Omega}(\mathbf{p}, \mathbf{p}) = A(\mathbf{p}, \mathbf{p}) \mp B'(\mathbf{p}, \mathbf{p}), \quad (5.44)$$

where we get from Eq. (5.42)

$$A(\mathbf{p}, \mathbf{p}) = \frac{1}{2\pi} \int_0^{2\pi} d\theta \int_{\Omega_{\bar{\mathbf{x}}}} d\bar{\mathbf{x}} \int_{\Omega_s} e^{-ik(\mathbf{p} - \mathbf{p}_\alpha) \cdot \mathbf{s}} d\mathbf{s}, \quad (5.45)$$

and from Eq. (5.43)

$$B'(\mathbf{p}, \mathbf{p}) = -\frac{1}{2\pi} \int_0^{2\pi} d\theta \int_{\Omega_{\bar{\mathbf{x}}}} e^{2ik\alpha\bar{y}\sin\theta} d\bar{\mathbf{x}} \int_{\Omega_s} e^{-ik[(p_x - \alpha \cos \theta)s_x + p_y s_y]} d\mathbf{s}. \quad (5.46)$$

5.4.2 Rectangular plates

For structures having a corner, the corner correction (image of image correction)

must be added to the correlation function. For a corner joining edge $x = 0$ and

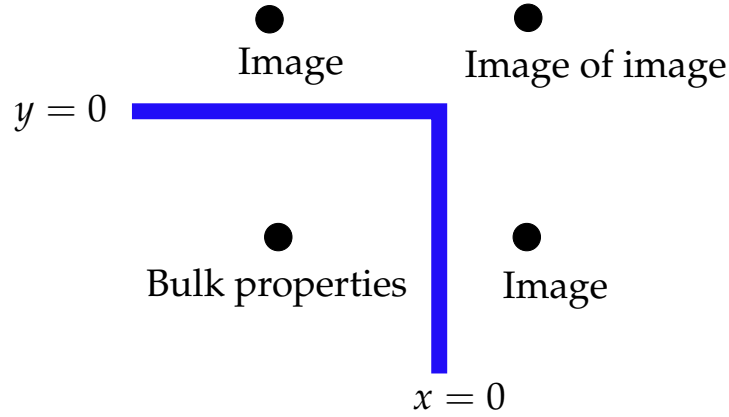


Figure 5.4: Method of image for a 90° corner joining edge $x = 0$ and $y = 0$.

$y = 0$ as shown in Fig. 5.4 the CF can be written as

$$\Gamma(\mathbf{x}, \mathbf{x}') = J_0(k_B |\mathbf{x} - \mathbf{x}'|) \pm J_0(k_B |\mathbf{x} - \mathcal{R}_y \mathbf{x}'|) \pm J_0(k_B |\mathbf{x} - \mathcal{R}_x \mathbf{x}'|) + J_0(k_B |\mathbf{x} - \bar{\mathcal{R}} \mathbf{x}'|), \quad (5.47)$$

where $\mathcal{R}_x \mathbf{x}'$ denotes a reflection of \mathbf{x}' through the edge $x = 0$, $\mathcal{R}_y \mathbf{x}'$ denotes a reflection of \mathbf{x}' through the edge $y = 0$, $\bar{\mathcal{R}} \mathbf{x}'$ denotes a reflection of \mathbf{x}' through the corner and the \pm signs apply to N_{bc} and D_{bc} , respectively. Therefore, for the corner joining edge $x = 0$ and $y = 0$, Eq. (5.47) can be written as

$$\Gamma(\mathbf{x}, \mathbf{x}') = \Gamma_0(\mathbf{x}, \mathbf{x}') \pm \Gamma_1(\mathbf{x}, \mathbf{x}') \pm \Gamma_2(\mathbf{x}, \mathbf{x}') + \Gamma_3(\mathbf{x}, \mathbf{x}'), \quad (5.48)$$

where Γ_0 and Γ_1 are given by Eq. (5.47),

$$\Gamma_2(\mathbf{x}, \mathbf{x}') = J_0(\alpha k_A |(x + x', y - y')|),$$

$$\Gamma_3(\mathbf{x}, \mathbf{x}') = J_0(\alpha k_A |\mathbf{x} + \mathbf{x}'|).$$

These additional terms will subsequently be added to the momentum representation of CF in Eq. (5.40))

$$\Gamma_{\Omega}(\mathbf{p}, \mathbf{p}') = A(\mathbf{p}, \mathbf{p}') \mp B'(\mathbf{p}, \mathbf{p}') \mp C'(\mathbf{p}, \mathbf{p}') + D(\mathbf{p}, \mathbf{p}'), \quad (5.49)$$

where

$$\begin{aligned} C'(\mathbf{p}, \mathbf{p}') &= - \left(\frac{2\pi}{k} \right)^{-2d} \int_{\mathbb{R}^{2d}} d\mathbf{p}'' d\mathbf{p}''' H(\mathbf{p} - \mathbf{p}'') \hat{\Gamma}_2(\mathbf{p}'', \mathbf{p}''') \bar{H}(\mathbf{p}' - \mathbf{p}'''), \\ &= - \left\langle H(\mathbf{p} - \mathbf{p}_{\alpha}) \bar{H}(p'_x + \alpha \cos \theta, p'_y - \alpha \sin \theta) \right\rangle, \end{aligned}$$

and

$$\begin{aligned} D(\mathbf{p}, \mathbf{p}') &= \left(\frac{2\pi}{k} \right)^{-2d} \int_{\mathbb{R}^{2d}} d\mathbf{p}'' d\mathbf{p}''' H(\mathbf{p} - \mathbf{p}'') \hat{\Gamma}_3(\mathbf{p}'', \mathbf{p}''') \bar{H}(\mathbf{p}' - \mathbf{p}'''), \\ &= \frac{1}{2} \left\langle H(\mathbf{p} - \mathbf{p}_{\alpha}) \bar{H}(\mathbf{p}' + \mathbf{p}_{\alpha}) \right\rangle. \end{aligned}$$

The momentum representation C' can be obtained using similar procedures as B' and see Appendix D for a derivation of D .

For a rectangular plate of length L_y and width L_x , as shown in the configuration Fig. 4.4, the characteristic function H in Eq. (5.30), and its complex conjugate \bar{H} are products of sinc functions. Therefore, the diagonal of the momentum representation of normal surface velocity for rectangular plate $\Gamma_{\Omega}(\mathbf{p}, \mathbf{p})$ to be substituted into the radiation efficiency formula Eq. (5.1) can be expressed as

$$\Gamma_{\Omega}(\mathbf{p}, \mathbf{p}) = A(\mathbf{p}, \mathbf{p}) \mp 2 \times B'(\mathbf{p}, \mathbf{p}') \mp 2 \times C'(\mathbf{p}, \mathbf{p}) + 4 \times D(\mathbf{p}, \mathbf{p}), \quad (5.50)$$

where

$$A(\mathbf{p}, \mathbf{p}) = \frac{1}{2\pi} \int_0^{2\pi} \left[\text{sinc} \left(\frac{kL_x(p_x - \alpha \cos \theta)}{2} \right) \text{sinc} \left(\frac{kL_y(p_y - \alpha \sin \theta)}{2} \right) \right]^2 d\theta,$$

$$B'(\mathbf{p}, \mathbf{p}) = -\frac{1}{2\pi} \int_0^{2\pi} \left[\text{sinc} \left(\frac{kL_x(p_x - \alpha \cos \theta)}{2} \right) \right]^2 \text{sinc} \left(\frac{kL_y(p_y - \alpha \sin \theta)}{2} \right) \\ \times \text{sinc} \left(\frac{kL_y(p_y + \alpha \sin \theta)}{2} \right) d\theta,$$

$$C'(\mathbf{p}, \mathbf{p}) = -\frac{1}{2\pi} \int_0^{2\pi} \text{sinc} \left(\frac{kL_x(p_x - \alpha \cos \theta)}{2} \right) \text{sinc} \left(\frac{kL_x(p_x + \alpha \cos \theta)}{2} \right) \\ \times \left[\text{sinc} \left(\frac{kL_y(p_y - \alpha \sin \theta)}{2} \right) \right]^2 d\theta,$$

and

$$D(\mathbf{p}, \mathbf{p}) = \frac{1}{4\pi} \int_0^{2\pi} \text{sinc} \left(\frac{kL_x(p_x - \alpha \cos \theta)}{2} \right) \text{sinc} \left(\frac{kL_y(p_y - \alpha \sin \theta)}{2} \right) \\ \times \text{sinc} \left(\frac{kL_x(p_x + \alpha \cos \theta)}{2} \right) \text{sinc} \left(\frac{kL_y(p_y + \alpha \sin \theta)}{2} \right) d\theta.$$

Thus, the radiation efficiency for a fixed k_B can be calculated either by substituting Eq. (5.50) into Eq. (5.27) or by directly substituting special representations Eq. (4.11) into Eq. (5.24).

In the next section, the radiation efficiency of mode shape excitation has been discussed to validate our results.

5.5 Radiation efficiency of finite plate: mode shape approach

Another method of calculating radiation efficiency of plates is described in this section and will be compared in the following sections to the methods described in Sec. 5.4. Since plate vibrations typically include several superimposed modes, in general, the radiation efficiency of a plate can be achieved by summing up

all the modes that make a significant contribution to the frequency range under consideration [197]. The modes radiate essentially independently of each other in the weak coupling regime studied here. Thus, we approach the radiation efficiency first via a single eigenmode. For convenience, simply supported plate and guided plate boundaries will be considered.

Denote the structural vibration for an individual mode by w_{nm} . By summing up all the structural vibration modes of the plate, the surface velocity $w(\mathbf{x})$ can be found at any position $\mathbf{x} = (x, y)$ on the plate. The total power radiated in a certain direction by a given eigenmode can then be calculated using Eq. (5.6), which is proportional to the far-field acoustic pressure square $|p(r, \theta, \varphi)|^2$. The radiated acoustic pressure $p(r, \theta, \varphi)$ in the fluid at large distances from the plate is given by Rayleigh's formula Eq. (4.12). Using the spherical coordinates shown in Fig. 5.3 [186], we may write

$$p(r, \theta, \varphi) = -i\rho_0\omega \frac{e^{-ikr}}{2\pi r} \hat{W}_{nm}(\mathbf{p}) \quad (5.51)$$

with

$$\mathbf{p} = (p_x, p_y), \quad p_x = \sin \theta \cos \varphi, \quad p_y = \sin \theta \sin \varphi,$$

and where \hat{W}_{nm} is the Fourier transform of w_{nm} and given by

$$\hat{W}_{nm}(\mathbf{p}) = \int_{\Omega} w_{nm}(\mathbf{x}) e^{-i\mathbf{kx} \cdot \mathbf{p}} d\mathbf{x}. \quad (5.52)$$

The radiated acoustic pressure is thus directly connected to the Fourier transformation of the plate's vibration amplitude. Physically, this means that a major role

is played by spatial coherence effects between various points on the plate. In practice, for arbitrary plate shapes, the numerical determination of the quantity (5.51) is a challenging issue, especially for high frequencies in which the spatial structure of the eigenmode is particularly complex, precisely because of the existence of these subtle spatial coherence effects [198]. In the previous section, the method used to solve this problem has been established (by writing the Fourier transformation of the vibration CF of the plate in terms of its characteristic function). Delande and Sornette have also developed a solution to this issue for arbitrary membrane shapes [198].

Substituting Eq. (5.51) into Eq. (5.6) results in

$$\Pi^{nm} = \rho_0 c_0 \int_{\phi=0}^{2\pi} \int_{\theta=0}^{\pi/2} \frac{k^2 |\hat{W}_{nm}(\mathbf{p})|^2}{8\pi^2} \sin \theta \, d\theta \, d\phi \quad (5.53)$$

with $k = \omega/c_0$. Radiation efficiency can then be calculated for individual modes (n, m) , $k_{n,m} = \sqrt{\left(\frac{n\pi}{L_x}\right)^2 + \left(\frac{m\pi}{L_y}\right)^2}$. Referencing Eq. (5.1), the radiation efficiency of individual modes (modal radiation efficiency) σ_{nm} can be obtained by [43]

$$\sigma_{nm} = \frac{\Pi^{nm}}{\Pi_0^{nm}}. \quad (5.54)$$

In general, w_{nm} is a product of the mode shape function, which depends on the considered boundary conditions, with the modal velocity amplitude, which depends on the frequency and the form of excitation. For a simply supported rectangular plate of length L_y and width L_x as shown in the configuration Fig. 4.4, the mode shape function is a product of sine functions along the x and y

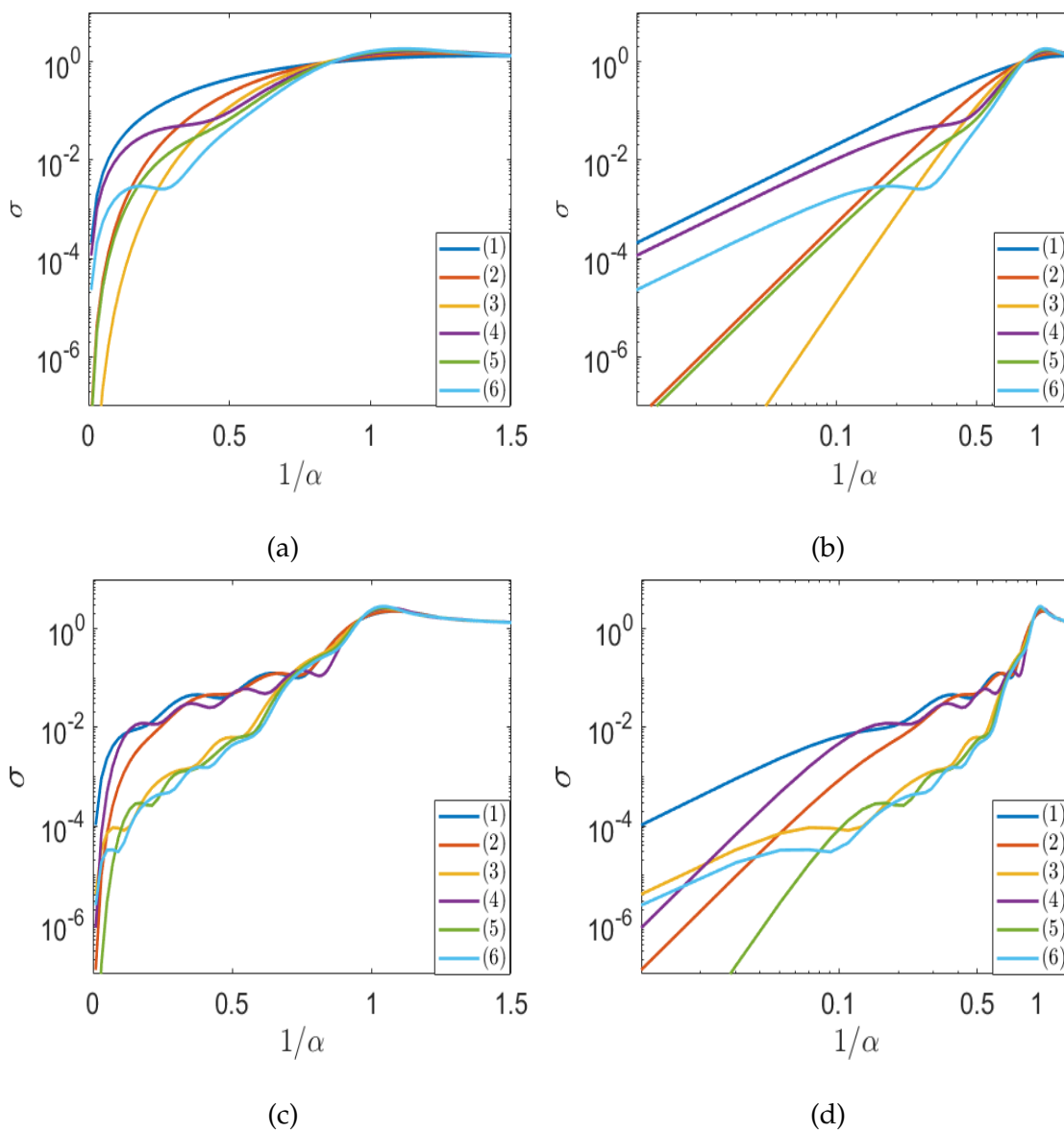


Figure 5.5: Modal radiation efficiencies σ_{nm} of simply supported plates (2×2 m plate) for the mode order 1: (1,1), 2: (1,2), 3: (1,3), 4: (2,2), 5: (2,3), 6: (3,3) (a) in a linear-log scale or (b) in a log-log scale; and for mode order 1: (8,8), 2: (1,7), 3: (1,10), 4: (2,7), 5: (7,7), 6: (9,9) (c) in a linear-log scale or (d) in a log-log scale.

directions and given by Eq. (2.3) (see Chapter 2). Thus

$$w_{nm}(x, y) = A_{nm} \sin\left(\frac{n\pi x}{L_x}\right) \sin\left(\frac{m\pi y}{L_y}\right), \quad (5.55)$$

where $n, m = 1, 2, \dots$, A_{nm} is the modal velocity amplitude of mode (n, m) , $k_x = n\pi/L_x$, $k_y = m\pi/L_y$ and $k_{n,m} = \sqrt{k_x^2 + k_y^2}$. The corresponding modal natural frequency is given by

$$\omega_{nm} = \sqrt{\frac{B}{\rho_s h} \left[\left(\frac{n\pi}{L_x}\right)^2 + \left(\frac{m\pi}{L_y}\right)^2 \right]}, \quad (5.56)$$

where B is the bending stiffness of the plate given by Eq. (2.2) and ρ_s is the density of the plate. Thus, the eigenfrequencies for each mode are defined by $f_{nm} = \omega_{nm}/2\pi$. Note that k_B and $k_{n,m}$ refer here to the structural wavenumber and the structural modal wavenumber for each mode (n, m) , respectively, where, k_B depends on the material properties of the plate and varies continuously with the frequency,

$$k_B^2 = \omega \sqrt{\frac{\rho_s h}{B}},$$

while $k_{n,m}$ is fixed through relation (5.55). The critical frequency is defined when the structural wavenumber k_B of a traveling bending wave in the plate is equal to the acoustic wavenumber k_A in the ambient air. In other words, when the phase velocity of structural bending waves c_p equals the speed of sound c_0 , the critical frequency is defined [88]. Thus, the critical frequency is given by

$$\omega_c = c_0 k_B = c_0 \sqrt{\frac{\rho_s h}{B}}.$$

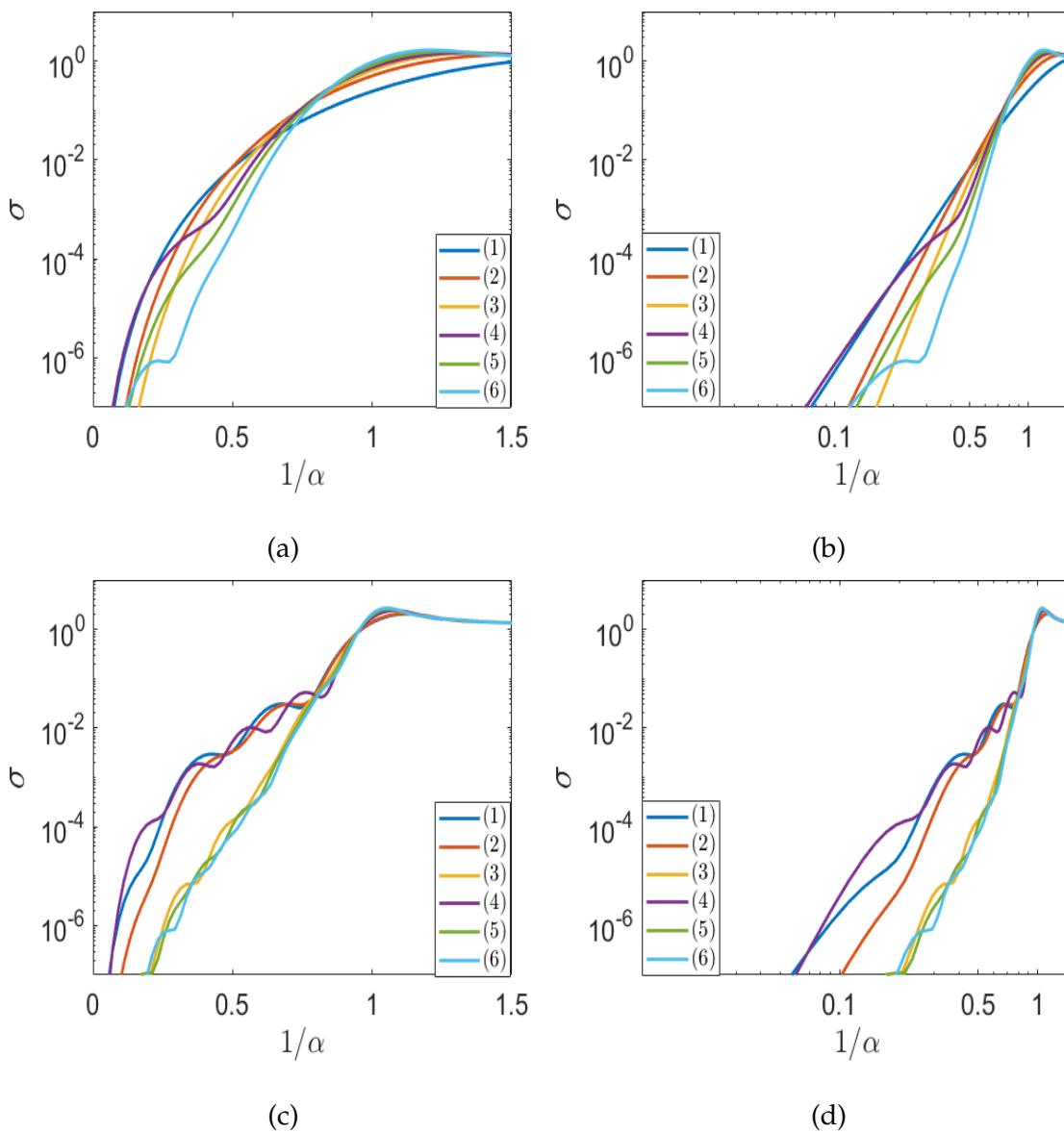


Figure 5.6: Modal radiation efficiencies σ_{nm} of guided plates for the mode order 1: (1,1), 2: (1,2), 3: (1,3), 4: (2,2), 5: (2,3), 6: (3,3) (a) in a linear-log scale and (b) in a log-log scale; and for mode order 1: (8,8), 2: (1,7), 3: (1,10), 4: (2,7), 5: (7,7), 6: (9,9) (c) in a linear-log scale and (d) in a log-log scale.

An analytical solution for \hat{W}_{nm} has been provided by Wallace [43] for simply supported rectangular plates by substituting Eq. (5.55) into Eq. (5.52), and is given by

$$\hat{W}_{nm}(\mathbf{p}_s) = \frac{nm\pi^2 A_{nm}}{L_x L_y} \frac{[(-1)^n e^{-iL_x k p_x} - 1] [(-1)^m e^{-iL_y k p_y} - 1]}{\left[(n\pi/L_x)^2 - k^2 p_x^2\right] \left[(m\pi/L_y)^2 - k^2 p_y^2\right]}. \quad (5.57)$$

The derivation of Eq. (5.57) is given in Appendix B. Substituting Eq. (5.57) into Eq. (5.53) gives the total power radiated by a single eigenmode for simply supported plates.

In the case of a rectangular plate with guided boundary conditions and having the same dimensions (length L_y and width L_x), the mode shape function is a product of cosine functions along the x and y directions and given by Eq. (2.4) (see Chapter 2). Thus

$$w_{nm}(x, y) = A_{nm} \cos\left(\frac{n\pi x}{L_x}\right) \cos\left(\frac{m\pi y}{L_y}\right), \quad (5.58)$$

where $n, m = 0, 1, 2, \dots$, $k_x = n\pi/L_x$, $k_y = m\pi/L_y$ and $k_{n,m} = \sqrt{k_x^2 + k_y^2}$. As for the simply supported plate, the corresponding modal natural frequency is given by Eq. (5.56). In the same way, substituting Eq. (5.58) into Eq. (5.52) results in the Fourier transformation of the velocity distribution \hat{W}_{nm} given by

$$\hat{W}_{nm}(\mathbf{p}_s) = k^2 p_x p_y A_{nm} \frac{[(-1)^n e^{-iL_x k p_x} - 1] [(-1)^m e^{-iL_y k p_y} - 1]}{\left[(n\pi/L_x)^2 - k^2 p_x^2\right] \left[(m\pi/L_y)^2 - k^2 p_y^2\right]}. \quad (5.59)$$

Substituting Eq. (5.59) into Eq. (5.53) gives the total power radiated by a single eigenmode for plates with guided boundary conditions. It is evident from

Eq. (5.57) and Eq. (5.59) that the main difference between W_{nm} for the simply supported plates and the guided plates is a prefactor.

The modal radiation efficiency σ_{nm} in Eq. (5.54) for a plate with simply supported or guided boundary conditions can be expressed as

$$\sigma_{nm} = \frac{\Pi^{nm}}{\rho_0 c_0 \mathcal{A} \langle \bar{w}_{nm}^2 \rangle}, \quad (5.60)$$

where the spatially averaged mean-square normal velocity of the plate $\langle \bar{w}_{nm}^2 \rangle$ is given by [40, 43, 175]

$$\langle \bar{w}_{nm}^2 \rangle = \begin{cases} \frac{|A_{nm}|^2}{2} & \text{for } n = 0 \text{ and } m = 0 \\ \frac{|A_{nm}|^2}{4} & \text{for } n = 0 \text{ or } m = 0 \\ \frac{|A_{nm}|^2}{8} & \text{for } n \neq 0 \text{ and } m \neq 0. \end{cases}$$

It is clear from Eq. (5.53) that the radiated power is directly proportional to $|\hat{W}_{nm}|^2$. If we compare Eq. (5.59) to Eq. (5.57), we notice that the guided plate produces lower sound radiation than the plainly supported plate, because if $\alpha = k_{n,m}/k > 1$, $|k_x k_y|^2 < |k_x k_y|^2$, where $k_{n,m}^2 = k_x^2 + k_y^2$ and $k_x = n\pi/L_x$ and $k_y = m\pi/L_y$. These results will also be seen later in the numerical calculation.

The results of the modal approach discussed in this section, together with the results of the diffusive field method developed in the previous section, will be presented and compared in the next section.

5.6 Comparison of the methods

This section is intended to compare the various methods of the radiation efficiency calculation of plates set in an infinite baffle. In order to obtain the radiation efficiency of the plates, the methods mentioned in Sec. 5.4 and in Sec. 5.5 are evaluated numerically. Before discussing the results, we need to highlight that radiation efficiency depends on acoustic and vibrational wavenumber, i.e. $\sigma(k, k_B)$ and modal radiation efficiency σ_{nm} is a function of $(k, k_{n,m})$. To distinguish between radiation efficiency assuming diffuse field method or modal approach, denote $\sigma_D(k, k_B)$ for radiation efficiency assuming diffuse field.

In order to make comparisons, we first calculate modal radiation efficiencies σ_{nm} , Eq. (5.60), of plates with simply supported and guided boundary conditions for a subset of modes (n, m) . We then evaluate Eq. (5.24) by a straightforward numerical integration assuming a diffusive field excitation at values of k_B corresponds to $k_{n,m}$ for the same modes order (n, m) , i.e. $\sigma_D(k, k_B = k_{n,m})$. The results for modal radiation efficiency, which will be seen later in the section, oscillate below the critical frequency and are therefore difficult to compare with the radiation efficiency of the diffuse field with the values of k_B correspond to the same $k_{n,m}$, hence the average radiation efficiency must be taken into account. Then in each case the average radiation efficiency of the possible structural wavenumber is calculated, and the average radiation efficiency for modal response can be defined

as a summation over all modes that contribute

$$\sigma = \frac{1}{N} \sum_{m=1}^N \sum_{n=1}^N \sigma_{nm}. \quad (5.61)$$

On the basis of the considered boundary conditions n and m start from either 0 or 1. Note that in practice $\sum_{n,m}$ is limited to a subset or a window of (n, m) 's. The average radiation efficiency assuming diffuse field can then be calculated using

$$\sigma = \frac{1}{N} \sum_{m=1}^N \sum_{n=1}^N \sigma_D(k, k_B = k_{n,m}). \quad (5.62)$$

In these numerical illustrations, we will always consider rectangular plates. Although the purposed methods in this chapter have been tested for rectangular plates, the underlying calculation applies to plates of arbitrary shape.

Figure 5.5 presents the results for several modes for a simply supported plate, some of which were also given by Wallace [43]. Results for modes (n, m) of the same order are shown in Fig. 5.6 for the guided plate, some of which were also provided by Gompert [44, 191]. In addition, the results for a plate assuming diffusive field excitation at values of k_B correspond to $k_{n,m}$ for the same modes order (n, m) , $\sigma_D(k, k_B = k_{n,m})$, are shown in Fig. 5.7. The results demonstrate that, as the frequency increases, the radiation efficiency increases and then converges to unity above a maximum peak at $k = k_{n,m}$. For a given mode order, the guided plate is shown to have a lower radiation efficiency than those of simply supported plates and plates with diffusive field excitation. For all three cases, however, similar radiation efficiency is obtained at and above the modal critical frequency. It can also be seen from Fig. 5.5, Fig. 5.6 and Fig. 5.7 that the radiation efficiency

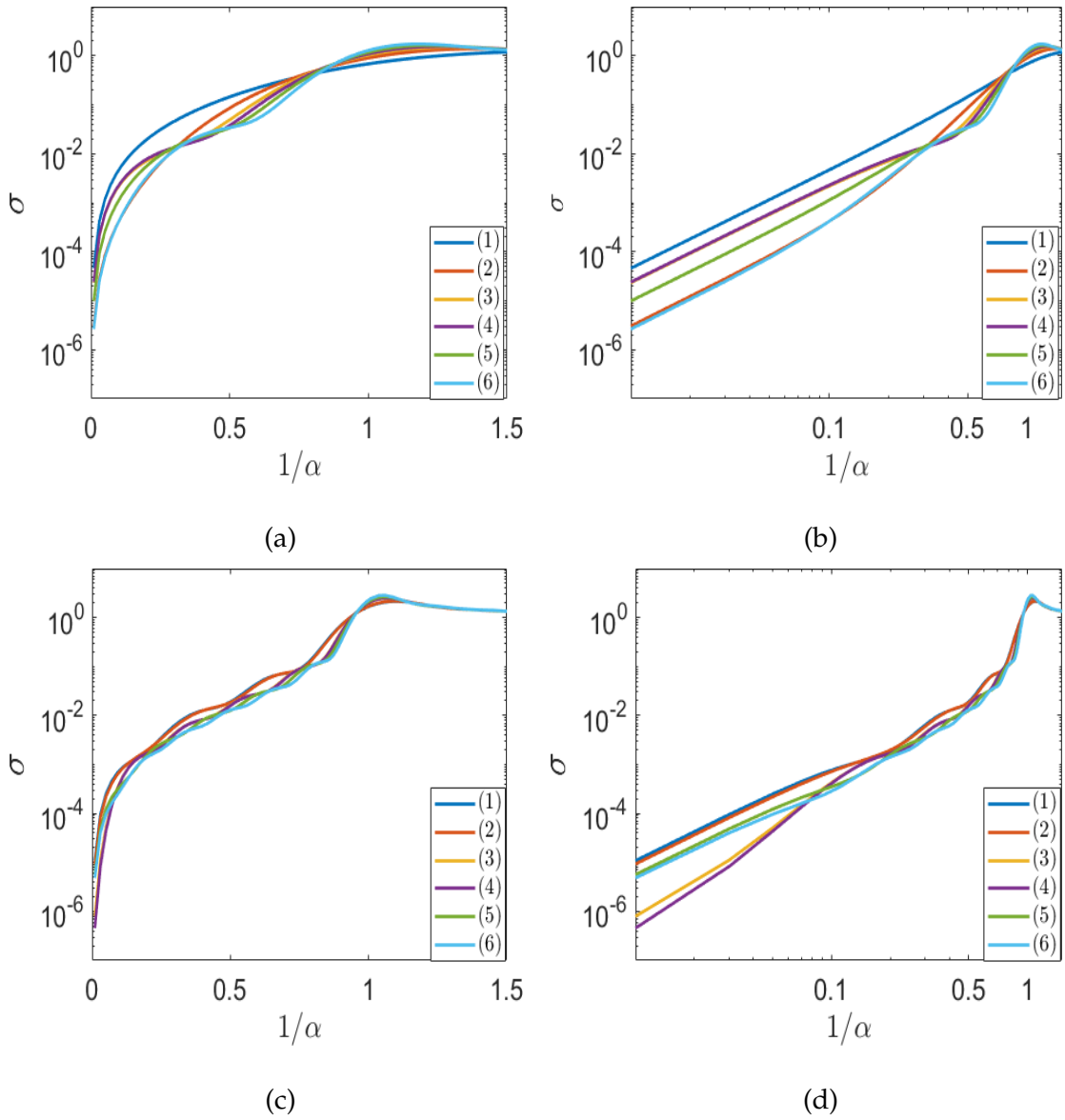


Figure 5.7: Radiation efficiencies of plates (2×2 m plate) assuming diffuse-field excitation, $\sigma_D(k, k_B = k_{n,m})$, without adding boundary corrections obtained by numerical calculation of Eq. (5.24) at values of k_B corresponding to different modes 1: $k_B = k_{n,m} = k_{1,1}$, 2: $k_B = k_{1,2}$, 3: $k_B = k_{1,3}$, 4: $k_B = k_{2,2}$, 5: $k_B = k_{2,3}$, 6: $k_B = k_{3,3}$ (a) in a linear-log scale and (b) in a log-log scale; and for values of k_B corresponding to 1: $k_B = k_{8,8}$, 2: $k_B = k_{1,7}$, 3: $k_B = k_{1,10}$, 4: $k_B = k_{2,7}$, 5: $k_B = k_{7,7}$, 6: $k_B = k_{9,9}$ (c) in a linear-log scale and (d) in a log-log scale.

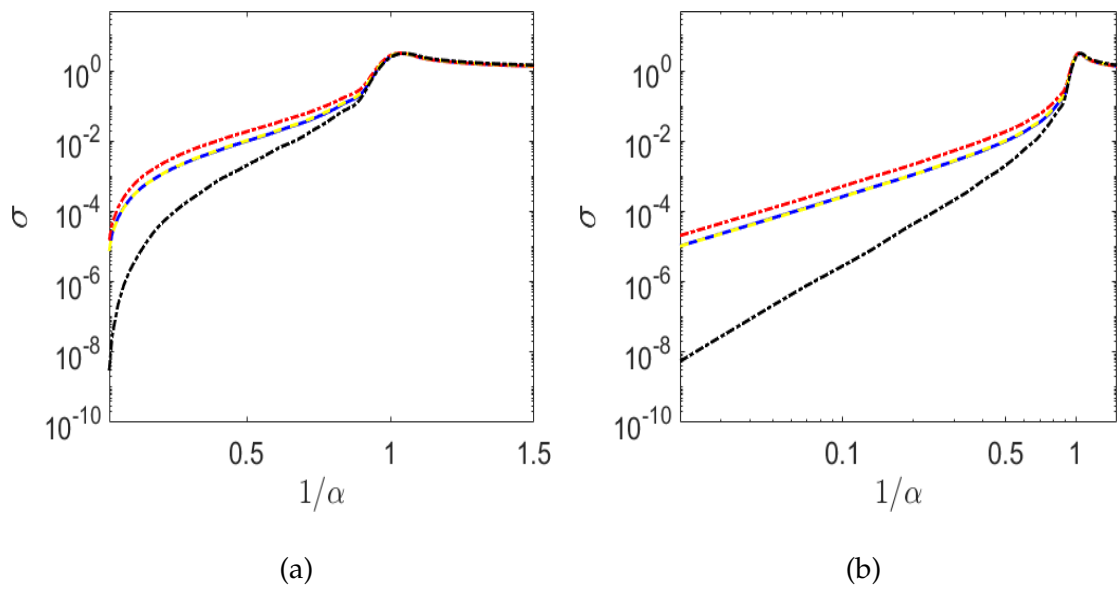


Figure 5.8: Average radiation efficiencies of plates. (a) Linear-log scale plot for plates assuming diffuse field excitation (—) using Eq. (5.62), simply supported plates (.-) using Eq. (5.61), guided plates (.-) using Eq. (5.61), and the mean value of average radiation efficiency of simply supported and guided plates (—); (b) log-log scale plot.

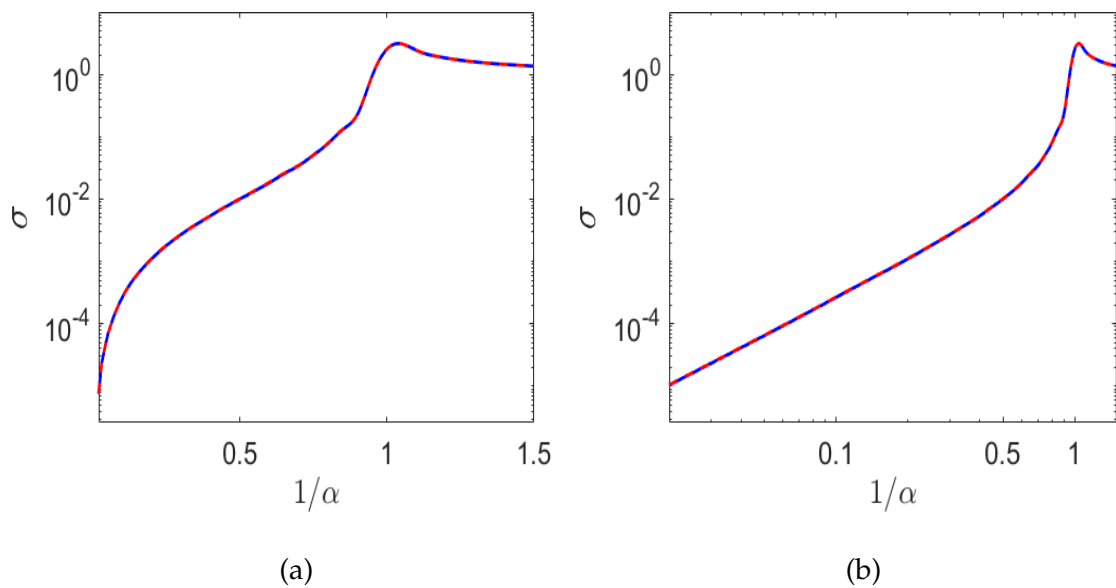


Figure 5.9: A comparison between the average radiation efficiency using the spatial space approach Eq. (5.24) shown in (— —) or the momentum space approach Eq. (5.27) (—) of a baffled rectangular plate assuming diffusive field excitation (a) Linear-log scale; log-log scale plot.

below the critical frequency predominated by low order modes, i.e. increasing modes order results in significantly smaller radiation efficiency and sharper transitions from below to above the critical frequency.

Similar results are found for the average radiation efficiency for all three cases, as shown in Fig. 5.8. Figure 5.8 also shows that the mean value of the average radiation efficiency of simply supported plates and the average radiation efficiency of guided plates gives the average radiation efficiency of plates assuming diffusive field excitation.

The main focus now and on words is on the calculation of the radiation effi-

ciency of the diffuse field.

It can also be shown that the same results for radiation efficiency using the spatial domain approach Eq. (5.24) are achieved using the momentum domain approach Eq. (5.27), given in Fig. 5.9. In order to obtain a result with reasonable precision, the spatial domain method requires a higher resolution of integration segments, which significantly increases the calculation time. In addition, for higher modes that are important at high frequencies, a finer resolution is required to provide good precision.

We account for boundary conditions using a single image correction as given in Eq. (4.10) based on the distance from the nearest straight edge. An exact treatment of boundary conditions for rectangular plates (or in general plate with corners) would need to include higher-order corrections in the form of "images of images", as shown in Eq. (4.11) and Fig. 4.3, but these are found not to affect the result significantly in the wavelength range treated. The numerical evaluation of Eq. (5.24) is compared to an average of modal radiation efficiencies for considered boundary conditions in Fig. 5.10.

The results of the numerical calculations of these methods are shown in Fig. 5.10 as a function of the wavenumber ratio $1/\alpha = k_A/k_B$. We note that the averaged modal calculation agrees well with the diffuse field model.

We find that the radiation efficiency for the Dirichlet case is greater than for the Neumann case below the critical frequency ($\alpha > 1$). Given that acoustic radiation above $\alpha = 1$ comes mainly from the boundaries of a plate, one might

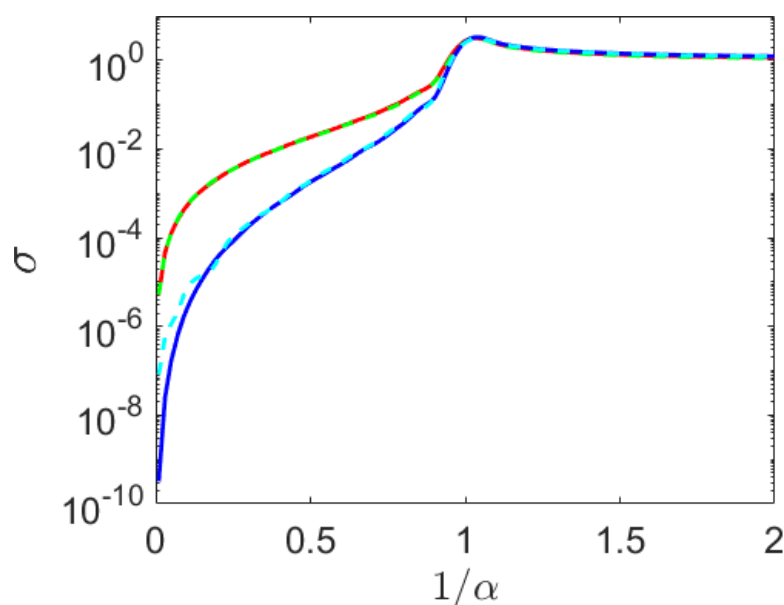


Figure 5.10: Average radiation efficiency of a baffled rectangular plate under different boundary conditions and assuming different excitation. Assuming diffusive field excitation with Dbc (—) or Nbc consideration (—) and assuming eigenmode excitation for simply supported plates (—), or guided plates (—).

have expected intuitively that the Neumann case with non-zero amplitude on the boundary becomes the more efficient radiator.

Since above the critical frequency $\alpha < 1$ the radiation efficiency is independent of the modal wave components, we will therefore restrict our focus to frequencies below the critical frequency $\alpha > 1$.

As stated above, radiation efficiency assuming diffusive field excitation including boundary contributions using either Eq(5.24) or Eq(5.27) is evaluated by numerical integration in this section and will be approximated analytically below the critical frequency later in the chapter.

In the next section, we give some insight into where the different contributions come from by looking at various approximations including a large- α asymptotics of the expression (5.24).

5.7 Boundary correction to radiated power: a local approximation

Maidanik [41] and Leppington et al. [194] have shown that below the critical frequency $\alpha > 1$, radiation from the modes of simply supported plates depends on the corners and edges of the plate. Therefore, for a diffusive field excitation, we also expect that the total power radiated from a finite plate also depends on edge and corner effects.

To better understand the relative strengths of radiation from Dirichlet and Neumann boundary conditions, we further approximate (5.10) or (5.20) in the following way. We have stated earlier that, for $\alpha > 1$, the integral in the total power radiated self-cancels unless \mathbf{x} and \mathbf{x}' are both close to the boundary (on the scale of the wavelengths). We have also shown in the previous chapter that, for rectangular plates in the case $\alpha > 1$, the acoustic disturbances of a finite plate are confined to a layer near its boundaries and decrease rapidly with distance away from the plate. In addition, we have shown in the previous section that the radiation efficiency is relatively small and increases as the frequency increases. Thus, for general boundary shapes, curvature effects are neglected at leading or-

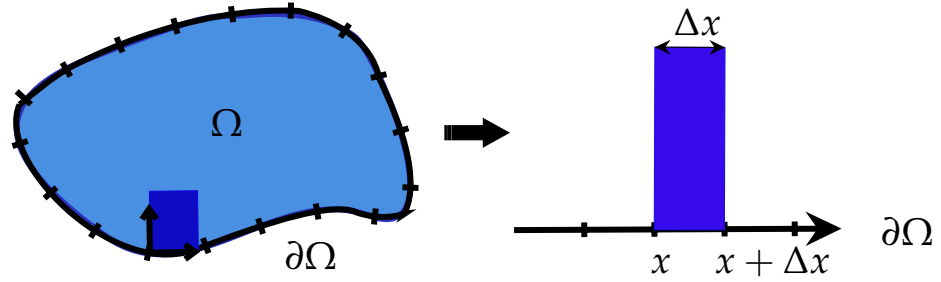


Figure 5.11: Parametrisation of the boundary of an arbitrary shaped plate per unit length.

der within this layer, see Fig. 5.2, and the integral in Eq. 5.20 can be locally approximated by an integration over an infinite half plane.

In order to isolate this edge calculation, consider the problem of a semi-infinite plate in the upper half plane (i.e. $\Omega = \{(x, y, z) : y > 0, -\infty < x < \infty, z = 0\}$) with edge at $y = 0$, adjoining a rigid baffle in the lower half plane ($y < 0, -\infty < x < \infty, z = 0$)) with normal velocity CF given by Eq. (5.28). Recall Eq. (5.10)

$$\Pi = \omega \rho_0 \int_{\Omega} \int_{\Omega} g(|\mathbf{x} - \mathbf{x}'|) \Gamma_{\Omega}(\mathbf{x}, \mathbf{x}') d\mathbf{x}' d\mathbf{x},$$

where g is defined by

$$g(|\mathbf{x} - \mathbf{x}'|) = \frac{\sin(k|\mathbf{x} - \mathbf{x}'|)}{4\pi|\mathbf{x} - \mathbf{x}'|} = \text{Im } G(\mathbf{x}, \mathbf{x}').$$

We now perform a change of variables as in Eq. (5.33), i.e. $(\mathbf{x}, \mathbf{x}') \rightarrow (\bar{\mathbf{x}}, \mathbf{s})$ and extend Ω for an infinite edge at $\bar{y} = 0$. The calculation of the radiated power from \bar{x} in a strip of width of Δx , see Fig. 5.11, is

$$\Pi(x, \Delta x) = \rho_0 c_0 k \int_x^{x+\Delta x} d\bar{x} \int_0^{\infty} d\bar{y} \int_{-\infty}^{\infty} ds_x \int_{-2\bar{y}}^{2\bar{y}} ds_y g(|\mathbf{s}|) \Gamma_{\Omega}(\bar{\mathbf{x}}, \mathbf{s}). \quad (5.63)$$

Denote the radiated power and radiation efficiency per unit length by Π_x and σ_x respectively. We can now write the radiated power per unit length Π_x in terms of the contribution of the radiated power from a strip of width Δx as

$$\Pi_x = \frac{\Pi(x, \Delta x)}{\Delta x} = \rho_0 c_0 k \int_0^\infty d\bar{y} \int_{-\infty}^\infty ds_x \int_{-2\bar{y}}^{2\bar{y}} ds_y g(|\mathbf{s}|) \Gamma_\Omega(\bar{\mathbf{x}}, \mathbf{s}). \quad (5.64)$$

Let's rewrite the normal surface velocity CF of the confined plate written in Eq. (5.28) in a semi-infinite plate approximation in terms of the normal surface velocity CF for an infinite strip of width Δx as follows

$$\Gamma_{\tilde{\Omega}}(\bar{\mathbf{x}}, \mathbf{s}) = \chi_{\Omega'}(\bar{\mathbf{x}}, s_y) \Gamma(\bar{\mathbf{x}}, \mathbf{s}), \quad (5.65)$$

where $\bar{\mathbf{x}}, \mathbf{s} \in \mathbb{R}^d$,

$$\tilde{\Omega} = \{(\bar{x}, \bar{y}, s_x, s_y) : \bar{x} \in [x, x + \Delta x], \bar{y} \in [0, \infty), s_x \in (-\infty, \infty), \text{ and } s_y \in [-2\bar{y}, 2\bar{y}]\},$$

$$\Omega' = \{(\bar{x}, \bar{y}, s_y) : \bar{x} \in [x, x + \Delta x], \bar{y} \in [0, \infty), \text{ and } s_y \in [-2\bar{y}, 2\bar{y}]\},$$

and $\chi_{\Omega'}$ denotes projection onto functions supported in Ω' . Thus

$$\Gamma_{\tilde{\Omega}}(\bar{\mathbf{x}}, \mathbf{s}) = \begin{cases} \Gamma(\bar{\mathbf{x}}, \mathbf{s}) & \text{if } \bar{\mathbf{x}}, s_y \in \Omega', \\ 0 & \text{otherwise.} \end{cases}$$

Now we can rewrite Eq. (5.64) as

$$\Pi_x = \frac{\rho_0 c_0 k}{\Delta x} \int_{\mathbb{R}^d} d\bar{\mathbf{x}} \int_{\mathbb{R}^d} d\mathbf{s} g(|\mathbf{s}|) \chi_{\Omega'}(\bar{\mathbf{x}}, s_y) \Gamma(\bar{\mathbf{x}}, \mathbf{s}), \quad (5.66)$$

where Γ is given by Eq. (5.29). Integrals in Eq. (5.66) can be further reduced as follows.

$$\begin{aligned}
\Pi_x &= \frac{\rho_0 c_0 k}{\Delta x} \int_{\mathbb{R}^d} d\bar{\mathbf{x}} \int_{\mathbb{R}^d} d\mathbf{s} g(|\mathbf{s}|) \chi_{\Omega'}(\bar{\mathbf{x}}, s_y) [\Gamma_0(\bar{\mathbf{x}}, \mathbf{s}) \pm \Gamma_1(\bar{\mathbf{x}}, \mathbf{s})], \\
&= \frac{\rho_0 c_0 k}{\Delta x} \mathcal{F} \{g(|\mathbf{s}|) \chi_{\Omega'}(\bar{\mathbf{x}}, s_y) [\Gamma_0(\bar{\mathbf{x}}, \mathbf{s}) \pm \Gamma_1(\bar{\mathbf{x}}, \mathbf{s})]\} \Big|_{\mathbf{q}=\bar{\mathbf{p}}=0}, \\
&= \frac{\rho_0 c_0 k}{\Delta x} \left[\underbrace{H * G * \Gamma_0(\mathbf{q}, \bar{\mathbf{p}})}_{\tilde{A}} \pm \underbrace{H * G * \Gamma_1(\mathbf{q}, \bar{\mathbf{p}})}_{\tilde{B}} \right] \Big|_{\mathbf{q}=\bar{\mathbf{p}}=0} \quad (5.67)
\end{aligned}$$

where $*$ is convolution,

$$H(\mathbf{q}, \bar{\mathbf{p}}) = \mathcal{F} \{ \chi_{\Omega'}(\bar{\mathbf{x}}, s_y) \} = \frac{2\pi}{k} \delta(p_x) \hat{H}(\mathbf{q}, \bar{p}_y),$$

$$G(\mathbf{q}, \bar{\mathbf{p}}) = \mathcal{F} \{ g(|\mathbf{s}|) \} = \frac{1}{4\pi} \left(\frac{2\pi}{k} \right)^3 \delta(\mathbf{q}) \frac{1}{T(\bar{\mathbf{p}})},$$

and $\Gamma_0(\mathbf{q}, \bar{\mathbf{p}})$ and $\Gamma_1(\mathbf{q}, \bar{\mathbf{p}})$ defined in Eq. (5.35) and Eq. (5.37) respectively. For convenience, we first solve \tilde{A}

$$\begin{aligned}
\tilde{A} &= \left(\frac{2\pi}{k} \right)^{-8} \int_{\mathbb{R}^8} d\mathbf{q}' d\mathbf{q}'' d\mathbf{p}' d\mathbf{p}'' H(\mathbf{q} - \mathbf{q}' - \mathbf{q}'', \bar{\mathbf{p}} - \mathbf{p}' - \mathbf{p}'') G(\mathbf{q}', \mathbf{p}') \Gamma_0(\mathbf{q}'', \mathbf{p}''), \\
&= \frac{1}{4\pi^2} \int_{\mathbb{R}^8} d\mathbf{q}' d\mathbf{q}'' d\mathbf{p}' d\mathbf{p}'' \hat{H}(\mathbf{q} - \mathbf{q}' - \mathbf{q}'', \bar{p}_y - p'_y - p''_y) \delta(\bar{p}_x - p'_x - p''_x) \delta(\mathbf{q}') \\
&\quad \frac{1}{T(\mathbf{p}')} \delta(\mathbf{q}'') \delta(\mathbf{p}'^2 - \alpha^2), \\
&= \frac{1}{4\pi^2} \int_{\mathbb{R}^4} d\mathbf{p}' d\mathbf{p}'' \hat{H}(\mathbf{q}, \bar{p}_y - p'_y - p''_y) \delta(\bar{p}_x - p'_x - p''_x) \frac{1}{T(\mathbf{p}')} \delta(\mathbf{p}'^2 - \alpha^2), \\
&= \frac{1}{8\pi^2} \int_{|\mathbf{p}'| \leq 1} d\mathbf{p}' \int_0^{2\pi} d\theta \hat{H}(\mathbf{q}, \bar{p}_y - p'_y - \alpha \sin \theta) \delta(\bar{p}_x - p'_x - \alpha \cos \theta) \frac{1}{T(\mathbf{p}')}, \\
&= \frac{1}{8\pi^2} \int_{|\mathbf{p}'| \leq 1} d\mathbf{p}' \frac{1}{T(\mathbf{p}') \sqrt{\alpha^2 - (\bar{p}_x - p'_x)^2}} \\
&\quad \left[\hat{H}(\mathbf{q}, \bar{p}_y - p'_y - \sqrt{\alpha^2 - (\bar{p}_x - p'_x)^2}) + \hat{H}(\mathbf{q}, \bar{p}_y - p'_y + \sqrt{\alpha^2 - (\bar{p}_x - p'_x)^2}) \right].
\end{aligned}$$

Therefore,

$$\tilde{A}\Big|_{\mathbf{q}=\bar{\mathbf{p}}=0} = \frac{1}{8\pi^2} \int_{|\mathbf{p}'|\leq 1} d\mathbf{p}' \frac{1}{T(\mathbf{p}')\sqrt{\alpha^2 - p_x'^2}} \left[\hat{H}(\mathbf{0}, -p_y' - \sqrt{\alpha^2 - p_x'^2}) + \hat{H}(\mathbf{0}, -p_y' + \sqrt{\alpha^2 - p_x'^2}) \right].$$

Now using Eq. (5.30) for \hat{H} we get

$$\begin{aligned} \hat{H}(\mathbf{0}, -p_y' - \sqrt{\alpha^2 - p_x'^2}) &= \Delta x \int_0^\infty d\bar{y} \int_{-2\bar{y}}^{2\bar{y}} ds_y e^{iks_y(p_y' + \sqrt{\alpha^2 - p_x'^2})}, \\ &= \Delta x \int_0^\infty d\bar{y} \frac{2 \sin(2\bar{y}k(p_y' + \sqrt{\alpha^2 - p_x'^2}))}{k(p_y' + \sqrt{\alpha^2 - p_x'^2})}, \\ &= \Delta x \int_0^\infty d\bar{y} \frac{\sin(\bar{y}k(p_y' + \sqrt{\alpha^2 - p_x'^2}))}{k(p_y' + \sqrt{\alpha^2 - p_x'^2})}, \\ &= \frac{\Delta x}{2ik(p_y' + \sqrt{\alpha^2 - p_x'^2})} \left[\frac{-1}{ik(p_y' + \sqrt{\alpha^2 - p_x'^2})} \right. \\ &\quad \left. - \frac{1}{ik(p_y' + \sqrt{\alpha^2 - p_x'^2})} \right], \\ &= \frac{\Delta x}{k^2} \frac{1}{(p_y' + \sqrt{\alpha^2 - p_x'^2})^2}. \end{aligned}$$

Similarly,

$$\hat{H}(\mathbf{0}, -p_y' + \sqrt{\alpha^2 - p_x'^2}) = \frac{\Delta x}{k^2} \frac{1}{(\sqrt{\alpha^2 - p_x'^2} - p_y')^2}.$$

Therefore,

$$\begin{aligned} \tilde{A}\Big|_{\mathbf{q}=\bar{\mathbf{p}}=0} &= \frac{\Delta x}{8\pi^2 k^2} \int_{|\mathbf{p}'|\leq 1} d\mathbf{p}' \frac{1}{T(\mathbf{p}')\sqrt{\alpha^2 - p_x'^2}} \\ &\quad \left[\frac{1}{(\sqrt{\alpha^2 - p_x'^2} + p_y')^2} + \frac{1}{(\sqrt{\alpha^2 - p_x'^2} - p_y')^2} \right], \\ &= \frac{\Delta x}{4\pi^2 k^2} \int_{|\mathbf{p}'|\leq 1} d\mathbf{p}' \frac{1}{T(\mathbf{p}')\sqrt{\alpha^2 - p_x'^2}} \frac{\alpha^2 - p_x'^2 + p_y'^2}{(\alpha^2 - \mathbf{p}')^2}. \end{aligned}$$

Now we can do the same procedure for \tilde{B}

$$\begin{aligned}
\tilde{B} &= \left(\frac{2\pi}{k}\right)^8 \int_{\mathbb{R}^8} d\mathbf{q}' d\mathbf{q}'' d\mathbf{p}' d\mathbf{p}'' H(\mathbf{q} - \mathbf{q}' - \mathbf{q}'', \bar{\mathbf{p}} - \mathbf{p}' - \mathbf{p}'') G(\mathbf{q}', \mathbf{p}') \Gamma_1(\mathbf{q}'', \mathbf{p}''), \\
&= \frac{1}{8\pi^2} \int_{\mathbb{R}^8} d\mathbf{q}' d\mathbf{q}'' d\mathbf{p}' d\mathbf{p}'' \hat{H}(\mathbf{q} - \mathbf{q}' - \mathbf{q}'', \bar{p}_y - p'_y - p''_y) \delta(\bar{p}_x - p'_x - p''_x) \delta(\mathbf{q}') \\
&\quad \frac{1}{T(\mathbf{p}')} \delta(q''_x) \delta(p''_y) \delta(p''_x{}^2 + \left(\frac{q''_y}{2}\right)^2 - \alpha^2), \\
&= \frac{1}{8\pi^2} \int_{\mathbb{R}^4} d\mathbf{p}' dp''_x dq''_y \hat{H}(q_x, q_y - q''_y, \bar{p}_y - p'_y) \delta(\bar{p}_x - p'_x - p''_x) \frac{1}{T(\mathbf{p}')} \\
&\quad \delta(p''_x{}^2 + \left(\frac{q''_y}{2}\right)^2 - \alpha^2), \\
&= \frac{1}{8\pi^2} \int_{|\mathbf{p}'| \leq 1} d\mathbf{p}' \int_0^{2\pi} d\theta \hat{H}(q_x, q_y - 2\alpha \sin \theta, \bar{p}_y - p'_y) \delta(\bar{p}_x - p'_x - \alpha \cos \theta) \frac{1}{T(\mathbf{p}')}, \\
&= \frac{1}{8\pi^2} \int_{|\mathbf{p}'| \leq 1} d\mathbf{p}' \frac{1}{T(\mathbf{p}') \sqrt{\alpha^2 - (\bar{p}_x - p'_x)^2}} \left[\hat{H}(q_x, q_y - 2\sqrt{\alpha^2 - (\bar{p}_x - p'_x)^2}, \bar{p}_y - p'_y) \right. \\
&\quad \left. + \hat{H}(q_x, q_y + 2\sqrt{\alpha^2 - (\bar{p}_x - p'_x)^2}, \bar{p}_y - p'_y) \right].
\end{aligned}$$

Thus

$$\begin{aligned}
\tilde{B} \Big|_{\mathbf{q}=\bar{\mathbf{p}}=0} &= \frac{1}{8\pi^2} \int_{|\mathbf{p}'| \leq 1} d\mathbf{p}' \frac{1}{T(\mathbf{p}') \sqrt{\alpha^2 - p_x'^2}} \\
&\quad \left[\hat{H}(0, -2\sqrt{\alpha^2 - p_x'^2}, -p'_y) + \hat{H}(0, 2\sqrt{\alpha^2 - p_x'^2}, -p'_y) \right].
\end{aligned}$$

Now using Eq. (5.30) for \hat{H} we get

$$\begin{aligned}
\hat{H}(0, 2\sqrt{\alpha^2 - p_x'^2}, -p_y') &= \Delta x \int_0^\infty d\bar{y} e^{2ik\bar{y}\sqrt{\alpha^2 - p_x'^2}} \int_{-2\bar{y}}^{2\bar{y}} ds_y e^{ikp_y' s_y}, \\
&= \Delta x \int_0^\infty d\bar{y} e^{2ik\bar{y}\sqrt{\alpha^2 - p_x'^2}} \frac{2 \sin(2kp_y'\bar{y})}{kp_y'}, \\
&= \frac{\Delta x}{kp_y'} \int_0^\infty d\bar{y} e^{ik\bar{y}\sqrt{\alpha^2 - p_x'^2}} \sin(kp_y'\bar{y}), \\
&= \frac{\Delta x}{2ikp_y'} \left[\frac{-1}{ik(\sqrt{\alpha^2 - p_x'^2} + p_y')} \right. \\
&\quad \left. + \frac{1}{ik(\sqrt{\alpha^2 - p_x'^2} - p_y')} \right], \\
&= \frac{\Delta x}{k^2} \frac{-1}{\alpha^2 - \mathbf{p}'^2}.
\end{aligned}$$

Similarly

$$\hat{H}(0, -2\sqrt{\alpha^2 - p_x'^2}, -p_y') = \frac{\Delta x}{k^2} \frac{-1}{\alpha^2 - \mathbf{p}'^2}.$$

Therefore,

$$\begin{aligned}
\tilde{B} \Big|_{\mathbf{q}=\mathbf{p}=0} &= \frac{\Delta x}{8\pi^2 k^2} \int_{|\mathbf{p}'| \leq 1} d\mathbf{p}' \frac{1}{T(\mathbf{p}')\sqrt{\alpha^2 - p_x'^2}} \\
&\quad \left[\frac{-1}{\alpha^2 - \mathbf{p}'^2} + \frac{-1}{\alpha^2 - \mathbf{p}'^2} \right], \\
&= \frac{-\Delta x}{4\pi^2 k^2} \int_{|\mathbf{p}'| \leq 1} d\mathbf{p}' \frac{1}{T(\mathbf{p}')\sqrt{\alpha^2 - p_x'^2}} \frac{1}{\alpha^2 - \mathbf{p}'^2}.
\end{aligned}$$

Therefore after substituting \tilde{A} and \tilde{B} back to Π_x in Eq. (5.67) we get

$$\begin{aligned}
\Pi_x &= \frac{\rho_0 c_0}{4k\pi^2} \int_{|\mathbf{p}'| \leq 1} d\mathbf{p}' \frac{1}{T(\mathbf{p}')\sqrt{\alpha^2 - p_x'^2}} \\
&\quad \left[\frac{\alpha^2 - p_x'^2 + p_y'^2}{(\alpha^2 - \mathbf{p}'^2)^2} \mp \frac{1}{\alpha^2 - \mathbf{p}'^2} \right].
\end{aligned}$$

This implies

$$\Pi_x = \frac{\rho_0 c_0}{2\pi^2 k} \int_{|\mathbf{p}'| \leq 1} d\mathbf{p}' \frac{1}{T(\mathbf{p}') \sqrt{\alpha^2 - p_x'^2}} \begin{cases} \frac{\alpha^2 - p_x'^2}{(\alpha^2 - \mathbf{p}'^2)^2} & \text{Dbc} \\ \frac{p_y'^2}{(\alpha^2 - \mathbf{p}'^2)^2} & \text{Nbc} \end{cases} \quad (5.68)$$

Therefore, the total power radiated of a semi-infinite plate per unit length can be written as

$$\Pi_x = \frac{\rho_0 c_0}{2\pi^2 k} f(\alpha) \quad (5.69)$$

where

$$f(\alpha) = \int_0^{2\pi} d\phi \int_0^1 dp_r \frac{p_r}{\sqrt{1 - p_r^2} \sqrt{\alpha^2 - p_r^2 \cos^2 \phi}} \begin{cases} \frac{\alpha^2 - p_r^2 \cos^2 \phi}{(\alpha^2 - p_r^2)^2} & \text{Dbc} \\ \frac{p_r^2 \sin^2 \phi}{(\alpha^2 - p_r^2)^2} & \text{Nbc} \end{cases} \quad (5.70)$$

Recall Eq. (5.27) for the radiation efficiency per unit length

$$\sigma_x = \frac{\Pi_x}{\Pi_0} = \frac{\Pi_x}{\frac{1}{2} \mathcal{A} \rho_0 c_0}. \quad (5.71)$$

Substituting Eq. (5.69) into Eq. (5.71) leads us to an approximation of radiation efficiency of the form

$$\begin{aligned} \sigma &= \int_{\partial\Omega} \sigma_x dx \simeq \frac{\int_{\partial\Omega} dx}{\mathcal{A}} \times \text{integrals independent of geometry} \\ &= \frac{\ell}{k\pi^2 \mathcal{A}} f(\alpha), \end{aligned} \quad (5.72)$$

where ℓ is the length of boundary of geometry. Note that the geometry of the plate enters this expression via its dependency on \mathcal{A} and ℓ alone, the boundary conditions have an effect on $f(\alpha)$ only.

An alternative way of approximating (5.10), which is obtained by approximating (5.20) for a semi-infinite plate, is discussed in the next section.

5.7.1 Local approximation of boundary contribution: momentum space approach

The momentum domain approach is an alternative way of approximating total radiated power for a semi-infinite plate. In this section we use it to provide a second derivation of Eq.s (5.69), (5.71) and (5.72).

Recall Eq. (5.20) for the total radiated power in momentum space,

$$\Pi = \frac{\rho_0 c_0 k^2}{8\pi^2} \int_{\Omega_r} \frac{\Gamma_{\Omega}(\mathbf{p}, \mathbf{p})}{T(\mathbf{p})} d\mathbf{p}.$$

The momentum representation of the CF, $\Gamma_{\Omega}(\mathbf{p}, \mathbf{p})$, in Eq. (5.44) for a semi-infinite plate with an edge at $y = 0$, where $\Omega = \{(x, y, z) : y > 0, -\infty < x < \infty, z = 0\}$, for a strip of width Δx can be expressed as

$$\Gamma_{\tilde{\Omega}}(\mathbf{p}, \mathbf{p}) = A(\mathbf{p}, \mathbf{p}) \mp B'(\mathbf{p}, \mathbf{p}), \quad (5.73)$$

for Nbc/Dbc (+/-) respectively, $A(\mathbf{p}, \mathbf{p})$ and $B'(\mathbf{p}, \mathbf{p})$ on an infinite strip domain $\tilde{\Omega}$, as shown in Fig. 5.11, are given by Eq. (5.45) and Eq. (5.46) respectively, where

$$\tilde{\Omega} = \{(\bar{x}, \bar{y}, s_x, s_y) : \bar{x} \in [x, x + \Delta x], \bar{y} \in [0, \infty), s_x \in (-\infty, \infty), \text{ and } s_y \in [-2\bar{y}, 2\bar{y}]\}.$$

Thus, from Eq. (5.45) we get

$$A(\mathbf{p}, \mathbf{p}) = \frac{1}{2\pi} \int_0^{2\pi} d\theta \int_x^{x+\Delta x} d\bar{x} \int_0^{\infty} d\bar{y} \int_{-\infty}^{\infty} ds_x \int_{-2\bar{y}}^{2\bar{y}} ds_y e^{-ik(\mathbf{p}-\mathbf{p}_\alpha) \cdot \mathbf{s}}, \quad (5.74)$$

and from Eq. (5.46) we get

$$B'(\mathbf{p}, \mathbf{p}) = \frac{-1}{2\pi} \int_0^{2\pi} d\theta \int_x^{x+\Delta x} d\bar{x} \int_0^{\infty} d\bar{y} e^{2ik\alpha\bar{y}\sin\theta} \int_{-\infty}^{\infty} ds_x \times \int_{-2\bar{y}}^{2\bar{y}} ds_y e^{-ik[(p_x - \alpha \cos\theta)s_x + p_y s_y]}. \quad (5.75)$$

The total radiated power per unit length Π_x can then be obtained from

$$\Pi_x = \frac{\rho_0 c_0 k^2}{8\pi^2 \Delta x} \int_{\Omega_r} \frac{\Gamma_{\tilde{\Omega}}(\mathbf{p}, \mathbf{p})}{T(\mathbf{p})} d\mathbf{p}. \quad (5.76)$$

The integrals in Eq. (5.74) and Eq. (5.75) can be further reduced as follows. Rearranging Eq. (5.74) yields

$$\begin{aligned} A(\mathbf{p}, \mathbf{p}) &= \frac{\Delta x}{2\pi} \int_0^{2\pi} d\theta \int_0^\infty d\bar{y} \int_{-\infty}^\infty ds_x e^{-ik(p_x - \alpha \cos \theta)s_x} \int_{-2\bar{y}}^{2\bar{y}} ds_y e^{-ik(p_y - \alpha \sin \theta)s_y}, \\ &= \frac{\Delta x}{k} \int_0^{2\pi} d\theta \delta(p_x - \alpha \cos \theta) \int_0^\infty d\bar{y} \frac{2 \sin(2k\bar{y}(p_y - \alpha \sin \theta))}{k(p_y - \alpha \sin \theta)}, \\ &= \frac{\Delta x}{k^2} \int_0^{2\pi} d\theta \frac{\delta(p_x - \alpha \cos \theta)}{p_y - \alpha \sin \theta} \underbrace{\int_0^\infty d\bar{y} e^{-a\bar{y}} \sin(k\bar{y}(p_y - \alpha \sin \theta))}_{\text{Laplace transformation } \mathcal{L}} \Big|_{a=0} \end{aligned}$$

As we concentrate on below the critical frequency, i.e. $\alpha > 1$, and the radiation circle corresponds to $|\mathbf{p}|^2 < 1$ and thus $\mathbf{p}^2 \neq \alpha^2$. Therefore, using the fact that, for $b \neq 0$

$$\mathcal{L} \{ \sin(bx) \} (a) \Big|_{a=0} = \frac{b}{a^2 + b^2} \Big|_{a=0} = \frac{1}{b}.$$

We further simplify the integrand as

$$A(\mathbf{p}, \mathbf{p}) = \frac{\Delta x}{k^2} \int_0^{2\pi} d\theta \frac{\delta(p_x - \alpha \cos \theta)}{p_y - \alpha \sin \theta} \frac{1}{k(p_y - \alpha \sin \theta)}$$

Now using the fact that

$$\alpha \sin \theta = \pm \sqrt{\alpha^2 - \alpha^2 \cos^2 \theta},$$

we arrive at

$$\begin{aligned}
 A(\mathbf{p}, \mathbf{p}) &= \frac{\Delta x}{k^3 \sqrt{\alpha^2 - p_x^2}} \frac{1}{\left(p_y - \sqrt{\alpha^2 - p_x^2}\right)^2} + \frac{1}{\left(p_y + \sqrt{\alpha^2 - p_x^2}\right)^2}, \\
 &= \frac{2 \Delta x}{k^3 \sqrt{\alpha^2 - p_x^2}} \frac{p_y^2 + \alpha^2 - p_x^2}{\left(p_y^2 - \alpha^2 + p_x^2\right)^2}, \\
 &= \frac{2 \Delta x}{k^3 \sqrt{\alpha^2 - p_x^2}} \frac{p_y^2 - p_x^2 + \alpha^2}{\left(\alpha^2 - \mathbf{p}^2\right)^2}. \tag{5.77}
 \end{aligned}$$

A similar procedure can be applied for $B'(\mathbf{p}, \mathbf{p})$. Rearranging Eq. (5.75) yields

$$\begin{aligned}
 B'(\mathbf{p}, \mathbf{p}) &= \frac{-\Delta x}{2\pi} \int_0^{2\pi} d\theta \int_0^\infty d\bar{y} e^{2ik\alpha\bar{y}\sin\theta} \int_{-\infty}^\infty ds_x e^{-ik(p_x - \alpha \cos\theta)s_x} \int_{-2\bar{y}}^{2\bar{y}} ds_y e^{-ikp_y s_y}, \\
 &= \frac{-\Delta x}{k} \int_0^{2\pi} d\theta \delta(p_x - \alpha \cos\theta) \int_0^\infty d\bar{y} e^{2ik\alpha\bar{y}\sin\theta} \int_{-2\bar{y}}^{2\bar{y}} ds_y e^{-ikp_y s_y}, \\
 &= \frac{-\Delta x}{k} \int_0^{2\pi} d\theta \delta(p_x - \alpha \cos\theta) \int_0^\infty d\bar{y} e^{2ik\alpha\bar{y}\sin\theta} \frac{2 \sin(2kp_y\bar{y})}{kp_y}, \\
 &= \frac{-\Delta x}{k^2} \int_0^{2\pi} d\theta \frac{\delta(p_x - \alpha \cos\theta)}{p_y} \int_0^\infty d\bar{y} e^{ik\alpha\bar{y}\sin\theta} \sin(kp_y\bar{y}), \\
 &= \frac{-\Delta x}{2ik^2} \int_0^{2\pi} d\theta \frac{\delta(p_x - \alpha \cos\theta)}{p_y} \int_0^\infty d\bar{y} \left[e^{ik\bar{y}(\alpha \sin\theta + p_y)} - e^{ik\bar{y}(\alpha \sin\theta - p_y)} \right],
 \end{aligned}$$

Again in the case $\mathbf{p}^2 \neq \alpha^2$ we obtain

$$\begin{aligned}
 B'(\mathbf{p}, \mathbf{p}) &= \frac{-\Delta x}{2ik^2} \int_0^{2\pi} d\theta \frac{\delta(p_x - \alpha \cos\theta)}{p_y} \left\{ \frac{1}{-ik(\alpha \sin\theta + p_y)} + \frac{1}{ik(\alpha \sin\theta - p_y)} \right\}, \\
 &= \frac{-\Delta x}{2k^3} \int_0^{2\pi} d\theta \frac{\delta(p_x - \alpha \cos\theta)}{p_y} \left\{ \frac{1}{\alpha \sin\theta + p_y} - \frac{1}{\alpha \sin\theta - p_y} \right\}, \\
 &= \frac{-\Delta x}{2k^3} \int_0^{2\pi} d\theta \frac{\delta(p_x - \alpha \cos\theta)}{p_y} \frac{-2p_y}{\alpha^2 \sin^2\theta - p_y^2},
 \end{aligned}$$

using the fact that

$$\alpha \sin\theta = \pm \sqrt{\alpha^2 - \alpha^2 \cos^2\theta}.$$

We simplify the above integral as

$$\begin{aligned} B'(\mathbf{p}, \mathbf{p}) &= \frac{2 \Delta x}{k^3 \sqrt{\alpha^2 - p_x^2}} \frac{1}{\alpha^2 - p_x^2 - p_y^2}, \\ &= \frac{2 \Delta x}{k^3 \sqrt{\alpha^2 - p_x^2}} \frac{1}{\alpha^2 - \mathbf{p}^2}. \end{aligned} \quad (5.78)$$

It is clear from Eq. (5.78) that in the case where structural waves propagate faster than acoustic waves $\alpha^2 > \mathbf{p}^2$, B' is a positive quantity. Therefore, in the case of $\mathbf{p}^2 \neq \alpha^2$, substituting Eq. (5.77) and Eq. (5.78) into Eq. (5.73) yields

$$\Gamma_{\tilde{\Omega}}(\mathbf{p}, \mathbf{p}) = \frac{2 \Delta x}{k^3 \sqrt{\alpha^2 - p_x^2}} \left[\frac{p_y^2 - p_x^2 + \alpha^2}{(\alpha^2 - \mathbf{p}^2)^2} \mp \frac{1}{\alpha^2 - \mathbf{p}^2} \right],$$

where "+" corresponds to Dbc and "-" corresponds to Nbc. This results shows that the amplitude of CF for Dirichlet case is greater than for the Neumann case. This leads to increased radiation power and thus increased radiation efficacy for Dbc. We can rewrite this in the form

$$\Gamma_{\tilde{\Omega}}(\mathbf{p}, \mathbf{p}) = \frac{2 \Delta x}{k^3 \sqrt{\alpha^2 - p_x^2}} \begin{cases} \frac{p_y^2 - p_x^2 + \alpha^2 + \alpha^2 - \mathbf{p}^2}{(\alpha^2 - \mathbf{p}^2)^2} & \text{Dbc,} \\ \frac{p_y^2 - p_x^2 + \alpha^2 - \alpha^2 + \mathbf{p}^2}{(\alpha^2 - \mathbf{p}^2)^2} & \text{Nbc,} \end{cases} \quad (5.79)$$

$$= \frac{2 \Delta x}{k^3 \sqrt{\alpha^2 - p_x^2}} \begin{cases} \frac{2\alpha^2 - 2p_x^2}{(\alpha^2 - \mathbf{p}^2)^2} & \text{Dbc,} \\ \frac{2p_y^2}{(\alpha^2 - \mathbf{p}^2)^2} & \text{Nbc,} \end{cases} \quad (5.80)$$

Thus, substituting $\Gamma_{\tilde{\Omega}}$ into Eq. (5.76) yields

$$\begin{aligned} \Pi_x &= \frac{\rho_0 c_0 k^2}{8\pi^2 \Delta x} \int_{\Omega_r} \frac{\Gamma_{\tilde{\Omega}}(\mathbf{p}, \mathbf{p})}{T(\mathbf{p})} d\mathbf{p}, \\ &= \frac{\rho_0 c_0}{2\pi^2 k} \int_0^{2\pi} d\phi \int_0^1 dp_r \frac{p_r}{\sqrt{1-p_r^2} \sqrt{\alpha^2 - p_r^2 \cos^2 \phi}} \begin{cases} \frac{\alpha^2 - p_r^2 \cos^2 \phi}{(\alpha^2 - p_r^2)^2} & \text{Dbc,} \\ \frac{p_r^2 \sin^2 \phi}{(\alpha^2 - p_r^2)^2} & \text{Nbc.} \end{cases} \end{aligned} \quad (5.81)$$

Equation (5.81) is the same as the Eq. (5.68). We have therefore shown that the spatial approach and the momentum approach give the same radiation efficiency outcome.

Furthermore, in the particular case of a rectangular plate, perhaps surprisingly, below the critical frequency, we find that the radiation efficiency contribution from corner approximation is zero when considering either Dirichlet or Neumann boundary conditions (see Appendix D.1 for the derivation).

In the next section, we approximate Eq. (5.68) in the limit $\alpha \rightarrow \infty$.

5.7.2 Asymptotic Approximation: the large α asymptotics

We further approximate Eq. (5.69) in the high frequency regime to better understand the relative strengths of radiation from Dirichlet and Neumann boundary

conditions. The function $f(\alpha)$ in Eq. (5.70) becomes in the limit $\alpha \rightarrow \infty$

$$f(\alpha) \simeq \int_0^{2\pi} d\phi \int_0^1 dp_r \frac{p_r}{\alpha \sqrt{1-p_r^2}} \begin{cases} \frac{\alpha^2}{\alpha^4} & \text{Dbc,} \\ \frac{p_r^2 \sin^2 \phi}{\alpha^4} & \text{Nbc,} \end{cases}$$

$$= 2\pi \int_0^1 dp_r \frac{p_r}{\alpha^5 \sqrt{1-p_r^2}} \begin{cases} \alpha^2 & \text{Dbc,} \\ \frac{1}{2} p_r^2 & \text{Nbc.} \end{cases}$$

Making use of the following results

$$\int_0^1 dp_r \frac{p_r}{\alpha \sqrt{1-p_r^2}} = 1,$$

$$\int_0^1 dp_r \frac{p_r^3}{\alpha \sqrt{1-p_r^2}} = \frac{2}{3}.$$

Then

$$f(\alpha) \simeq \frac{\pi}{\alpha^5} \begin{cases} 2\alpha^2 & \text{Dbc,} \\ \frac{2}{3} & \text{Nbc.} \end{cases} \quad (5.82)$$

Therefore the total power radiated per unit length in Eq. (5.69) becomes, in the limit $\alpha \rightarrow \infty$,

$$\Pi_x \simeq \frac{\rho_0 c_0}{2\pi^2 k} f(\alpha) \simeq \frac{\rho_0 c_0}{\pi k} \begin{cases} \frac{1}{\alpha^3} & \text{Dbc,} \\ \frac{1}{3\alpha^5} & \text{Nbc.} \end{cases}$$

The corresponding radiation efficiency of a semi-infinite plate with an edge $y = 0$ in the limit of large alpha thus becomes

$$\sigma_x \simeq \frac{2}{\mathcal{A}\pi k} \begin{cases} \frac{1}{\alpha^3} & \text{Dbc,} \\ \frac{1}{3\alpha^5} & \text{Nbc.} \end{cases}$$

Therefore, for general boundary shape, $\partial\Omega$ locally approximated by semi-infinite plate, in the limit $\alpha \rightarrow \infty$, the radiation efficiency σ can be calculated by

$$\sigma = \int_{\partial\Omega} \sigma_x d\bar{x} \simeq \frac{2 \int_{\partial\Omega} d\bar{x}}{\mathcal{A}\pi k} \begin{cases} \frac{1}{\alpha^3} & \text{Dbc,} \\ \frac{1}{3\alpha^5} & \text{Nbc.} \end{cases} \quad (5.83)$$

For the particular case of a rectangular plate with a length of L_x and a width of L_y , the result (5.83) can be written as

$$\sigma \simeq 2L_x\sigma_x + 2L_y\sigma_y = \frac{4(L_x + L_y)}{\mathcal{A}\pi k} \begin{cases} \frac{1}{\alpha^3} & \text{Dbc,} \\ \frac{1}{3\alpha^5} & \text{Nbc.} \end{cases} \quad (5.84)$$

Equation 5.84 consists of four parts, one part for each of the two edges of length L_x and one part for each of the two edges of length L_y .

In Fig. 5.12, these approximate and asymptotic calculations of σ are compared with the same modal average used for comparison in Fig. 5.10. The full calculation of $f(\alpha)$ agrees well throughout the regime $\alpha > 1$, but diverges for $\alpha \rightarrow 1$ (this because the "the boundary layer" shown in Fig. 5.2 and discussed in Sec. 5.2 becomes wider and covers whole plates as $\alpha \rightarrow 1$). The approximation (5.82) captures the qualitative behaviour for $\alpha > 1$ and agrees quantitatively for large α .

5.8 Conclusion

For baffled plates using the simplest case of homogeneously diffuse fields corresponding to uniform ray densities in phase space, the effect of plate bound-

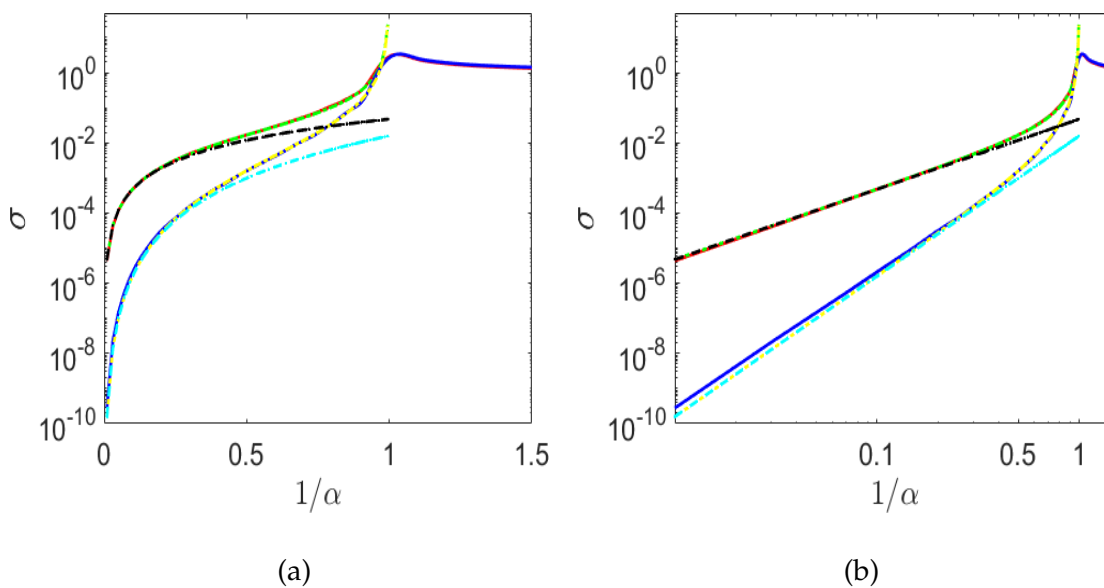


Figure 5.12: Average radiation efficiency under various boundary conditions of a baffled rectangular plate and assuming different excitations with different approximations (2×2 m plate). Assuming diffusive excitation in a semi-infinite plate approximation considering Dbc (—) or considering Nbc (—), or in large α limit considering Dbc (—) or considering Nbc (—), and assuming eigenmode excitation for simply supported plates (—), or guided plates (—); (b) log-log scale plot.

ary conditions has been considered in this chapter. This model has been modified to include corrections corresponding to boundary conditions near boundaries. This investigation has been made only for Dirichlet or Neumann boundary conditions, which serve as simplified models representing simply supported or guided boundary conditions for bending modes in plates. In addition, the theoretical model for radiation efficiency has been developed for Dirichlet and Neumann models by looking at various approximations including a large α asymptotics. For a given structural modal wavenumber $k_{n,m}$ (i.e. a given mode order (n, m)) radiation efficiency from eigenmode of plates with the guided or the simply supported boundary conditions, and from plates assuming diffusive field excitation with Dirichlet or Neumann boundary conditions have been calculated. As a result, their corresponding average radiation efficiencies were determined and comparisons were made. It has been shown that Neumann boundary conditions on plates lowers sound radiation compared to Dirichlet boundary conditions. Similar results are observed in the eigenmode approach; the guided plate produces lower sound radiation for the baffled case.

Chapter 6

Summary

Modelling vibro-acoustic emission from a mechanical structure using phase space methods is the primary goal of this thesis. In order to gain an understanding of the fundamental characteristics of mechanical vibrations as they contribute to sound radiation and sound propagation and also to assess structure-borne sound in more complicated geometries, models for basic structures such as plates and shell structures have been studied using a phase-space approach. The main conclusions of this thesis are summarised in this chapter and proposals are made for further work.

Chapter 2 set out basic material and special functions for the preparation of the main thesis material. The basic equations governing the structural vibration of thin plates and thin shells, described in order to study the theoretical results presented in later chapters. In addition, the background and governing equations of sound radiation from an arbitrary vibrating body are given.

An analysis of the transition between complete reflection and complete transmission of the bending waves incident on a curved section of a thin shell was given in Chapter 3. The study is focused on complex rays theory, extending previous treatment based on real ray dynamics, allowing us to model a smooth transition where transmission turns to complete reflection as the angle of incidence increases and to model resonance effects when reflective reflection increases through the combination of local modes trapped in the curved plate area. The analysis not only works extremely well in describing the smooth transition between complete reflection and complete transmission for a generic curvature profile, but also reproduces phenomena such as reflection mediated by trapped resonances in detail (resonant tunnelling). The model predictions for the scattering properties of curvature profiles with flat maxima have also been compared, and quantitative deviations from its predictions and assumptions made to derive the model are starting to fail. The model, however, succeeds in qualitatively describing the numerically calculated reflection and transmission rates from the shell equations' treatment, including resonance positions and fluctuations in reflection and transmission rates resulting from bifurcations of the underlying complex orbit to more complex forms.

A substantial opportunity has been given in this chapter to advance the understanding of: curvature impacts on mid-frequency wave transport and dispersion relationships, curved ray-tracing, solid structure resonant tunneling, complex ray-tracing, and resonance conditions. Furthermore, the results of this chap-

ter have been published in [199, 200].

The following chapters focus on the problem of sound radiation. Determining the distribution of vibrational energy in large build-up structures often shows apparently random fluctuations, so statistical methods are preferred in this case, which imply certain assumptions, such as diffusive behaviour, about the underlying ray dynamics. A random superposition of plane waves models the statistical properties of wavefunctions in complex or chaotic geometries. This approach completely avoids the need for detailed ray dynamics and can clarify the general, universal characteristics of wave systems; in Chapter 4, the techniques were discussed in detail. In addition, some of these techniques have been published in [201]. A wider goal is later to modify this work to account for variations of the ray densities described by phase space simulations obtained for example from DEA calculations.

Using DEA approximation, the propagation scheme for predicting the sound pressure from complex structures in both the near and far fields was established. DEA is a phase-space approximation of the wave dynamics. It can be used to make an analogy between the evolution of underlying ray trajectories and waves in configuration space. For the sound propagated from a baffled flat plate, a method based on the FFT is proposed, the physical understanding of which is easy and efficient in computation. Moreover, in the calculations, finite size effects and boundary effects on the sound pressure field were tested and observed.

In Chapter 5, the effect of plate boundary conditions is considered for baffled

plates that use the simplest case of homogeneously diffuse fields corresponding to uniform ray densities in phase space. In order to provide corrections corresponding to boundary conditions near boundaries, this model has been modified.

This investigation has been made in detail for Dirichlet or Neumann boundary conditions which usually only serve as simplified models representing simply supported or guided boundary conditions for bending modes in plates. In addition, for Dirichlet and Neumann models, the theoretical model for radiation efficiency has been established by looking at different approximations, including a large asymptotic expression of α , the ratio of bending to acoustic wavenumber.

Radiation efficiency of eigenmode of plates with simply supported and guided boundary conditions and from plates assuming diffusive field excitation with Dirichlet or Neumann boundary conditions was calculated for a given structural modal wavenumber k_b . As a consequence, their corresponding average radiation efficiencies were calculated and comparisons were made.

Compared to Dirichlet boundary conditions, it has been demonstrated that considering Neumann boundary conditions for plates gives less sound radiation. In the eigenmode approach, similar results are observed; the guided plate produces less sound radiation for the baffled case.

In special cases, it is possible to analytically solve the equations governing vibro-acoustic problems, for instance if the equations are linear and the geometry is separable. Nevertheless, numerical methods provide a much more practical means of solution for realistic acoustic problems [202, 203]. The aim of fu-

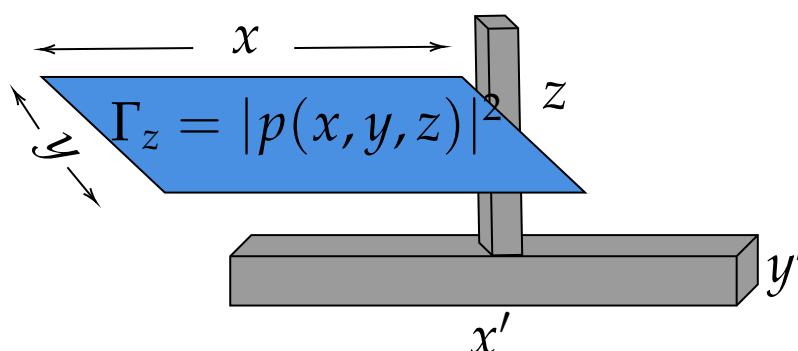


Figure 6.1: Schematic representation of the method of estimating the propagation of sound from a T-plate structure.

ture projects is to model the vibrational response of the gear-box casings due to the mechanics inside the box and to model the noise radiated off the structure. In order to model the vibro-acoustic response of metal casings, we will use the DEA method to work on meshed shell structures, and then use the Kirchhoff–Helmholtz integral equation to estimate the sound field.

Towards this goal, for example, a T-plate structure is a natural extension of the present study and discussion of the coupling of structural vibration calculations with estimate of acoustic radiation of the plate. We have started a Yanmar Holdings Co., Ltd-funded project to extend the methods discussed in Chapter 4 for estimating the propagated sound source using a phase-space approach from a T-plate structure (see Fig. 6.1).

Yanmar first provided the experimental data. Figure 6.2 shows the experimental setup for a T-steel plate structural with free-free boundary conditions and a thickness of $h = 1.2$ mm. The width and length of the base and vertical plates

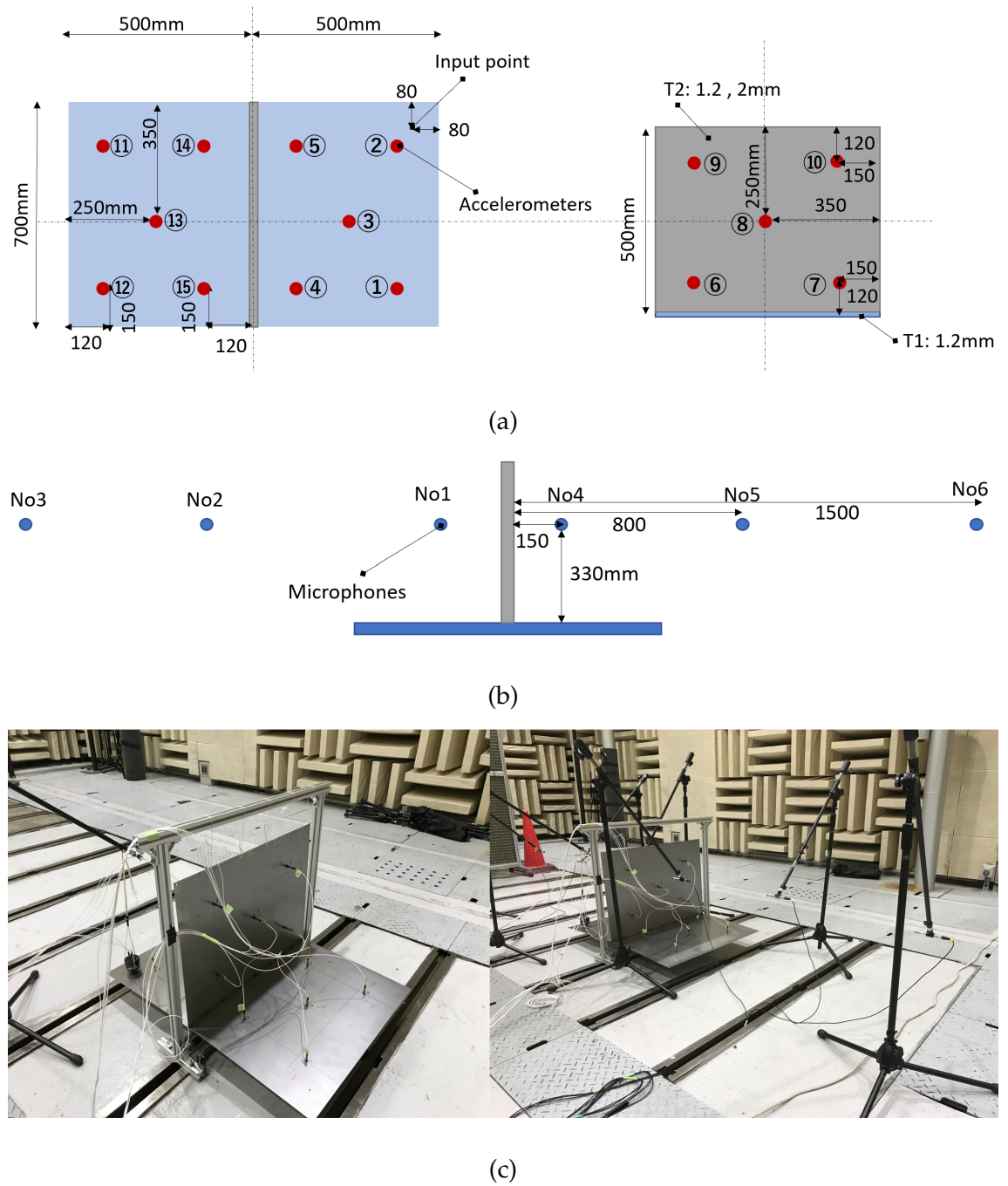


Figure 6.2: Experiment setup; primary figure: free-free boundary condition; acceleration, 5 points on each plate, and force and acceleration at excitation point. Six individual microphones are used to measure sound pressure.

are shown in Fig. 6.2a. A shaker vibrates the plate at the bottom.

At this point in our calculation, we divided the system into three subsystems and calculated sound radiation for each of them using phase space methods. The results of the subsystems were then coupled. Some of the results corresponding with the representation in Fig. 6.1 are shown in Fig. 6.3. We further compared the continuous sound power level obtained from our method to the experimental data provided by Yanmar; the results are shown in Fig. 6.4. We will examine and investigate these results first. Later, we will modify this work by taking into account the different ray densities described in the phase-space. In addition, we will use the actual DEA calculation on the meshed T-plate structures to estimate the corresponding propagated sound field.

The final objective of the wider project is therefore to develop computational tools based on phase space methods that will eventually be used in software packages to model vibro-acoustics of any shaped structure and thus propose design strategies for mechanical architectures.

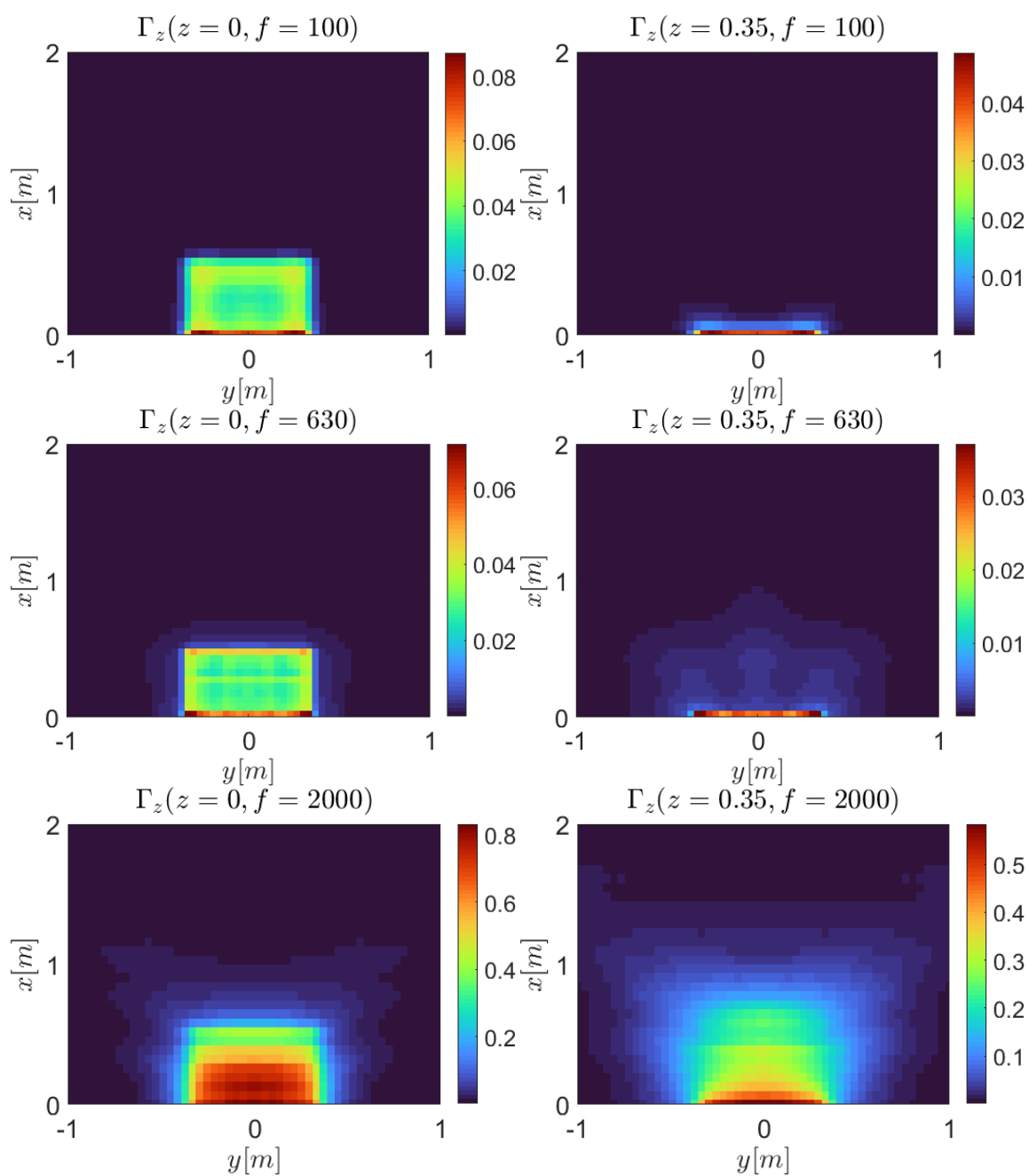


Figure 6.3: The scaled acoustic intensity $|p(\mathbf{x}, z)|^2 / (\rho_0 c_0)^2$ below the critical frequency: first column corresponds to sound radiation from the diffuse field propagation measured for various frequencies; the second column corresponds to sound radiation for the same frequencies measured at different distances.

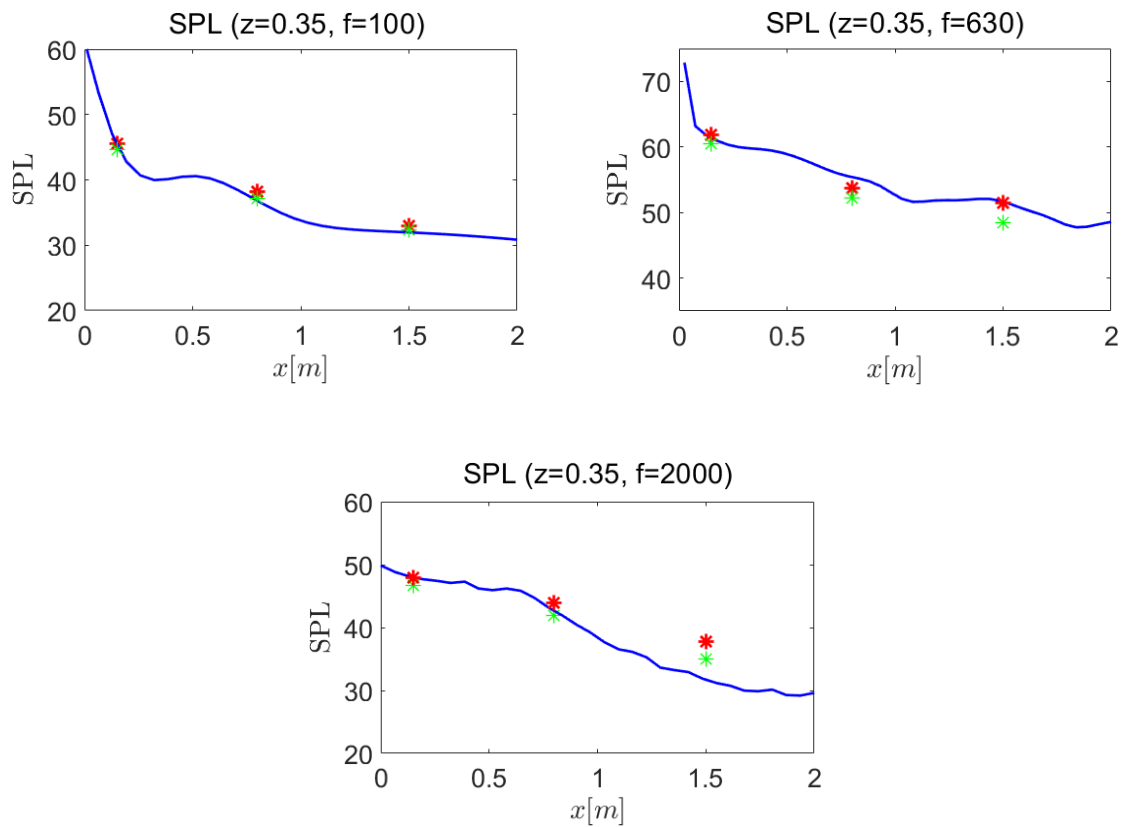


Figure 6.4: Stars are experimental data, red color for measured data from the plate on the left side of the T-plate in Fig. 6.3 and green from those in the right side of it; blue line is our model.

Appendix A

Preliminary and special functions

In the main part of this thesis, these identities and definitions will be used.

Definition A.0.1. Dirac delta is a distribution or generalized function which is zero everywhere on the real line except at the origin, where it is infinite:

$$\delta(x) = \begin{cases} +\infty & x = 0, \\ 0 & \textit{otherwise}. \end{cases}$$

Here, we will not need the formal theory behind the Delta function (The Applied Functional Analysis by D. Griffel [204] is a good book). We will, however, make use of the following property

•

$$\int_{-\infty}^{\infty} e^{ikp(x-a)} dx = \frac{2\pi}{k} \delta(x-a)$$

•

$$\int_{-\infty}^{\infty} \delta(x) dx = 1$$

•

$$\int_{-\infty}^{\infty} f(x-a)\delta(x)dx = f(a)$$

•

$$\int_{-\infty}^{\infty} \delta(x-a)\delta(x-b)dx = \delta(a-b)$$

•

$$\int_{-\infty}^{\infty} g(x)\delta(f(x))dx = \sum_i \frac{g(x_i)}{|f'(x_i)|} \quad x_i \text{'s are zeros of } f(x)$$

•

$$\delta(x) = \delta(-x)$$

•

$$\delta(ax) = \frac{1}{|a|}\delta(x)$$

•

$$\delta(x^2 - a^2) = \frac{1}{2|a|} [\delta(x-a) + \delta(x+a)]$$

Definition A.0.2. χ_{Ω} denotes projection onto functions supported in Ω defined in direct space by

$$\chi_{\Omega}(\mathbf{x}) = \begin{cases} 1 & \text{if } \mathbf{x} \in \Omega, \\ 0 & \text{otherwise.} \end{cases}$$

Thus

$$\chi_{\Omega}(\mathbf{x})f(\mathbf{x}) = \begin{cases} f(\mathbf{x}) & \text{if } \mathbf{x} \in \Omega, \\ 0 & \text{otherwise} \end{cases}$$

Definition A.0.3. The convolution of f and h is an operator with the symbol $*$ defined as the integral of the product of the two functions after one is reversed and shifted

$$(f * h)(\mathbf{x}) = \int_{\mathbb{R}^d} f(\mathbf{y})h(\mathbf{x} - \mathbf{y})d\mathbf{y} = \int_{\mathbb{R}^d} h(\mathbf{y})f(\mathbf{x} - \mathbf{y})d\mathbf{y}.$$

Some convolution identities:

•

$$(f * h * g)(\mathbf{x}) = \int_{\mathbb{R}^d} f(\mathbf{z})g(\mathbf{x} - \mathbf{y})h(\mathbf{y} - \mathbf{z})d\mathbf{z}d\mathbf{y} = \int_{\mathbb{R}^d} f(\mathbf{z})g(\mathbf{y})h(\mathbf{x} - \mathbf{y} - \mathbf{z})d\mathbf{z}d\mathbf{y}$$

•

$$(f * \delta)(\mathbf{x}) = f(\mathbf{0})$$

Definition A.0.4. Fourier transformation of an integrable function $g : \mathbb{R}^d \rightarrow \mathbb{C}^d$ defined as

$$g(\mathbf{p}) = \mathcal{F}\{g(\mathbf{x})\} = \int_{\mathbb{R}^d} g(\mathbf{x})e^{-ik\mathbf{x}\cdot\mathbf{p}}d\mathbf{x},$$

where d is dimension, k is wave number, and \mathbf{p} is the Fourier variables. Inverse Fourier transformation is defined as

$$g(\mathbf{x}) = \mathcal{F}^{-1}\{g(\mathbf{p})\} = \left(\frac{k}{2\pi}\right)^d \int_{\mathbb{R}^d} g(\mathbf{p})e^{ik\mathbf{x}\cdot\mathbf{p}}d\mathbf{p}.$$

Some identities and properties:

- If g is a separable function of x_i 's, i.e.

$$g(\mathbf{x}) = g_1(x_1)g_2(x_2)\dots g_d(x_d),$$

then

$$g(\mathbf{p}) = g_1(p_1)g_2(p_2)\dots g_d(p_d),$$

where

$$g_1(p_1) = \frac{2\pi}{k} \int_{\mathbb{R}} g_1(x_1) e^{-ikx_1 p_1} dp_1$$

•

$$\mathcal{F}\{f(\mathbf{x})g(\mathbf{x})\} = \left(\frac{k}{2\pi}\right)^{-d} (f * g)(\mathbf{p}) = \left(\frac{k}{2\pi}\right)^{-d} \int_{\mathbb{R}^d} f(\mathbf{q})h(\mathbf{p} - \mathbf{q})d\mathbf{q}$$

•

$$\mathcal{F}^{-1}\{f(\mathbf{p})g(\mathbf{p})\} = \left(\frac{k}{2\pi}\right)^d (f * g)(\mathbf{x}) = \left(\frac{k}{2\pi}\right)^d \int_{\mathbb{R}^d} f(\mathbf{y})h(\mathbf{x} - \mathbf{y})d\mathbf{y}$$

Appendix B

Fourier transformation of mode shapes

B.1 Infinite structures

Fourier transformation of $f(x) = \cos(ax)$ on the real line is

$$f(p) = \frac{2\pi}{k} \int_{\mathbb{R}} \cos(ax) e^{-ikxp} dx$$

using the fact that

$$\cos(ax) = \frac{e^{-iax} + e^{iax}}{2},$$

$$\begin{aligned} f(p) &= \frac{\pi}{k} \int_{\mathbb{R}} \left[e^{-ix(kp-a)} + e^{-ix(kp+a)} \right] dx, \\ &= \frac{\pi}{k} [\delta(kp-a) + \delta(kp+a)], \\ &= \frac{2\pi}{k} |a| \delta((kp)^2 - a^2). \end{aligned}$$

B.2 Finite structures

The Fourier transform of a mode $V(x, y) = \sin\left(\frac{n\pi}{L_x}x\right) \sin\left(\frac{m\pi}{b}y\right)$ of a simply supported rectangular plate of length L_x and width L_y

$$\hat{V}(p_x, p_y) = \int_0^{L_y} \int_0^{L_x} e^{-ik[p_x x + p_y y]} \sin\left(\frac{n\pi}{L_x}x\right) \sin\left(\frac{m\pi}{b}y\right) dx dy.$$

First solve the integral w.r. to x

$$\begin{aligned} & \int_0^{L_x} e^{-ikp_x x} \sin\left(\frac{n\pi}{L_x}x\right) dx, \\ &= \frac{1}{2i} \int_0^{L_x} \left[e^{ix\left(\frac{n\pi}{L_x} - kp_x\right)} - e^{-ix\left(\frac{n\pi}{L_x} + kp_x\right)} \right] dx, \\ &= \frac{1 - \frac{n\pi}{L_x} \left[-e^{-iL_x kp_x} \left[e^{in\pi} + e^{-in\pi} \right] - 2 \right]}{2 \left(\left(\frac{n\pi}{L_x} \right)^2 - k^2 p_x^2 \right)}, \\ &= -\frac{n\pi \left[(-1)^n e^{-iL_x kp_x} - 1 \right]}{L_x \left(\left(\frac{n\pi}{L_x} \right)^2 - k^2 p_x^2 \right)}. \end{aligned}$$

Solving the second integral for y similarly we obtain

$$\hat{V}(p_x, p_y) = \frac{nm\pi^2 \left[(-1)^n e^{-iL_x kp_x} - 1 \right] \left[(-1)^m e^{-iL_y kp_y} - 1 \right]}{L_x L_y \left(\left(\frac{n\pi}{L_x} \right)^2 - k^2 p_x^2 \right) \left(\left(\frac{m\pi}{L_y} \right)^2 - k^2 p_y^2 \right)}.$$

The Fourier transformation of the cosine functions for the guided boundary conditions can be obtained using similar procedures.

Appendix C

WKB-approximation

In this appendix we motivate the uniform approximation of nodal reflection and transmission coefficients given in (3.31a) and in (3.31b). These local scattering coefficients are characteristic of WKB solutions around generic hyperbolic fixed points as illustrated schematically in Fig. 3.10, and we justify them here by solving the simplest second order differential equation, of the form

$$\frac{d^2\psi(X)}{dX^2} + \chi(X)\psi(X) = 0, \quad (\text{C.1})$$

for which this topology guides WKB approximation. It can be shown for example in [205] that solution of more general differential equations can be transformed locally to these simpler equations. In this section, instead of using the symbol W , we will use ψ to avoid confusion between the symbols used here and the numerical solution in Sec. 3.2.7. To construct a local WKB solution for a tuning

point (a nodal point), such as α in Fig. C.1, the wave function $\psi(X)$ in (C.1) is divided into two parts, ψ^+ and ψ^- , which represent the waves travelling to the right and left of that turning point, respectively. In the classical region, this can be expressed as

$$\begin{aligned}\psi(X) &= \psi^+(X) + \psi^-(X) \\ &= A^+ e^{iS(X)} + A^- e^{-iS(X)},\end{aligned}$$

but in the classically forbidden region, the phase will be complex, therefore $\psi(X)$ can be described as

$$\psi(X) = B^- e^{-\Theta(X)} + B^+ e^{\Theta(X)},$$

where A s' and B s' are wave amplitudes. The phase integral S is defined as

$$S(X_1, X) = \int_{X_1}^X (\chi(X))^{1/2} dX = \int_{X_1}^X K_x dX,$$

and Θ is defined as

$$\Theta(X_1, X) = \int_{X_1}^X (-\chi(X))^{1/2} dX = i \int_{X_1}^X K_x dX.$$

The phase symbol $S(X)$ is sometimes used with a single argument, with the argument referring to the upper limit of integration and the lower limit being either unnecessary or understood. When we wish to indicate both limits of the integration we write

$$S(X_1, X_2) = \int_{X_1}^{X_2} K_X dX.$$

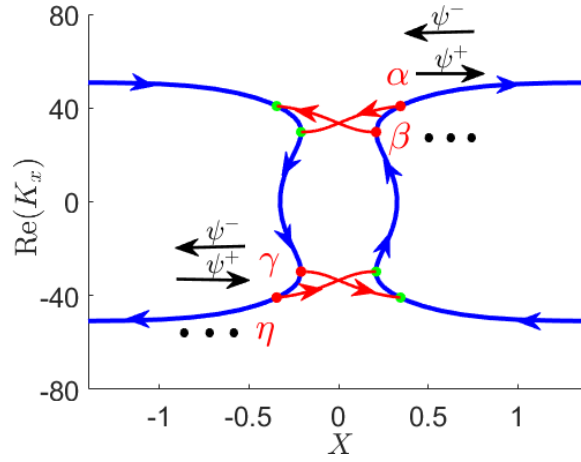


Figure C.1: Real orbits with turning points for the case $K_y > K_y^\sharp$.

The exact form of the reflection and transmission coefficients for a nodal point can be obtained using *comparison method* [157]. This method was used to treat scattering in a one-dimensional well [157], and we refer to that article and the references within for further information on the following calculation. However, it is worth reiterating a few key principles and emphasising the importance of flux calculations. The main points of this method is discussed in the next section.

C.1 The method of comparison equations

The uniform approximation seeks to approximate a solution to the differential equation (C.1) in terms of known solutions $\Phi(\zeta)$ to the equation

$$\frac{d^2\Phi(\zeta)}{d\zeta^2} + \Gamma(\zeta)\Phi(\zeta) = 0. \quad (\text{C.2})$$

$\Gamma(\zeta)$ is specified to be comparable to $\chi(X)$ but simpler, such that the solutions of (C.2) are known. By choosing an *equivalent* pair of points ζ_1 and X_1 , $\zeta(X)$ can be

written implicitly as a

$$\int_{\zeta_1}^{\zeta} (\Gamma(\zeta))^{1/2} d\zeta = \int_{X_1}^X (\chi(X))^{1/2} dX = S(X_1, X),$$

Or

$$\int_{\zeta_1}^{\zeta} (-\Gamma(\zeta))^{1/2} d\zeta = \int_{X_1}^X (-\chi(X))^{1/2} dX = \Theta(X_1, X).$$

The approximate solution of (C.1) is then given by

$$\psi(X) \simeq \left[\frac{\Gamma(\zeta(X))}{\chi(X)} \right]^{1/4} \phi(\zeta(X)). \quad (\text{C.3})$$

The most straightforward comparison potential for the solutions of this equation with two turning points is parabolic [157], with the choice of $\Gamma(\zeta) = \varepsilon + \zeta^2$.

Thus

$$\frac{d^2\Phi(\zeta)}{d\zeta^2} + (\varepsilon + \zeta^2)\Phi(\zeta) = 0, \quad (\text{C.4})$$

where the parameter ε is proportional to the action for the incident wave considered,

$$i\Theta(\gamma, \alpha) = i \int_{\gamma}^{\alpha} K_x dX \equiv i \int_{-\sqrt{-\varepsilon}}^{+\sqrt{-\varepsilon}} (-\varepsilon - \zeta^2)^{1/2} d\zeta = \frac{i\varepsilon\pi}{2}, \quad (\text{C.5})$$

where α and γ are the two turning points. The real mapping function $\zeta(X)$ is given implicitly by

$$S(\alpha, X) = \int_{\alpha}^X K_x dX = \int_{+\sqrt{-\varepsilon}}^{\zeta(X)} (\varepsilon + \zeta^2)^{1/2} d\zeta. \quad (\text{C.6})$$

The parabolic cylinder functions $D_{(i\varepsilon-1)/2}(\zeta\sqrt{2}e^{-i\pi/4})$ and $D_{(-i\varepsilon-1)/2}(\zeta\sqrt{2}e^{i\pi/4})$,

whose exact asymptotic behaviour is known, are the solutions of Eq. (C.4) [157],

$$\begin{aligned}\Phi(\zeta) &= D_{(i\varepsilon-1)/2}(\zeta\sqrt{2}e^{-i\pi/4}), \\ \Phi(\zeta) &= D_{(-i\varepsilon-1)/2}(\zeta\sqrt{2}e^{i\pi/4}).\end{aligned}\tag{C.7}$$

By considering the asymptotic behaviour of an appropriate linear combination of the parabolic cylinder functions (C.7), and using uniform approximations (C.3), the correct form of the local reflection and transmission coefficients for the turning point α can be derived

$$\frac{1}{(\varepsilon+\zeta^2(X))^{1/4}} e^{-i\int_{-\sqrt{-\varepsilon}}^{\zeta(X)}(\varepsilon+\zeta^2)^{1/2} d\zeta(X)} + \frac{r_{\text{node}}}{(\varepsilon+\zeta^2(X))^{1/4}} e^{i\int_{-\sqrt{-\varepsilon}}^{\zeta(X)}(\varepsilon+\zeta^2(X))^{1/2} d\zeta}\tag{C.8}$$

$$\leftarrow \psi(X) \rightarrow \frac{t_{\text{node}}}{(\varepsilon+\zeta^2(X))^{1/4}} e^{i\int_{+\sqrt{-\varepsilon}}^{\zeta(X)}(\varepsilon+\zeta^2(X))^{1/2} d\zeta},$$

where

$$r_{\text{node}} = \frac{-ie^{-i\delta}}{\sqrt{1 + e^{-2\int_{-\sqrt{-\varepsilon}}^{+\sqrt{-\varepsilon}}(-\varepsilon-\zeta^2)^{1/2} d\zeta}}},\tag{C.9a}$$

and

$$t_{\text{node}} = \frac{e^{-\int_{-\sqrt{-\varepsilon}}^{+\sqrt{-\varepsilon}}(-\varepsilon-\zeta^2)^{1/2} d\zeta - i\delta}}{\sqrt{1 + e^{-2\int_{-\sqrt{-\varepsilon}}^{+\sqrt{-\varepsilon}}(-\varepsilon-\zeta^2)^{1/2} d\zeta}}},\tag{C.9b}$$

where

$$\begin{aligned}\delta &= \frac{\int_{-\sqrt{-\varepsilon}}^{+\sqrt{-\varepsilon}}(-\varepsilon-\zeta^2)^{1/2} d\zeta}{\pi} \log \left| \frac{\int_{-\sqrt{-\varepsilon}}^{+\sqrt{-\varepsilon}}(-\varepsilon-\zeta^2)^{1/2} d\zeta}{\pi e} \right| + \\ &\quad \arg \Gamma \left(\frac{1}{2} - \frac{i\int_{-\sqrt{-\varepsilon}}^{+\sqrt{-\varepsilon}}(-\varepsilon-\zeta^2)^{1/2} d\zeta}{\pi} \right).\end{aligned}\tag{C.9c}$$

By substituting the form of ε in (C.5) and $\zeta(X)$ in (C.6) into (C.8) and (C.9), the exact expressions of r_{node} and t_{node} given in (3.31) can be derived. The same technique applies to the other turning points.

Appendix D

Corner correction in rectangular case

We go through steps similar to what has been done for $\hat{\Gamma}_0(\mathbf{p}, \mathbf{p}')$,

$$\begin{aligned}\hat{\Gamma}_2(\mathbf{p}, \mathbf{p}') &= \int_{\mathbb{R}^{2d}} \Gamma_2(\mathbf{x}, \mathbf{x}') e^{-ik\mathbf{p}\cdot\mathbf{x}+ik\mathbf{p}'\cdot\mathbf{x}'} d\mathbf{x} d\mathbf{x}' \\ &= \int_{\mathbb{R}^{2d}} J_0(\alpha k |\mathbf{x} + \mathbf{x}'|) e^{-ik\mathbf{p}\cdot\mathbf{x}+ik\mathbf{p}'\cdot\mathbf{x}'} d\mathbf{x} d\mathbf{x}'.\end{aligned}$$

Now we perform a change of variables as in Eq. (3.28)

$$\begin{aligned}\hat{\Gamma}_2(\bar{\mathbf{p}} - \mathbf{q}/2, \bar{\mathbf{p}} + \mathbf{q}/2) &= \int_{\mathbb{R}^{2d}} J_0(2\alpha k |\bar{\mathbf{x}}|) e^{-ik\mathbf{q}\cdot\bar{\mathbf{x}}-ik\bar{\mathbf{p}}\cdot\mathbf{s}} d\mathbf{s} d\bar{\mathbf{x}} \\ &= \left(\frac{2\pi}{k}\right)^d \delta(\bar{\mathbf{p}}) \int_{\mathbb{R}^d} J_0(2\alpha k |\bar{\mathbf{x}}|) e^{-ik\bar{\mathbf{p}}\cdot\mathbf{x}} d\bar{\mathbf{x}} \\ &= \frac{1}{4\pi} \left(\frac{2\pi}{k}\right)^{2d} \delta(\bar{\mathbf{p}}) \delta\left(\frac{\mathbf{q}^2}{2} - \alpha^2\right).\end{aligned}\tag{D.1}$$

Expressing this in terms of the original variables \mathbf{p} and \mathbf{p}' we obtain

$$\hat{\Gamma}_2(\mathbf{p}, \mathbf{p}') = \frac{1}{4\pi} \left(\frac{2\pi}{k}\right)^{2d} \delta\left(\frac{\mathbf{p} + \mathbf{p}'}{2}\right) \delta\left(\left(\frac{\mathbf{p} - \mathbf{p}'}{2}\right)^2 - \alpha^2\right).\tag{D.2}$$

$$\begin{aligned}
D(\mathbf{p}, \mathbf{p}') &= \left(\frac{2\pi}{k}\right)^{-2d} \int_{\mathbb{R}^{2d}} d\mathbf{p}'' d\mathbf{p}''' H(\mathbf{p} - \mathbf{p}'') \Gamma_2(\mathbf{p}'', \mathbf{p}''') \bar{H}(\mathbf{p}' - \mathbf{p}''') \\
&= \frac{1}{4\pi} \int_{\mathbb{R}^{2d}} d\mathbf{p}'' d\mathbf{p}''' H(\mathbf{p} - \mathbf{p}'') \delta\left(\frac{\mathbf{p}'' + \mathbf{p}'''}{2}\right) \delta\left(\left(\frac{\mathbf{p}'' - \mathbf{p}'''}{2}\right)^2 - \alpha^2\right) \bar{H}(\mathbf{p}' - \mathbf{p}''') \\
&= \frac{1}{2\pi} \int_{\mathbb{R}^d} d\mathbf{p}'' H(\mathbf{p} - \mathbf{p}'') \delta(\mathbf{p}''^2 - \alpha^2) \bar{H}(\mathbf{p}' + \mathbf{p}''),
\end{aligned}$$

and converting $\mathbf{p}'' = (p''_x, p''_y)$ to polar coordinate $\mathbf{p}_r = (p_r \cos \theta, p_r \sin \theta)$ yields

$$D(\mathbf{p}, \mathbf{p}') = \frac{1}{2\pi} \int_0^{4\pi} d\theta H(\mathbf{p} - \mathbf{p}_\alpha) \bar{H}(\mathbf{p}' + \mathbf{p}_\alpha) = \frac{1}{2} \langle H(\mathbf{p} - \mathbf{p}_\alpha) \bar{H}(\mathbf{p}' + \mathbf{p}_\alpha) \rangle.$$

Then recalling Eq. (5.30) for the function H , and \bar{H} its complex conjugate, we obtain

$$\begin{aligned}
D(\mathbf{p}, \mathbf{p}') &= \frac{1}{2} \langle H(\mathbf{p} - \mathbf{p}_\alpha) \bar{H}(\mathbf{p}' + \mathbf{p}_\alpha) \rangle \\
&= \frac{1}{4\pi} \int_0^{2\pi} d\theta \int_{\Omega} \int_{\Omega} e^{-ik(\mathbf{p} - \mathbf{p}_\alpha) \cdot \mathbf{x}} e^{ik(\mathbf{p}' + \mathbf{p}_\alpha) \cdot \mathbf{x}'} d\mathbf{x} d\mathbf{x}'.
\end{aligned}$$

After performing a change of variables of \mathbf{x} and \mathbf{x}' as in Eq. (3.28), we obtain

$$D(\mathbf{p}, \mathbf{p}') = \frac{1}{4\pi} \int_0^{2\pi} d\theta \int_{\Omega_{\bar{\mathbf{x}}}} \int_{\Omega_{\mathbf{s}}} e^{-ik(\mathbf{p} - \mathbf{p}' - 2\mathbf{p}_\alpha) \cdot \bar{\mathbf{x}}} e^{-ik(\frac{\mathbf{p} + \mathbf{p}'}{2}) \cdot \mathbf{s}} d\mathbf{s} d\bar{\mathbf{x}}.$$

Thus

$$D(\mathbf{p}, \mathbf{p}') = \frac{1}{4\pi} \int_0^{2\pi} d\theta \int_{\Omega_{\bar{\mathbf{x}}}} e^{-ik(\mathbf{p} - \mathbf{p}' - 2\mathbf{p}_\alpha) \cdot \bar{\mathbf{x}}} d\bar{\mathbf{x}} \int_{\Omega_{\mathbf{s}}} e^{-ik(\frac{\mathbf{p} + \mathbf{p}'}{2}) \cdot \mathbf{s}} d\mathbf{s}. \quad (\text{D.3})$$

Therefore we can obtain $D(\mathbf{p}, \mathbf{p})$ from Eq.(D.3),

$$D(\mathbf{p}, \mathbf{p}) = \frac{1}{4\pi} \int_0^{2\pi} d\theta \int_{\Omega_{\bar{\mathbf{x}}}} e^{2ik\mathbf{p}_\alpha \cdot \bar{\mathbf{x}}} d\bar{\mathbf{x}} \int_{\Omega_{\mathbf{s}}} e^{-ik\mathbf{p} \cdot \mathbf{s}} d\mathbf{s}. \quad (\text{D.4})$$

D.1 Infinite corner approximation

Now for upper half plane edge approximation the corner correction approximation would be over a quarter plane that is

$$\begin{aligned}
 D(\mathbf{p}, \mathbf{p}) &= \frac{1}{4\pi} \int_0^{2\pi} d\theta \int_0^\infty d\bar{x} \int_0^\infty d\bar{y} e^{2ik\mathbf{p}_\alpha \cdot \bar{\mathbf{x}}} \int_{-2\bar{x}}^{2\bar{x}} ds_x \int_{-2\bar{y}}^{2\bar{y}} ds_y e^{-ik\mathbf{p} \cdot \mathbf{s}}, \\
 &= \frac{1}{4\pi} \int_0^{2\pi} d\theta \int_0^\infty d\bar{x} \int_0^\infty d\bar{y} e^{2ik\mathbf{p}_\alpha \cdot \bar{\mathbf{x}}} \frac{4 \sin(2kp_x \bar{x}) \sin(2kp_y \bar{y})}{k^2 p_x p_y}, \\
 &= \frac{1}{4\pi k^2 p_x p_y} \int_0^{2\pi} d\theta e^{ik\mathbf{p}_\alpha \cdot \bar{\mathbf{x}}} \int_0^\infty d\bar{x} \int_0^\infty d\bar{y} \sin(kp_x \bar{x}) \sin(kp_y \bar{y}), \\
 &= \frac{1}{2k^2 p_x p_y} \int_0^\infty d\bar{x} \int_0^\infty d\bar{y} J_0\left(\alpha k \sqrt{\bar{x}^2 + \bar{y}^2}\right) \sin(kp_x \bar{x}) \sin(kp_y \bar{y}),
 \end{aligned}$$

and converting (\bar{x}, \bar{y}) to polar coordinate (r, ϕ) yields

$$D(\mathbf{p}, \mathbf{p}) = \frac{1}{2k^2 p_x p_y} \int_0^{\pi/2} d\phi \int_0^\infty dr J_0(\alpha kr) \sin(kp_x r \cos \phi) \sin(kp_y r \sin \phi),$$

using the fact that

$$\sin(ax) \sin(bx) = \frac{1}{2} \{ \cos(a-b) - \cos(a+b) \},$$

$$\begin{aligned}
 D(\mathbf{p}, \mathbf{p}) &= \frac{1}{4k^2 p_x p_y} \int_0^{\pi/2} d\phi \int_0^\infty dr J_0(\alpha kr) \times \\
 &\quad \left\{ \cos\left(kr \underbrace{(p_x \cos \phi - p_y \sin \phi)}_{q_-}\right) - \cos\left(kr \underbrace{(p_x \cos \phi + p_y \sin \phi)}_{q_+}\right) \right\}, \\
 &= \frac{1}{4k^2 p_x p_y} \sum_{\mp} \int_0^{\pi/2} d\phi \int_0^\infty dr J_0(\alpha kr) \cos(krq_{\mp}).
 \end{aligned}$$

Making use of the relation in the book by Gradshteyn and Ryzhik [206]

$$\int_0^\infty dr J_0(br) \cos(ar) = \begin{cases} 0 & 0 < a < b, \\ -a(a^2 - b^2)^{-3/2} & 0 < b < a. \end{cases}$$

Thus, we obtain

$$D(\mathbf{p}, \mathbf{p}) = \frac{1}{4k^2 p_x p_y} \begin{cases} 0 & |q_{\mp}| < \alpha k, \\ -|q_{\mp}| (q_{\mp}^2 - \alpha^2 k^2)^{-3/2} & |q_{\mp}| > \alpha k. \end{cases}$$

By construction, if $\alpha > 1$, $|q_{\mp}| < \alpha k$, thus

$$D(\mathbf{p}, \mathbf{p}) = 0.$$

Bibliography

- [1] J. F. Kennedy, "Address at rice university on the nation's space effort," *Rice University, Houston, Texas. NASA JSC*, pp. 1–4, 1962.
- [2] Z. I. Korca, V. Cojocar, N. Gillich, and C. O. Miclosina, "Comparative assessment of noise reduction in helical gearboxes," *J. Vib. Eng. Technol.*, vol. 5, no. 3, pp. 263–268, 2017.
- [3] B. R. Höhn, "Improvements on noise reduction and efficiency of gears," *Meccanica*, vol. 45, no. 3, pp. 425–437, 2010.
- [4] "UK Romax Technology Launches State-of-the-Art Hybrid Drivetrain Design." <https://www.offshorewind.biz/2012/09/20/uk-romax-technology-launches-state-of-the-art-hybrid-drivetrain-design/>. Accessed: 2012-09-20.
- [5] T. Wu, *Boundary element acoustics: fundamentals and computer codes*, vol. 7. Wit Pr/Computational Mechanics, 2000.

- [6] J. S. Lamancusa, "Acoustic finite element modeling using commercial structural analysis programs.," *Noise Control Eng. J.*, vol. 30, no. 2, pp. 65–71, 1988.
- [7] N. Atalla and R. Bernhard, "Review of numerical solutions for low-frequency structural-acoustic problems," *Appl. Acoust.*, vol. 43, no. 3, pp. 271–294, 1994.
- [8] M. Gennaretti, A. Giordiani, and L. Morino, "A third-order boundary element method for exterior acoustics with applications to scattering by rigid and elastic shells," *J. Sound Vib.*, vol. 222, no. 5, pp. 699–722, 1999.
- [9] S. Kirkup, "The boundary element method in acoustics: A survey," *Appl. Sci.*, vol. 9, no. 8, p. 1642, 2019.
- [10] O. C. Zienkiewicz, R. L. Taylor, P. Nithiarasu, and J. Zhu, *The finite element method*, vol. 3. McGraw-hill London, 1977.
- [11] M. Petyt, *Introduction to finite element vibration analysis*. Cambridge University Press, 2010.
- [12] P. K. Banerjee and R. Butterfield, *Boundary element methods in engineering science*, vol. 17. McGraw-Hill London, 1981.
- [13] C. T. Ross, *Finite element programs for structural vibrations*. Springer Science & Business Media, 2012.

- [14] C. S. Desai and J. F. Abei., "Introduction to the finite element method," *Van Nostrand Reinhold*, vol. 477, 1972.
- [15] M. Petyt, "Finite element techniques for acoustics," in *Theoretical Acoustics and Numerical Techniques*, pp. 51–103, Springer, 1983.
- [16] S. M. Kirkup, *The boundary element method in acoustics*. Integrated Sound Software, 2007.
- [17] R. H. Lyon, R. G. DeJong, and M. Heckl, "Theory and application of statistical energy analysis," *J. Acoust. Soc. Am.*, vol. 98, no. 6, pp. 3021–3021, 1995.
- [18] A. J. Keane and W. G. Price, *Statistical energy analysis: an overview, with applications in structural dynamics*. Cambridge University Press, 1997.
- [19] R. J. Craik, "The prediction of sound transmission through buildings using statistical energy analysis," *J. Sound Vib.*, vol. 82, no. 4, pp. 505–516, 1982.
- [20] R. Langley, "A wave intensity technique for the analysis of high frequency vibrations," *J. Sound Vib.*, vol. 159, no. 3, pp. 483–502, 1992.
- [21] A. Le Bot and A. Bocquillet, "Comparison of an integral equation on energy and the ray-tracing technique in room acoustics," *J. Acoust. Soc. Am.*, vol. 108, no. 4, pp. 1732–1740, 2000.

- [22] A. Le Bot, "Energy transfer for high frequencies in built-up structures," *J. Sound Vib.*, vol. 250, no. 2, pp. 247–275, 2002.
- [23] C. Hopkins, "Statistical energy analysis of coupled plate systems with low modal density and low modal overlap," *J. Sound Vib.*, vol. 251, no. 2, pp. 193–214, 2002.
- [24] R. Langley, "Wave motion and energy flow in cylindrical shells," *J. Sound Vib.*, vol. 169, no. 1, pp. 29–42, 1994.
- [25] J. T. Kajiya, "The rendering equation," in *ACM Siggraph Computer Graphics*, vol. 20, pp. 143–150, ACM, 1986.
- [26] H. Kuttruff, *Room acoustics*. CRC Press, 2016.
- [27] G. Tanner and N. Søndergaard, "Wave chaos in acoustics and elasticity," *J. Phys. A Math. Theor.*, vol. 40, no. 50, p. R443, 2007.
- [28] G. Tanner, "Dynamical energy analysis—determining wave energy distributions in vibro-acoustical structures in the high-frequency regime," *J. Sound Vib.*, vol. 320, no. 4, pp. 1023 – 1038, 2009.
- [29] T. Hartmann, S. Morita, G. Tanner, and D. J. Chappell, "High-frequency structure- and air-borne sound transmission for a tractor model using dynamical energy analysis," *Wave Motion*, vol. 87, pp. 132 – 150, 2019. Innovations in Wave Modelling II.

- [30] D. Chappell, D. Löchel, N. Søndergaard, and G. Tanner, "Dynamical energy analysis on mesh grids: A new tool for describing the vibro-acoustic response of complex mechanical structures," *Wave Motion*, vol. 51, no. 4, pp. 589 – 597, 2014. Innovations in Wave Modelling.
- [31] N. Søndergaard, D. J. Chappell, and G. Tanner, "Tracking vibrational energy on curved shell structures in the mid-high frequency limit—a ray-tracing approach," *Proceedings of Noise and Vibration-Emerging Technologies (NOVEM)*, vol. 251, no. 1, pp. 195–204, 2015.
- [32] N. Søndergaard and D. J. Chappell, "Ray and wave scattering in smoothly curved thin shell cylindrical ridges," *J. Sound Vib.*, vol. 377, pp. 155 – 168, 2016.
- [33] L. L. Thompson, "A review of finite-element methods for time-harmonic acoustics," *J. Acoust. Soc. Am.*, vol. 119, no. 3, pp. 1315–1330, 2006.
- [34] G. Liu, "Formulation of multifield finite element models for helmholtzproblems," *HKU Theses Online (HKUTO)*, 2010.
- [35] J. M. Parot, C. Thirard, and C. Puillet, "Elimination of a non-oscillatory instability in a retarded potential integral equation," *Eng. Anal. Bound. Elem.*, vol. 31, no. 2, pp. 133–151, 2007.

- [36] S. Langer and M. Schanz, "Time domain boundary element method," in *Computational Acoustics of Noise Propagation in Fluids-Finite and Boundary Element Methods*, pp. 495–516, Springer, 2008.
- [37] D. Chappell, P. Harris, D. Henwood, and R. Chakrabarti, "A stable boundary element method for modeling transient acoustic radiation," *J. Acoust. Soc. Am.*, vol. 120, no. 1, pp. 74–80, 2006.
- [38] T. Qiu, *Time domain boundary integral equation methods in acoustics, heat diffusion and electromagnetism*. PhD thesis, University of Delaware, 2016.
- [39] T. Hartmann, S. Morita, G. Tanner, and D. J. Chappell, "High-frequency structure-and air-borne sound transmission for a tractor model using dynamical energy analysis," *Wave Motion*, vol. 87, pp. 132–150, 2019.
- [40] F. Fahy and P. Gardonio, *Sound and Structural Vibration: Radiation, Transmission and Response*. EngineeringPro collection, Elsevier Science, 2007.
- [41] G. Maidanik, "Response of ribbed panels to reverberant acoustic fields," *J. Acoust. Soc. Am.*, vol. 34, no. 6, pp. 809–826, 1962.
- [42] C. E. Wallace, "Radiation resistance of a baffled beam," *J. Acoust. Soc. Am.*, vol. 51, no. 3B, pp. 936–945, 1972.
- [43] C. E. Wallace, "Radiation resistance of a rectangular panel," *J. Acoust. Soc. Am.*, vol. 51, no. 3B, pp. 946–952, 1972.

- [44] M. Gomperts, "Radiation from rigid baffled, rectangular plates with general boundary conditions," *Acta Acustica united with Acustica*, vol. 30, no. 6, pp. 320–327, 1974.
- [45] M. Heckl, "Radiation from plane sound sources," *Acustica*, vol. 37, pp. 155–166, 1977.
- [46] F. G. Leppington, E. G. Broadbent, and K. H. Heron, "The acoustic radiation efficiency of rectangular panels," *Proc. Roy. Soc. A Math. Phys. Sci.*, vol. 382, no. 1783, pp. 245–271, 1982.
- [47] E. G. Williams, "A series expansion of the acoustic power radiated from planar sources," *J. Acoust. Soc. Am.*, vol. 73, no. 5, pp. 1520–1524, 1983.
- [48] L. Rayleigh, "Xxxvii. on the passage of waves through apertures in plane screens, and allied problems," *London, Edinburgh Dublin Philos. Mag. J. Sci.*, vol. 43, no. 263, pp. 259–272, 1897.
- [49] M. V. Berry, "Regular and irregular semiclassical wavefunctions," *J. Phys. A Math. Gen.*, vol. 10, no. 12, p. 2083, 1977.
- [50] A. Leissa, *Vibration of Plates*. NASA SP, Scientific and Technical Information Division, National Aeronautics and Space Administration, 1969.
- [51] A. L. Goldenveizer, G. Herrmann, and P. M. Naghdi, "Theory of elastic thin shells," *J. Appl. Mech.*, vol. 30, no. 3, p. 479, 1963.

- [52] S. A. Ambarcumyan, *Theory of anisotropic plates: strength, stability, vibration*. Technomic Publishing, 1970.
- [53] L. H. Donnell, *Beams, Plates, and Shells*. New York, NY, McGraw-Hill, 1976.
- [54] E. Ventsel, T. Krauthammer, and E. J. A. M. R. Carrera, "Thin Plates and Shells: Theory, Analysis, and Applications," *Appl. Mech. Rev.*, vol. 55, pp. B72–B73, 07 2002.
- [55] S. Timoshenko and S. Woinowsky-Krieger, *Theory of Plates and Shells*. Engineering mechanics series, McGraw-Hill, 1959.
- [56] K. Chau. Le, "Vibrations of shells and rods," *J. Acoust. Soc. Am.*, vol. 109, no. 2, pp. 443–443, 2001.
- [57] M. Levinson, "An accurate, simple theory of the statics and dynamics of elastic plates," *Mech Res Comm*, vol. 7, no. 6, pp. 343–350, 1980.
- [58] J. N. Reddy, "A Simple Higher-Order Theory for Laminated Composite Plates," *J. Appl. Mech.*, vol. 51, pp. 745–752, 12 1984.
- [59] J. N. Reddy, *Mechanics of laminated composite plates and shells: theory and analysis*. CRC Press, 2003.
- [60] J. Reddy and C. Liu, "A higher-order shear deformation theory of laminated elastic shells," *Int. J. Eng. Sci.*, vol. 23, no. 3, pp. 319–330, 1985.

- [61] Ö. Civalek, "Harmonic differential quadrature-finite differences coupled approaches for geometrically nonlinear static and dynamic analysis of rectangular plates on elastic foundation," *J. Sound Vib.*, vol. 294, no. 4-5, pp. 966–980, 2006.
- [62] K. Bhaskar and T. K. Varadan, *Plates: Theories and Applications*. Ane/Athena Books, Wiley, 2014.
- [63] A. D. Pierce, "2 - variational formulations in acoustic radiation and scattering," in *Physical Acoustics*, vol. 22 of *Physical Acoustics*, pp. 195 – 371, Academic Press, 1993.
- [64] E. G. Williams, *Fourier acoustics: sound radiation and nearfield acoustical holography*. Elsevier, 1999.
- [65] W. Li, X. Zhang, J. Du, and Z. Liu, "An exact series solution for the transverse vibration of rectangular plates with general elastic boundary supports," *J. Sound Vib.*, vol. 321, no. 1, pp. 254 – 269, 2009.
- [66] C. Bert and M. Malik, "Frequency equations and modes of free vibrations of rectangular plates with various edge conditions," *Proc. Inst. Mech. Eng. C J. Mech. Eng. Sci.*, vol. 208, no. 5, pp. 307–319, 1994.
- [67] S. J. W. Rayleigh, "On the infinitesimal bending of surfaces of revolution," *Proc. London Math. Soc.*, vol. s1-13, no. 1, pp. 4–16, 1881.

- [68] S. J. W. Rayleigh, "Note on the free vibrations of an infinitely long cylindrical shell," *Proc. Roy. Soc. Lon.*, vol. 45, pp. 443–448, 1888.
- [69] S. J. W. Rayleigh, "On the bending and vibration of thin elastic shells, especially of cylindrical form," *Proc. Roy. Soc. Lon.*, vol. 45, no. 273-279, pp. 105–123, 1889.
- [70] H. Lamb, "On the vibrations of a spherical shell," *Proc. London Math. Soc.*, vol. s1-14, no. 1, pp. 50–56, 1882.
- [71] A. E. H. Love and G. H. Darwin, "The small free vibrations and deformation of a thin elastic shell," *Philos. Trans. Roy. Soc. A*, vol. 179, pp. 491–546, 1888.
- [72] A. Leissa, *Vibration of Shells*. NASA SP, Scientific and Technical Information Office, National Aeronautics and Space Administration, 1973.
- [73] L. Pope, E. Wilby, C. Willis, and W. Mayes, "Aircraft interior noise models: Sidewall trim, stiffened structures, and cabin acoustics with floor partition," *J. Sound Vib.*, vol. 89, no. 3, pp. 371 – 417, 1983.
- [74] C. Fuller, J. Maillard, M. Mercadal, and A. von Flotow, "Control of aircraft interior noise using globally detuned vibration absorbers," *J. Sound Vib.*, vol. 203, no. 5, pp. 745 – 761, 1997.

- [75] J. E. Cole III, A. W. Stokes, J. M. Garrelick, and K. F. Martini, "Analytical modeling of the structureborne noise path on a small twin-engine aircraft," *NASA*, vol. CR, no. 4136, 1988.
- [76] J. Cole, "Vibrations of a framed cylindrical shell submerged in and filled with acoustic fluids: Spectral solution," *Computers and Structures*, vol. 65, no. 3, pp. 385 – 393, 1997.
- [77] L. Koval, "On sound transmission into a stiffened cylindrical shell with rings and stringers treated as discrete elements," *J. Sound Vib.*, vol. 71, no. 4, pp. 511 – 521, 1980.
- [78] J. F. Gieras, C. Wang, and J. C. Lai, *Noise of polyphase electric motors*. CRC Press, 2005.
- [79] A. D. Pierce, "Waves on Fluid-Loaded Inhomogeneous Elastic Shells of Arbitrary Shape," *Journal of Vibration and Acoustics*, vol. 115, pp. 384–390, 10 1993.
- [80] A. N. Norris and D. A. Rebinsky, "Membrane and Flexural Waves on Thin Shells," *Journal of Vibration and Acoustics*, vol. 116, pp. 457–467, 10 1994.
- [81] I. P. Getman and O. N. Lisitskii, "Reflection and transmission of sound waves through the interfacial boundary of two joined elastic half-strips," *J. Appl. Math. Mech.*, vol. 52, no. 6, pp. 816–820, 1988.

- [82] A. S. Zilbergreit and E. B. Suslova, "Contact waves of bend in thin plates," *Akoust Journal*, vol. 29, no. 2, pp. 186–191, 1985.
- [83] R. Stoneley, "The elastic waves at the interface of two solids," *Proc. Roy. Soc. London A*, vol. 106, no. 738, pp. 416–428, 1924.
- [84] J. D. Kaplunov and M. V. Wilde, "Free interfacial vibrations in cylindrical shells," *JASA*, vol. 111, no. 6, pp. 2692–2704, 2002.
- [85] G. Mikhasev and P. Tovstik, *Localized Dynamics of Thin-Walled Shells*. Chapman & Hall/CRC Monographs and Research Notes in Mathematics, CRC Press, 2020.
- [86] J. B. Lawrie and J. Kaplunov, "Edge waves and resonance on elastic structures: an overview," *Math. Mech. Solids*, vol. 17, no. 1, pp. 4–16, 2012.
- [87] A. V. Belov, J. D. Kaplunov, and E. V. Nolde, "A refined asymptotic model of fluid-structure interaction in scattering by elastic shells," *Flow, Turbulence and Combustion*, vol. 61, no. 1, pp. 255–267, 1998.
- [88] M. Junger and D. Feit, *Sound, Structures, and Their Interaction*. MIT Press classic, MIT Press, 1986.
- [89] A. D. Pierce, *Acoustics: an introduction to its physical principles and applications*. Springer, 2019.

- [90] G. A. Briggs, *Acoustic Microscopy*. Monographs on the physics and chemistry of materials, Clarendon Press, 1992.
- [91] W. B. Joyce, "Sabine's reverberation time and ergodic auditoriums," *J. Acoust. Soc. Am.*, vol. 58, no. 3, pp. 643–655, 1975.
- [92] M. C. Gutzwiller, *Chaos in classical and quantum mechanics*, vol. 1. Springer, New York, NY, 2013.
- [93] R. L. Weaver, "Spectral statistics in elastodynamics," *J. Acoust. Soc. Am.*, vol. 85, no. 3, pp. 1005–1013, 1989.
- [94] R. Weaver, "On the ensemble variance of reverberation room transmission functions, the effect of spectral rigidity," *J. Sound Vib.*, vol. 130, no. 3, pp. 487–491, 1989.
- [95] C. Ellegaard, T. Guhr, K. Lindemann, H. Q. Lorensen, J. Nygård, and M. Oxborrow, "Spectral statistics of acoustic resonances in aluminum blocks," *Phys. Rev. Lett.*, vol. 75, pp. 1546–1549, Aug 1995.
- [96] C. Ellegaard, T. Guhr, K. Lindemann, J. Nygård, and M. Oxborrow, "Symmetry breaking and spectral statistics of acoustic resonances in quartz blocks," *Phys. Rev. Lett.*, vol. 77, pp. 4918–4921, Dec 1996.
- [97] M. Fink, "Time reversed acoustics.," *Phys. Today*, vol. 50, no. 3, pp. 34–40, 1997.

- [98] F. Tappert and M. Brown, "Asymptotic phase errors in parabolic approximations to the one-way helmholtz equation," *J. Acoust. Soc. Am.*, vol. 99, pp. 1405–1413, Mar. 1996.
- [99] V. P. Maslov and M. Fedoriuk, *Semi-classical approximation in quantum mechanics*. Mathematical Physics and Applied Mathematics, Springer Netherlands, 1981.
- [100] J. Heading, *An Introduction to Phase-Integral Methods*. Dover books on mathematics, Dover Publications, Incorporated, 2013.
- [101] M. V. Berry and K. E. Mount, "Semiclassical approximations in wave mechanics," *Rep. Prog. Phys.*, vol. 35, pp. 315–397, jan 1972.
- [102] K. V. Shajesh, "Eikonal approximation." <http://www.nhn.ou.edu/~shajesh/eikonal/sp.pdf>, 2010.
- [103] L. Brekhovskikh, *Waves in layered media*, vol. 16 of *Applied Mathematics and Mechanics*. Elsevier, 2012.
- [104] J. Achenbach, A. Gautesen, and H. McMaken, *Ray Methods for Waves in Elastic Solids: with Applications to Scattering by Cracks*. Pitman Advanced Publishing Program, 1982.
- [105] J. B. Keller and F. C. Karal Jr., "Surface wave excitation and propagation," *J. Appl. Phys.*, vol. 31, no. 6, pp. 1039–1046, 1960.

- [106] J. B. Keller and F. C. Karal Jr., "Geometrical theory of elastic surface-wave excitation and propagation," *J. Acoust. Soc. Am.*, vol. 36, no. 1, pp. 32–40, 1964.
- [107] B. Rulf, "Rayleigh waves on curved surfaces," *J. Acoust. Soc. Am.*, vol. 45, no. 2, pp. 493–499, 1969.
- [108] M. Razavy, *Quantum Theory of Tunneling*. World Scientific, 2003.
- [109] J. Jortner and B. Pullman, "Tunneling, reidel publ," *Co., Boston*, 1986.
- [110] V. A. Benderskii, V. Goldanskii, and J. Jortner, "Tunneling in chemical reactions," 1993.
- [111] B. Chance, D. C. Devault, H. Frauenfelder, R. Marcus, J. Schrieffer, and N. Sutin, "Tunneling in biological system," *Academic Press, New York*, vol. 1, p. 211, 1979.
- [112] C. Zhu, H. Nakamura, N. Re, and V. Aquilanti, "The two-state linear curve crossing problems revisited. i. analysis of stokes phenomenon and expressions for scattering matrices," *J. Chem. Phys.*, vol. 97, no. 3, pp. 1892–1904, 1992.
- [113] H. Nakamura, "What are the basic mechanisms of electronic transitions in molecular dynamic processes?," *Int. Rev. Phys. Chem.*, vol. 10, no. 2, pp. 123–188, 1991.

- [114] L. D. Landau and E. M. Lifshitz, *Quantum mechanics: non-relativistic theory*. Elsevier, 1977.
- [115] C. G. Callan and S. Coleman, "Fate of the false vacuum. ii. first quantum corrections," *Phys. Rev. D*, vol. 16, pp. 1762–1768, Sep 1977.
- [116] D. Bohm, *Quantum Theory*. Dover Publications, New York, Dover Publications, 1989.
- [117] B. Ricco and M. Y. Azbel, "Physics of resonant tunneling. the one-dimensional double-barrier case," *Phys. Rev. B*, vol. 29, no. 4, p. 1970, 1984.
- [118] E. Granot and M. Y. Azbel, "Resonant tunneling in two dimensions via an impurity," *Phys. Rev. B*, vol. 50, no. 12, p. 8868, 1994.
- [119] E. Granot and M. Y. Azbel, "Resonant angular dependence in a weak magnetic field," *J. Condens. Matter Phys.*, vol. 11, no. 20, p. 4031, 1999.
- [120] M. Y. Azbel, "Eigenstate assisted activation," *Phys. Rev. Lett.*, vol. 68, no. 1, p. 98, 1992.
- [121] G. Zangwill and E. Granot, "Eigenstate suppressed activation," *Physica B*, vol. 461, pp. 140–146, 2015.
- [122] M. Settnes, S. R. Power, D. H. Petersen, and A. P. Jauho, "Theoretical analysis of a dual-probe scanning tunneling microscope setup on graphene," *Phys. Rev. Lett.*, vol. 112, no. 9, p. 096801, 2014.

- [123] Z. Qi, D. A. Bahamon, V. M. Pereira, H. S. Park, D. K. Campbell, and A. H. C. Neto, "Resonant tunneling in graphene pseudomagnetic quantum dots," *Nano. Lett.*, vol. 13, no. 6, pp. 2692–2697, 2013.
- [124] V. Kashcheyevs and J. Timoshenko, "Quantum fluctuations and coherence in high-precision single-electron capture," *Phys. Rev. Lett.*, vol. 109, no. 21, p. 216801, 2012.
- [125] K. N. Kwok, *Complete Guide to Semiconductor Devices*. Wiley, 2010.
- [126] H. B. Gray and J. R. Winkler, "Electron tunneling through proteins," *Q. Rev. Biophys.*, vol. 36, no. 3, pp. 341–372, 2003.
- [127] N. Pavliček, I. Swart, J. Niedenführ, G. Meyer, and J. Repp, "Symmetry dependence of vibration-assisted tunneling," *Phys. Rev. Lett.*, vol. 110, no. 13, p. 136101, 2013.
- [128] R. Tsu and L. Esaki, "Tunneling in a finite superlattice," *App. Phys. Lett.*, vol. 22, no. 11, p. 562, 1973.
- [129] L. L. Chang, L. Esaki, and R. Tsu, "Resonant tunneling in semiconductor double barriers," *App. Phys. Lett.*, vol. 24, no. 12, p. 593, 1974.
- [130] M. Hirose, M. Morita, and Y. Osaka, "Resonant tunneling through si/sio₂ double barriers," *Jpn. J. Appl. Phys.*, vol. 16, p. 561, 1977.

- [131] T. C. L. G. Sollner, W. D. Goodhue, P. E. Tannenwald, C. D. Parker, and D. D. Peck, "Resonant tunneling through quantum wells at frequencies up to 2.5 thz," *App. Phys. Lett.*, vol. 43, no. 6, p. 588, 1983.
- [132] M. O. Vassell, J. Lee, and H. F. Lockwood, "Multibarrier tunneling in $\text{Ga}_{1-x}\text{Al}_x$ as/gaas heterostructures," *J. Appl. Phys.*, vol. 54, no. 9, p. 5206, 1983.
- [133] T. J. Shewchuk, P. C. Chapin, P. D. Coleman, W. Kopp, R. Fischer, and H. Morkoc, "Resonant tunneling oscillations in a $\text{Ga}_{1-x}\text{Al}_x$ as heterostructure at room temperature," *App. Phys. Lett.*, vol. 46, no. 5, p. 508, 1985.
- [134] E. E. Mendez, W. I. Wang, B. Ricco, and L. Esaki, "Resonant tunneling of holes in $\text{Al}_x\text{Ga}_{1-x}\text{As}$ heterostructures," *App. Phys. Lett.*, vol. 47, no. 4, pp. 415–417, 1985.
- [135] G. Tanner, "Dynamicall energy analysis—determining wave energy distributions in vibro-acoustical structures in the high-frequency regime," *J. Sound Vib.*, vol. 320, no. 4, pp. 1023–1038, 2009.
- [136] D. J. Chappell, G. Tanner, D. Löchel, and N. Søndergaard, "Discrete flow mapping: transport of phase space densities on triangulated surfaces," *Proc. Roy. Soc. A Math. Phys. Eng. Sci.*, vol. 469, no. 2155, p. 20130153, 2013.

- [137] D. J. Chappell and G. Tanner, "A boundary integral formalism for stochastic ray tracing in billiards," *Chaos: An Interdisciplinary Journal of Nonlinear Science*, vol. 24, no. 4, p. 043137, 2014.
- [138] J. Kaplunov, L. Yu Kossovich, and E. Nolde, *Dynamics of Thin Walled Elastic Bodies*. London: Academic Press, 1998.
- [139] V. Babich and A. Kiselev, *Elastic Waves: High Frequency Theory*. Chapman & Hall/CRC Monographs and Research Notes in Mathematics, CRC Press, 2018.
- [140] A. Shudo, Y. Ishii, and K. S. Ikeda, "Julia sets and chaotic tunneling: I," *J. Phys. A Math. Theor.*, vol. 42, p. 265101, jun 2009.
- [141] A. Shudo, Y. Ishii, and K. S. Ikeda, "Julia sets and chaotic tunneling: II," *J. Phys. A Math. Theor.*, vol. 42, p. 265102, jun 2009.
- [142] S. C. Creagh and N. D. Whelan, "Complex periodic orbits and tunneling in chaotic potentials," *Phys. Rev. Lett.*, vol. 77, pp. 4975–4979, Dec 1996.
- [143] O. Brodier, P. Schlagheck, and D. Ullmo, "Resonance-assisted tunneling," *Annals of Physics*, vol. 300, no. 1, pp. 88 – 136, 2002.
- [144] J. Ankerhold, *Quantum Tunneling in Complex Systems: The Semiclassical Approach*, vol. 224. Springer, 2007.

- [145] S. Keshavamurthy and P. Schlagheck, *Dynamical tunneling: theory and experiment*. CRC Press, 2011.
- [146] S. C. Creagh, "Tunnelling in multidimensional systems," *J. Phys. A Math. Gen.*, vol. 27, pp. 4969–4993, jul 1994.
- [147] L. H. Donnell, "Stability of thin-walled tubes under torsion," Tech. Rep. 479, 1933.
- [148] M. S. Qatu, "Recent research advances in the dynamic behavior of shells: 1989–2000, Part 2: Homogeneous shells," *Appl. Mech. Rev.*, vol. 55, pp. 415–434, 09 2002.
- [149] J. D. Kaplunov, G. A. Rogerson, and P. E. Tovstik, "Localized vibration in elastic structures with slowly varying thickness," *Q. J. Mech. Appl. Math.*, vol. 58, no. 4, pp. 645–664, 2005.
- [150] J. Postnova and R. V. Craster, "Trapped modes in 3d topographically varying plates," *IMA J. Appl. Math.*, vol. 73, no. 6, pp. 950–963, 2008.
- [151] D. Gridin, R. V. Craster, and A. T. Adamou, "Trapped modes in curved elastic plates," *Proc. Roy. Soc. A Math. Phys. Eng. Sci.*, vol. 461, no. 2056, pp. 1181–1197, 2005.
- [152] A. Pichugin, "Topographically guided waves in a thin plate," *J. Sound Vib.*, vol. 332, no. 1, pp. 1–6, 2013.

- [153] J. Gieras, C. Wang, and J. Lai, *Noise of Polyphase Electric Motors*. Electrical and Computer Engineering, CRC Press, 2018.
- [154] T. Uzer, C. Jaffé, J. Palacián, P. Yanguas, and S. Wiggins, "The geometry of reaction dynamics," *Nonlinearity*, vol. 15, pp. 957–992, apr 2002.
- [155] A. N. Norris, "Reflection and transmission of structural waves at an interface between doubly curved shells," *Acta Acustica United with Acustica*, vol. 84, no. 6, pp. 1066–1076, 1998.
- [156] S. Gnutzmann and U. Smilansky, "Quantum graphs: Applications to quantum chaos and universal spectral statistics," *Adv. Phys.*, vol. 55, no. 5-6, pp. 527–625, 2006.
- [157] M. V. Berry and K. E. Mount, "Semiclassical approximations in wave mechanics," *Rep. Prog. Phys.*, vol. 35, pp. 315–397, jan 1972.
- [158] S. C. Creagh, "Semiclassical transmission across transition states," *Nonlinearity*, vol. 18, no. 5, pp. 2089–2110, 2005.
- [159] C. Hansen, S. Snyder, X. Qiu, L. Brooks, and D. Moreau, *Active control of noise and vibration*. CRC Press, 2012.
- [160] S. C. Creagh, G. Gradoni, T. Hartmann, and G. Tanner, "Propagating wave correlations in complex systems," *J. Phys. A Math. Theor.*, vol. 50, no. 4, p. 045101, 2016.

- [161] M. O. S. M. Hillery, R. F. O'Connell, M. O. Scully, and E. P. Wigner, "Distribution functions in physics: fundamentals," *Phys. Rep.*, vol. 106, no. 3, pp. 121–167, 1984.
- [162] H. Stöckmann, *Quantum Chaos: An Introduction*. Cambridge University Press, 2007.
- [163] A. Torre, *Linear ray and wave optics in phase space: bridging ray and wave optics via the Wigner phase-space picture*. Elsevier, 2005.
- [164] M. A. Alonso, "Wigner functions in optics: describing beams as ray bundles and pulses as particle ensembles," *Advances in Optics and Photonics*, vol. 3, no. 4, pp. 272–365, 2011.
- [165] R. G. Littlejohn and R. Winston, "Corrections to classical radiometry," *JOSA A*, vol. 10, no. 9, pp. 2024–2037, 1993.
- [166] R. Winston, A. Kim, and K. Mitchell, "Measuring radiance: a paradigm for coherence optics in six-dimensional phase space," *J. Mod. Opt.*, vol. 53, no. 16-17, pp. 2419–2429, 2006.
- [167] T. Dittrich and L. A. Pachón, "Time-domain scars: resolving the spectral form factor in phase space," *Phys. Rev. Lett.*, vol. 102, no. 15, p. 150401, 2009.
- [168] N. Marcuvitz, "The quasiparticle view of wave propagation," *Proceedings of the IEEE*, vol. 79, no. 10, pp. 1350–1358, 1991.

- [169] G. Gradoni, S. C. Creagh, G. Tanner, C. Smartt, and D. W. Thomas, "A phase-space approach for propagating field-field correlation functions," *New J. Phys.*, vol. 17, no. 9, p. 093027, 2015.
- [170] G. Gradoni, L. R. Arnaut, S. C. Creagh, G. Tanner, M. H. Baharuddin, C. Smartt, and D. W. Thomas, "Wigner-function-based propagation of stochastic field emissions from planar electromagnetic sources," *IEEE Transactions on Electromagnetic Compatibility*, vol. 60, no. 3, pp. 580–588, 2018.
- [171] G. Gradoni, D. M. Ramapriya, S. C. Creagh, G. Tanner, M. H. Baharuddin, H. Nasser, C. Smartt, and D. W. Thomas, "Near-field scanning and propagation of correlated low-frequency radiated emissions," *IEEE Transactions on Electromagnetic Compatibility*, vol. 60, no. 6, pp. 2045–2048, 2018.
- [172] G. Gradoni, J. H. Yeh, B. Xiao, T. M. Antonsen, S. M. Anlage, and E. Ott, "Predicting the statistics of wave transport through chaotic cavities by the random coupling model: A review and recent progress," *Wave Motion*, vol. 51, no. 4, pp. 606–621, 2014.
- [173] S. Hemmady, T. M. Antonsen, E. Ott, and S. M. Anlage, "Statistical prediction and measurement of induced voltages on components within complicated enclosures: A wave-chaotic approach," *IEEE Transactions on Electromagnetic Compatibility*, vol. 54, no. 4, pp. 758–771, 2012.

- [174] A. Berry, J. L. Guyader, and J. Nicolas, "A general formulation for the sound radiation from rectangular, baffled plates with arbitrary boundary conditions," *J. Acoust. Soc. Am.*, vol. 88, no. 6, pp. 2792–2802, 1990.
- [175] J. W. Yoo, "Study on the general characteristics of the sound radiation of a rectangular plate with different boundary edge conditions," *J. Mech. Sci. Technol.*, vol. 24, no. 5, pp. 1111–1118, 2010.
- [176] P. Cvitanovic, R. Artuso, R. Mainieri, G. Tanner, G. Vattay, N. Whelan, and A. Wirzba, "Chaos: classical and quantum," *ChaosBook.org (Niels Bohr Institute, Copenhagen 2005)*, vol. 69, 2005.
- [177] P. M. Morse and R. H. Bolt, "Sound waves in rooms," *Rev. Mod. Phys.*, vol. 16, no. 2, p. 69, 1944.
- [178] M. R. Schroeder, "Measurement of sound diffusion in reverberation chambers," *J. Acoust. Soc. Am.*, vol. 31, no. 11, pp. 1407–1414, 1959.
- [179] M. R. Schroeder, "Frequency-correlation functions of frequency responses in rooms," *J. Acoust. Soc. Am.*, vol. 34, no. 12, pp. 1819–1823, 1962.
- [180] R. H. Lyon, "Statistical analysis of power injection and response in structures and rooms," *J. Acoust. Soc. Am.*, vol. 45, no. 3, pp. 545–565, 1969.
- [181] S. Schlotzhauer, *Elementary Statistics Using JMP*. SAS Press, SAS Press, 2007.

- [182] Statistical Office of the European Communities, *New Techniques and Technologies for Statistics II: Proceedings of the Second Bonn Seminar*. IOS Press, 1997.
- [183] D. M. Ramapriya, G. Gradoni, S. C. Creagh, G. Tanner, E. Moers, and I. López Arteaga, "Nearfield acoustical holography – a wigner function approach," *J. Sound Vib.*, vol. 486, p. 115593, 2020.
- [184] D. M. Ramapriya, *Mathematical modelling of wireless chip-to-chip communication within enclosures*. PhD thesis, The University of Nottingham, 2020.
- [185] M. V. Berry, "Statistics of nodal lines and points in chaotic quantum billiards: perimeter corrections, fluctuations, curvature," *J. Phys. A Math. Gen.*, vol. 35, no. 13, p. 3025, 2002.
- [186] E. G. Williams and J. D. Maynard, "Numerical evaluation of the rayleigh integral for planar radiators using the fft," *J. Acoust. Soc. Am.*, vol. 72, no. 6, pp. 2020–2030, 1982.
- [187] G. Barton, *Elements of Green's functions and propagation: potentials, diffusion, and waves*. Oxford University Press, 1989.
- [188] E. W. Weisstein, "Fast fourier transform," <https://mathworld.wolfram.com/>, 2015.
- [189] M. Norton and D. Karczub, *Fundamentals of Noise and Vibration Analysis for Engineers*. Cambridge University Press, 2003.

- [190] L. Xu and X. Jia, "Electromechanical coupled vibration for double coupled micro beams," *Int. J. Acoust. Vib.*, vol. 12, no. 1, pp. 51–24, 2007.
- [191] M. Gomperts, "Sound radiation from baffled, thin, rectangular plates," *Acta Acustica united with Acustica*, vol. 37, no. 2, pp. 93–102, 1977.
- [192] L. Cremer, M. Heckl, and E. Ungar, *Structure-borne Sound; Structural Vibrations and Sound Radiation at Audio Frequencies*. Springer-Verlag, 1973.
- [193] G. Maidanik, "Radiation efficiency of panels," *J. Acoust. Soc. Am.*, vol. 35, no. 1, pp. 115–115, 1963.
- [194] F. Leppington, E. G. Broadbent, and K. Heron, "Acoustic radiation from rectangular panels with constrained edges," *Proc. Roy. Soc. A Math. Phys. Sci.*, vol. 393, no. 1804, pp. 67–84, 1984.
- [195] S. D. Snyder and N. Tanaka, "Calculating total acoustic power output using modal radiation efficiencies," *J. Acoust. Soc. Am.*, vol. 97, no. 3, pp. 1702–1709, 1995.
- [196] B. Korenev, *Bessel Functions and Their Applications*. Analytical Methods and Special Functions, CRC Press, 2002.
- [197] G. Xie, D. J. Thompson, and C. J. C. Jones, "The radiation efficiency of baffled plates and strips," *J. Sound Vib.*, vol. 280, no. 1-2, pp. 181–209, 2005.

- [198] D. Delande and D. Sornette, "Acoustic radiation from membranes at high frequencies: The quantum chaos regime," *J. Acoust. Soc. Am.*, vol. 101, no. 4, pp. 1793–1807, 1997.
- [199] N. M. Mohammed, S. C. Creagh, and G. Tanner, "Tunnelling around bends—wave scattering in curved shell structures," *Wave Motion*, vol. 101, p. 102697, 2021.
- [200] N. M. Mohammed, S. C. Creagh, G. Tanner, and D. J. Chappell, "Tunnelling corrections to wave transmissions on shell structures," in *28th Proc. Int. Conf. on Noise and Vibration Engineering ISMA*, pp. 2349–2362, 2018.
- [201] N. M. Mohammed, S. C. Creagh, and G. Tanner, "Sound radiation from complex vibrating mechanical structures using wignertransformation techniques," in *14th Proc. Int. Conf. on Mathematical and Numerical Aspects of Wave Propagation WAVES*, p. 530, 2019.
- [202] P. M. Pinsky and T. J. Hughes, "Research in computational methods for structural acoustics.," tech. rep., Department of the Navy, Seattle, USA, 1996.
- [203] M. Petyt and C. J. C. Jones, *Numerical methods in acoustics*. Spon Press: London, UK, 2004.
- [204] D. Griffel, *Applied Functional Analysis*. Dover Books on Mathematics, Dover Publications, 2012.

- [205] H. Waalkens, R. Schubert, and S. Wiggins, "Wigner's dynamical transition state theory in phase space: classical and quantum," *Nonlinearity*, vol. 21, no. 1, p. R1, 2007.
- [206] I. S. Gradshteyn and I. M. Ryzhik, *Table of integrals, series, and products*. Academic Press, 2014.